

ENERGY STORAGE CERAMICS: SYNTHESIS AND CHARACTERIZATION

Ph.D. THESIS

by

ABHISHEK KUMAR GUPTA



**DEPARTMENT OF METALLURGICAL AND MATERIALS ENGINEERING
INDIAN INSTITUTE OF TECHNOLOGY ROORKEE
ROORKEE – 247667 (INDIA)
MARCH, 2021**

ENERGY STORAGE CERAMICS: SYNTHESIS AND CHARACTERIZATION

A THESIS

Submitted in partial fulfilment of the requirements for the award of the degree

of

DOCTOR OF PHILOSOPHY

in

METALLURGICAL AND MATERIALS ENGINEERING

by

ABHISHEK KUMAR GUPTA



**DEPARTMENT OF METALLURGICAL AND MATERIALS ENGINEERING
INDIAN INSTITUTE OF TECHNOLOGY ROORKEE
ROORKEE – 247667 (INDIA)
MARCH, 2021**



**©INDIAN INSTITUTE OF TECHNOLOGY ROORKEE, ROORKEE-2021
ALL RIGHTS RESERVED**




INDIAN INSTITUTE OF TECHNOLOGY ROORKEE

STUDENT'S DECLARATION

I hereby certify that the work presented in the thesis entitled “ENERGY STORAGE CERAMICS: SYNTHESIS AND CHARACTERIZATION” is my own work carried out during a period from August, 2014 to November, 2020 under the supervision of Prof. Anjan Sil, Department of Metallurgical and Materials Engineering, Indian Institute of Technology Roorkee.

The matter presented in the thesis has not been submitted for the award of any other degree of this or any other Institute.

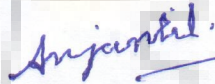
Dated: 3/3/21


(ABHISHEK KUMAR GUPTA)

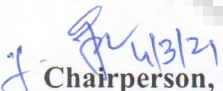
SUPERVISOR'S DECLARATION


This is to certify that the above mentioned work is carried out under my supervision.

Dated: 3/3/2021



(ANJAN SIL)

The Ph.D. Viva-Voce Examination of Mr. Abhishek Kumar Gupta, Research Scholar, has been held on 3 March 2021.


Chairperson, SRC


Dr SOMADITYA SEN
PHYSICS dept., IIT Indore
3rd March 2021
External Examiner

This is to certify that the student has made all the corrections in the thesis.


Supervisor
Dated: 4/3/21


Head of Department
विभागाध्यक्ष/Head
धातुकर्म एवं पदार्थ अभियान्त्रिकी विभाग
Metallurgical & Materials Engg. Deptt.
भा० प्रौ० सं० रुड़की/ I.I.T. Roorkee

Abstract

In today's era, where the world is moving towards miniaturization, light weight, cheaper electronics, easy integration etc., high energy density dielectric capacitors are essential to increase its volumetric efficiency. If the energy density of dielectric capacitors come at par with electrochemical capacitors or even batteries, the diversity of energy storage applications will increase dramatically. Lead zirconate titanate ($\text{Pb}(\text{Zr}_{1-x}\text{Ti}_x)\text{O}_3$ or PZT) ferroelectric ceramics exhibit high dielectric and piezoelectric properties and are widely used in many applications such as sensors, actuators, transducers, ceramic capacitors, FRAM chips etc. The sintering of PZT ceramics has been challenging due to the volatile nature of PbO at temperatures $>600^\circ\text{C}$ which is detrimental to dielectric and energy storage performance. Spark plasma sintering (SPS) technique has been successfully used for sintering ceramics to high density at lower sintering temperature than required for conventional sintering process.

The tetragonal, rhombohedral, orthorhombic and MPB phase composition of PZT ceramics are synthesized by using SPS technique. Each sintered specimen showed density greater than 98% of theoretical density. The effect of SPS temperature (800, 850, 900, 950 $^\circ\text{C}$) on phase composition, phase constitution, grain size and permittivity was investigated for MPB phase composition of PZT ceramics. It was observed that the rapid sintering technique causes compositional fluctuation and optimization of SPS temperature is essential. Rietveld refinement was carried out to identify the phases in the sintered specimens. The PZT specimens sintered at or above 900 $^\circ\text{C}$ showed presence of multiple phases instead of single tetragonal phase. It was proposed that the highest permittivity observed for 900 $^\circ\text{C}$ sintered specimen was due to the presence of monoclinic phase resulting in enhanced polarization in PZT.

The impedance and electric modulus studies were conducted on the PZT samples at room temperature over the frequency range 0.01 Hz to 1 MHz to investigate the different electrical relaxation mechanisms. The analysis revealed approximated Debye type behaviour for low frequency relaxation process for all the samples. The separation of grain and grain boundary relaxation processes was observed in the frequency dependent imaginary electrical modulus M''

plots and complex modulus spectra rather than in Bode plots and Nyquist plots. Such contrast was attributed to high resistance and low capacitance of the bulk contribution. PZT sintered at 900°C compared to samples sintered at other temperatures, has shown unique combination of tetragonal and monoclinic crystal structures of constituent phases and the material exhibits highest impedance, electrical modulus and energy storage performance among all the samples sintered at different temperatures.

The transition of micron-sized grains to nano-sized grains in these ceramics significantly influences its phase transition, ferroelectric properties and energy storage performance. Generally, the low permittivity grain boundary layers were reported as the key factor in influencing the dielectric properties in nano ceramics. $\text{PbZr}_{0.52}\text{Ti}_{0.48}\text{O}_3$ compound was synthesized via solid state reaction and sintered by both SPS and conventional sintering (CS) techniques. The sintering time was greatly reduced in SPS samples with time period of the order of minutes relative to time requirement of hours for CS samples. The SPS specimen exhibited dense microstructure with grains in nano-scale region whereas for CS specimen, the microstructure shows broad grain size distribution with micro-scale grains. The Rietveld refinement data revealed that the SPS specimen has the desired phase composition and constitution which is in agreement to the distinct narrow peaks observed at each phase transition in the permittivity curves. In addition, the energy storage efficiency of SPS sample is two times that of CS sample. The underlying reason for such behaviour is due to the suppression of hysteresis behaviour in fine-grained SPS samples due to the increased clamping of domain wall motion that leads to lower remnant polarization.

In spite of high dielectric and electromechanical properties of PZT, even for compositions close to the MPB, they are rarely used in commercial devices in pristine form. The effect of 2 mol% La^{3+} doping on phase composition, microstructure, dielectric permittivity and energy storage performance of PZT(52/48) ceramics has been studied. The spark plasma sintering profile adopted was similar to undoped PZT ceramics and the relative density of the sintered specimen becomes greater than 99%. The analysis of microstructure revealed decrease in grain size of PLZT ceramics over PZT ceramics due to smaller ionic radii of La^{3+} . The room temperature dielectric constant of SPS ceramics was significantly higher than the conventionally sintered counterparts reported which is attributed to enhanced domain wall motion. The temperature dependent permittivity curves are more broadened compared to that of undoped ceramics suggesting increased diffusivity of La^{3+} ions. The impedance and modulus studies confirm the presence of grain and grain boundary relaxation mechanisms in the PLZT ceramics where the

bulk resistance of grain boundaries are higher. Low frequency conductivity behaviour suggests hopping of charge carriers whereas long range conductivity is revealed at high frequency region. The saturation polarization has increased for PLZT ceramics, however, the energy efficiency is decreased by 20% due to large hysteresis in PLZT ceramics.

Nejezchleb et al. 1980 reported that the oxygen partial pressure during sintering influences the dielectric properties of the material. The chromium ion has been known to exist in multiple valence states and is doped in PZT to increase the mechanical quality factor when Cr exhibits +3 oxidation state. Therefore, it is interesting to see how SPS technique influences the oxidation state of Cr to affect the dielectric properties and energy storage performance of Cr doped PZT ceramics. The microstructure, phase analysis, impedance and modulus spectroscopy, dielectric and energy storage characteristics have been investigated on Cr doped (0.2, 0.4, 0.6, 0.8 wt %) PZT (52/48) ceramics. The particle size lies between 200 and 500 nm and the particles mostly exhibit faceted morphology. The perovskite structure is not distorted by introduction of Cr ions and no separate peaks related to Cr has been detected which indicates solubility of Cr ions in the PZT ceramics. The Cr doped specimens exhibit ≥ 99.3 % relative density with average grain size lower than the average grain size of undoped PZT specimens. The dielectric permittivity of the materials was found to increase up to 0.6 wt% Cr doping which is explained on the basis of multivalent nature of chromium ion. The energy storage studies reveal increase in remnant polarization and coercive field up to 0.6 wt% Cr content and the results are in agreement with the dielectric behavior. The impedance and modulus spectroscopic studies reveal the contributions from grain relaxation in the material and confirm the non-debye type of relaxation in the material. The DC conductivity curves show a typical Arrhenius type behaviour of electrical conductivity.

Acknowledgements

This doctoral thesis is a result of perseverance, hard work and invaluable support. Therefore, I would like to grab this opportunity to express my debt towards all those who were directly or indirectly a part of this challenging yet exciting journey. First and foremost of all, I would like to acknowledge my thesis supervisor, PROF. ANJAN SIL, who introduced me to the wonderful world of energy materials. His stature, poise and honesty has always inspired and motivated me to be a better human being in life. I have always admired your patient and diligent approach towards solving research problems and understood the importance of strengthening core knowledge of any subject/ topic. I also appreciate your numerous suggestions on scientific writing which has further improved my English writing skill. It has been an honor to learn and work beside you.

I would like to bestow my sincere thanks to DR. G.P. CHAUDHARI, Professor and Head of Department of Metallurgical and Materials Engineering in addition to the former Heads of the department for providing the necessary instrumentation facilities. I express my profound gratitude to the SRC members namely PROF. B.V. MANOJ KUMAR, PROF. TAPAS MANDAL, PROF. B.S.S. DANIEL and PROF. UJJWAL PRAKASH for their constructive criticism and suggestions at each progress seminar. I especially thank PROF. B.V. MANOJ KUMAR who gave me an opportunity to use and operate the Spark Plasma Sintering instrumentation facility as it was one of the core components of my doctoral thesis. In addition, I also thank MR. DHAN PRAKASH, technical staff of Ceramic lab for his invaluable support during my Ph.D. work.

I gratefully acknowledge the research group of Prof. K.L. Yadav and PROF. YOGESH SHARMA, Department of Physics for their warm hospitality and technical support to help me carry out dielectric and energy storage experiments in their respective labs. I am also thankful to Institute Instrumentation centre (IIC) for providing me with the essential characterization facilities.

It cannot be stressed enough that no challenging journey is complete without the support of friends and colleagues. I especially thank my seniors, DR. SOBHIT SAXENA, DR. SIDDHARTH,

DR. SANDAN SHARMA, DR. SUTHARAVEL MUTHAIAH, DR. RAM KISHORE ANANT and DR. SOUMYA SHANKAR GHOSH for guiding me and providing useful information during my doctoral program in advance. A special thanks to DR. SANDAN SHARMA for appreciating and guiding me towards future opportunities even after leaving IIT. I have really enjoyed the everyday conversations and company of my batch mates and colleagues, SURENDRA CHOURASIYA, ATUL SHARMA, MRINMOY SINHA, ANIRUDDHA MALAKAR, HIMANSHU KALA, PANKAJ RAWAT, SUMIT KUMAR and RATNAKAR SINGH. I also acknowledge and thank my junior colleagues, HARI RAJ, HITESH, YASHPAL, AKESHWAR, LEKHRAJ and LAVINA for being a part of our “Lockdown Celebs” group. The joyous memories and ever-lasting laughter among us even in the harsh times of on-going pandemic will forever be etched in my memory.

I feel privileged to have a wonderful Energy materials research group that created a soothing atmosphere and helped me swiftly progress throughout my Ph.D. I express my heartfelt praise towards DR. SOBHIT SAXENA who stands out in particular among the crowd due to his joyous and kind nature, comic timing and supporting others financially even when broke. He has the Gift of the gab, to which I always told him, that he could easily be a wonderful teacher. We both really enjoyed eating due to our foodie nature. I would always remember our endless chats on numerous topics to no end. I am thankful to DR. SIDDHARTH for guiding and encouraging me whenever I was set off course. I will remember DR. SOUMYA’s deliciously made non-veg recipes which always lifted my mood. I would also like to thank Mr. Hari Raj, whose utmost hard work and dedication has always inspired me, a true role model for anyone who is deep into research. I express my thanks to MR. AYUSH PUNDIR, an epitome of positively refreshing attitude in whom I see my own shadow. I also acknowledge MR. BHARAT VERMA whose administrative skills regarding purchasing of items always intrigued me. Lastly, I extend my special thanks to MR. HITESH BASITTI, who recently joined our group. Due to his utmost supporting nature, we bonded really fast and is more like a younger brother to me. I will always cherish the innumerable memories with the group such as trekking, long tea-breaks, never ending conversations etc.

The endless love and the source of my strength has been the support of my family members. I extend my sincere gratitude towards my father, PROF. S.K. GUPTA and mother, MRS. NILIMA GUPTA, who have been my pillar of support at every step of this challenging journey. Even-though, I have been reckless here and there, they have always been the endless fuel for all my life. A special and sincere thanks to my father, who has always been the role model for me in my academic career. His sense of dedication, hard work, honesty and care for the family as well as his students never ceases to amaze me. I would never be at my current position and

standing if not for him. I am so thankful to my younger brother, MR. ANIMESH GUPTA, whose level of maturity even extends mine at his age. He has been the true support system for our parents in my absence and has managed to solve countless family problems. I also acknowledge my youngest brother, Mr. Nitin Chandra for his love, encouragement and support.

I acknowledge and extend special thanks to my life partner, DR. VINEETA GUPTA, who came into my life as a breath of fresh air and love in the midst of my PhD journey. Her hard working, foresightedness and resourceful nature helped in eradicating my procrastination behaviour. Having been preoccupied with her medical duties, she still managed and supported me throughout the programme. I would never forget how she encouraged and persuaded me to help me focus on my doctoral thesis writing. This thesis would not be complete in its present form and in the specified time if not for you. I am also in debt on how she motivated me to be physically active outdoors and to keep my BMI on check, as the PhD program consumed a lot of sitting hours. Whenever you read this my progeny, know that I felt so blessed and fortunate on having heard about you during the final stage of my PhD. The thought of you always made me smile even in the toughest of times.

This work was funded by the Ministry of Human Resource and Development (MHRD), Government of India.

Contents

<i>Abstract</i>	i
<i>Acknowledgements</i>	v
<i>Contents</i>	ix
<i>List of Figures</i>	xv
<i>List of Tables</i>	xxi
<i>List of Publications</i>	xxiii
<i>List of Conferences</i>	xxv
<i>List of Abbreviations</i>	xxvii
Chapter 1 Introduction	1
1.1 Introduction	1
1.2 Thesis overview	4
Chapter 2 Literature review	7
2.1 Ferroelectric Materials	7
2.2 Ferroelectric Domains	15
2.3 PZT solid solution	16
2.4 Phase coexistence near MPB compositions	17
2.5 Modification/doping on PZT	21
2.5.1 Types of dopants	21
2.6 Literature survey	25
2.6.1 Types of dopants	25
2.6.2 Domain configurations in PZT ceramics	27
2.6.3 Impedance and modulus spectroscopic studies on undoped and doped PZT ceramics	28

2.6.4 Probable reasons for dielectric maxima at MPB	29
2.6.5 Energy storage properties of undoped and doped PZT ceramics	30
2.6.6 Sintering concepts	31
2.6.7 Basics of Spark plasma sintering	32
2.6.8 Effect of Spark plasma sintering method on dielectric and ferroelectric properties of undoped and doped PZT ceramics	32
2.6.9 Motivation and objectives of the present thesis work	37
Chapter 3 Experimental procedures	39
3.1 Introduction	39
3.2 Composition selection	39
3.3 Bulk processing of materials	40
3.4 Spark plasma sintering (SPS)	42
3.4.1 Introduction	42
3.4.2 SPS configuration	44
3.4.3 Mechanism/working of SPS	45
3.4.3.1 Electrical effects	45
3.4.3.2 Mechanical effects	46
3.4.3.3 Thermal effects	47
3.4.4 Temperature and pressure profiles used in Spark plasma sintering	48
3.5 Characterization techniques	49
3.5.1 Density	49
3.5.2 X-ray diffraction (XRD)	49
3.5.2.1 Rietveld refinement	51
3.5.3 Scanning electron microscopy (SEM)	53
3.5.3.1 Energy dispersive X-ray spectroscopy (EDS)	54
3.5.4 Electroding of sample surface	55
3.5.5 Dielectric properties	55
3.5.6 Complex impedance and modulus spectroscopy	56
3.5.7 Energy storage properties	59

3.6 Summary	61
Chapter 4 Structural and dielectric characterization of PbZr_xTi_{1-x}O₃	63
4.1 Introduction	63
4.1.1 Composition selection	63
4.1.2 SEM and EDX analysis of calcined PZT compositions	64
4.1.3 Structural characterization of PZT specimens	65
4.1.4 Spark plasma sintering of PZT specimens	66
4.1.5 Microstructural observation of sintered PZT samples	67
4.1.6 Compositional fluctuation in PZT specimens	69
4.2 Phase composition and dielectric properties of spark plasma sintered PbZr _{0.52} Ti _{0.48} O ₃	69
4.2.1 SEM analysis	70
4.2.2 XRD analysis	71
4.2.3 Temperature and pressure profiles used in Spark plasma sintering	71
4.2.4 Structural analysis	73
4.2.5 Microstructural analysis of spark plasma sintered samples	76
4.2.6 Dielectric measurements	79
4.2.7 Summary	82
Chapter 5 Effect of sintering temperature on spark plasma sintered PZT with MPB composition: Impedance and energy storage analyses	83
5.1 Introduction	83
5.2 X-ray diffraction analysis of spark plasma sintered PbZr _{0.52} Ti _{0.48} O ₃	83
5.3 Variation of Z' with frequency	85
5.4 Variation of M' with frequency	86
5.5 Variation of Z'' with frequency	87
5.6 Variation of M'' with frequency	88
5.7 Analysis of combined impedance (Z'') and electric modulus (M'') spectroscopic plots against frequency	89

5.8 Analysis of Nyquist plots and complex modulus spectra	91
5.9 Conductivity studies	92
5.10 Energy storage studies	93
5.11 Summary	95
Chapter 6 Comparative evaluation of spark plasma and conventional sintering of PZT ceramic with MPB composition	99
6.1 Introduction	99
6.2 SEM analysis of calcined powder used for SPS and CS samples	99
6.3 Sintering profiles used for SPS and CS samples	100
6.4 Microstructure analysis	101
6.5 XRD analysis	102
6.6 Dielectric studies	103
6.7 Conductivity studies	105
6.8 Temperature dependent dielectric studies	105
6.9 Energy storage studies	108
6.10 Summary	109
Chapter 7 Dielectric and energy storage studies of 2 mol % La doped $\text{PbZr}_{0.52}\text{Ti}_{0.48}\text{O}_3$ spark plasma sintered ceramics	111
7.1 Introduction	111
7.2 Experimental descriptions	111
7.3 SEM analysis of calcined PLZT ceramic	112
7.4 X-ray diffraction studies of PLZT ceramic	114
7.5 SPS profile adopted for PLZT ceramic	115
7.6 SEM analysis of sintered PLZT ceramic	116
7.7 Dielectric studies of PLZT ceramic	116
7.8 Impedance and modulus spectroscopy studies	119
7.9 Conductivity studies	125
7.10 Energy storage studies of PLZT ceramic	126

7.11 Summary	127
Chapter 8 Dielectric characterization and energy storage performance of Cr (0.2, 0.4, 0.6, 0.8 wt.%) doped $\text{PbZr}_{0.52}\text{Ti}_{0.48}\text{O}_3$ ceramics	129
8.1 Introduction	129
8.2 Experimental descriptions	129
8.3 SEM analysis of calcined Cr doped PZT ceramics	130
8.4 XRD analysis of calcined Cr doped PZT ceramics	131
8.5 SPS profile employed for Cr doped PZT ceramics	132
8.6 SEM analysis of sintered Cr doped PZT ceramics	133
8.7 XRD analysis of sintered Cr doped PZT ceramics	134
8.8 XPS analyses of Cr doped PZT ceramics	136
8.9 Dielectric studies of Cr doped PZT ceramics	138
8.10 Impedance and modulus spectroscopic studies of Cr doped PZT ceramics	141
8.11 Conductivity studies of Cr doped PZT ceramics	149
8.12 Energy storage studies of Cr doped PZT ceramics	151
8.13 Summary	153
Chapter 9 Conclusion and Future scope	155
9.1 Conclusions	155
9.2 Comparative features	157
9.2.1 Variation in lattice parameters, crystallite size and lattice strain with sintering temperature	157
9.2.2 Variation in crystallite size and lattice strain with composition of PZT	158
9.2.3 Variation of dielectric properties with different composition of the PZT samples	159
9.2.4 Variation of ferroelectric properties with different composition of the PZT samples	160
9.3 Future scope	161
Bibliography	163



List of Figures

1.1	Ragone plot of different energy storage devices (Christen and Carlen 2000)	2
2.1	Flowchart representation of Piezoelectric, Pyroelectric and Ferroelectric materials.	7
2.2	The unit cell of perovskite structure of ABO_3 in the (a) cubic phase, (b) tetragonal phase, (c) orthorhombic phase and (d) rhombohedral phase.	11
2.3	Representation of Poling in ferroelectric materials.	12
2.4	Typical $P E$ loop characteristics of ferroelectrics.	13
2.5	Formation of domains in perovskite ferroelectric $PbTiO_3$.	15
2.6	Phase diagram of PZT by (Jaffe, Cook, and Jaffe 1971).	17
2.7	Phase diagram of $PbZr_{1-x}Ti_xO_3$ (PZT) solid solution along MPB (Noheda et al.).	19
2.8	Dependence of dielectric constant of PZT with composition.	21
2.9	Temperature dependence of the dielectric constant of soft and hard PZT ferroelectric ceramics measured from 4.2 to 300 K. The experimental data are after (X. L. Zhang et al. 1983).	25
3.1	XRD patterns of $PbZr_{0.52}Ti_{0.48}O_3$ powders calcined at 800°C, 850°C, 900°C and 950°C.	41
3.2	Mass transfer path during sintering (Suarez et al. 2013).	42
3.3	Schematic representation of (a) SPS and (b) HP process (Suarez et al. 2013).	43
3.4	Power supply characteristics used in (a) PAS and (b) SPS techniques (Suarez et al. 2013).	44
3.5	Configuration of SPS apparatus.	45
3.6	Basic mechanism of neck formation by mechanical pressure during SPS (Tokita 2013).	47
3.7	SPS profile adopted for representative sample sintered at 950°C showing different temperature and pressure stages during a sintering cycle.	49

3.8	Peak splitting's in XRD pattern for a cubic material transforming to a phase of lower symmetry.	51
3.9	Schematic of electron scattering in SEM.	54
3.10	Nyquist plot of (a) Debye single relaxation time model (b) distribution of relaxation time model (Essaleh et al. 2016).	56
3.11	Nyquist plot for two parallel RC elements connected in series (Essaleh et al. 2016).	58
3.12	Schematic illustration of ferroelectric P-E loops for typical relaxor ferroelectrics (Yang et al. 2019).	61
4.1	Flow chart showing the materials synthesis to property determination.	64
4.2	Scanning electron micrographs and EDS spectra of $\text{PbZr}_{0.3}\text{Ti}_{0.7}\text{O}_3$, $\text{PbZr}_{0.7}\text{Ti}_{0.3}\text{O}_3$ and $\text{PbZr}_{0.97}\text{Ti}_{0.03}\text{O}_3$ calcined at 900°C.	65
4.3	Diffraction profiles of $\text{PbZr}_{0.3}\text{Ti}_{0.7}\text{O}_3$, $\text{PbZr}_{0.7}\text{Ti}_{0.3}\text{O}_3$ and $\text{PbZr}_{0.97}\text{Ti}_{0.03}\text{O}_3$ calcined at 900°C.	66
4.4	SPS profile adopted for $\text{PbZr}_{0.3}\text{Ti}_{0.7}\text{O}_3$ sample sintered at 900°C subjected to uniaxial load of 60 MPa.	67
4.5	Density and relative density of $\text{PbZr}_{0.3}\text{Ti}_{0.7}\text{O}_3$, $\text{PbZr}_{0.7}\text{Ti}_{0.3}\text{O}_3$ and $\text{PbZr}_{0.97}\text{Ti}_{0.03}\text{O}_3$ sintered at 900°C by SPS method.	67
4.6	SEM images of sintered pellets of $\text{PbZr}_{0.7}\text{Ti}_{0.3}\text{O}_3$, $\text{PbZr}_{0.3}\text{Ti}_{0.7}\text{O}_3$ and $\text{PbZr}_{0.97}\text{Ti}_{0.03}\text{O}_3$.	68
4.7	Variation of XRD pattern of calcined, sintered and annealed $\text{PbZr}_{0.3}\text{Ti}_{0.7}\text{O}_3$ along with its reference pattern.	70
4.8	(a) Scanning electron micrograph and (b) EDS spectrum of $\text{PbZr}_{0.52}\text{Ti}_{0.48}\text{O}_3$ powders calcined at 900°C for 4 hours.	70
4.9	XRD patterns of $\text{PbZr}_{0.52}\text{Ti}_{0.48}\text{O}_3$ powders calcined at 800°C, 850°C, 900°C and 950°C.	71
4.10	SPS profile adopted for sample sintered at 950°C (SPS-950) showing different temperature and pressure stages during a sintering cycle.	72
4.11	Observed, calculated and difference profiles generated in Rietveld refinement of samples sintered at 800°C, 850°C, 900°C and 950°C by SPS method.	74
4.12	Room temperature XRD (110), (111) and (200) peaks of SPS-800, SPS-850, SPS-900 and SPS-950.	75

4.13	Microstructures of $\text{PbZr}_{0.52}\text{Ti}_{0.48}\text{O}_3$ samples spark plasma sintered at different temperatures (a) 800°C, (b) 850°C, (c) 900°C and (d) 950°C.	77
4.14	Histogram of grain size distribution in (a) SPS-800, (b) SPS-850, (c) SPS-900 and (d) SPS-950.	78
4.15	EDS spectra of SPS-800, SPS-850, SPS-900 and SPS-950 samples.	79
4.16	Variation of (a) dielectric constant, (b) dielectric loss tangent with frequency of SPS-800, SPS-850, SPS-900 and SPS-950 samples at room temperature.	80
4.17	Room temperature dielectric constant of SPS-800, SPS-850, SPS-900 and SPS-950 samples as a function of temperature measured at 100 kHz.	81
5.1	XRD patterns of SPS-800, SPS-850, SPS-900 and SPS-950 samples along with magnified views of {002} splitting.	85
5.2	Frequency dependent plots of (a) real part of impedance, Z' (b) real part of electric modulus, M' of SPS-800, SPS-850, SPS-900 and SPS-950 samples at room temperature.	85
5.3	Frequency dependent Z'' plots of SPS-800, SPS-850, SPS-900 and SPS-950 samples at room temperature.	87
5.4	Frequency dependent M'' plots of SPS-800, SPS-850, SPS-900 and SPS-950 samples at room temperature along with inset showing the same from 0.01 Hz to 100 Hz.	89
5.5	Frequency dependent Z'' and M'' plots of (a) SPS-800, (b) SPS-850, (c) SPS-900 and (d) SPS-950 at room temperature.	90
5.6	(a) Complex impedance and (b) complex modulus plots of SPS-800, SPS-850, SPS-900 and SPS-950 samples at room temperature.	91
5.7	Frequency dependent conductivity plots of SPS-800, SPS-850, SPS-900 and SPS-950 samples at room temperature.	93
5.8	Ferroelectric hysteresis loops of SPS-800, SPS-850, SPS-900 and SPS-950 samples at room temperature with an applied electric field maximum up to 50 kV/cm.	94
6.1	(a) Scanning electron micrograph and (b) EDS analyses of $\text{PbZr}_{0.52}\text{Ti}_{0.48}\text{O}_3$ powders calcined at 900°C.	100
6.2	SPS profile adopted for $\text{PbZr}_{0.52}\text{Ti}_{0.48}\text{O}_3$ showing different temperature and pressure stages during a sintering cycle.	101

6.3	Scanning electron micrographs of $\text{PbZr}_{0.52}\text{Ti}_{0.48}\text{O}_3$ sintered by (a) SPS at 900°C and (b) conventional sintering at 1200°C.	102
6.4	X-ray diffractograms of $\text{PbZr}_{0.52}\text{Ti}_{0.48}\text{O}_3$ sintered by CS and SPS method.	102
6.5	Variation of dielectric constant with frequency of $\text{PbZr}_{0.52}\text{Ti}_{0.48}\text{O}_3$ at room temperature sintered by SPS and CS method.	103
6.6	Variation of dielectric loss tangent with frequency of $\text{PbZr}_{0.52}\text{Ti}_{0.48}\text{O}_3$ at room temperature sintered by SPS and CS method.	104
6.7	Frequency dependent AC conductivity plots of $\text{PbZr}_{0.52}\text{Ti}_{0.48}\text{O}_3$ sintered by SPS and CS method.	105
6.8	Variation of dielectric constant with temperature of (a) spark plasma and (b) conventionally sintered $\text{PbZr}_{0.52}\text{Ti}_{0.48}\text{O}_3$ sample at 0.5, 1, 5, 10, 50, 100 and 1000 kHz frequencies.	107
6.9	Ferroelectric hysteresis loop of $\text{PbZr}_{0.52}\text{Ti}_{0.48}\text{O}_3$ sintered by SPS and CS method under maximum applied electric field of ~50 kV/cm.	108
7.1	The ball milled PLZT powders separated from zirconia balls by a 600 μm stainless steel mesh.	112
7.2	SEM image along with histogram of particle size distribution of PLZT powders calcined at 900°C.	113
7.3	EDS mapping of Pb, Zr, La and Ti elements in the studied PLZT sample.	113
7.4	XRD pattern of PLZT powders calcined at 900°C along with magnified views of {111} and {002} splitting.	114
7.5	SPS profile adopted for PLZT ceramic sintered at 900°C subjected to a uniaxial load of 60 MPa.	115
7.6	SEM image along with histogram of grain size distribution of PLZT ceramic sintered at 900°C.	116
7.7	Variation of dielectric constant (ϵ') and dielectric loss tangent ($\tan \delta$) with frequency of PLZT ceramic at room temperature.	117
7.8 (a)	Temperature dependent plots of dielectric constant (ϵ') at selected frequencies of PLZT ceramic. The inset shows the same for frequencies other than 100 Hz.	118
7.8 (b)	Temperature dependent plots of dielectric loss tangent ($\tan \delta$) at selective frequencies of PLZT ceramic.	119
7.9	Frequency dependent plots of (a) real part of impedance, Z' (b) imaginary part of impedance, Z'' of PLZT ceramic at room temperature.	120

7.10	Frequency dependent plots of (a) real part of complex electric modulus, M' (b) imaginary part of complex electric modulus, M'' of PLZT ceramic at room temperature.	121
7.11	Complex impedance and complex modulus spectra of PLZT ceramic at room temperature.	121
7.12	(a) Frequency dependent plots of real part of impedance, Z' (b) frequency dependent plots of imaginary part of impedance, Z'' at 100°C, 200°C, 300°C, 350°C and 400°C temperatures; (c) variation of relaxation time estimated from impedance plot, $\ln(\tau_z)$ as a function of inverse of absolute temperature of $(\text{Pb}_{0.98}\text{La}_{0.02})(\text{Zr}_{0.52}\text{Ti}_{0.48})\text{O}_3$.	122
7.13	(a) Frequency dependent plots of real part of electric modulus, M' (b) frequency dependent plots of imaginary part of electrical modulus, M'' at 100°C, 200°C, 300°C, 350°C and 400°C temperatures; (c) variation of relaxation time estimated from modulus plot, $\ln(\tau_m)$ as a function of inverse of absolute temperature of $(\text{Pb}_{0.98}\text{La}_{0.02})(\text{Zr}_{0.52}\text{Ti}_{0.48})\text{O}_3$.	124
7.14	(a) Complex impedance and (b) complex modulus plane plots of $(\text{Pb}_{0.98}\text{La}_{0.02})(\text{Zr}_{0.52}\text{Ti}_{0.48})\text{O}_3$ ceramic measured at 100°C, 200°C, 300°C, 350°C and 400°C temperatures.	125
7.15	Frequency dependent conductivity plots of PLZT ceramics at (a) room temperature and (b) 100, 200, 300, 350, 400 °C temperatures.	126
7.16	Ferroelectric hysteresis loops of PLZT sample under an applied maximum electric field of ~45 kV/cm at room temperature.	127
8.1	Scanning electron micrographs of $\text{PbZr}_{0.52}\text{Ti}_{0.48}\text{O}_3 - x\text{Cr}$ powders calcined at 900°C.	130
8.2	EDS graphs of $\text{PbZr}_{0.52}\text{Ti}_{0.48}\text{O}_3 - x\text{Cr}$ powders calcined at 900°C.	131
8.3	XRD patterns of $\text{PbZr}_{0.52}\text{Ti}_{0.48}\text{O}_3 - x\text{Cr}$ powders for $x = 0, 0.2, 0.4, 0.6$ and 0.8 calcined at 900°C.	132
8.4	SPS profiles adopted for $\text{PbZr}_{0.52}\text{Ti}_{0.48}\text{O}_3 - x\text{Cr}$ ceramics sintered at 900°C.	133
8.5	Microstructure of $\text{PbZr}_{0.52}\text{Ti}_{0.48}\text{O}_3 - x\text{Cr}$ ceramics sintered by SPS method at 900°C.	134
8.6	Histogram of grain size distribution of $\text{PbZr}_{0.52}\text{Ti}_{0.48}\text{O}_3 - x\text{Cr}$ ceramics sintered by SPS method at 900°C.	135
8.7	XRD patterns of $\text{PbZr}_{0.52}\text{Ti}_{0.48}\text{O}_3 - x\text{Cr}$ ceramics for $x = 0, 0.2, 0.4, 0.6$ and 0.8 sintered at 900°C.	136

8.8	XPS spectra of Cr 2p _{3/2} of PbZr _{0.52} Ti _{0.48} O ₃ – xCr for (a) x = 0.2, (b) x = 0.4, (c) x = 0.6 and (d) x = 0.8 ceramics.	138
8.9	Temperature dependent plots of dielectric constant (ϵ_r) of PbZr _{0.52} Ti _{0.48} O ₃ – xCr ceramics at 1, 10, 100, 1000 kHz frequencies.	140
8.10	Temperature dependent plots of dielectric loss tangent ($\tan \delta$) of PbZr _{0.52} Ti _{0.48} O ₃ – xCr ceramics at 1, 10, 100, 1000 kHz frequencies.	141
8.11	Frequency dependent plots of real part of impedance (Z') of PbZr _{0.52} Ti _{0.48} O ₃ – xCr ceramics at 150°C, 200°C, 250°C, 300°C, 350°C and 400°C temperatures.	142
8.12	Frequency dependent plots of imaginary part of impedance (Z'') of PbZr _{0.52} Ti _{0.48} O ₃ – xCr ceramics at 300°C, 350°C and 400°C temperatures. The inset shows the same for 150°C, 200°C and 250°C temperatures.	143
8.13	Variation of relaxation time estimated from impedance plot, $\log(\tau_z)$ as a function of inverse of absolute temperature of PbZr _{0.52} Ti _{0.48} O ₃ – xCr ceramics. The calculated activation energy (E _a) values are marked onto the fitted data.	144
8.14	Nyquist plot of PbZr _{0.52} Ti _{0.48} O ₃ – xCr ceramics at 300°C, 350°C and 400°C temperatures. The inset shows the same for 150°C, 200°C and 250°C temperatures.	145
8.15	Frequency dependent plots of real part of electric modulus (M') of PbZr _{0.52} Ti _{0.48} O ₃ – xCr ceramics at 150°C, 200°C, 250°C, 300°C, 350°C and 400°C temperatures.	147
8.16	Frequency dependent plots of imaginary part of electric modulus (M'') of PbZr _{0.52} Ti _{0.48} O ₃ – xCr ceramics at 150°C, 200°C, 250°C, 300°C, 350°C and 400°C temperatures.	148
8.17	Variation of relaxation time estimated from modulus plot, $\log(\tau_m)$ as a function of inverse of absolute temperature of PbZr _{0.52} Ti _{0.48} O ₃ – xCr ceramics. The calculated activation energy (E _a) values are marked onto the fitted data.	149
8.18	Frequency dependent plots of AC conductivity of PbZr _{0.52} Ti _{0.48} O ₃ – xCr ceramics at 150°C, 200°C, 250°C, 300°C, 350°C and 400°C temperatures.	150
8.19	Variation of dc conductivity as a function of inverse of absolute temperature of PbZr _{0.52} Ti _{0.48} O ₃ – xCr ceramics. The calculated activation energy (E _a) values are marked onto the fitted data.	151

- 8.20 Ferroelectric hysteresis loops of $\text{PbZr}_{0.52}\text{Ti}_{0.48}\text{O}_3 - x\text{Cr}$ ceramics for (a) $x = 0.2$, (b) $x = 0.4$, (c) $x = 0.6$ and (d) $x = 0.8$; (e) variation of coercive field and remnant polarization with Cr_2O_3 content. 153





List of Tables

2.1	Modification in PZT with different dopants (Helke and Lubitz 2008).	22
2.2	Major effects of additives on characteristic properties of PZT. Ionic radius is given in parentheses in 'nm' units.	23
2.3	Energy storage properties of undoped and doped PZT ceramics reported.	30
2.4	Comparison of dielectric and ferroelectric properties of PZT compositions by conventional and spark plasma sintering.	33
3.1	Raw material components used in the synthesis of doped and undoped PZT.	40
4.1	Theoretical density and abbreviations of different PZT compositions used.	64
4.2	Physical properties of $\text{PbZr}_{0.3}\text{Ti}_{0.7}\text{O}_3$, $\text{PbZr}_{0.7}\text{Ti}_{0.3}\text{O}_3$ and $\text{PbZr}_{0.97}\text{Ti}_{0.03}\text{O}_3$ samples.	68
4.3	Calcination, sintering and annealing temperature along with relative densities of samples sintered at 800°C, 850°C, 900°C and 950°C by SPS method.	73
4.4	Refined structural parameters for samples sintered at 800°C, 850°C, 900°C and 950°C by SPS method.	76
5.1	Calculated relaxation time, capacitance, resistance parameters for grain and grain boundary relaxation.	90
5.2	Energy storage parameters for different samples.	95
6.1	Sintering parameters for $\text{PbZr}_{0.52}\text{Ti}_{0.48}\text{O}_3$ ceramics sintered by SPS and CS method.	101
6.2	Lattice parameters and tetragonality of $\text{PbZr}_{0.52}\text{Ti}_{0.48}\text{O}_3$ ceramics sintered by SPS and CS method.	103
6.3	Energy storage parameters for $\text{PbZr}_{0.52}\text{Ti}_{0.48}\text{O}_3$ sintered by SPS and CS method.	109
7.1	Calculated values of τ_{gb} , R_g , R_{gb} and C_{gb} at selective temperatures of PLZT specimen.	124

7.2	Energy storage parameters of PLZT sample compared to undoped PZT.	127
8.1	Atomic concentration of individual peak profile in Cr 2p _{3/2} XPS spectra of PbZr _{0.52} Ti _{0.48} O ₃ – xCr ceramics.	137
8.2	The observed values of Curie temperature (°C) and maximum dielectric constant (ϵ_m) at 1, 10, 100 and 1000 kHz of PbZr _{0.52} Ti _{0.48} O ₃ – xCr ceramics.	139
8.3	Calculated values of τ_g , R_g and C_g at selective temperatures of PbZr _{0.52} Ti _{0.48} O ₃ – xCr ceramics.	145
8.4	Energy storage parameters calculated from the <i>P-E</i> hysteresis loops of PbZr _{0.52} Ti _{0.48} O ₃ – xCr ceramics.	152



List of Publications

1. **Gupta, Abhishek Kumar**, and Anjan Sil. 2020. “Phase Composition and Dielectric Properties of Spark Plasma Sintered $\text{PbZr}_{0.52}\text{Ti}_{0.48}\text{O}_3$.” *Materials Research Express* 7(3): 036301.
2. **Gupta, Abhishek Kumar**, and Anjan Sil. 2020. “Effect of sintering temperature on spark plasma sintered $\text{PbZr}_{0.52}\text{Ti}_{0.48}\text{O}_3$: Impedance and energy storage analysis”, *Physica B: Condensed Matter*, 601: 412641.
3. **Gupta, Abhishek Kumar**, and Anjan Sil. 2020. “Dielectric characterization and energy storage performance of Cr (0.2, 0.4, 0.6, 0.8 wt.%) doped $\text{PbZr}_{0.52}\text{Ti}_{0.48}\text{O}_3$ ceramics”, *Journal of European ceramic society: Under review*.

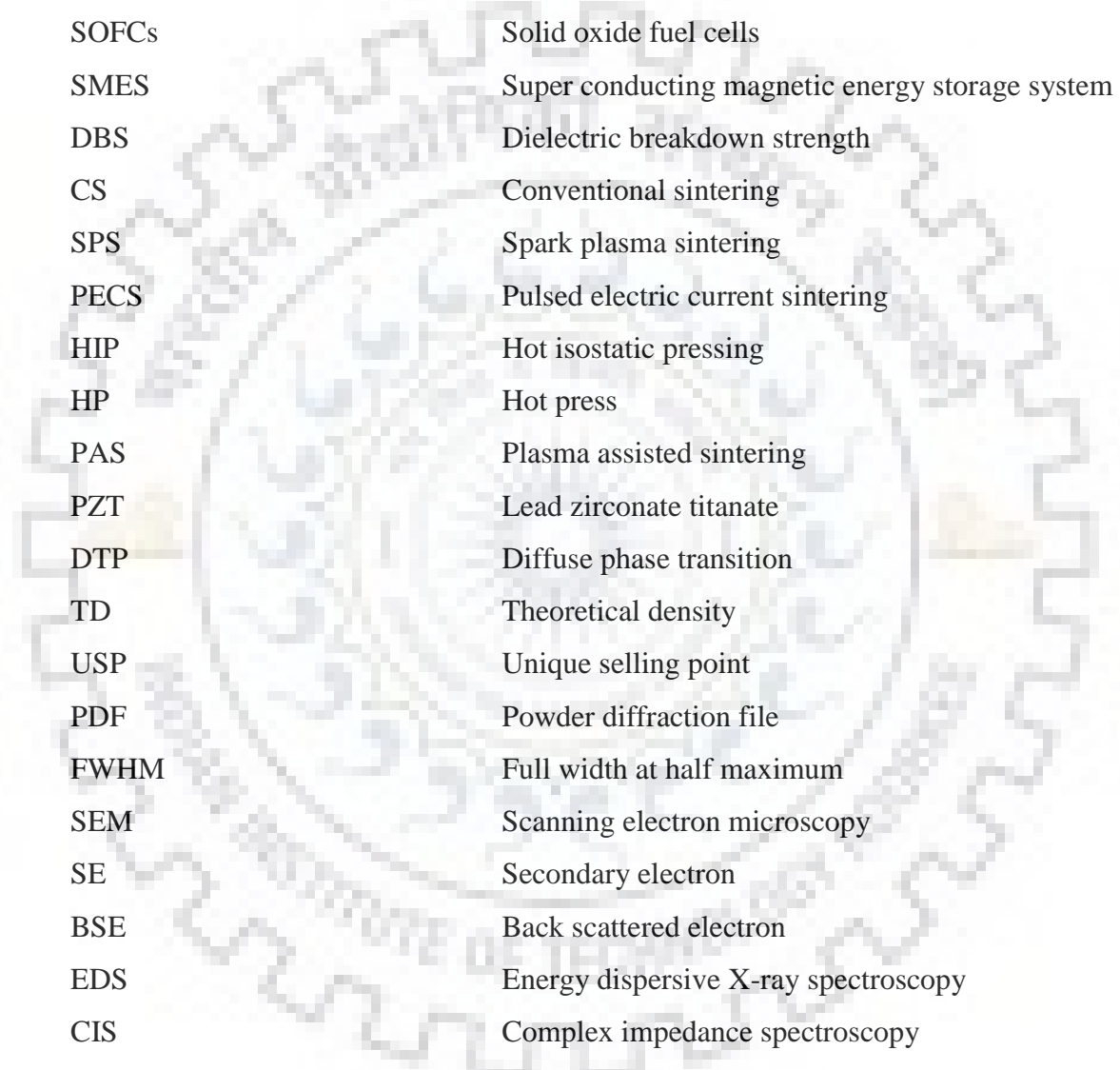


List of Conferences

1. **Abhishek K. Gupta** and Anjan Sil “Energy storage performance of $(\text{Pb}_{0.97}\text{Ba}_{0.01}\text{La}_{0.02})(\text{Zr}_{0.68}\text{Sn}_{0.24}\text{Ti}_{0.08})\text{O}_3$ ceramic fabricated by spark plasma sintering” The International Conference on Recent Advances in Materials & Manufacturing Technologies (IMMT-19), BITS Pilani, Dubai campus, UAE, 20-23rd November, 2019.
2. **Abhishek K. Gupta** and Anjan Sil “Temperature dependant stability of energy storage properties of spark plasma sintered $\text{PbZr}_{0.52}\text{Ti}_{0.48}\text{O}_3$ for pulsed power applications” International meeting on Energy storage devices (IMESD-18), IIT Roorkee, Roorkee, 10-12th December, 2018.
3. **Abhishek K. Gupta** and Anjan Sil “Comparative studies on dielectric and energy storage performance of conventional and spark plasma sintered $\text{PbZr}_{0.52}\text{Ti}_{0.48}\text{O}_3$ ” International Conference on Nanotechnology (ICN:3I-2017), IIT Roorkee, Roorkee, 6-8th December, 2017.
4. **Abhishek K. Gupta** and Anjan Sil “Energy storage performance of spark plasma sintered antiferroelectric $\text{PbZr}_{0.97}\text{Ti}_{0.03}\text{O}_3$ ceramic” International Conference on Advances in Materials & Processing: Challenges & Opportunities” (AMPCO-2017), IIT Roorkee, Roorkee, 30th Nov. – 2nd December, 2017. [**Best Poster Award**]
5. **Abhishek K. Gupta** and Anjan Sil “Energy storage performance of $\text{PbZr}_{0.52}\text{Ti}_{0.48}\text{O}_3$ ” ceramic fabricated by spark plasma sintering” 55th National Metallurgists’ Day (NMD ATM-2017), BITS Pilani- KK Birla, Goa campus, 11-14th November, 2017.



List of Abbreviations



IEA	The International Energy Agency
SOFCs	Solid oxide fuel cells
SMES	Super conducting magnetic energy storage system
DBS	Dielectric breakdown strength
CS	Conventional sintering
SPS	Spark plasma sintering
PECS	Pulsed electric current sintering
HIP	Hot isostatic pressing
HP	Hot press
PAS	Plasma assisted sintering
PZT	Lead zirconate titanate
DTP	Diffuse phase transition
TD	Theoretical density
USP	Unique selling point
PDF	Powder diffraction file
FWHM	Full width at half maximum
SEM	Scanning electron microscopy
SE	Secondary electron
BSE	Back scattered electron
EDS	Energy dispersive X-ray spectroscopy
CIS	Complex impedance spectroscopy
CPE	Constant phase element
ESD	Estimated standard deviation

Chapter 1

Introduction

1.1 Introduction

The accelerated growth in world population and the surge in global economy have increased the energy consumption at a very rapid rate. The International Energy Agency (IEA) reports total primary energy supply of 1.66×10^{14} Wh (5.98×10^{17} joules) in the year 2019 relative to 1.015×10^{14} Wh (3.66×10^{17} joules) in 1990 (International Energy Agency 2020). Various clean and renewable energy solutions need to be utilized to counter the environmental problems such as global warming, air/water pollution, climate change, depletion of natural resources etc. (Guney and Tepe 2017; Ibrahim, Ilinca, and Perron 2008; Liu et al. 2010; Panwar, Kaushik, and Kothari 2011). Even though more than half of the energy consumption is through fossil fuels, renewable energy sources namely biomass, hydropower, geothermal, wind and solar are becoming more dominant since the last decade (International Energy Agency 2020). Renewable energy sources are naturally inexhaustible but limited in amount available per unit of time, thereby, posing a challenge to harness these energy sources.

Transforming renewable energy to electrical energy is of prime necessity. Therefore, electrical energy storage solutions that provide efficient and reliable energy storage are required (H. Chen et al. 2009; Dincer 2000; Gross, Leach, and Bauen 2003; Hall and Bain 2008; Kousksou et al. 2014). The electrical energy storage technologies comprise mainly of batteries, solid oxide fuel cells (SOFCs), electrochemical capacitors, dielectric capacitors, superconducting magnetic energy storage systems (SMES). Batteries and SOFCs produce high energy density but low power density whereas dielectric capacitors possess high power density and low energy density. The electrochemical capacitors produce medium power and energy density, however their operating voltage is low (< 3 V) and leakage current is high (\sim mA)(Kusko and Dedad 2007; K. Yao et al. 2011). Dielectric capacitors are more suited towards low cost, high voltage and large scale applications.

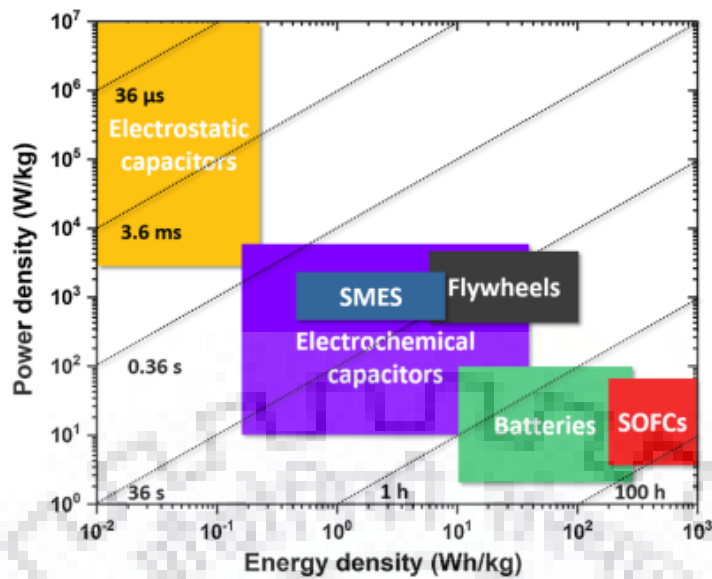


Fig. 1.1 Ragone plot of different energy storage devices (Christen and Carlen 2000).

The Ragone plot named after David V. Ragone is a plot used for comparison of different energy storage devices and is shown in Fig. 1.1. It can be observed that there is not a single energy storage device that can simultaneously possess both high energy density and high power density (Christen and Carlen 2000). The dielectric capacitors have higher charge/discharge rates relative to batteries and SOFCs as observed by the dashed lines in the figure. This is because the dielectric capacitors store energy by the displacement of charges and batteries store energy by chemical reactions. Capacitors have been exhaustively used in electronic circuits as decoupling devices which shunts the quick changes in input voltage (providing energy when voltage drops and absorbing energy when voltage spikes) and AC components in the circuit and as coupling capacitors to filter out the DC components. In addition, the capacitors are widely used in microwave applications, hybrid electric vehicles, pulsed power systems etc. Different capacitors are designed as per application requirement. For example microwave applications require very low dielectric loss capacitors and decoupling circuits require capacitors that have large capacitance per unit volume. The flow of renewable energy sources is non periodic, which can be efficiently harnessed by the capacitors (Sherrill et al. 2011). However, the energy density of dielectric capacitors (Whittingham 2008) is low as depicted in Fig. 1.1. In today's era, where the world is moving towards miniaturization, light weight, cheaper electronics, easy integration etc., high energy density dielectric capacitors are essential to increase its volumetric efficiency (Hao 2013; Li et al. 2014; Whittingham 2008; Z. Yao et al. 2017). If the energy density of dielectric capacitors come up to par with electrochemical capacitors or even batteries, the diversity of their energy storage applications will increase dramatically (K. Yao et al. 2011).

Commercially available solid state dielectric capacitors for high power applications are composed mainly of polymer and dielectric ceramics. However, the energy density produced is limited ($< 2 \text{ J/cm}^3$) (Hao 2013; Z. Yao et al. 2017). The dielectric breakdown strength (DBS) of ceramics is generally low and their dielectric permittivity is high while polymers exhibit the opposite features. Therefore, the polymers are generally fabricated into thin film form ($\sim \mu\text{m}$), and are stacked multiple times to achieve higher cumulative capacitance in real life applications. Leakage current of polymer based film capacitors increases rapidly under high electric fields due to space charges (Dissado and Fothergill 1992). As a result, polymer based capacitors cannot maintain high energy efficiency under high electric fields where the conduction losses act as a limiting factor for energy density (Q. Chen et al. 2008). In addition, the DBS of polymer capacitors also decreases sharply at high temperatures due to conduction losses (Choi et al. 2015; Li et al. 2015; Zhou et al. 2009). On the contrary, dielectric ceramics possess high permittivity and are stable at high temperatures, but they have low DBS. For energy storage, energy density of the material is directly proportional to the square of its DBS value. The dielectric breakdown strength is one of the most important factor since it's a measure of the maximum voltage that can be applied across the material. The literature survey indicates a negative relationship between permittivity and DBS (Jain and Rymaszewski 2002; Jia et al. 1995; Kim, Kim, and Oh 1994; J. McPherson et al. 2002; Joe W. McPherson et al. 2003; Neusel and Schneider 2014; Udayakumar et al. 1995; Ulrich et al. 2000) which may be due to the electrostrictive effect. Generally, it is observed that the highest energy density is observed for materials having medium permittivity and higher DBS (S. Chen et al. 2014; Y. Shen et al. 2017).

Dielectric materials can be fabricated into thin films, thick films and bulk materials. Thin films ($< 1 \mu\text{m}$) and thick films ($1\text{--}10 \mu\text{m}$) can tolerate higher applied electric field ($> 1000 \text{ kV/cm}$) due to their smaller volume associated with less defects and impurities (J. W. McPherson 2016). Therefore, they usually possess much higher energy density. Due to their small volume and low capacity, however, the total energy that can be stored in film materials is less than for their bulk counterparts. Lead-based materials have been extensively studied for bulk dielectrics, exhibiting high energy storage performance. For example, a large recoverable energy density of 6.4 J/cm^3 has been achieved in lead-based antiferroelectric ceramics (Zhang et al. 2015).

To achieve a compact, highly dense, pore-free bulk nanostructured ceramic has been difficult for several years. Consequently many dopants and sintering aids have been used with the base perovskite systems to achieve optimal results. The sintering of ceramics to achieve highly dense compacts with sub-micron sized grains is difficult to accomplish by conventional sintering methods. Therefore, many researchers are diverging towards using hybrid sintering

techniques utilizing pressure and temperature together for producing sintered compacts (Q. Chen et al. 2015; Kakegawa et al. 2003; Z. Shen et al. 2002; Takeuchi et al. 2000; Wada et al. 2003; Wu, Uekawa, and Kakegawa 2003). Spark plasma sintering (SPS) is the answer to many if not most problems faced while synthesizing bulk ceramics. SPS technique has received much attention due to its ability to densify specimens by very high heating rates, low sintering temperature and short sintering cycles. SPS utilizes current as a medium for heating and the plasma generated during sintering facilitates diffusion between particles uniformly throughout the calcined powders. This sintering technique can not only help us achieve highly dense nano-structured ceramics but also provides better energy storage properties since DBS directly correlates with high density of the ceramic.

In this work, SPS method has been exploited to synthesize high density doped and undoped PZT bulk ceramics so as to enhance its dielectric properties and energy storage performance. The influence of SPS method on the phase composition, phase constitution, microstructure, dielectric properties and energy storage performance has been investigated. Furthermore, it is of interest to see whether compositional fluctuation during synthesis of PZT bulk ceramics can be controlled by SPS method. The effect of doping in PZT bulk ceramic on dielectric and energy storage properties has also been studied.

1.2 Thesis Overview

The thesis is divided into nine chapters: -

Introduction (Chapter 1)

In this chapter, the technical background and motivation of research is presented along with objectives of the thesis.

Literature Review (Chapter 2)

The fundamental concepts of ferroelectric, ferroelectric domains, crystal structure, dielectric properties etc. are presented here. This chapter discusses the detailed survey of the previous works reported in relation to enhancing dielectric and energy storage properties in PZT systems along with the literature gap.

Experimental procedures (Chapter 3)

PZT ceramics have been synthesized by various routes since the early 1950s which primarily includes chemical route (sol-gel, polymer- sol-gel) and solid state route (milling). The

processing of PZT ceramics has been reported and refined over the years since the ultra-high properties at the morphotropic phase boundary (MPB) were reported. The objective in this chapter is not to devise any innovative way of synthesis of PZT ceramics, rather is to adopt a synthesis route that is efficient to reproduce PZT specimens of uniform microstructure to aid in comparative studies. However, special emphasis has been given to the sintering method used i.e. spark plasma sintering to produce highly dense and uniform microstructure of PZT ceramics. Also, characterization techniques to identify phase constitution, density, dielectric properties and ferroelectric properties are presented in this chapter.

Structural and dielectric characterization of $PbZr_xTi_{1-x}O_3$ (Chapter 4)

In this chapter, the methodology, synthesis and structural characterization of tetragonal, rhombohedral and orthorhombic phase compositions of PZT ceramic oxides are discussed. The compositions of these oxides have been selected from the PZT phase diagram. However, this chapter emphasizes on the MPB composition of PZT oxide ($PbZr_{0.52}Ti_{0.48}O_3$), as near the MPB, the functional properties of the material are superior. Rietveld refinement is conducted to detect the stoichiometric variation with sintering (SPS) temperature. In addition, the dielectric and energy storage investigations for MPB composition of PZT are also conducted. An effort has been made to correlate the dielectric and energy storage properties of $PbZr_{0.52}Ti_{0.48}O_3$ to its microstructure and phase constituents.

Effect of sintering temperature on spark plasma sintered PZT with MPB composition: Impedance and energy storage analyses (Chapter 5)

In this chapter, the impedance and electric modulus studies on the PZT samples at room temperature to investigate the different electrical relaxation mechanisms are presented. In addition, the energy storage properties have been investigated for the different PZT specimens. An effort is made to correlate the energy storage performance of the PZT specimens to their electrical relaxation processes.

Comparative evaluation of spark plasma and conventional sintering of PZT ceramic with MPB composition (Chapter 6)

This chapter discusses how $PbZr_{0.52}Ti_{0.48}O_3$ compound was synthesized via solid state reaction and sintered by both SPS as well as conventional sintering (CS). The microstructure, X-ray diffraction analysis and sintering parameters have been discussed for both the PZT specimens. The difference in physical properties and phase constitution has been noted.

Thereafter, dielectric, electrical conductivity and energy storage studies have been made. The probable causes for enhanced dielectric as well as energy storage performance of spark plasma sintered specimens have been discussed.

Dielectric and energy storage studies of 2 mol % La doped $PbZr_{0.52}Ti_{0.48}O_3$ spark plasma sintered ceramics (Chapter 7)

In this chapter, the phase composition, microstructure, dielectric permittivity and energy storage performance of 2 mol% La doped PZT (52/48) ceramics have been presented. Since La^{3+} is a soft dopant, it is expected to increase the dielectric permittivity of PZT ceramics. The enhanced dielectric permittivity will directly influence the energy storage performance due to polarization enhancement. In addition, the functional properties of PLZT ceramics are compared with that of undoped PZT ceramics. The different relaxation mechanisms in the material were analysed by complex impedance and complex modulus spectroscopic studies.

Dielectric characterization and energy storage performance of Cr (0.2, 0.4, 0.6, 0.8 wt. %) doped $PbZr_{0.52}Ti_{0.48}O_3$ ceramics (Chapter 8)

In this chapter, the microstructure, phase analysis, impedance and modulus spectroscopy, dielectric and energy storage characteristics of Cr doped (0.2, 0.4, 0.6, 0.8 wt.%) PZT (52/48) ceramics have been presented. (Nejezchleb 1980; Uchida and Ikeda 1967) reported that the Cr ions exists in +3, +5 or +6 multiple valence states in the PZT ferroelectric system. (Nejezchleb 1980) reported that the trivalent Cr ions oxidise into hexavalent Cr ions during PZT material synthesis. In addition, the author stated that the dielectric properties of Cr doped PZT ceramics depend on the oxygen partial pressure during sintering process. Therefore, the present chapter emphasizes on the effect of spark plasma sintering technique on the functional properties of Cr doped PZT ceramics.

Conclusion and Future scope (Chapter 9)

A conclusion of the experimentation and basic achievements is presented. Few suggestions were made for future scope of research to have a better knowledge about the SPS processing-structure-property relation.

Chapter 2

Literature Review

2.1 Ferroelectric Materials

The crystalline materials that exhibit spontaneous electric polarization are known as ferroelectric materials. In such materials, the direction of polarization can be reversed by applied electric field. This characteristic feature is only present in certain types of materials having non centrosymmetry in the arrangement of atoms. Among the 32 crystal classes, twenty one of them are non-centrosymmetric. The crystal classes that lack an inversion center as one of the symmetry element (non-centrosymmetric) can be polar, chiral or both. Among the twenty crystal classes that exhibit piezoelectric effect, ten classes have a unique polar axis and exhibit pyroelectricity. However, only some of them exhibit ferroelectricity since the strength of the electric field required to reorient the polarization direction may be higher than the dielectric breakdown strength of the material. Ferroelectric materials lose their ferroelectricity above the Curie temperature, T_C and the resulting phase is termed as paraelectric phase. Above T_C , the dependence of dielectric permittivity on temperature follows the Curie-Weiss law (eq. 2.1) similar to how magnetic permeability of ferromagnetic materials do. A representation portraying the ferroelectrics, pyroelectrics and piezoelectrics is given in Fig. 2.1.

$$\frac{\epsilon}{\epsilon_0} = \frac{C}{T - T_c} \quad (2.1)$$

where ϵ is the permittivity of the material, ϵ_0 is the permittivity of vacuum, T_c is the Curie temperature and C is the Curie constant.

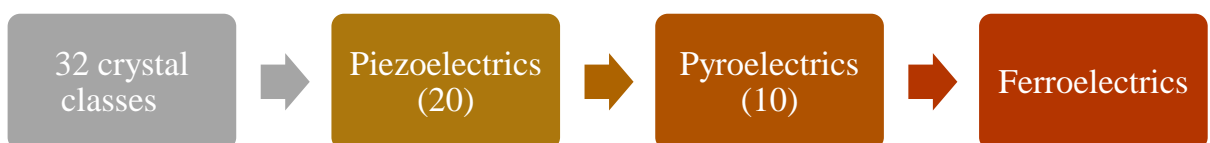


Fig. 2.1 Flowchart representation of Piezoelectric, Pyroelectric and Ferroelectric materials.

The piezoelectric and allied phenomena were first discovered in Rochelle Salt ($\text{KNaC}_4\text{H}_4\text{O}_6 \cdot 4\text{H}_2\text{O}$) by Valasek (Valasek 1921). It was found that the Rochelle salt shows an electric hysteresis in polarization analogous to magnetic hysteresis in case of iron. Generally ferroelectric materials possess single T_C , however, Rochelle salt possesses two T_C s at -18°C and 23°C (G. Shirane, Jona, and Pepinsky 1955). The ferroelectric state exists in between the Curie temperatures, whereas the paraelectric state exists above and below T_C . The non-polar paraelectric phases for $T > 23^\circ\text{C}$ and $T < -18^\circ\text{C}$ are orthorhombic. The polar phase at the ferroelectric state for temperatures between -18°C to 23°C is monoclinic. The Rochelle salt is composed of a row of tartrate ions parallel to the $[100]$ axis, linked along the $[010]$ axis by rows of alternating K and Na ions. As proposed by Pepinsky, the ferroelectric result is produced by two nonequivalent chains along the a -axis, each with a different polarization vector parallel to the a -axis (G. Shirane, Jona, and Pepinsky 1955). Rochelle salt exhibits a rather poor mechanical strength and low disintegration temperature. The crystal decomposes at a low temperature of about 55°C . The dielectric constant is strongly frequency-dependent and may differ by several orders of magnitude, depending on the frequency used for the measurement. For uniaxial ferroelectrics, such as Rochelle salt, the dielectric constant measured along the principal ferroelectric axis is much larger than that normal to it, simply because the ions shift only along one principal ferroelectric axis and do not shift in any direction other than the principal axis. For Rochelle salt, the corresponding dielectric constants along and normal to the principal axis are 1000 and 10 respectively.

Two decades later after the discovery of ferroelectricity, barium titanate was identified during the World War II by (Haertling 1999). BaTiO_3 was the first man made ferroelectric ceramic in absence of the hydrogen bond which made it really significant in those times. The prevailing opinion in that period was that ceramics cannot be piezoelectrically active due to the random orientation of grains (Haertling 1999). However, the domains within the grains could be reoriented by electric field for polycrystalline ferroelectric ceramics. This method of aligning the domains by means of electric field is known as poling and proved to be a key feature in turning the inert ceramic into an electromechanically active material. Thereafter, many researchers made several investigations and studies on ferroelectricity and piezoelectricity. Various crystal transitions of BaTiO_3 were accounted for by expanding the Gibbs free energy as function of polarization and strain (Devonshire 1949) followed by the development of a phenomenological model to obtain expressions of dielectric and piezoelectric constant in terms of other physical constants (Devonshire 1951). This model was developed on the earlier investigations of Landau

and Ginzberg and proved to be a useful tool to understand ferroelectrics. It is popularly known as the Landau-Devonshire-Ginzberg theory of ferroelectrics.

Landau theory was developed by Lev Davidovich Landau (1908–1968), a Russian physicist. This model is based on two basic assumptions: the free energy F of the system must be analytical and follows the symmetry of the Hamiltonian. In this sense, the free energy is considered as a function of powers of an order parameter ‘ ξ ’ and reads as

$$F(\xi, T) = -g_1\xi + \frac{1}{2}g_2\xi^2 + \frac{1}{4}g_4\xi^4 + \frac{1}{6}g_6\xi^6 + \dots$$

where, the multiplier parameters, g_i , can be, in principle, dependent on the temperature: $g_i = g_i(T)$. The linear term on ξ which is added to the free energy expansion represents an external force that breaks the symmetry of the system. It is negative (and g_1 positive) to favor the minimum of energy at positive values of the order parameter.

Landau developed this general theory to mainly describe the second order phase transitions in a material. In this theory, the emphasis was given to incorporate an order parameter, for which a non-zero value indicates the low temperature phase and a null value signifies the high temperature phase. The order parameter is directly related to the lattice mode which is frozen-in at the transition temperature. At or near the phase transition, the amplitude of a particular lattice mode whose restoring mode is soft becomes significantly larger than the other modes present. As a result, the total energy, which is the sum of all lattice modes can be approximated to the series expansion of the amplitude of this mode only (Cao 2008).

In 1949, Devonshire independently derived a phenomenological theory similar to Landau and successfully described ferroelectric phase transitions and the temperature dependence of dielectric properties of BaTiO_3 . He showed that the free energy expansion method could be extended to a first order phase transition. For crystalline materials, one important aspect of Landau theory must be preserved i.e. one could add different terms involving quantities, which may not have any relation to the soft mode, to the free energy expansion as long as the symmetry constraints are preserved. For example, in a ferroelectric system, elastic strain as well as polarization changes at the phase transition. However, the elastic strain is not proportional to the soft mode amplitude. Therefore, one can also add the elastic strain expansion terms to the order parameter in the free energy model to explain the piezoelectric and transformation strain behavior. It is to be noted that the elastic strain secondary order parameter is independent of the primary order parameter. Similar order parameters can be added to the free energy model so long

as they are related to the phase transition and preserve the crystal symmetry of the prototype phase.

The addition of the order parameter gradient terms was first introduced by Ginzburg and Landau for describing superconductivity (Ginzburg and Landau 2008). For a ferroelectric system, such gradient energy terms are important for describing inhomogeneous structures, such as domain walls and interfaces. Time dependent Ginzburg-Landau (TDGL) models described the kinetic process of domains during the phase transition of the material by adding a relaxation type or diffusion type phase of time dependence in the energy minimization process. Ginzburg also laid the criterion for which the Landau theory approximation is correct. It is stated that the average of the fluctuations in the order parameter must be lower than the order parameter itself. Ginzburg criterion does not show that Landau's effective field theory approach is wrong. It shows only that the mean field approximation used in Landau's approximation does not work for lower dimensions.

Lead zirconium titanate (PZT) was initially developed around 1952 at the Tokyo Institute of Technology (Jaffe, Cook, and Jaffe 1971). PZT exhibits enhanced sensitivity and possesses higher operating temperature relative to BaTiO₃. Due to the ease in tailoring the electrical properties of PZT ceramic to adhere to different energy demands, high mechanical strength and low manufacture costs, it has become the prime choice for a piezoelectric ceramic.

The structure of the mineral, CaTiO₃ (calcium titanate) is the prototype for perovskite structure. Most of the important ferroelectric ceramics such as barium titanate and lead zirconate titanate possess the perovskite structure (Bhalla, Guo, and Roy 2000; Tejuca 1992). The perovskite oxides have a general formula of ABO₃ where A denotes the cation of larger ionic radius and B denotes the cation of smaller ionic radius. A cations have oxidation states of +1 to +3 (e.g. Pb²⁺, Bi³⁺, Ba²⁺, K⁺, La³⁺, Na⁺, Sr²⁺, Nd³⁺ etc.) whereas B cations have valence of +3 to +6 (e.g. Zn⁴⁺, Ti⁴⁺, Sn⁴⁺, Nb⁵⁺, Ta⁵⁺, Sb⁵⁺ etc.). The perovskite structure framework is generally considered cubic in which the A cation resides at the corners of the cubic unit cell, B cations in the center and oxygen resides on the face centers of the unit cell. The perovskite structure can also be visualized as the network of corner linked oxygen octahedra in which the B cation fills the octahedral voids and the A cation fills the dodecahedral holes (Jaffe, Cook, and Jaffe 1971). Fig. 2.2 depicts the perovskite structure in cubic, tetragonal, orthorhombic and rhombohedral unit cell (Y. Xu 1991). The high symmetry cubic paraelectric phase (Fig. 2.2(a)) on cooling below T_C undergoes transition into lower symmetry ferroelectric phases in which the common phases are tetragonal, orthorhombic and rhombohedral. The phase transitions undergo distortion

in the unit cell. The distortion occurs along c axis [001] for a cubic paraelectric phase transitioning into a tetragonal phase (Fig. 2.2(b)). In orthorhombic phase (Fig. 2.2(c)), distortion occurs along the face diagonal [110] whereas, for rhombohedral phase (Fig. 2.2(d)), the unit cell elongates along the [111]. In each phase, the polarization occurs due to displacement of B cation along the direction of distortion and the direction of polarization is parallel to [001], [110], [111] respectively (Jaffe, Cook, and Jaffe 1971). Generally, the phase transition takes place from paraelectric to ferroelectric phase at the Curie temperature for most of the ferroelectric materials. However this is not true for all ferroelectric materials, for e.g. phase transitions in BaTiO_3 transfers from the paraelectric cubic phase ($> 120^\circ\text{C}$) to tetragonal ($< 120^\circ\text{C}$) and orthorhombic ferroelectric phase ($\sim 5^\circ\text{C}$) into the rhombohedral ferroelectric phase ($< -90^\circ\text{C}$) while cooling from T_C (120°C) (Johnsson and Lemmens 2005). On the other hand, PbTiO_3 undergoes transition from cubic paraelectric phase with space group (s.g.) $Pm\bar{3}m$ to tetragonal ferroelectric phase (s.g. $P4mm$) on cooling from T_C (487°C).

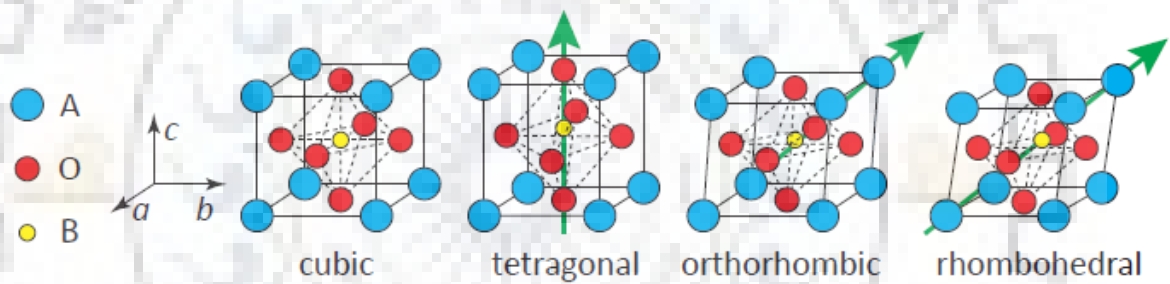


Fig. 2.2 The unit cell of perovskite structure of ABO_3 in the (a) cubic phase, (b) tetragonal phase, (c) orthorhombic phase and (d) rhombohedral phase.

The stability of the perovskite structure is dependent on the relative ionic radii of the cations (A and B) and anion (O^{2-}). The term “tolerance factor” (t) indicates the stability of the perovskite structure (Goldschmidt and Rait 1943). For a cubic perovskite structure, ‘ t ’ = 1, however the cubic structure is found to be stable if, ‘ t ’ lies between 0.88 and 1.09. On the other hand, if ‘ t ’ < 1 , due to the smaller cation A, the $[\text{BO}_6]$ octahedra will tilt to compensate for unfilled space whereas if ‘ t ’ > 1 , the structure developed by the B cation and A-O distance becomes too small for the oxygen octahedra, so hexagonal variants of the perovskite structure become stable (Cordero et al. 2011).

$$t = \frac{r_A + r_O}{\sqrt{2}(r_B + r_O)} \quad (2.2)$$

where, r_A , r_B , r_O are the ionic radii of the A, B cations and O anion respectively.

The ferroelectric ceramics do not exhibit any ferroelectric properties due to the random alignment of ferroelectric domains without poling. Poling is required to force or reorient the ferroelectric domains in the direction of applied field by applying sufficient DC electric field (at least equal to coercive field ' E_c ' of the ceramic material). The ferroelectric domains do not perfectly align with the applied field unless the grain is coincidentally aligned with its c -axis or a -axis in the direction of electric field. However, poling ensures to align the polarization vectors of the domains to maximize the component of polarization in the field direction. After poling, on removal of applied DC field, polarization still remains in the material which shows ferroelectricity as shown in Fig. 2.3 (Q. Xu et al. 2015).

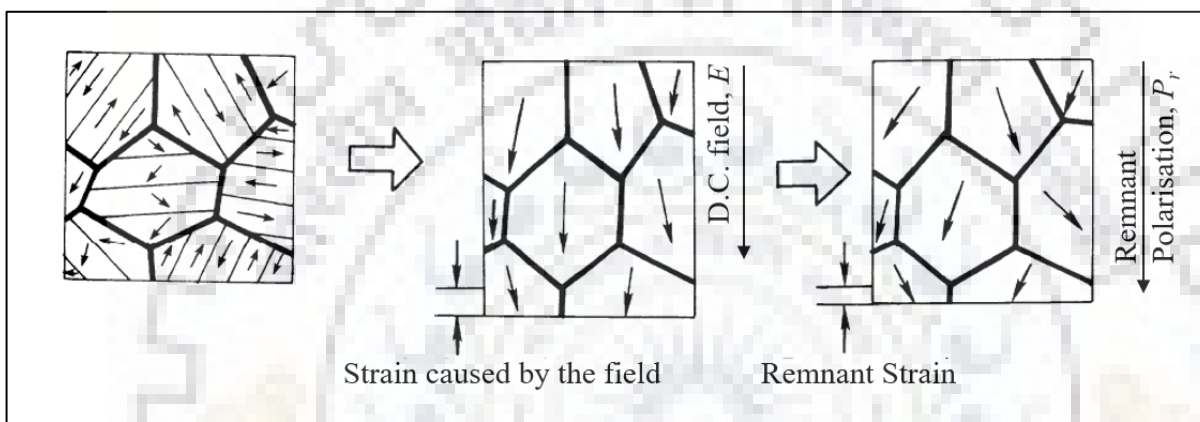


Fig. 2.3 Representation of Poling in ferroelectric materials.

If the applied DC field is high enough, it can even reverse the polarization direction of the domains or in other words change from one spontaneously polarized state to another, the phenomenon is known as domain switching. In polycrystalline materials that incorporate many random oriented grains, domains in one grain while switching get constrained by the neighbouring domains oriented in different directions. Such resistance to domain switching leads to hysteresis in polarization of ferroelectric materials, which is another important attribute of ferroelectrics. A typical ferroelectric hysteresis loop for polycrystalline ferroelectric ceramic is shown in Fig. 2.4 (L. Jin, Li, and Zhang 2014). For an unpoled ferroelectric ceramic, there is no remnant polarization which is represented by the position ' O ' in the figure. When a small electric field is applied, a linear relationship between P and E is observed as represented by section OA . At this stage, the electric field is not strong enough to reorient any domains. Therefore, the material behaves as a normal dielectric (paraelectric). On increasing the electric field further, the domains in the ferroelectric material start to reorient in the direction of applied field and results in a nonlinear sharp increase in polarization, P with respect to electric field, E as represented by section AB . Most of the ferroelectric domain switching takes place at the coercive field, E_c . Further increase of electric field aligns all ferroelectric domains to the direction of applied field

(section BC) and the crystal becomes composed of a single domain only. On extrapolating the section BC on the polarization axis (point E) gives the value of spontaneous polarization, P_s . When the applied field is reduced to zero, few domains in the crystal are still oriented in the direction of applied field and the ferroelectric material produces remnant polarization, P_r . The P_r of the material can be reduced to zero only by further increase of electric field in the reverse direction until it reaches a point F . The electric field required to reduce the polarization of the material to zero is called the coercive field, E_c . On further increase of electric field in the negative direction, dipoles will reorient in the same direction and the hysteresis loop can be completed by reversing the direction of electric field again. In addition, the external field also induces a spontaneous strain in the material which results in a “butterfly like” form in the strain-electric field curve (L. Jin, Li, and Zhang 2014).

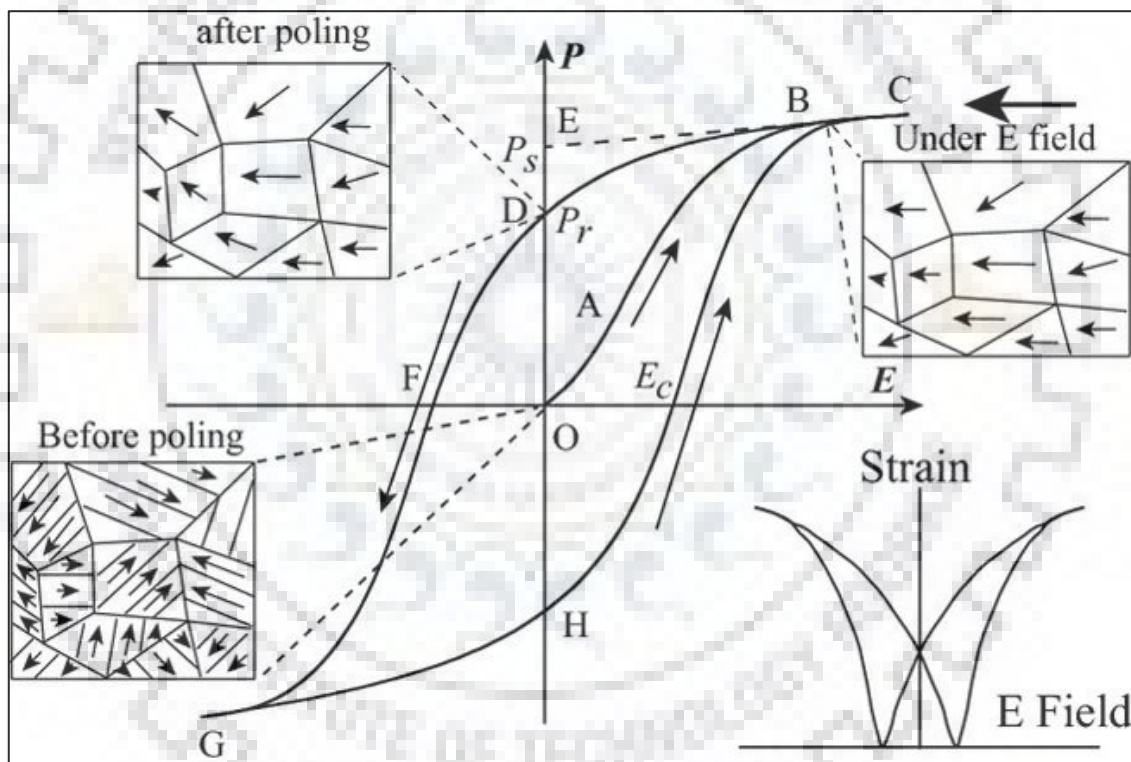


Fig. 2.4 Typical $P E$ loop characteristics of ferroelectrics.

The various characteristics of ferroelectric materials and the ease of ability to tune their properties have led them to be used in variety of electronic applications. The various applications are categorized as per the property of the ferroelectric ceramics.

1. Piezoelectric property: Ferroelectric materials utilize their piezoelectric property in transducers, piezo spark generators, actuators, sensors etc. Piezoelectric devices such as sonars for military use, energy harvesters, Langevin actuators, ultrasonic motors etc. are developed. The market share of such piezoelectric devices is accounted for \$26.87 billion

in the year 2018 and reported to reach an expected value of \$42.41 billion by 2027 (Global Piezoelectric Devices Market, Forecast to 2027. 2019). In addition, new relaxor ferroelectrics like compounds of lead magnesium niobate achieve strain that is 10 times to that of conventional piezoelectrics (Scott 2007).

2. Dielectric property: The ferroelectric materials that exhibit high dielectric constant and possess good stability at wide frequency range and operate at wide temperature range are suitable for most commercially manufactured capacitors. For e.g., a ferroelectric bypass capacitor for operation in 2.3 GHz frequency range in digital mobiles was awarded the “Product of the year award” in Japan (Scott 2007).
3. Memory applications: Recent advancement in ferroelectric materials have brought non-volatile, high packing density and high speed random access computer memory (RAM’s) to commercial reality. The data is stored in terms of binary information as positive and negative polarization states (Kulkarni and Rohrer 1989). Commercial magnetic random access memory (4 Mb MRAM) from Freescale CO, 2006 have been superseded by Samsung’s 64 Mb PZT FeRAM’s. In addition, Symetrix and Matsushita Electronics Corporation have produced FERAM’s based on SBT with breakdown strength of 1.5 MV/cm (Scott 2007).
4. Pyroelectric applications: The ferroelectric materials can generate a temporary voltage when they are heated or cooled. The change in temperature causes the atomic positions within the crystal to change thereby inducing change in polarization. The converse of the above process in adiabatic conditions is known as “electrocaloric effect”. As a result, such ferroelectric materials provide an alternative to the usage of greenhouse gases in domestic and industrial refrigeration (Mischenko et al. 2006).
5. Electrooptic effects: The electrooptic properties of the materials are dependent on their ferroelectric properties. When the applied electric field over the material is changed, the resulting polarization changes which in turn changes the electrooptic properties.

Moreover, the magnitude of the electrooptic properties like absorption, refractive index, electrochromic effect etc. depends on the strength of the applied field and its direction (Haertling 1999).

The applications of ferroelectric materials in other areas such as microwave, transistors, photoelastic modulators are reported here (Bain and Chand 2017).

Generally, the 180° domain walls are ferroelectrically active and do not couple with mechanical stress. The formation of these domain walls reduce the electrostatic energy created by depolarizing fields and are only excited by applied electric fields. Therefore, the contribution of 180° domain walls is towards dielectric properties of the materials only. On the other hand, the formation of non- 180° domain walls reduce both electrostatic and elastic energy of the material. As a result, these domain walls can be excited by both electric field and mechanical stress and contribute towards dielectric as well as piezoelectric properties of the material.

(Arlt 1987, 1989, 1990; Herbiet et al. 1989) suggested in qualitative terms, that the domain wall motion plays a significant role in deciding the dielectric and piezoelectric properties of a material. Thereafter (Q. M. Zhang et al. 1994) proposed a method to separate the intrinsic and extrinsic dielectric response quantitatively in PZT ceramics by stating that the domain wall motion doesn't cause any volumetric change. The experimental method was also utilized to deduce the temperature dependence of the intrinsic and extrinsic contributions in the material. The domain wall motion is caused by weak external electric fields since the strong fields will favor domain wall switching thereby generating local stress and volumetric change. Moreover, the reports suggest that the major contributions towards dielectric and piezoelectric properties of the material are due to the extrinsic domain wall motion.

2.3 PZT solid solution

The discovery of lead zirconate titanate, $\text{PbZr}_x\text{Ti}_{1-x}\text{O}_3$ (PZT) was made by Sawaguchi et al. (G. Shirane, Sawaguchi, and Takagi 1951). Fig. 2.6 shows the phase diagram of PZT with temperature range from room temperature (RT) to 500°C . The detailed phase diagram is based on the works reported by several authors (Barnett 1962; D. Berlincourt, Krueger, and Jaffe 1964; Jaffe, Roth, and Marzullo 1955, 1955; Gen Shirane and Suzuki 1952; Gen Shirane, Suzuki, and Takeda 1952; Gen Shirane and Tokyo 1952). It was finally summarized by Cook and Jaffe in their treatise of piezoelectric ceramics (Jaffe, Cook, and Jaffe 1971). At room temperature, the binary solid solution of PbZrO_3 and PbTiO_3 shows three symmetries namely antiferroelectric orthorhombic phase, ferroelectric rhombohedral and ferroelectric tetragonal phase.

For $\text{PbZr}_{1-x}\text{Ti}_x\text{O}_3$, with $x = 0.48$ to 1.00 , tetragonal symmetry (F_T , $P4mm$) is present. As the Ti^{4+} ions are partially replaced by Zr^{4+} ions, the c/a decreases along with decrease in T_C . The phase symmetry now changes to rhombohedral phase (F_R) which is divided into high temperature ($F_{R(HT)}$, $R3m$) and low temperature ($F_{R(LT)}$, $R3C$) phase. Further replacement of Ti^{4+} ions, generates an orthorhombic phase (A_O , $Pbam$). At temperatures close to T_C , another symmetry is observed of antiferroelectric tetragonal phase in a limited composition range.

It is to be noted that, the phase boundary which separates the tetragonal and rhombohedral phases is independent of temperature, unlike the phase boundary between the A_0 and F_R . This boundary is termed as the “morphotropic phase boundary” in which the term “morphotropic” means that there is an abrupt change in structure within the solid solution with variation in composition (Jaffe, Roth, and Marzullo 1955). Paraelectric cubic symmetry (P_C , $Pm3m$) exists above the T_C in the entire composition range of the phase diagram.

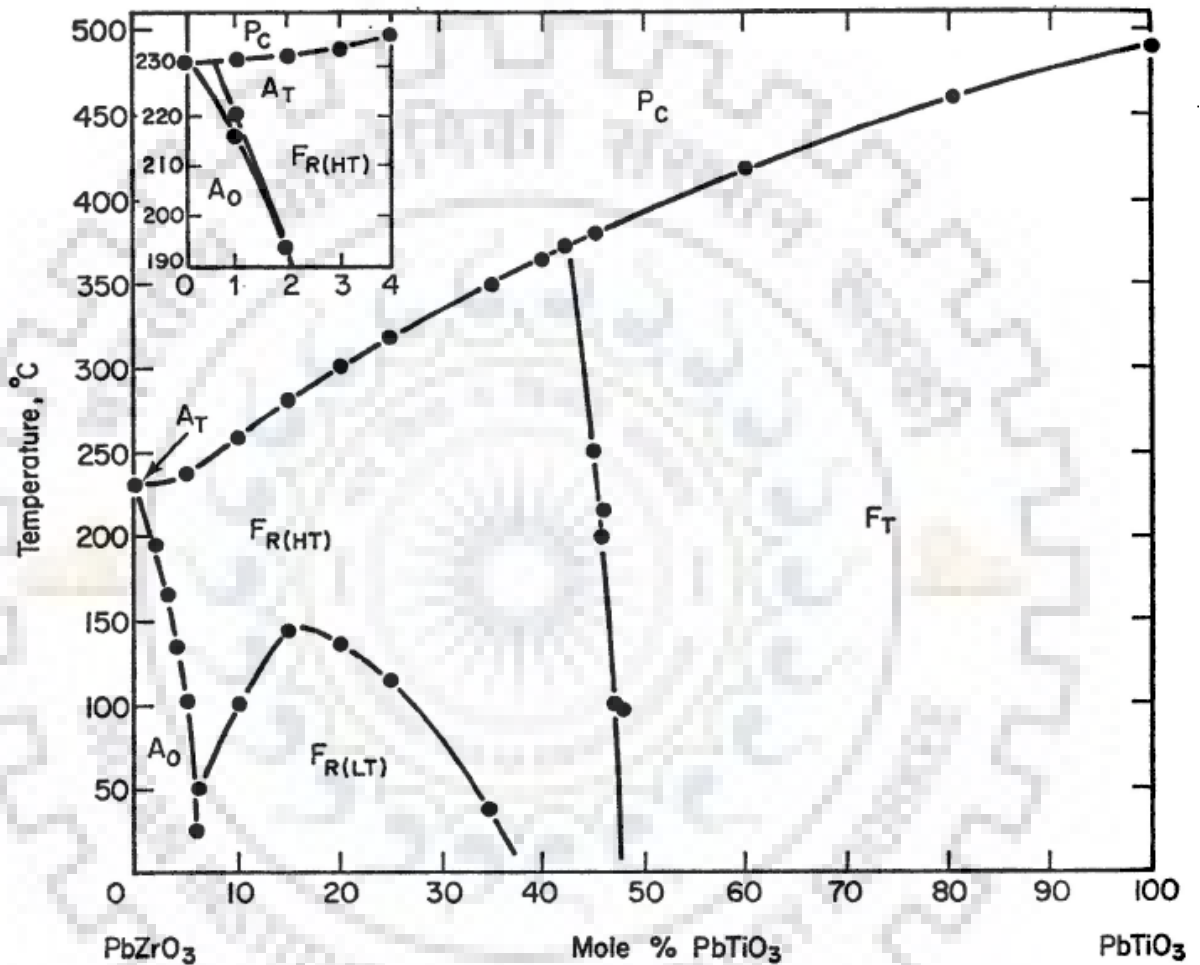


Fig. 2.6 Phase diagram of PZT by (Jaffe, Cook, and Jaffe 1971).

2.4 Phase coexistence near MPB compositions

A comprehensive review of the phase diagram of PZT solid solution near MPB region is beyond the scope of the thesis. A brief summary of the progress over the studies of MPB region in PZT ceramic is presented here since the compositions lying in this region will be discussed in the following chapters. The MPB is represented as a vertical one dimensional line boundary which is nearly temperature independent located at 0.48 mol % PbTiO₃. When the MPB in the PZT phase diagram was reported, it immediately sparked an array of questions as to how such a line boundary could exist. A line phase boundary implies that the atomic diffusion is totally frozen

and the transformation between phases is diffusionless. According to Gibbs phase rule, if the atomic diffusion is not totally frozen, the line boundary should be replaced by a two phase region (Gharb and Trolier-Mckinstry 2005). Until 1999, it had been generally accepted that the region in the MPB is the coexistence of F_T and F_R . The variable width of the coexistence region depended on the homogeneity of the powders (Isupov 1975; K. Kakegawa et al. 1977; Mishra, Pandey, and Singh 1996) and grain size (Cao and Cross 1993b). (Glazer et al. 2004) made a comprehensive review on MPB and suggested that the change in structural order plays a significant role in enhanced electrical and electromechanical properties near MPB.

In 1999, (Noheda et al. 1999) discovered the monoclinic phase using high resolution synchrotron x-ray diffraction technique in $\text{PbZr}_{0.52}\text{Ti}_{0.48}\text{O}_3$. The symmetry of the monoclinic phase belonged to space group C_M , which has only a mirror plane and no symmetry axis. Noheda et al. reported that the monoclinic phase symmetry C_M is common to both R ($R3m$) and T phases ($P4mm$), and is positioned in between the two phases along the MPB. Thus, the phase diagram remains a diffusionless diagram without coexistence of phases along the MPB.

After the discovery of monoclinic phase, extensive novel studies were carried out since, prior to this, ferroelectric phase with symmetry lower than orthorhombic symmetry in perovskite oxides was not reported. (Noheda et al. 2000a, 2001) reported lattice parameters as a function of temperature and composition in ferroelectric PZT and proposed a phase diagram around the MPB as shown in Fig. 2.7. (Bellaiche, García, and Vanderbilt 2000) calculated finite-temperature properties of $\text{PbZr}_{1-x}\text{Ti}_x\text{O}_3$ using first principles and affirmed the stability of monoclinic phase in a narrow region along the MPB for a random Zr/Ti cation distribution. However, the conventional Ginzburg-Landau-Devonshire theory of second and weak first order phase transitions could not justify any ferroelectric states with symmetry lower than orthorhombic symmetry. In 2001, Vanderbilt and Cohen (Vanderbilt and Cohen 2001) expanded the Devonshire theory to the eighth order allowing for three types of equilibrium phases for which the polarization is confined to a symmetry plane rather than a symmetry axis. Therefore, special conditions are required for the stability of monoclinic phase in PZT.

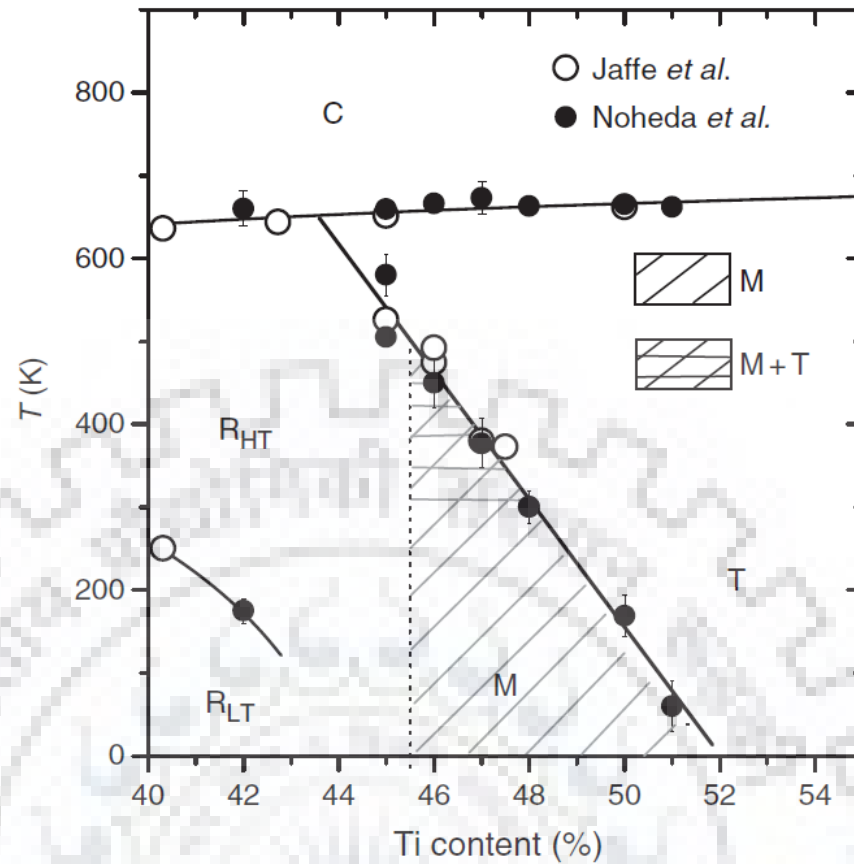


Fig. 2.7 Phase diagram of $\text{PbZr}_{1-x}\text{Ti}_x\text{O}_3$ (PZT) solid solution along MPB (Noheda et al.).

PZT ceramics are widely used in electro-active devices and in other technological applications due to the enhanced piezoelectric, dielectric and elastic properties that occur along MPB where this solid solution shows structural change with variation in composition. Fig. 2.8 shows the dependence of dielectric permittivity of PZT with variation in composition. The reason behind such an unusual response is still not resolved, so far. However, researchers have put forward the probable causes, viz. the coexistence of phases (Isupov 1968), the existence of a tricritical point near MPB (Mishra, Singh, and Pandey 1997; Solanki et al. 2013), lattice instability at room temperature (Guo et al. 2000; Mishra, Pandey, and Singh 1998), softening of elastic modulus (Cordero, Craciun, and Galassi 2007), availability of more polarization directions (Bellaiche, García, and Vanderbilt 2001; Fu and Cohen 2000) etc. Moreover, the coexistence of phases has been known to induce ultra-high dielectric response due to an increase in the number of allowable polarization domain states. (Noheda et al. 2000b) reported that the monoclinic phase permits rotation along the symmetry plane whereas polarization vector in tetragonal phase and rhombohedral phase lies along fixed [001] and [111]. Moreover, PZT-based solutions have other desirable characteristics as follows: mechanically strong, chemically inert, relatively inexpensive to manufacture, high operating temperature, high coupling coefficient, and they can be easily

tailored by adjusting the Zr/Ti ratio or by introducing dopants to meet the requirements of a specific application.

Ideally, MPB should be approximately temperature independent as in Fig. 2.6. Thus the material composition always remains close to MPB with variations in temperature. But if the MPB is dependent on temperature, then the properties would be maximal only at the temperature of phase transition (MPB) as in case of BZT- x BCT system (Gao et al. 2011) and as the temperature is increased or decreased, desirable properties may not be achievable. There have been evidences of property enhancements at the MPB of many solid solutions.

Electromechanical and dielectric behaviour of various systems are maximized significantly at the MPB where more than one phases co-exist. Hence many of the systems exhibiting MPB between polar phases find huge utility in applications such as transducers, actuators, MEMS devices and sensors. These advances included the development of a new class of polycrystalline electro-optic ceramics based on lanthanum-substituted lead zirconate titanate (PLZT) and to ultrahigh strain piezoelectric single crystals based on solid solutions of lead titanate with lead magnesium niobate (PMN-PT), lead zinc niobate (PZN-PT), and other relaxor ferroelectric compounds. Even the Pb-free materials exhibit same kind of behavioural changes around the morphotropic phase boundary. An electric field induced volume change for NBT-BT ceramics revealed a high amount of axial and radial strain for MPB compositions (Simons et al. 2011). BCT-BZT solid solution also shows such changes in terms of dielectric permittivity (Tuan et al. 2015). Many such evidences are found in literature (Eitel et al. 2001; Hinterstein et al. 2015; Liu and Ren 2009; Su et al. 2011; Upadhyay and Singh 2016; Walker et al. 2016). Investigation of ferroelectric solid solution systems that display MPBs continues to the present time with the twin goals of improving operational stability to higher temperatures over current lead-based systems and of finding lead-free alternatives to these systems to meet environmental regulations in Europe and elsewhere.

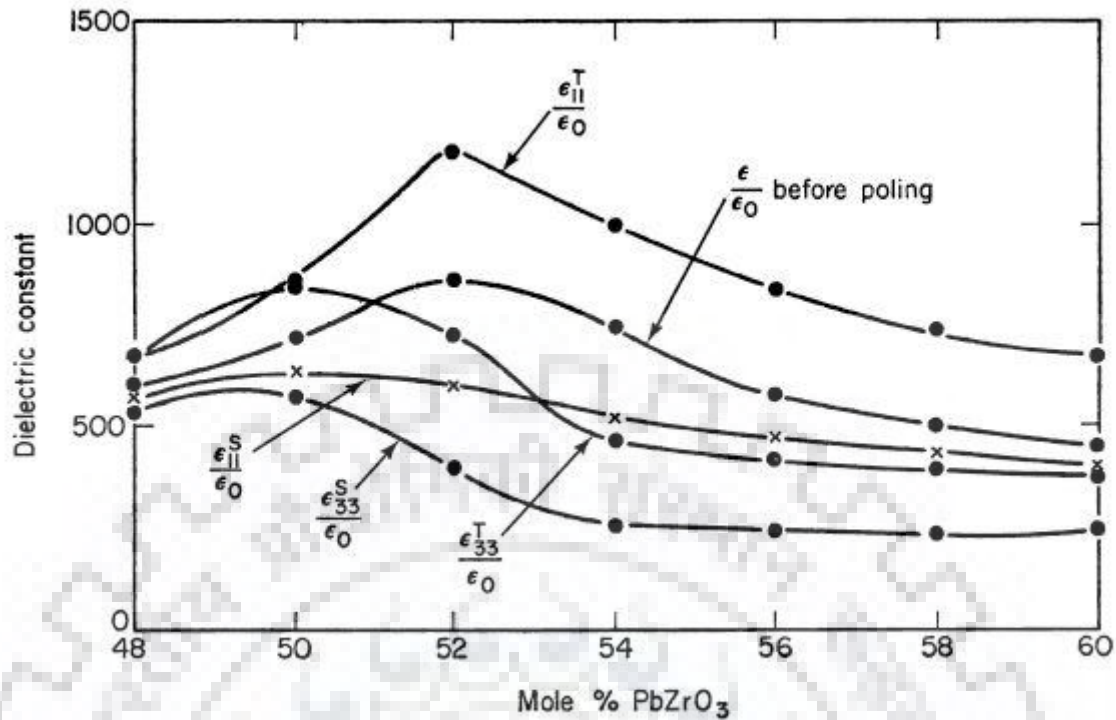


Fig. 2.8 Dependence of dielectric constant of PZT with composition.

2.5 Modification/doping on PZT

In spite of high dielectric and electromechanical properties of PZT having compositions close to the MPB, they are rarely used in commercial devices in pristine form. Due to the specific requirement of functional properties in different applications, the PZT ceramics are modified accordingly by varying the composition or doping. The studies of the doping effects on PZT have been carried out as early as the 1950s (R. Gerson and Jaffe 1963; Robert Gerson 1960; KULCSAR 1959, 1965). The ferroelectric properties depend on the ease of domain wall motion or domain wall mobility and domain switching in the material. Therefore, on controlling the domain wall motion, the ferroelectric properties of the material can be controlled. The substitution of metal ions in PZT by incorporation of low amounts (0.5 – 2.0 mol % typically) of suitable aliovalent elements can either generate cation (metal) vacancies to promote domain mobility or anion (oxygen) vacancies to restrict domain wall motion (Don Berlincourt 1992).

2.5.1 Types of dopants

Generally the dopants can be classified into two groups i.e. donor and acceptor depending on their valence states and the substitution site (A- or B-).

The dopants where the charge on the cation is higher than the cation they are substituting in the PZT structure are called donor dopants. For e.g. higher valence cations like Nb^{5+} or Sb^{5+}

replacing (Zr^{4+}/Ti^{4+}) (*B*- site) or Eu^{3+} , La^{3+} or Gd^{3+} replacing Pb^{2+} (*A*- site) that create lead vacancies (V_A^{2-}) and restrict the growth of oxygen vacancies (Takahashi 1982). The dielectric and piezoelectric properties are enhanced when PZT ceramic is doped with donor dopants, and are typically called soft PZT ceramics. Moreover, they exhibit symmetric hysteresis loops along with good degree of “squareness” and low coercive field pertaining to high fields. The application areas lie where high coupling or high charge sensitivity are required.

On the other hand, the dopants where the charge on the cation is smaller than the ion to be replaced are called hard dopants. For e.g. Fe^{2+} or Mg^{2+} substituting the *B*- site or Na^+ , K^+ substituting the *A*- site thereby forming oxygen vacancies (V_O^{2+}) in PZT lattice (Eric Cross 1995). The hard dopants typically reduce the dielectric and piezoelectric properties and produce highly asymmetric *P-E* loops. In addition, they exhibit larger coercivity along with high electrical and mechanical quality factor (Q_m).

Besides the two major types of dopants, the other one is isovalent type in which the valence and the size of the substituting ion is similar to the one it replaces. It is to be noted that the first additives used for modifying PZT were the isovalent ones (Don Berlincourt 1992). For e.g. Ba^{2+} , Sr^{2+} and/or Ca^{2+} substituting Pb^{2+} in the *A*- site, Sn^{4+} substituting Zr^{4+} in the *B*- site etc. The range of solid solution with these additives is high and may produce lower dielectric loss and high aging rates as reported in the composition series $Pb_{1-x}Sr_x(Zr_{0.53}Ti_{0.47})O_3$ (KULCSAR 1959). Moreover, it is also possible to obtain enhanced dielectric and piezoelectric properties and better stability of piezoelectric activity by complex doping of heterovalent ions of both donor and acceptor dopants. Such a system is also characterized by low sintering temperature and high Curie temperature (Helke and Lubitz 2008). A typical set of dielectric and permittivity data for modification on PZT with different dopants is shown in Table 2.1 and the major effects of additives are summarized in Table 2.2.

Table 2.1 Modification in PZT with different dopants (Helke and Lubitz 2008).

	Dopant	$T_C, ^\circ C$	$\epsilon_{33}^T/\epsilon_0$	$\tan \delta, 10^{-3}$	k_P	$d_{33}, pC/m$	Q_m
	soft						
(1)	Nb^{5+}	365	1700	15	0.60	374	85
(2)	Sb^{5+}	>350	1510	15	0.46	410	95
(3)	Nd^{3+}	330	1600	20	0.60	355	100
	hard						
(4)	Fe^{3+}	300	820	4	0.59	240	500
(5)	Ni^{3+}	330	1000	8	0.50	200	350

Table 2.2 Major effects of additives on characteristic properties of PZT. Ionic radius is given in parentheses in ‘nm’ units.

Additives	Major Effects
<u>Isovalent additives:</u> Ba^{2+} (0.134) or Sr^{2+} (0.112) for Pb^{2+} (0.132) Sn^{4+} (0.071) for Zr^{4+} (0.068) or Ti^{4+} (0.079)	Lower Curie point Higher permittivity
<u>Soft dopants:</u> La^{3+} (0.122), Nd^{3+} (0.115), Sb^{3+} (0.090), Bi^{3+} (0.114) or Th^{4+} (0.110) for Pb^{2+} (0.132) Nb^{5+} (0.069), Ta^{5+} (0.068), Sb^{5+} (0.063) or W^{6+} (0.065) for Ti^{4+} (0.068) or Zr^{4+} (0.079)	Higher permittivity Higher K_p Much Lower Q_m Resistivity about 10^3 higher
<u>Hard dopants:</u> K^+ (0.133) or Na^+ (0.094) for Pb^{2+} (0.132) Fe^{3+} (0.067), Al^{3+} (0.057), Sc^{3+} (0.083), In^{3+} (0.092) or Cr^{3+} (0.064) for Ti^{4+} (0.068) or Zr^{4+} (0.079)	Lower permittivity Lower dielectric loss Lower K_p Much higher Q_m

It is largely believed that the dopants influence the dielectric and piezoelectric properties of the material by their interaction with the domain wall. Fig. 2.9 represents the dependence of dielectric permittivity on temperature of hard and soft PZT ceramics (X. L. Zhang et al. 1983). It can be observed that the dielectric constants of the materials are significantly different at room temperature. However, when the temperature is reduced to near 0 K, the dielectric constant decreases and coincides with the intrinsic dielectric constant values deduced from the phenomenological theory for that composition. The theoretical curve present in Fig. 2.9 is the average of the intrinsic dielectric properties of single domain values derived from the phenomenological theory for that respective composition (Randall et al. 2005). It is believed that the hardening mechanism in hard PZT ceramics is associated with the stability of domain walls. There are three main models which are usually discussed in the literatures (Morozov and Damjanovic 2008):

- 1) The **bulk / volume effect** caused by the charged defects that are aligned within the ferroelectric domains. Such defects can occupy energetically favorable positions in the lattice and form anisotropic centers that favor a certain direction of spontaneous polarization. Such preference of polarization direction is reflected experimentally as internal bias.
- 2) The **domain wall effect** in which the charges diffuse towards the domain walls and create pinning centers. The driving forces may be elastic (neutralization of internal stresses) or electric (compensation of electric charges). This domain wall effect has been suggested as an explanation of hysteresis features in barium titanate and lead titanate zirconate.
- 3) **Surface or grain boundary effect:** Many of the technically interesting ferroelectric ceramics contain a small proportion of a phase which is liquid at the sintering temperature and covers the grain surface as a thin film. Such second phases always occur at high dopant concentrations if the concentration of the dope exceeds the solubility limit. Second phases lead to surface charges at the grain boundaries, which stabilize the domain configurations. Once the domain configurations have established during aging, the individual crystallite is biased by an overall preferred direction of polarization, but the individual domain wall remains mobile.

In case of soft PZT ceramics, it is generally believed that the domain wall moves irreversibly in a random potential energy profile. The randomness or ordering of pinning centers is usually associated with charged defects with respect to polarization within domains. The formation of dipoles of donor ions with cation vacancies are anticipated here. It is to be noted, that the mobility is not equal for all defects. The mobility behavior of oxygen vacancies have been extensively reported in literature (W. L. Warren et al. 1995, 1996; William L. Warren et al. 1996; L. X. Zhang and Ren 2005), which is not the case for cation vacancies. As a result, the structure of defects induced by donor doping and the relationship between these defects and the domain walls are not clear. Nevertheless, taking into account the geometry of the perovskite structure and the coordination of atoms in it, it is reasonable to assume that oxygen-site defects have advantageous prerequisites for diffusion. Hence the anticipated ordering and disordering structure of defects in, correspondingly, hard and soft ferroelectric materials may serve as basic assumption in the understanding of hardening and softening mechanisms.

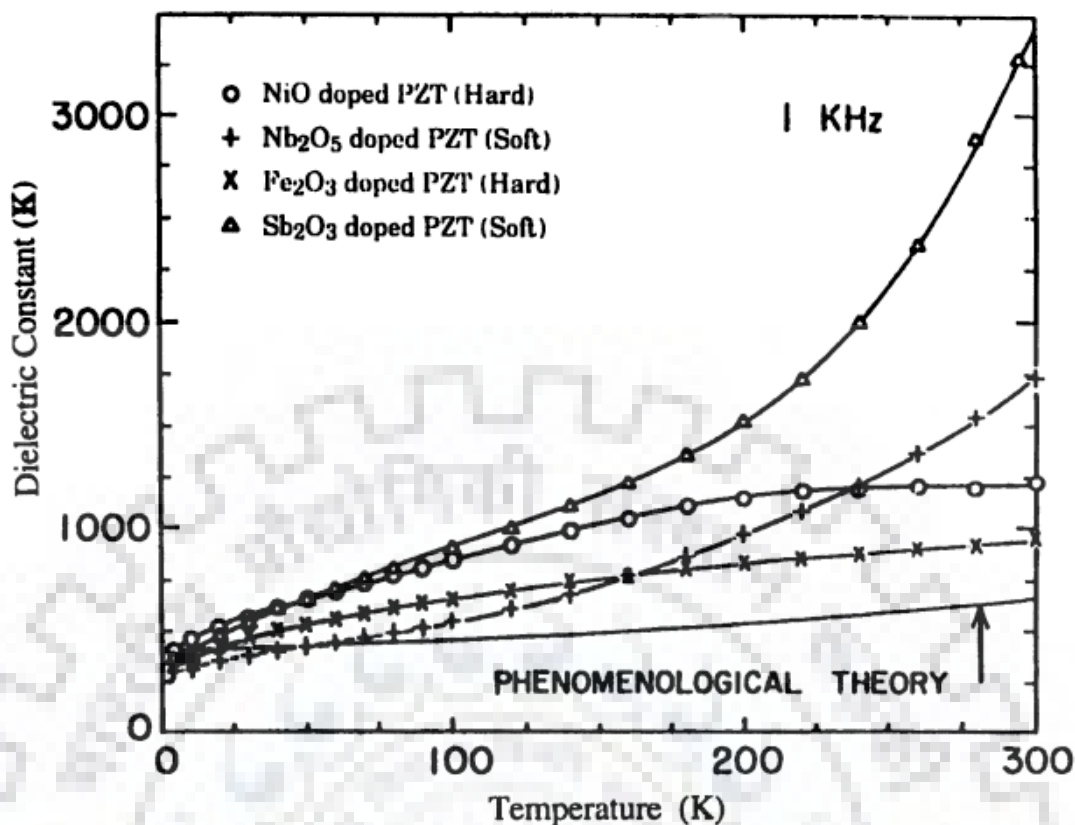


Fig. 2.9 Temperature dependence of the dielectric constant of soft and hard PZT ferroelectric ceramics measured from 4.2 to 300 K. The experimental data are after (X. L. Zhang et al. 1983).

2.6 Literature survey

This section provides a brief review on several factors (viz. domain structure, grain size, phase constitution, density etc.) that influence the dielectric and ferroelectric properties of undoped and doped PZT ceramics. The literature review on impedance and modulus studies, reasons for dielectric maxima at MPB, effect of sintering parameters and energy storage properties are presented. An attempt was made to highlight the underlying reasons on how each contributing factor enhances or degrades the properties of PZT ceramics especially near MPB composition. In addition, the advantage of using SPS method to sinter PZT ceramics and its effect on dielectric and ferroelectric performance have also been explained.

2.6.1 Influence of grain size on dielectric and ferroelectric properties of undoped and doped PZT ceramics

(B. M. Jin, Kim, and Kim 1997) investigated the electrical properties of PZT having Zr content (52 mol %) as a function of grain size. They observed that the dielectric permittivity decreases and transition temperature increases with reduction in grain size. It was also reported that the

coarse grained ceramics undergo second order phase transition whereas the medium and fine grained ceramics show diffuse phase transition (DPT).

(Pdungsap et al. 2005) reported the optimum conditions for synthesis of $\text{PbZr}_{0.52}\text{Ti}_{0.48}\text{O}_3$ and La doped PZT for high dielectric and piezoelectric properties. The XRD patterns of the specimens revealed tetragonal perovskite structure. As the La concentration increases, the tetragonality decreases which is due to the smaller size of La^{3+} relative to Pb^{2+} ion. On increasing sintering temperature, for PZT ceramics, lattice parameters a and c decrease and tetragonality remains constant whereas, for PLZT ceramics, lattice parameter c and tetragonality slightly increase and lattice parameter a tends to remain constant. The average grain size was found to decrease on increasing La concentration. The dielectric constant for La doped PZT ceramics increases with increasing La content and decreasing grain size.

(Mazumder and Sen 2008) added LiBO_2 as sintering aid for $\text{PbZr}_{0.52}\text{Ti}_{0.48}\text{O}_3$ and managed to sinter to 95% of theoretical density (TD) at temperatures as low as 715°C . They reported that the dielectric and piezoelectric properties of LiBO_2 added PZT were on par with and even better for some compositions relative to conventionally sintered PZT ceramics.

The 0.7PMN–0.3PT ceramics were successfully densified by SPS at temperatures as low as 700°C (Shimojo et al. 2008). They reported that the SPS samples show higher dielectric constant and temperature stability over wide range of temperatures relative to conventional sintered samples. The underlying reason for better performance of SPS samples was attributed to size effect.

(Geetika and Umarji 2010) investigated the effect of Zr/Ti content on the MPB composition of PZT-PZN system. The addition of PZN in PZT shifts the MPB to the rhombohedral side. The increase in Zr content increases the phase content of monoclinic phase and decreases the tetragonality. (Cao and Cross 1993a) stated that a well-defined width of MPB cannot exist in a complete solid solution system, since it is inversely proportional to the volume of the element (e.g. grain size) present in a statistical ensemble. Lower the grain size, wider is the MPB region of the system. Geetika et al. supported the findings of Cao et al. as it was observed that the width of MPB in PZN-PZT ceramics increased as the grain size reduced on addition of PZN.

(M. P. Zheng et al. 2013) prepared Co doped 0.2PZN–0.8PZT system by solid state method. The Co ions were found to be present in both +2 and +3 valence states. The solubility limit observed for added CoCO_3 was 0.2 wt.%. Below 0.2 wt.% CoCO_3 , the hard dopant was

found to prefer +3 valence state and B-site substitution of the perovskite lattice. Above the solubility limit, the excess Co ions were observed at the grain boundaries forming Co-Pb liquid rich phase accelerating the grain growth. The dielectric and ferroelectric results obtained for the samples suggested that the size effect is stronger and neutralized the hard dopant behaviour and reformed the permittivity of the sample.

(Srivastava, Goswami, and Umarji 2013) reported temperature dependent dielectric properties of $\text{PbZr}_{0.5}\text{Ti}_{0.5}\text{O}_3$ by using two step sintering method. Low calcination temperature of 700°C was used to avoid grain growth. Rietveld refinement was conducted as the XRD patterns showed multiple peak splitting of the {200} relative to two peak splitting's indicative of the characteristic tetragonal phase. The method was also used to quantify the tetragonal and monoclinic phase present in the PZT system. The dielectric studies of the PZT specimens were investigated from temperature range 35°C to 450°C . First transition temperature of $290\text{-}300^\circ\text{C}$ indicated phase transformation to tetragonal phase. Second transition temperature of 384°C was correlated to phase transformation from tetragonal to cubic phase. Hence, to achieve better dielectric properties, it was suggested to do poling of the ceramics at a temperature below 270°C .

(Joshi and Acharya 2016a) investigated the structural and dielectric properties of glass ($\text{ZnO-B}_2\text{O}_3$) added $\text{PbZr}_{0.52}\text{Ti}_{0.48}\text{O}_3$. They observed that the addition of glass promoted liquid phase sintering which helped to reduce the sintering temperature and to achieve good relative density ($> 91\%$). The optimum amount of glass to be added to achieve superior dielectric properties was not more than 1%. Even though the grain size of glass added PZT ceramics was lower than the undoped PZT ceramics, superior dielectric properties were observed. Joshi et al. stated that the superior properties for 1% ZB + PZT was achieved due to the increase in tetragonality and increase in number of defect dipoles at the grain boundaries.

2.6.2 Domain configurations in PZT ceramics

(C. A. Randall, Barber, and Whatmore 1987) reported the ferroelectric domain configurations in PZT ceramics modified by Fe and Nb and observed rhombohedral symmetry with wedge shaped domains and fine lamellar domains.

Modification of rhombohedral PZT with *Zr/Ti* ratio of 80/20 and 65/35 by addition of La was investigated (Schmitt et al. 2007). It was observed that the normal ferroelectric state was transformed to relaxor state by increase in Zr^{4+} concentration. As the La concentration was increased, polar nano domains were observed from normal micron sized domains. The evolution of relaxor behaviour was attributed to lattice strain of the undoped composition.

2.6.3 Impedance and modulus spectroscopic studies on undoped and doped PZT ceramics

(Gonnard and Troccaz 1978) has reported the effect of doping oxides on $\text{PbZr}_{0.95}\text{Ti}_{0.05}\text{O}_3$ composition and stated that the phase transition temperature depends on the cation radius of the dopant and its distribution between the A and B sites.

(Tandon 1998) suggested a means of separating the bulk and grain boundary contributions by impedance spectroscopy. He stated that the bulk permittivity for La modified PZT can be represented by linear Curie-Weiss law.

(Prasad, Sekhar, and Kumar 2008) made impedance spectroscopic studies on PZT, PLZT, PMN-PT perovskite ceramics in frequency range of 0.1 Hz – 1 MHz. They reported that the Z'' and M'' spectroscopic peaks coincide at the same frequency region thereby correlating it to Debye type behaviour. AC conductivity was found to be independent of frequency at low frequency region. The conductivity in PZT and PLZT at high temperatures was mainly through mobility of oxygen vacancies whereas, for PMN-PT ceramics, it is due to mobility of both lead and oxygen vacancies.

(Wongdamnern et al. 2008) investigated the effect of temperature on the ferroelectric hysteresis of soft and hard PZT ceramics. They observed that the ferroelectric properties decrease on increase of temperature for both types of PZT. The cause of ferroelectric degradation is reduced ferroelectric interaction due to high thermal fluctuation.

(H. Liu et al. 2015) studied the effect of MnO_2 doping on dielectric and ferroelectric properties of PNN—PZT ceramics. The dielectric constant and remnant polarization decrease on addition of MnO_2 , since the doping of lower valence cation generates oxygen vacancies and restrict domain wall motion. The saturation polarization and remnant polarization for 3.5 mol % MnO_2 doped ceramics were the lowest among all samples which suggests strong domain pinning. On the other hand, dielectric loss decreased significantly with composition up to 2 mol % and then rises again from 2 - 3.5 mol %. This is due to the conductivity resulted from high concentrations of MnO_2 .

(Tiwari and Srivastava 2015) studied the effect of Li_2CO_3 on dielectric properties of PZT ceramics. They reported that the addition of Li_2CO_3 promoted liquid phase sintering and thereby improved the sinterability of the ceramics. It even lowered the sintering temperature from 1280°C to 1000°C and the density achieved was 92% of theoretical density. 2 wt.% Li_2CO_3 was stated as the optimum amount to achieve superior dielectric properties. However, the addition of Li^+ ions

shifted the MPB to the tetragonal side. Therefore, the Zr/Ti ratio was also modified accordingly to achieve MPB composition.

2.6.4 Probable reasons for dielectric maxima at MPB

(Soares, Senos, and Mantas 2000) made investigations on the probable cause of high dielectric response of PZT at the phase coexistence region. It was observed that the experimental permittivity values matched the theoretical values obtained by considering the statistical distribution model (Cao and Cross 1993b) instead of the solubility gap model. The applicability of the statistical model on the dielectric properties was analyzed by finding a relation between crystal structure and permittivity outside the coexistence region and extrapolating it to collect permittivity values inside the region. Over the complete composition range, the tetragonal ($c_T/a_T \sim 1$) and the rhombohedral phase ($\alpha \sim 90^\circ$) achieved minimum structural distortion (approaching cubic structure) and increased permittivity on approaching the coexistence region. It was observed that the dielectric permittivity values inside the coexistence region were inferior to hypothetical ceramics composed of tetragonal phase alone. On the basis of above observations, it was concluded that the dielectric maxima was not due to coexistence of phases and the multiplicity of polarization directions, rather it was due to the reduction in structural distortion or the proximity to cubic symmetry of the phases.

(Fu and Cohen 2000) suggested that the ultrahigh piezoelectric response for PZN-PT and PMN-PT single crystals is due to the large increase of c -axis polarization (P_z) and polarization rotation along the minimum free energy path i.e. rotation of polarization directions along rhombohedral \rightarrow tetragonal rather than rhombohedral \rightarrow orthorhombic \rightarrow tetragonal. The factors that contribute to giant piezoelectric response in these materials in addition to a rhombohedral phase at zero field, and high strain in the tetragonal phase were (i) flat energy surface so that even small fields could initiate large ferroelectric displacements by large change of polarization angle, (ii) coupling of large c -axis polarization with applied field, (iii) coupling of other degrees of freedom and strain.

(Takahiro, Masako, and Norikazu 2000) stated that the influence of poling electric field and poling time becomes insignificant when the poling temperature is high enough (180°C) for PZT ceramics. Such behavior suggests that sufficient poling can be achieved by high poling temperature with voltage well below the DBS of the material.

(Vittayakorn et al. 2003) reported that high dielectric permittivity can be obtained by controlling the loss of PbO during heat treatment and preventing the synthesized material from

pyrochlore phase formation in 0.5PNN–(0.5 – x)PZN–xPZT ceramic system. They accomplished this by utilizing double crucibles during calcination and added excess PbO (~2 mol %) to the raw mixture. In addition, they used high heating/cooling rates (~20°C/min) and observed that the Curie temperature and dielectric properties increase with increase in concentration of PZT.

2.6.5 Energy storage properties of undoped and doped PZT ceramics

(Z. Liu et al. 2015) reported the stability of temperature dependent energy storage properties of $\text{Pb}_{0.97}\text{La}_{0.02}(\text{Zr}_{0.58}\text{Sn}_{0.335}\text{Ti}_{0.085})\text{O}_3$. The studies were conducted over temperature range from 20°C to 100°C and frequency range from 0.01 Hz to 100 Hz under 8.6 kV/mm. AFE phase and paraelectric phase were found to coexist in the temperature range 100 – 170 °C. The variation of recoverable energy density was less than 15% and energy efficiency for the specimens were not less than 75%.

(L. Zhang et al. 2015) utilized SPS method to synthesize AFE composite ceramics of composition $(\text{Pb}_{0.858}\text{Ba}_{0.1}\text{La}_{0.02}\text{Y}_{0.008})(\text{Zr}_{0.65}\text{Sn}_{0.3}\text{Ti}_{0.05})\text{O}_3 - (\text{Pb}_{0.97}\text{La}_{0.02})(\text{Zr}_{0.9}\text{Sn}_{0.05}\text{Ti}_{0.05})\text{O}_3$. They reported that SPS process suppresses the diffusion behaviour between the two phases and in turn allows the PLZST phase to contribute towards FE-AFE phase transition electric field. As a result, a large recoverable energy density of 6.4 J/cm³ of the ceramics were obtained.

(Jo and Lynch 2016) reported the energy storage properties of $(\text{Pb}_{0.88}\text{La}_{0.08})(\text{Zr}_{0.91}\text{Ti}_{0.09})\text{O}_3$ for pulsed power applications. La⁺ ions were chosen so as to obtain slim and slanted hysteresis loops and to stabilize antiferroelectric phase. Such type of hysteresis was found to increase the energy storage density and energy efficiency. They reported energy efficiency of 92% and energy density of 3.04 J/cm³ for the PLZT antiferroelectric ceramics.

Table 2.3 Energy storage properties of undoped and doped PZT ceramics reported.

Journal publications	Energy storage Properties
(Joshi and Acharya 2016b) Influences of Liquid-Phase sintering on Structure, Grain Growth, and Dielectric behaviour of $\text{PbZr}_{0.52}\text{Ti}_{0.48}\text{O}_3$ Ceramics	Recoverable energy=0.127 J/cm ³ Energy efficiency=14.2% DBS=32 kV/cm
(Prabakar and Mallikarjun Rao 2007) Complex impedance spectroscopy studies on fatigued soft and hard PZT ceramics.	Recoverable energy=0.128 J/cm ³ Energy efficiency=6.5% DBS=20 kV/cm

(B. M. Jin, Kim, and Kim 1997) Effects of grain size on the electrical properties of $\text{PbZr}_{0.52}\text{Ti}_{0.48}\text{O}_3$ ceramics.	Recoverable energy=0.0021 J/cm ³ Energy efficiency=11.4% DBS=37 kV/cm
(Prabu et al. 2013) Electrical and ferroelectric properties of undoped and La-doped PZT (52/48) electroceramics synthesized by sol–gel method.	Recoverable energy=0.0544 J/cm ³ Energy efficiency=47.75% DBS=3.5 kV/cm
(Peláiz-Barranco et al. 2014) Energy Storage Power of antiferroelectric and relaxor ferroelectric Ceramics PLZT(4/90/10).	Recoverable energy=1.23 J/cm ³ Loss Energy=1.52 J/cm ³ Energy efficiency=45% DBS=32 kV/cm
(Prabu et al. 2013) Electrical and ferroelectric properties of undoped and La-doped PZT (52/48) electroceramics synthesized by sol–gel method.	Recoverable energy=0.0021 J/cm ³ Energy efficiency=11.4% DBS=37 kV/cm
(Hao, Zhai, and Yao 2009) Improved Energy Storage Performance and Fatigue Endurance of Sr-Doped PbZrO_3 Antiferroelectric Thin Films.	Recoverable energy=14.127 J/cm ³ Energy efficiency=78%
(Peng et al. 2015) Magnetoelectric effect of $\text{CoFe}_2\text{O}_4/\text{Pb}(\text{Zr},\text{Ti})\text{O}_3$ composite ceramics sintered via spark plasma sintering technology.	Recoverable energy=0.1067 J/cm ³ Loss Energy=0.338 J/cm ³ Energy efficiency=24% DBS=20 kV/cm

2.6.6 Sintering concepts

Sintering of PZT materials by conventional techniques has been challenging since high sintering temperature of ~1200 °C is needed, however such high temperature causes PbO evaporation degrading the dielectric performance of the material and proving to be hazardous to the environment (Ryu, Choi, and Kim 2001). If sintering aids are added in PZT, the inter-diffusion of constituent elements at high sintering temperature degrades the resulting dielectric performance (Neumeister et al. 2014; W. Zhang and Eitel 2013).

Moreover, it is well known that grain size and porosity play a major role in deciding dielectric and electro-mechanical performance. The phase transition from cubic to tetragonal

state at ~ 763 K incorporates a large transformation strain, resulting in crack formation and large anisotropy of the sintered samples on cooling from the soaking temperature to ambient temperature intermediating through the Curie temperature. This transformation strain has been known to be attributed to grain-grain separation. The stress generated at the grain boundary regions can be minimized by increasing the area of grain boundary. This is accomplished by decrease in grain size i.e. inhibition of grain growth (Ueda 1972). Therefore, sintering techniques that can lower the sintering temperature of PZT ceramics along with suppressed grain growth are required.

2.6.7 Basics of Spark plasma sintering

Spark plasma sintering (SPS) method utilizes presumed electrical discharge between the particles under pressure of compaction to generate a local high-temperature state. This causes vaporization and melting of the surface of powder particles. The electrical current application creates satisfactory conditions for the removal of impurities and activation of the powder particle surface. This activation ensures direct grain-to-grain contact and promotes densification of the powder compact instead of grain growth. The SPS process enables materials to be sintered to high degree of density at lower temperature than required for conventional sintering process within a few minutes time period. SPS is characterized by its very high heating and cooling rates of $1000^{\circ}\text{C}/\text{min}$ and short sintering periods (\sim min). High mechanical pressure helps in increasing particle to particle contacts and thereby aiding diffusion of the grains and ensuring high densification. SPS is a useful tool to control parameters like grain size and porosity which play a fundamental role in dielectric response. Therefore, SPS method has been widely used to sinter PZT and doped PZT ceramic oxides for electrical applications.

2.6.8 Effect of Spark plasma sintering method on dielectric and ferroelectric properties of undoped and doped PZT ceramics

(Takeuchi et al. 2000) synthesized lead titanate ceramics of average grain size $\leq 1 \mu\text{m}$ by spark plasma sintering technique. They reported that the dielectric permittivity showed no frequency dependence up to 1 MHz due to negligible pores in the ceramic. In addition, the SPS ceramics showed higher coercive fields than their conventional counterparts due to larger grain-boundary area thereby inhibiting domain wall mobility.

(J.-K. Park et al. 2001) synthesized dense PMN-PT ceramics by SPS technique and achieved high density $> 99\%$ whereas for conventional ceramics, the density observed was only 92% of theoretical density.

(Wu, Uekawa, Kakegawa, et al. 2002) made investigations on spark plasma sintered $\text{PbZr}_{0.3}\text{Ti}_{0.7}\text{O}_3$ and stated that SPS combined with heat treatment can be used to control compositional fluctuation in PZT. It was observed that the compositional distribution width was reduced by providing longer annealing time to the sintered specimens.

Similarly, (Wu, Uekawa, Sasaki, et al. 2002) reported that the increase of heat treatment temperature by 300°C post SPS produced high and stable pyroelectric coefficient ($> 100 \text{ nC}\cdot\text{cm}^{-2}\cdot\text{K}^{-1}$) over wide temperature range for PZ-PT-PZN ceramics.

(Wu, Kimura, et al. 2002) reported a novel method of preparing transparent PZ-PT-PZN ceramics by SPS followed by heat treatment. The densities of the samples obtained were of near theoretical density and the samples were optically transparent.

Since spark plasma sintering enables to sinter materials with very low compositional distribution, (Kazuyuki Kakegawa et al. 2003) synthesized three component system, $x\text{Pb}(\text{Zn}_{1/3}\text{Nb}_{2/3})\text{O}_3 - y\text{PbZrO}_3 - (1-x-y) \text{PbTiO}_3$ by mixture of calcined materials with different compositions and sintered by SPS to obtain high pyroelectric coefficient over wide temperature range.

(Takeuchi et al. 2004) synthesized PbTiO_3 ceramics by SPS technique and obtained dense ceramics with grain size $\leq 1 \mu\text{m}$. The ceramics showed no dielectric dispersion up to 1 MHz and possessed high coercive field due to fine grained microstructures.

(L. J. Zhou et al. 2004) synthesized both SPS and conventionally prepared lead zirconate stannate titanate (PZSnT) ceramics and compared their dielectric and ferroelectric properties. It was observed that SPS samples densified at 900°C and 950°C with grain size $\sim 300 \text{ nm}$ and showed higher permittivity values than their conventional counterparts which was attributed to higher relative density or low porosity of the SPS samples. The higher dielectric loss for SPS samples was attributed to the presence of larger grain boundary area. However, the dependence of dielectric permittivity and dielectric loss on frequency were similar for CS and SPS samples. In addition, Zhou et al. stated that SPS ceramics exhibit larger c/a ratio or less tetragonality in comparison to CS samples. The decrease in grain size in SPS samples also led to the suppression of asymmetry degree in tetragonal structure. Thus, the FWHM of SPS samples are larger in comparison to CS samples which leads to the overlap of characterization peaks, whereas, in CS samples, the characteristic $\{002\}$ peaks can be distinctly separated.

(Wu et al. 2005) reported that transmittance of PLZT ceramics is strongly dependent on SPS temperature. The transmittance increases on increase of density as sintering temperature

increases up to 900°C and decreases thereafter. The sample sintered at 900°C and heat treated at 800°C exhibited transmittance of 31%.

(J. K. Park, Chung, and Kim 2006) examined the effect of SPS on ferroelectric properties of Pb (Mg_{1/3}Nb_{2/3})O₃-35 mol% PbTiO₃ ceramics. Conventional sintering at 1200°C produced ceramics with density up to 92% of theoretical density. However, SPS of the ceramics increased the relative density up to 99% and maintained its density even after heat treatment. Higher density of the SPS ceramics resulted in large improvement in dielectric and piezoelectric properties.

(L. Zhou et al. 2006) reported that spark plasma sintered PZST samples show lower remnant polarization than their conventionally sintered counterparts. In addition, the SPS samples showed maximum strain and higher coercive field. The distinct behaviour of SPS samples was attributed towards its fine microstructure.

(Zuo et al. 2007) prepared PMN-PT ceramics by spark plasma sintering as well as conventional pressureless sintering. SPS specimens showed microstructure inhomogeneity and grain size was eight times smaller than that of CS samples. CS samples transformed from normal ferroelectric to relaxor behaviour on increase of PT content. Whereas, SPS samples exhibited relaxor like behaviour in all compositions. Low dielectric permittivity, frequency dispersion and diffuse phase transition typical of relaxors were observed for SPS samples. This was attributed to the heterogeneity in composition, microstructure and fine grain size of SPS samples.

(Hungria et al. 2008) prepared nano structured 0.92PZN-0.08PT by combination of mechanosynthesis and SPS. They reported that the relaxor behaviour still existed for the PZN-PT solid solution for grain sizes as low as 15-20 nm.

(Mesquita et al. 2012) made investigations on Ba doped PZT (Pb_{0.90}Ba_{0.10}Zr_{0.40}Ti_{0.60}O₃) ceramics sintered by SPS method having average grain size of $\sim 62 \pm 5$ nm. Broad dielectric anomaly was observed in temperature dependent permittivity curves depicting diffuse phase transition (DPT) which is due to the spread of different Curie temperatures. The DPT depends on the grain size distribution related to the degree of tetragonality. The decrease in dielectric permittivity values for SPS ceramics was attributed to large amount of grain boundaries which are non-ferroelectric in nature.

(Peng et al. 2015) reported magnetoelectric effects of Co₂Fe₂O₄ (8 - 15 wt.%) added PZT ceramics sintered by SPS. As the concentration of CFO increased from 8 wt.% to 15 wt.%, the dielectric constant decreased due to low dielectric permittivity of CFO. The low frequency dielectric relaxation was also increased on adding CFO content which was attributed to high

electrical conductivity of CFO. Therefore, high amounts of CFO leads to undesirable dielectric and magnetoelectric properties.

(Han et al. 2017) reported the dielectric and ferroelectric behaviour of $\text{Pb}(\text{Zr}_{0.52}\text{Ti}_{0.42}\text{Sn}_{0.02}\text{Nb}_{0.04})\text{O}_3$ synthesized by SPS method at 1050°C . Lorentz fitting was used to deconvolute the overlapping of peaks at (002) and presented a coexistence of tetragonal and rhombohedral phases. Dielectric loss factor varied $< 7.5\%$ throughout the temperature range (20 - 500°C) which suggested good temperature stability. The dielectric properties show an increase with temperature, however, ferroelectric properties depicted temperature insensitivity.

(M. Zheng et al. 2017) reported the domain configuration and ferroelectric behaviour of quaternary $\text{Pb}(\text{Zr}_{0.47}\text{Ti}_{0.53})\text{O}_3\text{-Pb}[(\text{Ni}_{0.6}\text{Zn}_{0.4})_{1/3}\text{Nb}_{2/3}]\text{O}_3$ (PZT–PNZN) ceramics. SPS method was used to sinter ceramics of average grain size ~ 130 nm compared to $0.4 - 3.6$ μm in conventionally sintered ceramics. Even though the difference in grain size between the CS and SPS samples are significant, the dielectric constant values were found to be similar. The authors having acknowledged the increase in grain boundary layers (non-ferroelectric) in the SPS samples, stated that the similarity in dielectric constant values may be due to increase in internal stress. In addition, the SPS ceramics were found to be more temperature insensitive than the coarse grained ceramics. The hysteresis loops obtained for SPS samples were slim and slanted which were attributed to the decrease in tetragonality and the clamping of domains due to larger area of grain boundaries. They reported that in the fine grained ceramics, it is energetically favourable to form a single grain – single domain structure in which domain walls are clamped by grain boundaries.

Table 2.4 Comparison of dielectric and ferroelectric properties of PZT compositions by conventional and spark plasma sintering.

Phase composition	Conventional sintering (CS)	Spark plasma sintering (SPS)
PbTiO_3 (Takeuchi et al. 2000)	Sintering temp. : 1200°C Avg. Grain size: $\geq 1\mu\text{m}$ $\epsilon_r = \text{lower}$ $P_r = 0.74 \mu\text{C}/\text{cm}^2$ $P_s = 2.0 \mu\text{C}/\text{cm}^2$ $E_c = 2.7 \text{ kV}/\text{cm}$	Sintering temp. : 900°C Avg. Grain size: $\leq 1\mu\text{m}$ $\epsilon_r = 130 - 170$ $P_r = 1.2 \mu\text{C}/\text{cm}^2$ $P_s = 2.8 \mu\text{C}/\text{cm}^2$ $E_c = 8.9 \text{ kV}/\text{cm}$

(Pb(Mg _{1/3} Nb _{2/3})O ₃ – PbTiO ₃) (J.-K. Park et al. 2001)	Sintering temp. : 1200°C Avg. Grain size: 23.2 μm $\epsilon_r = 28000$	Sintering temp. : 900°C Avg. Grain size: 1.1 μm $\epsilon_r = 33000$
PLZSnT (L. J. Zhou et al. 2004)	Sintering temp. : 1200°C Avg. Grain size: 6.5 μm $\epsilon_r = 900$	Sintering temp. : 900°C Avg. Grain size: 300 nm $\epsilon_r = 1400$
PMN-PT (J. K. Park, Chung, and Kim 2006)	Sintering temp. : 1200°C Avg. Grain size: 21.3 μm $\epsilon_r = 23000$	Sintering temp. : 900°C Avg. Grain size: 1.4 μm $\epsilon_r = 24000$
PZT (Koo et al. 2006)	Sintering temp. : 1350°C Avg. Grain size: 3 μm	Sintering temp. : 950°C Avg. Grain size: 800 nm
PMN-PT (Zuo et al. 2007)	Sintering temp. : 1200°C Avg. Grain size: 7 μm $\epsilon_r = \sim 26000$ $P_r = 27.0 \mu\text{C}/\text{cm}^2$ $E_c = 3.6 \text{ kV}/\text{cm}$	Sintering temp. : 950°C Avg. Grain size: 0.8 μm $\epsilon_r = \sim 7700$ $P_r = 16.5 \mu\text{C}/\text{cm}^2$ $E_c = 5.6 \text{ kV}/\text{cm}$
Pb _{0.90} Ba _{0.10} Zr _{0.40} Ti _{0.60} O ₃ (Mesquita et al. 2012)	Sintering temp. : 1100°C Avg. Grain size: 2.7 ± 0.1 μm $\epsilon_r = \sim 12000$	Sintering temp. : 950°C Avg. Grain size: 62 ± 5 nm $\epsilon_r = \sim 4500$
(Pb _{0.858} Ba _{0.1} La _{0.02} Y _{0.008}) (Zr _{0.65} Sn _{0.3} Ti _{0.05})O ₃ – (Pb _{0.97} La _{0.02})(Zr _{0.9} Sn _{0.05} Ti _{0.05})O ₃ (L. Zhang et al. 2015)	Recoverable Energy= 4.65 J/cm ³ Energy Storage Density (ESD)= 7.6 J/cm ³ DBS =130 kV/cm Energy Efficiency: 61.2%	Recoverable Energy= 6.40 J/cm ³ Energy Storage Density (ESD)= 10.25 J/cm ³ DBS=162 kV/cm Energy Efficiency: 62.4%
PZT-PNZN (M. Zheng et al. 2017)	Sintering temp. : 1150°C Avg. Grain size: 1.66 μm $\epsilon_r = 9485$ $P_r = 19.3 \mu\text{C}/\text{cm}^2$ $E_c = 11.3 \text{ kV}/\text{cm}$	Sintering temp. : 800°C Avg. Grain size: 130 nm $\epsilon_r = 2518$ $P_r = 3.8 \mu\text{C}/\text{cm}^2$ $E_c = 7.4 \text{ kV}/\text{cm}$

2.6.9 Motivation and objectives of the present thesis work

Solid solutions of lead zirconate titanate [$\text{PbZr}_{1-x}\text{Ti}_x\text{O}_3$ (PZT)] are extensively used in electro-active devices and in other technological applications due to the maxima in ferroelectric, elastic, and dielectric properties that occur near the MPB, where this solid solution changes structure as a function of the chemical composition (around $x = 0.48$). One of most commonly accepted reasons for the enhanced properties near the MPB is that the rhombohedral ($R3m$) and tetragonal ($P4mm$) ferroelectric phases coexist at or near the MPB and as such the number of possible spontaneous polarization directions are increased. Phase coexistence is commonly observed near the MPB in PZT at room temperature. However, the origin of the phase coexistence, the width of the two-phase region, and the average structure of PZT near the MPB are still controversial.

As per the brief literature review mentioned in section 2.6, there are still few concepts which need better understanding. The phase constitution at MPB is still unresolved, primarily due to the volatility of PbO, size effect, domain structure, sintering behaviour etc. The size effect i.e. effect of grain size on dielectric properties of PZT ceramics is uncertain. Many researchers have reported the enhancement of dielectric and ferroelectric properties with increase of grain size. This is primarily attributed to the reduction in grain boundaries which are non-ferroelectric layers in the ceramic. However, other authors have observed increase in permittivity with decrease in grain size, stating that the larger area of grain boundaries increases interfacial polarization leading to increase in dielectric permittivity. It has been observed that authors have reported contradictory dielectric behaviour above and below the submicrometer grain size.

To achieve better ferroelectric properties, authors have either chosen a suitable dopant to achieve higher polarization or have changed the sintering parameters to achieve high density thereby increasing the dielectric breakdown strength. The PZT ceramics cannot be densified >95% TD by conventional sintering method unless some modifications are applied (Two step/multi stage sintering). This leads to the presence of inherent defects and pores undesirable for ferroelectric properties. The energy storage density (E.S.D.) of ceramics depends on the polarization of the material and applied electric field (E) by the following equation:

$$E_{st.} = \int_0^{P_{max}} E dP \quad (2.3)$$

The polarization ' P ' is an inherent property of the material dependent on phase constitution and domain structure whereas the maximum value of E depends on the dielectric breakdown strength (D.B.S.) correlated to the density of the material. Therefore, if the density of the PZT ceramics can be increased, the E.S.D. can be strengthened as well. Here, the novel sintering technique, SPS has been proven to be useful to achieve better ferroelectric properties.

SPS produces ceramics of very high density (> 98%) due to the difference in the inherent sintering mechanism. As a result, high density of ceramics leads to enhanced E.S.D. of the material. In addition, the sintering temperature is significantly lowered in SPS relative to conventional sintering methods. This property is very useful in restricting the evaporation of PbO during sintering which translates to better dielectric and ferroelectric properties.

In the present thesis, an attempt has been made to investigate the effect of SPS method on dielectric and ferroelectric properties of doped and undoped PZT. The research work tries to provide a clear understanding of the positive and negative effects of SPS towards dielectric and ferroelectric performance.

The main objectives of the thesis are: -

- I. To synthesize oxide ceramics for energy storage applications in the PZT system using spark plasma sintering as well as conventional sintering.
- II. To characterize the sintered ceramics for their morphology, phase and dielectric properties.
- III. To study the effect of doping on the properties of dielectric and energy storage behaviour.

Chapter 3

Experimental procedures

3.1 Introduction

PZT ceramics have been synthesized by various routes since the early 1950's which primarily includes chemical route (sol-gel, polymer- sol-gel) and solid state route (milling). The processing of PZT ceramics has been reported and refined over the years since the ultra-high properties at the MPB were reported. The chapter does not present any innovative way of synthesis of PZT ceramics, rather a synthesis route that is efficient to reproduce PZT specimens of uniform microstructure to aid in comparative studies. However, special emphasis has been given to the sintering method used i.e. spark plasma sintering to produce highly dense and uniform microstructure of PZT ceramics. Also, characterization techniques to identify phase constitution, density, dielectric properties and ferroelectric properties are presented in this chapter.

3.2 Composition selection

The composition of the $\text{PbZr}_x\text{Ti}_{1-x}\text{O}_3$ ceramics are selected as per the phase diagram of PZT reported by (Jaffe, Cook, and Jaffe 1971). Tetragonal ($\text{PbZr}_{0.1}\text{Ti}_{0.9}\text{O}_3$), rhombohedral ($\text{PbZr}_{0.68}\text{Ti}_{0.32}\text{O}_3$) and orthorhombic ($\text{PbZr}_{0.97}\text{Ti}_{0.03}\text{O}_3$) compositions of PZT have been chosen to study their dielectric and ferroelectric properties. However, a major part of this thesis is concentrated upon the MPB composition of PZT due to maxima in the dielectric and ferroelectric properties. The Zr/Ti ratio of 52:48 has been commonly reported to be the MPB composition in the PZT phase diagram (Noheda et al. 1999) and the same has been selected for the present thesis work . To study the effect of dopant behaviour on microstructure, dielectric and ferroelectric properties of PZT, partial substitution of donor (La^{2+}) and acceptor (Cr^{3+}) ions to A- and B- sites of the PZT lattice has been presented. The doped specimens comprise of 2 mol % La^{3+} doped $\text{PbZr}_{0.52}\text{Ti}_{0.48}\text{O}_3$ ceramics and x wt.% Cr_2O_3 added $\text{PbZr}_{0.52}\text{Ti}_{0.48}\text{O}_3$ ceramics where $x = 0.2, 0.4, 0.6$ and 0.8 wt.%.

3.3 Bulk processing of materials

The most trivial method to synthesize PZT ceramics is the mixed oxide method which was adopted by (Shirane and Suzuki 1952; Shirane, Suzuki, and Takeda 1952; Shirane and Tokyo 1952) for synthesis of PZT solid solutions. The discovery of ultra-high dielectric properties at MPB composition by (Jaffe, Roth, and Marzullo 1955) also utilized the same method.

The raw materials were of analytical reagent grade and were used in their oxide form to synthesize PZT ceramics. The purity and manufacturer of the powders are mentioned in Table 3.1.

Table 3.1 Raw material components used in the synthesis of doped and undoped PZT.

Raw Materials	Purity	Manufacturer
Lead oxide (PbO)	99.5 %	Merck
Zirconium oxide (ZrO ₂)	99.7 %	Merck
Titanium oxide (TiO ₂)	99.6 %	Merck
Lanthanum oxide (La ₂ O ₃)	99.2 %	Alfa Aesar GmbH
Chromium oxide (Cr ₂ O ₃)	99.5 %	HiMedia

The powders were weighed in stoichiometric proportion according to the desired composition using a Mettler PM 200 analytical balance. The powder mixture was wet-milled in a planetary ball mill (Retsch PM 100) using zirconia jar and balls for 8 hours at 450 rpm maintaining the ball-to-charge ratio of 10:1 for complete homogenous mixing. Toluene was used as a solvent media for proper mixing of raw materials. Thereafter, the slurry obtained was dried in glass beakers at 100°C for complete removal of the solvent.

The powder mixture was placed in a high density alumina boat for calcination in a muffle furnace (Carbolite, EHA-12). The calcination temperature was optimized after the samples were calcined at different temperatures from 800 to 950°C. Fig. 3.1 presents the XRD patterns of PbZr_{0.52}Ti_{0.48}O₃ powders calcined at 800, 850, 900 and 950 °C for 4 hours with a heating rate of 5°C/min. The analysis of the patterns indicates that all the samples show the typical perovskite structure and are indexed as a tetragonal crystal system having P4mm space group matching with PDF file no. 04-011-8847. It can be observed that samples calcined at 800°C and 850°C have pyrochlore impurity phase (Vittayakorn et al. 2003) and sample calcined at 950 °C has unreacted ZrO₂ phase, which occurs due to volatilization of PbO at higher temperature. The calcination temperature 900°C appears to be the optimum temperature to get a pure perovskite phase with

no detectable traces of the pyrochlore phase. As the sample calcined at 900°C shows the relevant phases, the same material was studied for further investigations.

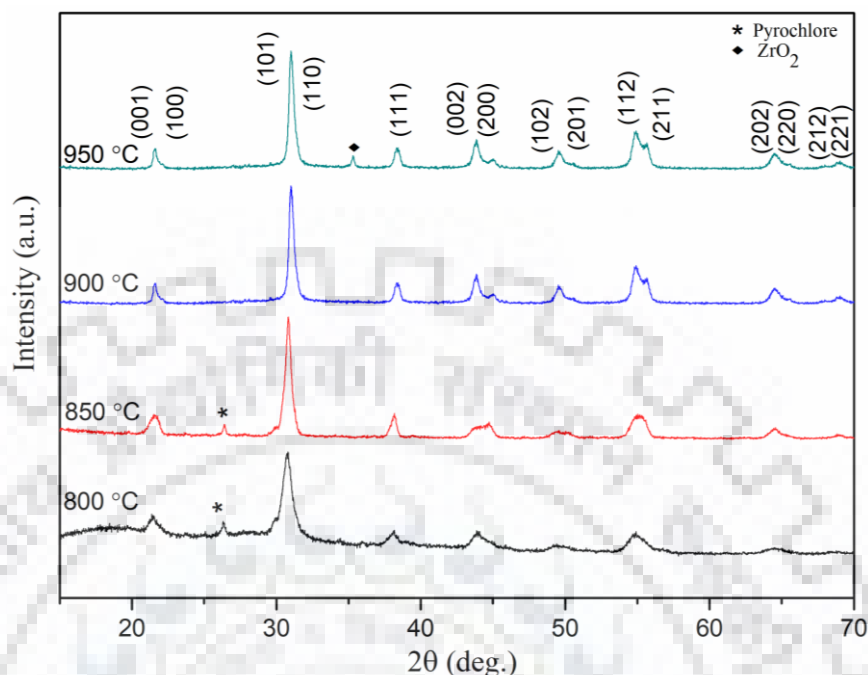


Fig. 3.1 XRD patterns of $\text{PbZr}_{0.52}\text{Ti}_{0.48}\text{O}_3$ powders calcined at 800°C, 850°C, 900°C and 950°C.

For pressureless sintering i.e. conventional sintering, powder compaction is required before sintering. A 5% PVA solution was used as a binder to increase the cohesion among the granules of powder mixture. The weight ratio kept between the powders and PVA solution was 20:1. The solution mixture was mixed in a mortar and compacted uniaxially in a powder compaction machine. An applied load of 125 MPa was used to compact the powder mixture into pellets of 10 mm in diameter and thickness ranging from 2 - 5 mm. Thereafter, the pellets were heat treated at 600°C for 2 hours to remove the binder completely. The heating rate applied was low to prevent formation of cracks and blistering in the ceramics. The pellets were covered with powders of same composition in the alumina boat to prevent intensive evaporation of lead oxide during sintering. A typical sintering profile consisted of a heating rate of 5°C/min, a dwell of 240 min at desired sintering temperature (1100 - 1200°C) and furnace cooling up to the ambient temperature.

For spark plasma sintered specimens, the calcined powders were directly placed on to the graphite dies (dia.: 10 mm; length: 40 mm) and sintered according to the desired SPS profiles as mentioned in the upcoming section 3.4.4.

3.4 Spark plasma sintering (SPS)

3.4.1 Introduction

Spark plasma sintering (SPS) also known as pulsed electric current sintering (PECS) is a novel sintering technique that utilizes pulsed DC electric current and uniaxial load to rapidly consolidate powders under vacuum condition. The direct heating of the powders allow very high heating/cooling rates to promote densification over grain growth. This allows the nanoparticles to maintain their intrinsic properties in their fully sintered bodies. Fig.3.2 shows the diffusion mechanisms that operate while sintering.

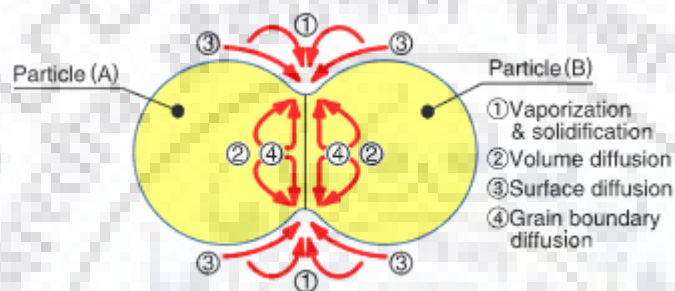


Fig. 3.2 Mass transfer path during sintering (Suarez et al. 2013).

In this technique, the material is not only heated at the macroscopic scale, but the heating power is distributed exactly at the microscopic locations where energy is required for consolidation. This results in sintering behaviour with less grain growth and high densification of calcined powders.

SPS technique offers many advantages over conventional sintering techniques such as conventional atmospheric furnaces, hot isostatic pressing (HIP) or hot press (HP) sintering. SPS provides accurate sintering control, rapid sintering, high reproducibility, flexibility and safety. The difference between SPS and HP technique lies in the type of heat source (Fig. 3.3). In SPS, the application of electric current generates rapid heating of powder compact, whereas in HP, the material is heated through radiation from the heating elements of the furnace and convection of inert gases if applicable. Therefore, in SPS, high heating rates of up to 1000°C/min can be achieved which significantly cuts the sintering time and energy costs. The heating rate depends on the sample's thermal properties and the specifications of the die used. On the contrary, in HP technique, the sample is heated by conduction through heat transfer from the external heating elements of furnace to the sample. This results in a lot of heat being wasted and the heating rate becomes typically low leading to increase in sintering time (~ hours).

It is noteworthy to mention that the distribution of temperature through electrical current in SPS is particularly acute. As a result, the electrical current may assume different intensity and waveform depending on the DC power supply characteristics. The temperature distribution inside the specimen depends on the sample's electrical conductivity, thickness of the enclosing die and the graphite foils that separate the die and the sample. In order to achieve homogenous distribution of temperature, the temperature gradients have to be minimized. In our present work, the temperature gradients have been controlled by choosing the length of graphite die almost four times the thickness of sample and by encapsulating the sample by graphite foils to prevent direct contact to the die and to ensure proper electrical contacts between all parts.

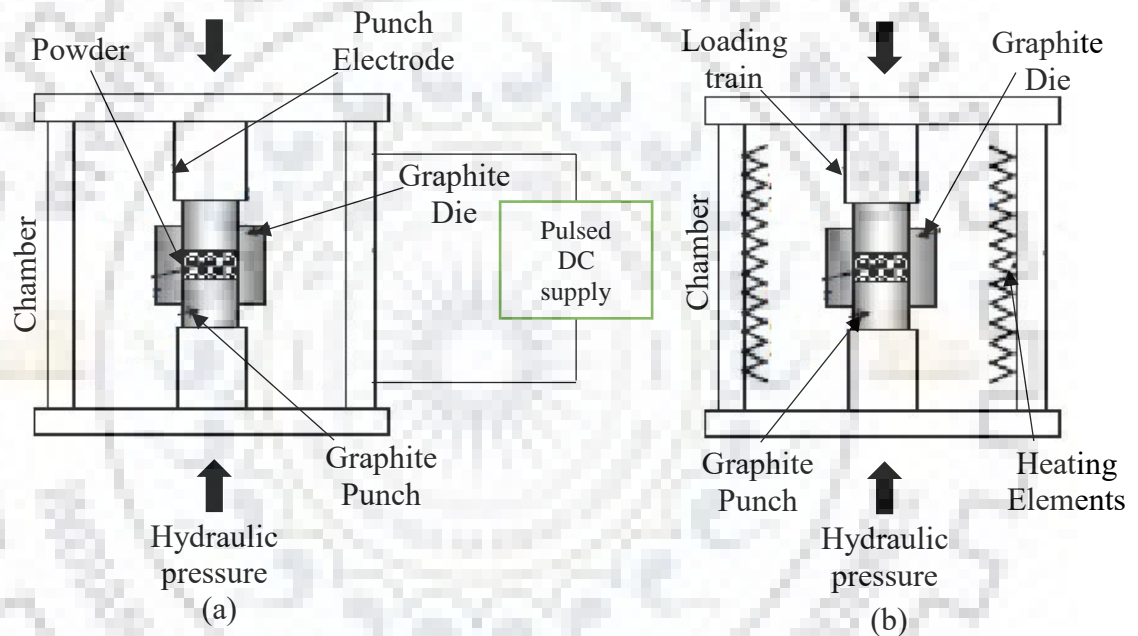


Fig. 3.3 Schematic representation of (a) SPS and (b) HP process (Suarez et al. 2013).

Spark plasma sintering and plasma assisted sintering (PAS) machines were first developed by Sumitomo Heavy Industries Ltd. Japan in 1990. The die enclosures and punches were made of high density graphite. The unique selling point (USP) of these machines was that in addition to sintering electrically conductive powders, it also achieved high density for insulating materials. The machines differed in their DC power supply characteristics namely “single pulse cycle process” and “multiple pulse cycle process” wherein, the duration of a pulse is typically in the order of milliseconds. In single pulse cycle process, a pulsed DC is applied at the start of sintering stage followed by a constant DC applied until the end of sintering stage. This process was utilized in PAS machines whereas in SPS, pulsed DC is repeatedly applied throughout the sintering process. Fig. 3.4 shows the DC supply parameters used in PAS and SPS.

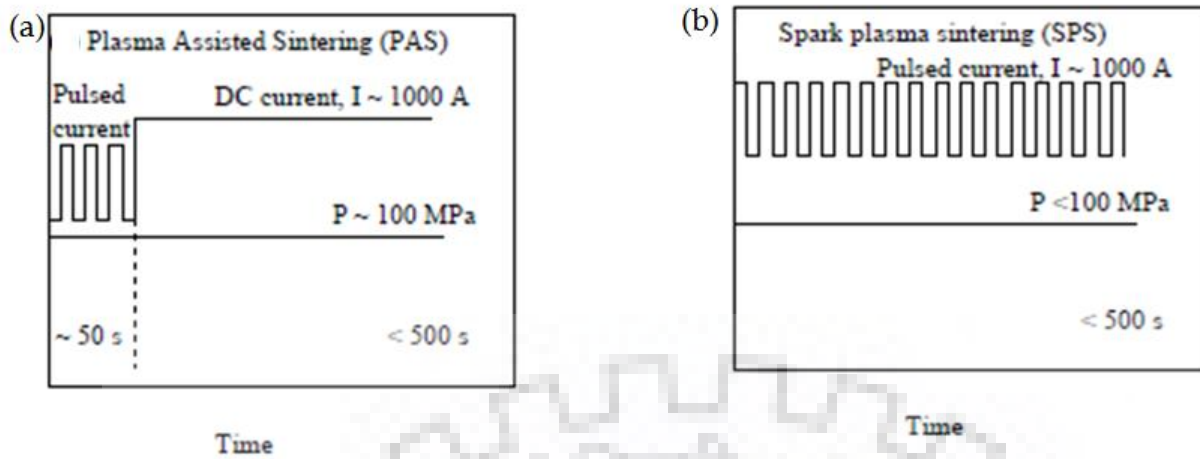


Fig. 3.4 Power supply characteristics used in (a) PAS and (b) SPS techniques (Suarez et al. 2013).

3.4.2 SPS configuration

Fig. 3.5 depicts the basic configuration of the SPS apparatus. The system consists of a DC pulsed power generator system that generates low voltage, high current electrical supply to act as a heating source for the graphite dies and punches that enclose the sample in a controlled atmosphere. The hydraulic rams are located near the electrode for applying a uniaxial load to the sample. The vacuum chamber houses a water cooled piping system to act as a heat sink to prevent high temperature degradation of chamber walls. Specific lubricant based on sintering temperature (Boron nitride/graphite foil) is applied on the inner surface of the die to ensure proper removal of sample pellet after sintering. The calcined powder is placed between the graphite die and punch to be placed in the vacuum chamber. Thereafter, the graphite die is held at minimal contact pressure between the two electrodes including proper arrangement of other graphite parts to maintain axial symmetry. The sintering cycle can be controlled by temperature feedback systems (thermocouples or pyrometers) as shown in fig. 3.5. The sample powder is rapidly consolidated under high pressure and pulsed power, generating heating rates up to $1000^{\circ}\text{C}/\text{min}$ and producing high density compact within a time period of minutes.

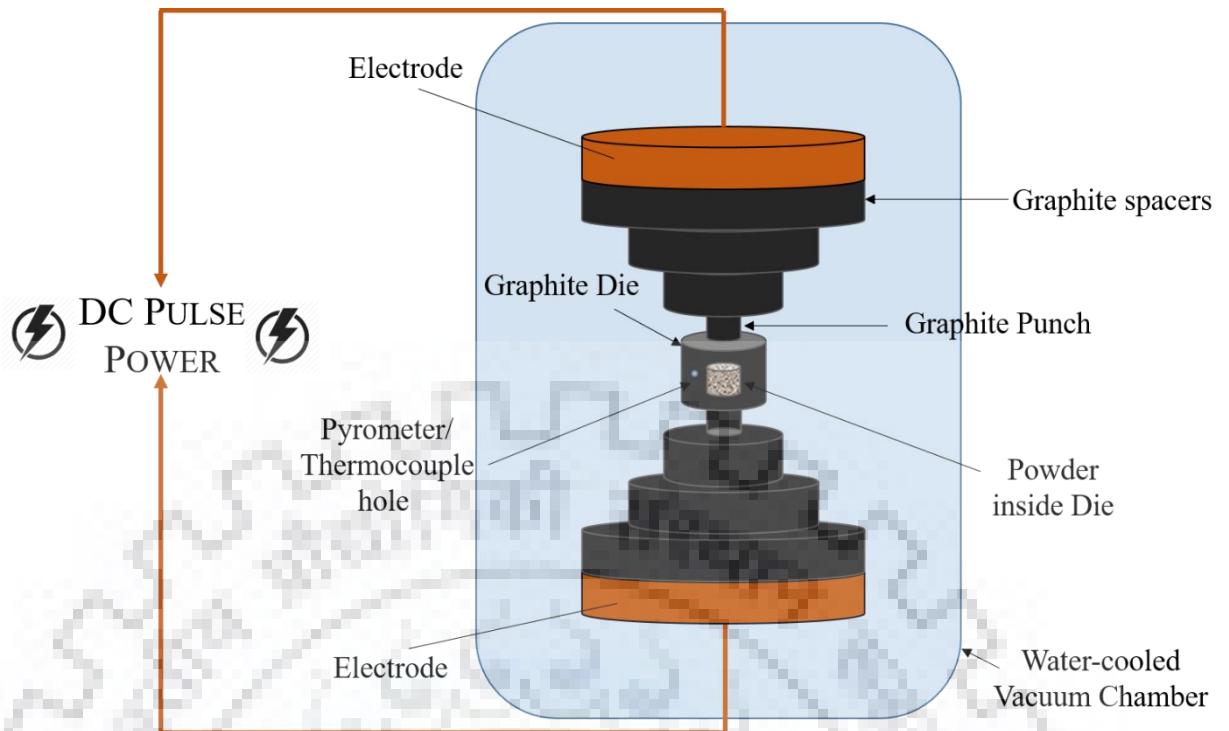


Fig. 3.5 Configuration of SPS apparatus.

3.4.3 Mechanism/working of SPS

The SPS process utilizes low voltage (≤ 10 V), high current (~ 5000 A) power supply and generates a so called “spark discharge” or “plasma” over the surface of powder particles or the contact points between the particles. This discharge phenomenon promotes fast thermal diffusion between the particles due to generation of very high temperature ($\sim 10000^{\circ}\text{C}$). The sintering temperatures in SPS are $200 - 500^{\circ}\text{C}$ lower than in conventional sintering techniques. High heating rates ($\sim 1000^{\circ}\text{C}/\text{min}$) promotes vaporization, melting and sintering to take place simultaneously. Several investigations to deduce the mechanisms occurring in SPS have been conducted from which some mechanisms are proposed below:

3.4.3.1 Electrical effects

The electrical effects can be divided into current and field effects for which a comprehensive review is given here (Anselmi-Tamburini et al. 2012; Zuhair A. Munir, Quach, and Ohyanagi 2012). If an electrically conducting material is sintered by SPS, the DC currents flow through the raw material directly instead of passing through the graphite parts surrounding it. The effect of electrical current on microstructure of the material during sintering are (i) percolation of current flow through the green compact (McWilliams and Zavaliangos 2008; Schwesig et al. 2011), (ii) the Peltier effect generated between the graphite punch and green compact (Becker et al. 2012), (iii) electromigration (Z. A. Munir, Anselmi-Tamburini, and Ohyanagi 2006). Since the green

compact is not completely dense, the electrical current cannot flow uniformly throughout the material. Therefore, a convoluted pattern of percolating currents form which creates local temperature gradients throughout the green body. The Joule heating acts along these percolation paths and generates local hotspots in which the temperatures exceed the average temperature of the sintering process.

(Inoue 1965; Yanagisawa, Hatayama, and Matsugi 1994) claimed that the DC pulsed supply generates spark and plasma discharge in the contact points between the powder particles. As a result, they named the processes as “spark plasma sintering” or “plasma activated sintering”. They stated that the plasma discharge causes ionization at the particle contacts and facilitates diffusion of atoms. (Groza and Zavaliangos 2000) stated that the pulsed current effectively cleans the surface of particles i.e. breakdown of surface films, after they observed no oxidation at the boundaries between ceramic particles. Plasma generation has been a topic of debate since it has not been observed experimentally (which is a very difficult task), and therefore any conclusive remarks on the effect of plasma generation in SPS cannot be made. However, it has been widely accepted that the pulsed electrical current occasionally causes spark discharge on a microscopic scale (Groza and Zavaliangos 2000).

3.4.3.2 Mechanical effects

The uniaxial compressive stress applied to the sample powder during SPS process breaks down particle agglomerates, enhances particle rearrangement, reduces pore size and increases packing density between the particles. It also enhances the existing densifying mechanisms i.e. grain boundary diffusion, lattice diffusion, viscous flow etc. The mechanical pressure is not expected to affect the non-densifying mechanisms, e.g. surface diffusion or evaporation/condensation (Rahaman 2017). However, at high temperatures, it may activate additional densifying mechanisms namely plastic flow as yield stress decreases on increase in temperature. As a result, lower temperatures are required for complete densification. Also, grain growth is delayed and reduced under mechanical pressure, but not suppressed. Fig. 3.6 depicts the basic mechanism of neck formation under mechanical pressure.

The intrinsic role of mechanical pressure can be assessed relative to driving force for sintering by the equation:

$$\frac{d\rho}{(1-\rho)dt} = B \left(g \frac{\gamma}{x} + P \right) \quad (3.1)$$

where ρ is the fractional density, t is time, B is a term that depends on coefficient of diffusion and temperature, g is geometric constant, γ is the surface energy, x represents particle size and P is applied load/pressure. The term $B \left(g \frac{\gamma}{x} \right)$ denotes the intrinsic driving force for sintering whereas the term ' BP ' represents the intrinsic contribution to the driving force by applied mechanical pressure. Thus, the contribution of pressure to sintering depends on the relative values of these two terms. If the particle size (that relates to γ) is small, the relative contribution of the applied pressure will be small, but becomes significant with increase in particle size. (Skandan et al. 1994) observed no change in the relative density of nano-sized zirconia particles (~ 6 nm) up to an applied pressure of ~ 35 MPa. However, the density showed a sharp increase when the pressure was increased further. The same behaviour was found for larger sized particles (~ 12 nm) for an applied pressure of 10 MPa.

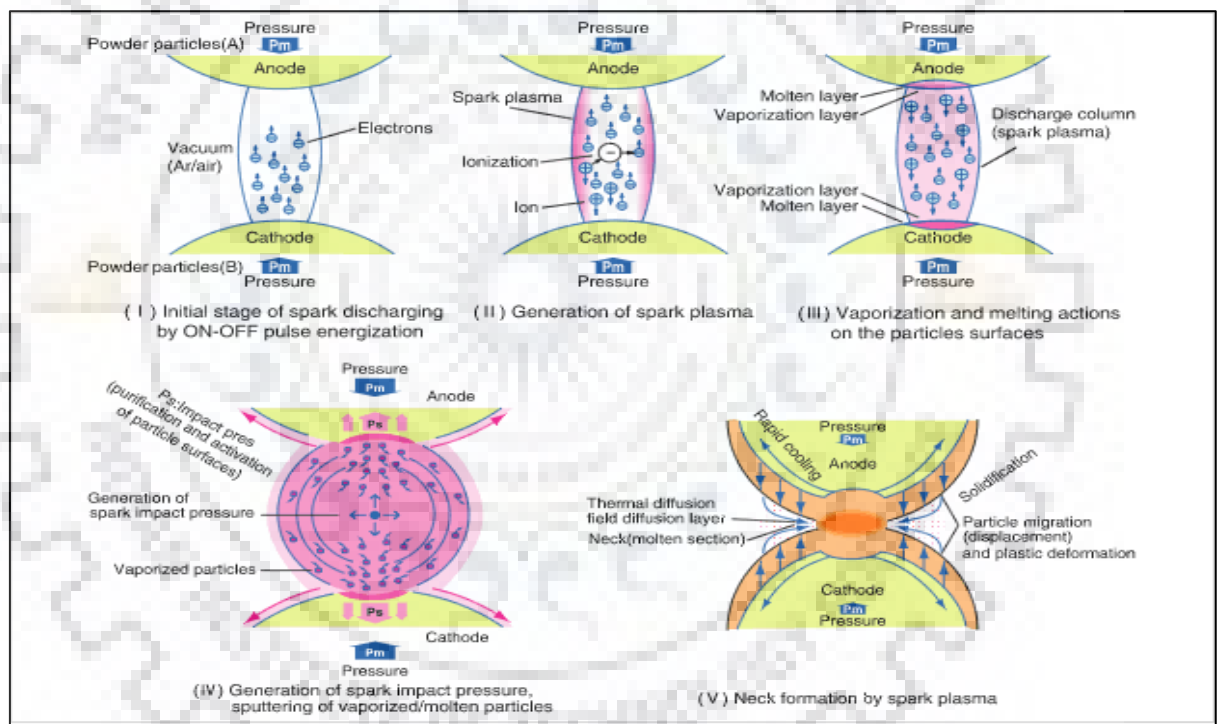


Fig. 3.6 Basic mechanism of neck formation by mechanical pressure during SPS (Tokita 2013).

3.4.3.3 Thermal Effects

SPS has another important factor besides the application of pressure, which is the capability of achieving very high heating rates. Grain boundary diffusion mechanism has higher activation energy in comparison to surface diffusion or coarsening mechanism. Therefore, the ability to bypass the low temperature densifying mechanisms by reaching high temperatures rapidly proves to be beneficial to achieve high densification with retarded grain growth.

(Skandan et al. 1994; Tokita 2013) reported that for all heating rates ranging from a few tens to hundreds of degree celsius per minute, the final sintered body always achieved a finer microstructure when rapidly heated relative to coarser microstructure for slow-heated counterparts. Grain growth increases with time at higher temperature region. Therefore, lesser the holding time at high temperature, higher is the suppression of grain growth.

Other thermal effects are related to local microscopic temperature gradients formed during sintering. These gradients act as another driving force for diffusion also known as Ludwig-Soret thermal diffusion and may even cause melting. However, the formation of such gradients depends on the physical properties of the material (Holland et al. 2012).

3.4.4 Temperature and pressure profiles used in Spark plasma sintering

The spark plasma sintering of calcined samples was conducted by using graphite die (ID: 10 mm; OD: 30 mm) and graphite punch of length 30 mm. The grounded powders were encapsulated by thin graphite foil (~ 0.5 mm thickness) to ensure proper removal of specimen after sintering. The sintering of all ceramic oxide samples was conducted in a vacuum atmosphere (at ~ 6 Pa). The selection of the sintering profile was finalized after several trials on raw PZT material and ensuring that the ceramic pellets do not crack while removing them. A similar sintering profile has also been reported here (Wu et al. 2005).

Fig. 3.7 shows a representative sintering profile for a PZT sample sintered at 950°C. The temperature profile is divided into three stages: (i) T1 over which a heating rate of 100°C/min was applied from room temperature to the temperature which is 100°C below the sintering temperature; (ii) T2 over which a heating rate of 33°C/min was applied up to sintering temperature; (iii) T3 over which soaking was done. At stage T1, higher heating rate was chosen to reduce grain growth leading to higher bulk density of the samples (Stanciu, Kodash, and Groza 2001). At stage T2, lower heating rate is applied to allow sufficient time for atomic diffusion (mainly through grain boundary and the initiation of lattice diffusion). The pressure profile is also divided into three stages namely P1, P2, and P3. At stage P1, the pressure (12 - 15 MPa) is just sufficient to maintain powder particles in contact which is maintained until the sintering temperature is attained to allow the liquid phase to flow (PbO liquid phase) to aid the sintering process. At P2, the pressure is increased to 60 MPa at the beginning of the soaking stage. The increased pressure tends to make closure of the remaining pores in the samples. At P3, the pressure is released just before the cooling process begins to prevent cracking of ceramic samples (Stanciu, Kodash, and Groza 2001).

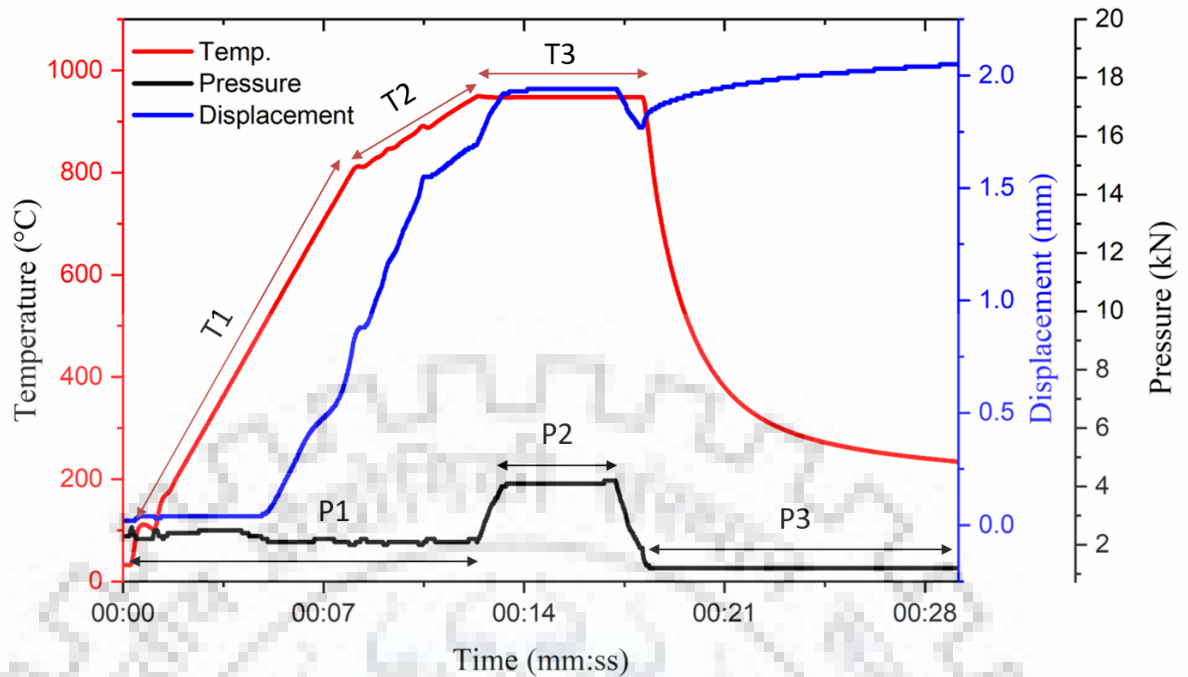


Fig. 3.7 SPS profile adopted for representative sample sintered at 950°C showing different temperature and pressure stages during a sintering cycle.

3.5 Characterization techniques

3.5.1 Density

The bulk density of the ceramic oxides was determined based on the “Archimedes principle”. The weight of the sample in air (m_a) was measured using a Mettler PM 200 analytical balance. The weight in liquid (m_w), was measured by suspending the sample in distilled water in a glass beaker. The bulk density (ρ_b) of the sample relative to theoretical density (ρ_{th}) was calculated using eq. 3.2:

$$\rho_b = \left(\frac{m_a}{m_a - m_w} \right) * \rho_{th} \quad (3.2)$$

Relative density (ρ_{rel}) is a measure of the sample density and is equal to the ratio of expected bulk density to theoretical density by eq. 3.3.

$$\rho_{rel} = \left[\left(\frac{\rho_b}{\rho_{th}} \right) * 100 \right] \% \quad (3.3)$$

3.5.2 X-ray diffraction (XRD)

The structural information of the crystalline materials is commonly gathered by a non-destructive technique known as X-ray diffraction. In this technique, X-rays which have wavelength λ , comparable to atomic spacings in a crystal structure is used. X-ray beam is directed to the surface

of the material to be tested, and it gets diffracted at specific angles based on the ordered interplanar spacings (d_{hkl}) of the material. A peak of the diffraction pattern correlates to set of planes (d_{hkl}) with similar interplanar spacing.

$$n\lambda = 2d_{hkl}\sin\theta \quad (3.4)$$

The crystallite size is typically the size of a single crystal in powder form. When the sample is irradiated with X-rays, the X-rays scatter coherently through the crystallite. The Scherrer's equation as given below is used to determine the size of particles of crystals in the form of powder:

$$L = \frac{k_s \lambda}{(\cos \theta) T} \quad (3.5)$$

where, L is the mean size of the ordered (crystalline) domains, k_s is a shape factor constant in the range 0.8–1.2 (typically equal to 0.9), λ is the X-ray wavelength, T is peak width at FWHM, θ is the Bragg angle. On the other hand, grain is either a single crystalline or polycrystalline material, and is present either in bulk or thin film form. During the processing, smaller crystallites tend to grow and become larger. Therefore, in general a grain is larger than a crystallite. The grain morphology is commonly determined by SEM.

The phase characterization and crystalline purity was examined by the X-ray diffraction at room temperature. Powder XRD patterns were obtained by using the X-ray diffractometer (Smart Lab Rigaku, Japan) employing $\text{CuK}\alpha$ radiation ($\lambda = 1.5418 \text{ \AA}$) and $\text{CoK}\alpha$ radiation ($\lambda = 1.79 \text{ \AA}$) with scanning range $2\theta = 20 - 70^\circ$, scanning speed of $2^\circ/\text{min}$ and step of 0.01° . The phase analysis of the XRD patterns is done using PDXL software with PDF-4+ ICDD database. The reference powder diffraction files (PDF) were used to index the diffraction peaks for compositions in tetragonal, rhombohedral and MPB. The characteristic (110) peak for PZT samples lie near $2\theta = 31^\circ$ for incident Co X-ray target. The impurity pyrochlore phase can be deduced by identification of peaks near $2\theta = 27^\circ$. The phase symmetry of the material can be deduced by observing the peak splitting's and peak profile in the XRD patterns. Fig. 3.8 depicts the peak splitting in (100), (110), (111) reflections for different phase symmetries for the sake of reference.

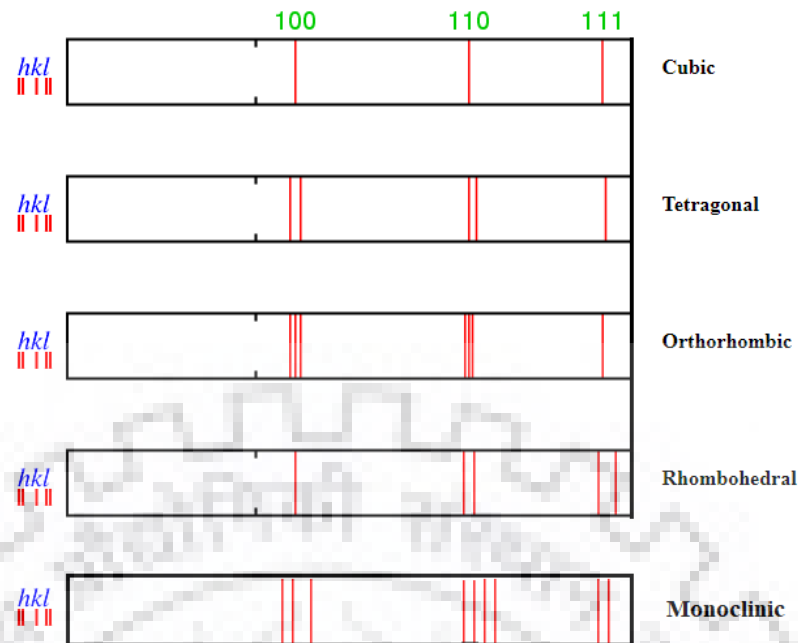


Fig 3.8 Peak splitting's in XRD pattern for a cubic material transforming to a phase of lower symmetry.

3.5.2.1 Rietveld refinement

Rietveld refinement uses a non-linear least square fit to minimize the differences between the peak profiles calculated from a reference crystal structure and the peak profiles observed in a 1D diffractogram by adjusting the different variables that describe the diffraction pattern. The model function includes contribution from both the sharp peak intensities and the background underlying the peaks. The computations involved in refinement are exhaustive and require to minimize the sum of weighted and squared differences from the observed and reference intensities at every step in the refinement cycle. The Rietveld method requires prior knowledge of the approximate crystal structure of every phase present in the sample. Although, accurate description of every peak in a diffraction pattern remains a challenge, but many successful profile shape functions have been developed. The Voigt, the pseudo-Voigt and the Pearson VII profile functions are of prime interest to be used in Rietveld refinement. The Voigt function is essentially a convolution of Gaussian and Lorentzian peak profiles. The pseudo-Voigt function incorporates a mixture of fractions of both Gaussian and Lorentzian components needed to fit the desired peak shape. The Pearson VII also allows for variation in peak shape from Gaussian to Lorentzian and can easily be split to explain the asymmetric diffraction peaks. The FWHM analysis for a pseudo-Voigt profile function was defined by (Caglioti, Paoletti, and Ricci 1958) in the following equation:

$$H_k^2 = U \tan^2 \theta + V \tan \theta + W = F_{instr} \quad (3.6)$$

where H_k is full width at half maximum (FWHM) of the k^{th} Bragg reflection and U , V and W are refinable parameters related to peak shape.

The principle of Rietveld refinement is to minimize a function M , which is the sum of difference between observed data and calculated profiles as reported by (Rietveld 1969) in eq. 3.7.

$$M = \sum W_i \left\{ y_i^{\text{obs}} - \frac{1}{c} y_i^{\text{cal}} \right\}^2 \quad (3.7)$$

where W_i is the statistical weight and c is the overall scale factor.

The quality of refinement is based on reliability factors such as Profile factor (R_p), weighted profile factor (R_{wp}), expected weight factor (R_{exp}) and reduced (χ^2) defined as follows:

$$R_p = 100 \frac{\sum |y_i^{\text{obs}} - y_i^{\text{cal}}|}{\sum y_i^{\text{obs}}} \quad (3.8)$$

$$R_{wp} = 100 \left[\frac{\sum \omega_i |y_i^{\text{obs}} - y_i^{\text{cal}}|^2}{\sum \omega_i y_i^{\text{obs}^2}} \right]^{\frac{1}{2}} \quad (3.9)$$

$$R_{exp} = 100 \left[\frac{n - p}{\sum \omega_i y_i^{\text{obs}^2}} \right]^{\frac{1}{2}} \quad (3.10)$$

where ' n ' is total number of experimental points, ' p ' is the number of refined parameters and $(n - p)$ is number of degrees of freedom.

$$\chi^2 = \left[\frac{R_{wp}}{R_{exp}} \right]^2 \quad (3.11)$$

Thus the Rietveld technique can be used to describe all the crystal structure information and complete orientation distribution function of the specimen. It is the most accurate method available for quantitative analysis of powder diffraction data and also provides estimated standard deviation (e.s.d.) for each of the refined parameters.

Table 3.2 CIF files used in Rietveld refinement. Here PZT stands for $\text{PbZr}_{0.52}\text{Ti}_{0.48}\text{O}_3$.

CIF files	DB card number	Registered database
Tetragonal PZT	4-18-5315	ICDD (PDF-4+ 2018 RDB)
Monoclinic PZT	4-11-8860	ICDD (PDF-4+ 2018 RDB)
Rhombohedral PZT	4-12-8156	ICDD (PDF-4+ 2018 RDB)
Tetragonal PbO	4-03-4541	ICDD (PDF-4+ 2018 RDB)

“The reference CIF files mapped were of tetragonal, rhombohedral and monoclinic symmetry of PZT(52/48). In addition, the CIF file of PbO phase was also incorporated to account for any excess PbO phase present in the sample. The peak intensity data have been refined using pseudo-Voigt peak function, whereas the function chosen for mapping the background data underlying the peaks is the B-spline function. The individual scale factors correlated to the concentration of each phase, profile, background, and lattice parameters are varied in a typical refinement cycle. In favorable cases, the atomic positions, site occupancies and thermal parameters were also refined to obtain the correct crystal structure model. The exact variation of parameters involved in refinement for each composition are described in detail in Chapter 4.”

3.5.3 Scanning electron microscopy (SEM)

The scanning electron microscopy is a technique used to identify the topography, morphology and approximate composition (using energy dispersive spectroscopy mode) of the specimen. A beam of high energy electrons generated by an electron gun are focused on to the specimen which thereby ejects secondary electron (SE), back scattered electrons (BSE) and X-rays. The release of photons or electrons depends on the interaction between the beam of electrons and the atoms at or near the surface of the specimen. Fig. 3.9 depicts the scattering process of the electron beam in SEM. The energy distribution of emitted electrons and X-rays are collected by the respective detectors and converted into display form for further analysis.

In the present research work, the microstructural features such as particle size and shape, grain size, grain boundary, pores, elemental composition etc. were characterized by using field emission scanning electron microscope (FE-SEM), Carl-Zeiss Ultra 55, Germany. The characterization of powder samples were conducted by taking very small amount of powder (~ mg) and deposited directly on a carbon foil fixed to an aluminium stub. The powder particles were ultrasonicated for about 4 minutes before transferring onto the carbon foil. Sintered ceramic disks were polished down to optical quality before SEM observation. Since the ceramic powders and pellets are non-conducting, a very thin layer of gold (~ 20 nm) was sputter coated on their surface, to avoid electron accumulation/charging effect. Thermal etching of doped and undoped

PZT sintered disks was done to get better image contrast of the grain boundaries. The determination of average grain size of the sintered specimens from the SEM micrographs of polished and fractured surfaces was made using Image J software.

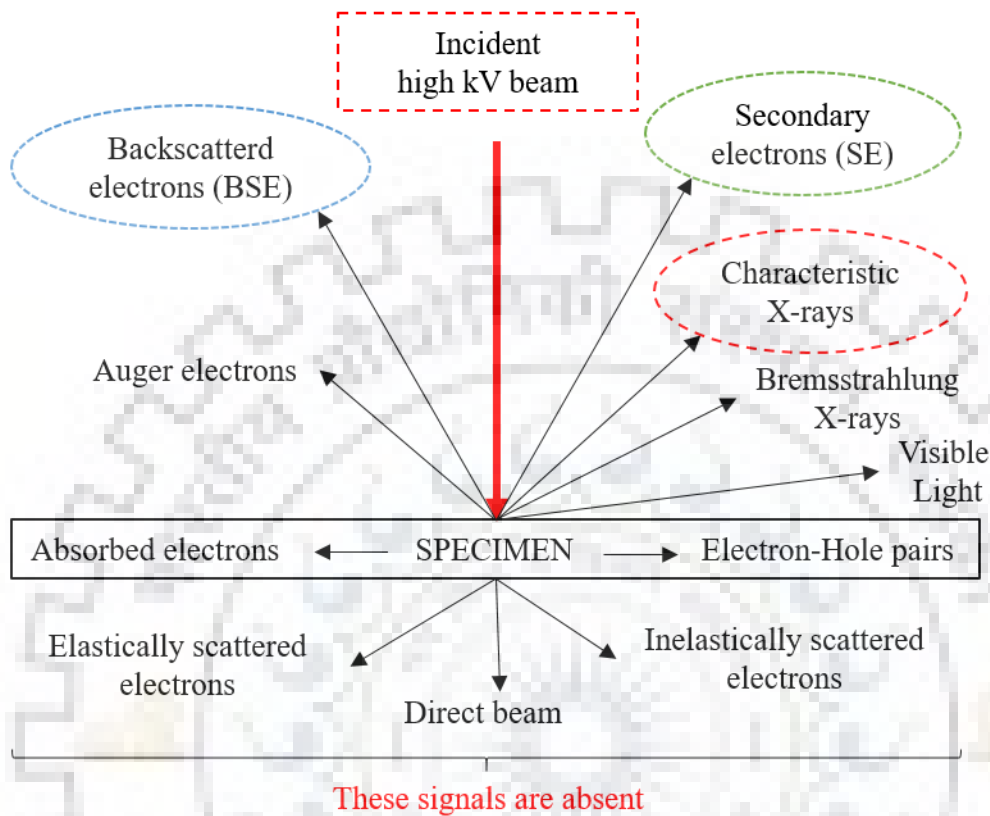


Fig. 3.9 Schematic of electron scattering in SEM.

3.5.3.1 Energy dispersive X-ray spectroscopy (EDS)

Energy dispersive X-ray spectroscopy is an analytical technique to identify the elemental or chemical composition of a material. This technique is one of the variants of X-ray fluorescence which analyzes the emitted X-rays when the material is subjected to a high energy beam of electrons. The emitted X-rays contain information regarding the crystallographic structure of the specimen which are collected by the EDS detector and processed further. There are four parts of an EDS setup namely, (i) beam source, (ii) X-ray detector, (iii) pulse processor, (iv) Analyzer. There are many standalone EDS systems, however, they are commonly fitted onto SEM systems (SEM-EDS). In the present research work, EDS has been used to determine elemental compositions in doped and undoped PZT ceramics since the resulting phase constitution is directly dependent on composition.

3.5.4 Electroding of sample surface

The use of a suitable electrode for electrical measurements is important since (i) it prevents error caused due to air gap between the electrode and surface of the specimen, (ii) measurement of dielectric parameters are inaccurate in non-contact electrode setups. The sintered ceramic disks were coated with a thin layer of conducting silver paste on flat surfaces. The coated disks were dried at 100°C in an oven for 6 - 8 hours before dielectric and ferroelectric studies.

3.5.5 Dielectric properties

The dielectric characterization of materials provide insight about the phase transition temperature and the Curie point of ferroelectric materials. The analysis of dielectric permittivity as a function of temperature is a common tool to detect phase transitions in ferroelectrics. On the other hand, analysis of dielectric loss as a function of temperature and frequency provides an additional information on dielectric properties, for e.g., the electrical conductivity.

In the current research work, dielectric measurements on the electrode samples were made using an impedance analyzer, HIOKI 3532-50 LCR HiTester. The sample holder was fitted onto a high temperature (Model: DPI-1200) furnace having temperature controller with heating rate 2°C/min for measuring dielectric parameters above room temperature. The LCR meter was connected to a computer via RS232 interface for recording dielectric parameters as a function of temperature at different frequencies with an AC input voltage 1.1 V. The dielectric and impedance parameters namely, real part of impedance (Z'), imaginary part of impedance (Z''), parallel capacitance (C_p), conductance (G) were measured directly over the frequency range of 42 Hz - 5 MHz in the temperature range 30 - 450°C. The dielectric constant of the material can be calculated in terms of C_p (eq. 3.12) and impedance parameters (eq. 3.13) as follows:

$$\epsilon_r = \frac{C_p \cdot d}{A \cdot \epsilon_0} \quad (3.12)$$

$$\epsilon_r = \frac{t}{\omega A \epsilon_0} \left[\frac{Z''}{Z'^2 + Z''^2} \right] \quad (3.13)$$

where ϵ_r is the dielectric permittivity, ω is the angular frequency ($\omega = 2\pi f$), f is frequency, ϵ_0 is the permittivity of free space (8.854×10^{-12} F/m), t is the thickness and A is the surface area of the specimen.

The dielectric loss of the material is given by: -

$$\epsilon'' = \frac{t}{\omega A \epsilon_0} \left[\frac{Z'}{Z'^2 + Z''^2} \right] \quad (3.14)$$

The dielectric loss tangent ($\tan\delta$) of the material quantitatively represents the dissipation of electrical energy due to electrical conduction, dielectric relaxation, dielectric loss etc. and given by: -

$$\tan\delta = \frac{\epsilon''}{\epsilon'} \quad (3.15)$$

The AC conductivity of the material can be calculated as per equation given below: -

$$\sigma_{ac} = \omega\epsilon_0\epsilon_r\tan\delta \quad (3.16)$$

3.5.6 Complex impedance and modulus spectroscopy

Complex impedance spectroscopy (CIS) (MacDonald 1987) is a technique to study the electrical characteristics of materials. It helps to distinguish between the contributions of grain and grain boundary (inter grain) in electrical transport properties of the material. The electro-active regions can be assigned with respective RC elements by observing the impedance spectrum. The values of individual R and C elements can then be quantified after proper fitting of the impedance spectrum to the electrical circuit diagram. The variation of dielectric properties with frequency are represented in terms of, complex impedance Z^* , complex modulus M^* , complex permittivity ϵ^* , complex admittance Y^* and dielectric loss tangent ($\tan\delta$). The impedance spectrum is also commonly known as Cole-Cole plot or Nyquist plot.

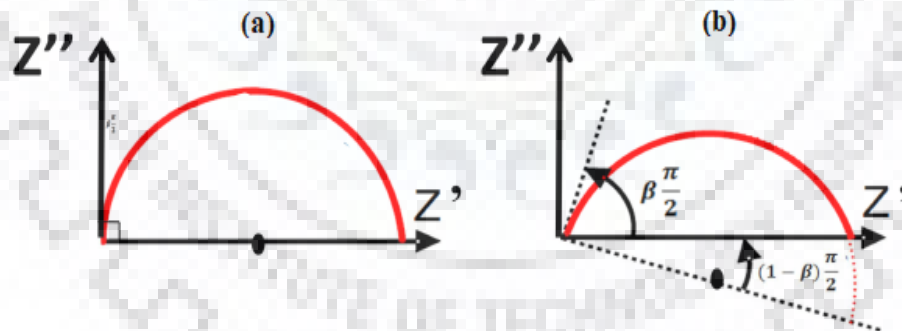


Fig. 3.10 Nyquist plot of (a) Debye single relaxation time model (b) distribution of relaxation time model (Essaleh et al. 2016).

Debye relaxation is the dielectric relaxation response of an ideal material (usually liquids) exhibiting single relaxation time given by $\omega_{max}\tau = 1$ to applied external AC field, where ω_{max} is the angular frequency at peak maxima in Z'' or M'' and τ is the relaxation time. The Nyquist plot is constructed by plotting Z'' (y-axis) against Z' (x-axis). Fig. 3.10 (a) depicts the impedance spectrum for an ideal Debye material, for which the arc can be fitted using an ideal capacitor C. The complex impedance Z^* then follows the eq. 3.17.

$$Z^* = \frac{R_g}{1 + j\omega\tau} \quad (3.17)$$

where, $\omega = 2\pi f$, the angular frequency, R_g is the resistance of grain or bulk and $\tau = RC$ is the relaxation time. On the contrary, for a non-Debye material, the semi-circular arc is depressed due to difference in relaxation times of the electro-active regions. As a result, deconvolution of semi-circular arc is essential to gather information about the different relaxation processes. The center of semicircle is shifted below the Z' (x -axis) by an angle ϕ as shown in Fig. 3.10 (b). The resulting relaxation arc cannot be fitted by an ideal capacitor alone and should be replaced by a constant phase element (CPE), for which the impedance is given by eq. 3.18.

$$Z_{CPE} = \frac{1}{Q(j\omega)^n} \quad (3.18)$$

where Q is a constant independent of frequency and ' n ' is an exponent that represents the distortion of the Nyquist plot characteristics. For a Debye material, $n = 1$ and for an ideal resistor, $n = 0$. The R value is calculated from the intercept on Z' axis in the impedance spectrum, whereas, C is calculated by relation, $\omega_{max}RC = 1$.

However, real materials usually exhibit non-Debye type relaxation and broad relaxation time distribution. The impedance spectrum for a polycrystalline material as shown in Fig. 3.11 depicts distinguishing features of grain and grain boundary contributions in the form of semi-circular arcs. The high frequency arc with diameter R_g in the Nyquist plot corresponds to the bulk contribution of the material, whereas, the arc in the lower frequency region with diameter R_{gb} corresponds to the grain boundary contribution. A spike at the lowest frequency is generally attributed towards the electrode effects.

On the other hand, the complex plane modulus plots reveal complementary information to complex impedance plots. The electric modulus physically corresponds to the relaxation of the electric field in the material, so that the electric modulus represents the real dielectric relaxation process. The complex modulus also provides an alternative approach (i) to analyze the electrical response of the materials and has been adopted by scientists to study relaxation phenomena in ceramics materials and ionic conductors, (ii) which helps to confirm the ambiguity arising from the grain or grain boundary effect at elevated temperatures which may not be distinguished from complex impedance plots. The modulus formalisms are given as follows:

$$M^* = j\omega C_o Z^* \quad (3.19)$$

$$M' = \omega C_o Z'' \quad (3.20)$$

$$M'' = \omega C_o Z' \quad (3.21)$$

where, M' and M'' are real and imaginary parts of complex modulus, ' ω ' is the angular frequency and C_o is the capacitance due to vacuum.

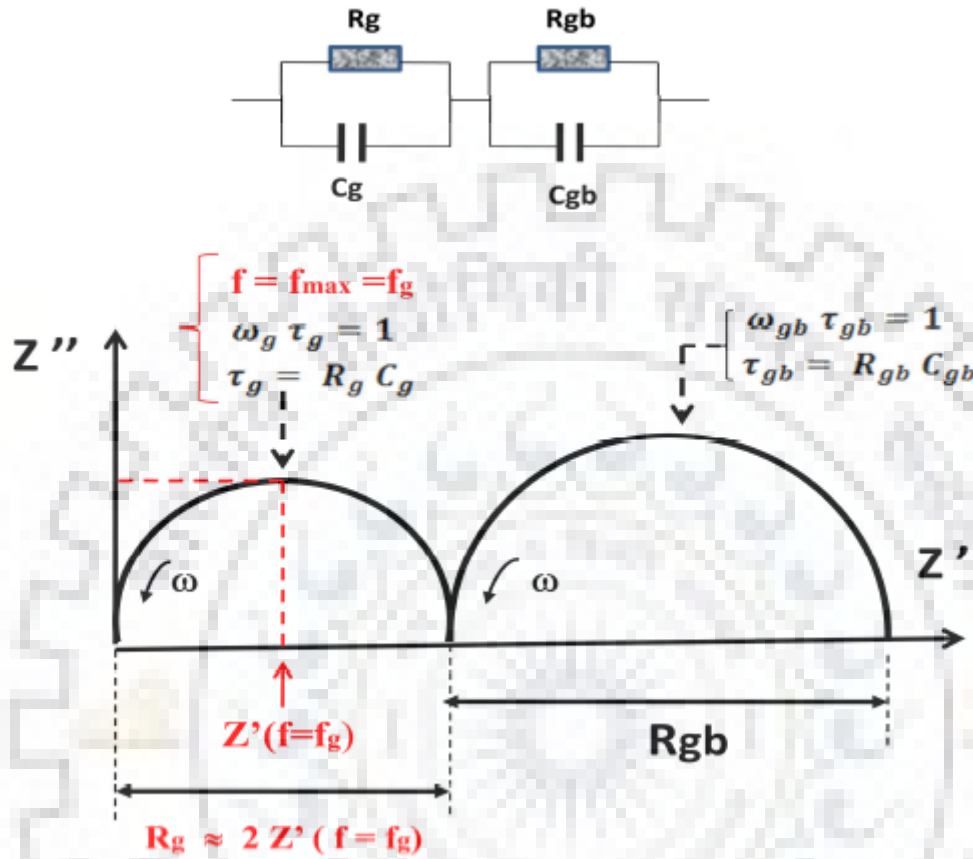


Fig. 3.11 Nyquist plot for two parallel RC elements connected in series (Essaleh et al. 2016).

For an equivalent circuit diagram shown in Fig. 3.11, that shows a series combination of parallel RC elements corresponding to bulk and grain boundary region, it is desired to separate each of the RC elements and measure their R and C values. This is best achieved by using both the impedance and modulus formalisms as each parallel RC component gives rise to a semi-circle in the complex plane and a loss peak in the imaginary plots. Sinclair et al. (Sinclair and West 1989) derived the following equations for the above equivalent circuit diagram as follows:

$$Z' = \left[\frac{R_g}{1 + (\omega R_g C_g)^2} \right] + \left[\frac{R_{gb}}{1 + (\omega R_{gb} C_{gb})^2} \right] \quad (3.22)$$

$$Z'' = R_1 \left[\frac{(\omega R_g C_g)}{1 + (\omega R_g C_g)^2} \right] + R_2 \left[\frac{(\omega R_{gb} C_{gb})}{1 + (\omega R_{gb} C_{gb})^2} \right] \quad (3.23)$$

$$M' = \frac{C_o}{C_g} \left[\frac{(\omega R_g C_g)^2}{1 + (\omega R_g C_g)^2} \right] + \frac{C_o}{C_{gb}} \left[\frac{(\omega R_{gb} C_{gb})^2}{1 + (\omega R_{gb} C_{gb})^2} \right] \quad (3.24)$$

$$M'' = \frac{C_o}{C_g} \left[\frac{(\omega R_g C_g)}{1 + (\omega R_g C_g)^2} \right] + \frac{C_o}{C_{gb}} \left[\frac{(\omega R_{gb} C_{gb})}{1 + (\omega R_{gb} C_{gb})^2} \right] \quad (3.25)$$

To illustrate the significance of both impedance and modulus data, the difference between R_g and R_{gb} was kept at a factor of 100, but the capacitances C_g and C_{gb} were kept equal. As per the above equations, it can be seen that the impedance response is dominated by that RC component which has the largest resistance, whereas the modulus response is dominated by that which has the smallest capacitance. It is observed that the complex impedance plot showed a single semi-circle whereas the complex modulus plot showed two semi-circles of equal radii (same capacitance). Therefore, the combined analysis of complex and modulus spectroscopic plots can be used to estimate the different RC elements.

Relaxation time (τ) can be calculated from the formula $\omega_{max} \tau = (2\pi f_{max}) \tau = 1$ for the peaks in M'' vs frequency plots. It can be defined in terms of resistance and capacitance for an equivalent circuit diagram involving two parallel RC elements simulating grain and grain boundary components connected in series as:

$$\tau = RC \quad (3.26)$$

$$\tau_g = R_g C_g; \tau_{gb} = R_{gb} C_{gb} \quad (3.27)$$

The real and imaginary part of electrical modulus can be written in terms to the above parameters as:

$$M' = \frac{C_o}{C} \left[\frac{(\omega RC)^2}{1 + (\omega RC)^2} \right] = \frac{C_o}{C} \left[\frac{(\omega R_g C_g)^2}{1 + (\omega R_g C_g)^2} \right] + \frac{C_o}{C} \left[\frac{(\omega R_{gb} C_{gb})^2}{1 + (\omega R_{gb} C_{gb})^2} \right] \quad (3.28)$$

$$M'' = \frac{C_o}{C} \left[\frac{(\omega RC)}{1 + (\omega RC)^2} \right] = \frac{C_o}{C} \left[\frac{(\omega R_g C_g)}{1 + (\omega R_g C_g)^2} \right] + \frac{C_o}{C} \left[\frac{(\omega R_{gb} C_{gb})}{1 + (\omega R_{gb} C_{gb})^2} \right] \quad (3.29)$$

where, ' ω ' is the angular frequency, ' C_o ' the geometrical capacitance and ' C ' the complex capacitance. The grain and grain boundary capacitances are calculated at the relaxation points ($\omega_{max} \tau = 1$) in M'' vs frequency plots by the relation $M'' = C_o/2C$.

3.5.7 Energy storage properties

The ferroelectric characterization of materials is primarily done by analyzing the hysteresis loop of the materials. Hysteresis loops serve as a fingerprint of the ferroelectric materials and are recorded by plotting the polarization (P) on y -axis against the applied electric field (E) on x -axis. In this work, the P - E loops are recorded using a modified Sawyer-Tower circuit (automated P - E

loop tracer system, Marine India Electro. Pvt. Ltd.) with a high voltage power supply and the measurements for the samples were made at room temperature and at 50 Hz.

When an external field is applied on a parallel plate capacitor housing a dielectric with thickness d and surface area A , charges of opposite sign and equal in magnitude start to develop on the electrodes. This in turn, creates an internal electric field directed oppositely to the applied field. As the amount of charges (Q) increase (charging process), the internal electric field increases until the field matches the external electric field (V/d). During the charging process, the external field exerts force on the charges, and the electrostatic energy stored in the dielectric is given by:

$$W = \int_0^{Q_{max}} V dq \quad (3.30)$$

where V is the external voltage, dq is the incremental charge and Q_{max} is the maximum charge induced when charging gets completed.

The ability to store energy in electrostatic capacitors is measured by energy density (J) which is expressed as ratio of stored energy and the volume of dielectric capacitor.

$$J = \frac{W}{Ad} = \frac{\int_0^{Q_{max}} V dq}{Ad} = \int_0^{D_{max}} E dD \quad (3.31)$$

where D is electrical displacement and E is the induced electric field. D ($D = \epsilon_0 \epsilon_r E$) can be approximated to be equal to polarization P for high permittivity dielectrics. Therefore eq. 3.31 can be rewritten as:

$$J = \int_0^{P_{max}} E dP = \int_0^{E_{max}} \epsilon_0 \epsilon_r E dE \quad (3.32)$$

Thus, the energy density can be easily obtained by integrating the area between polarization and electric field in the P - E curves as shown in fig. 3.12. The shaded area represents the recoverable energy density (E_{re}) and the hatched area represents the energy loss or hysteresis of the ferroelectric material. The sum of these two areas equate to the total stored energy or energy density (E_{st}) stored in the charging process. The energy efficiency (η) is defined as the ratio between the recoverable energy density and the total stored energy as per eq. 3.33. While recording experimental data, the values of polarization parameters P_S , P_R , and E_C were averaged over several hysteresis loops.

$$\eta = \left[\frac{E_{re}}{E_{st}} * 100 \right] \% \quad (3.33)$$

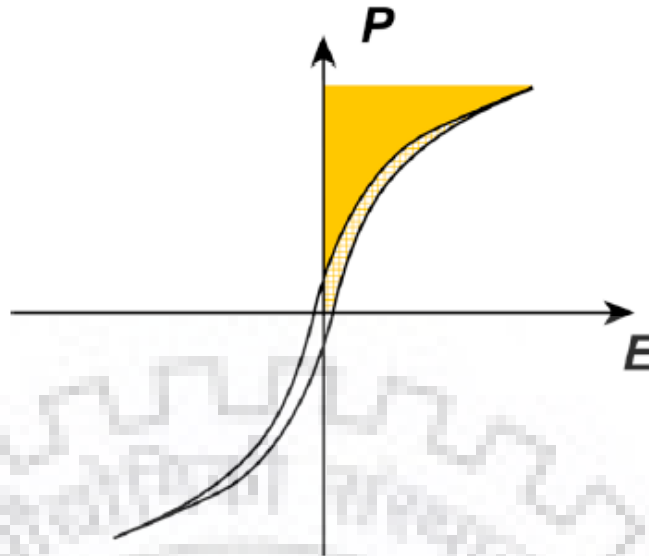


Fig. 3.12 Schematic illustration of ferroelectric P-E loops for typical relaxor ferroelectrics (Yang et al. 2019).

3.6 Summary

The doped and undoped PZT samples of tetragonal, rhombohedral and morphotropic phase boundary compositions were selected to study the dielectric and energy storage properties. The volatilization of PbO during the heat treatment of PZT ceramics leads to fluctuation in the desired stoichiometric composition. Ceramic oxides have inherent defects which make it hard to densify via conventional sintering techniques. Spark plasma sintering technique has been selected as a possible solution to the above mentioned problems since the sintering temperature can be lowered by 300 - 400°C along with suppression of grain growth. High quality ceramic powders were prepared by solid state method. The samples were characterized by SEM, XRD and EDX for their morphology, phase constitution and composition respectively. The principles and mechanisms involved in SPS method followed by appropriate selection of sintering profiles were discussed in detail. Rietveld refinement has been carried out to deduce the phase constitution of PZT sintered disks especially near MPB composition. The effect of spark plasma sintering on the dielectric and ferroelectric properties of the PZT ceramics were evaluated by measuring/calculating dielectric and energy storage parameters.

Chapter 4

Structural and dielectric characterization of $\text{PbZr}_x\text{Ti}_{1-x}\text{O}_3$

4.1 Introduction

In this chapter, the methodology, synthesis and structural characterization of tetragonal, rhombohedral and orthorhombic phase compositions of PZT ceramic oxides are discussed. The compositions of these oxides have been selected from the PZT phase diagram given in Fig. 2.6. However, this chapter emphasizes on the MPB composition of PZT oxide ($\text{PbZr}_{0.52}\text{Ti}_{0.48}\text{O}_3$), as near the MPB, the functional properties of the material are superior. Rietveld refinement is conducted to detect the stoichiometric variation with sintering (SPS) temperature. In addition, the dielectric and energy storage investigations for MPB composition of PZT are also conducted. An effort has been made to correlate the dielectric and energy storage properties of $\text{PbZr}_{0.52}\text{Ti}_{0.48}\text{O}_3$ to its microstructure and phase constituents.

Fig. 4.1 shows a flowchart depicting the methodology adopted for synthesis and characterization of PZT oxides which involves the stoichiometric calculations, mixing of raw materials, heat treatment and measurement of functional properties.

4.1.1 Composition selection

Table 4.1 depicts the respective compositions and theoretical density for rhombohedral, tetragonal, orthorhombic and MPB compositions of PZT oxides. The theoretical density of the materials for all the compositions was collected from the CIF files from the PDF-4+ ICDD database.

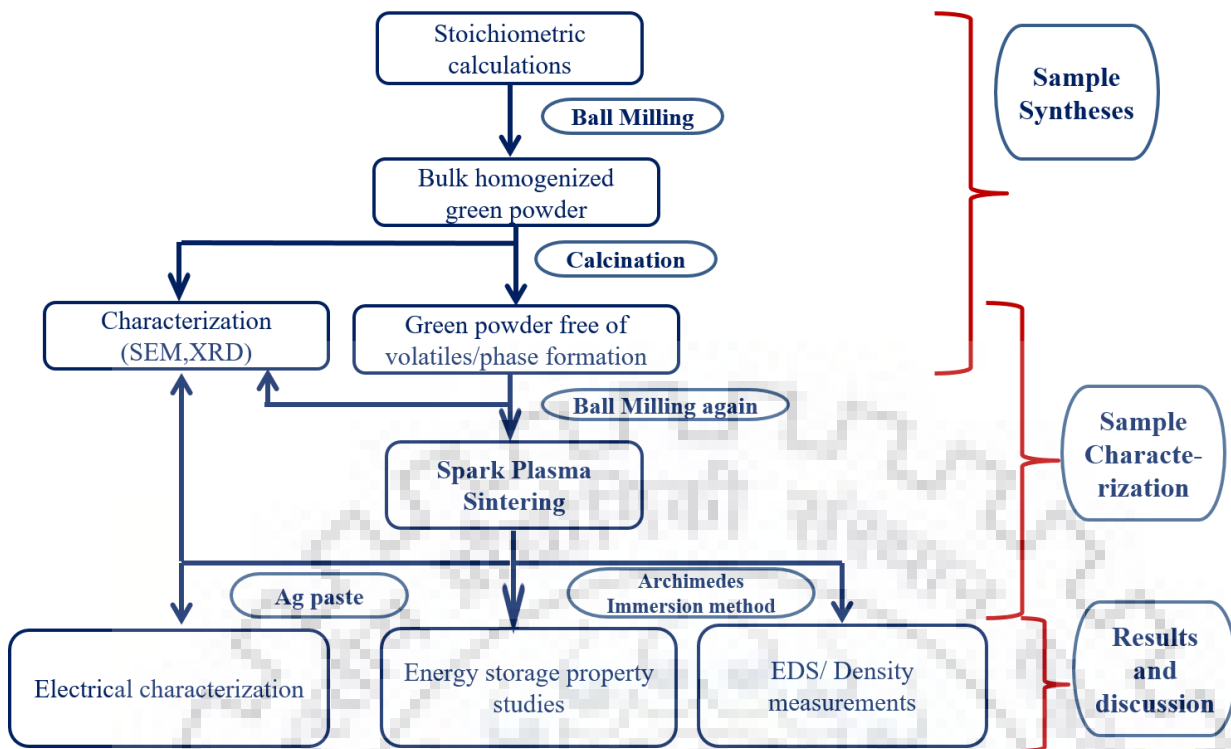


Fig. 4.1 Flow chart showing the materials synthesis to property determination.

Table 4.1 Theoretical density and abbreviations of different PZT compositions used.

Sample composition	Abbreviation	Theoretical density
$\text{PbZr}_{0.7}\text{Ti}_{0.3}\text{O}_3$	PZT (70/30)	7.96 g/cm ³
$\text{PbZr}_{0.3}\text{Ti}_{0.7}\text{O}_3$	PZT (30/70)	7.99 g/cm ³
$\text{PbZr}_{0.97}\text{Ti}_{0.03}\text{O}_3$	PZT (97/3)	8.11 g/cm ³
$\text{PbZr}_{0.52}\text{Ti}_{0.48}\text{O}_3$	PZT (52/48)	8.00 g/cm ³

4.1.2 SEM and EDX analysis of calcined PZT compositions

Prior to SEM observation, the raw powders of each composition were calcined at 900°C for 4 hours in a muffle furnace. The scanning electron micrographs of calcined powders for PZT composition (PZT(30/70), PZT(70/30), PZT(97/03)) were obtained and shown in Fig. 4.2. The morphology of the calcined powders of different compositions are similar in nature. The particles largely show agglomeration and faceted morphology. The average particle size of these powders were calculated by using linear intercept method. The smaller particles lie in the range 128 - 300 nm with an average particle size of ~ 208 nm, whereas the bigger particles lie in 235 - 550 nm with an average particle size of ~ 450 nm. It can be seen that, the number of smaller sized particles increases as Zr/Ti content increases. The Energy-dispersive X-ray spectroscopy (EDS) spectra of the respective samples are also shown along with SEM micrographs. The EDS spectra clearly

show the presence of different elements and the ratio of their at % correlates to the selected PZT phase composition.

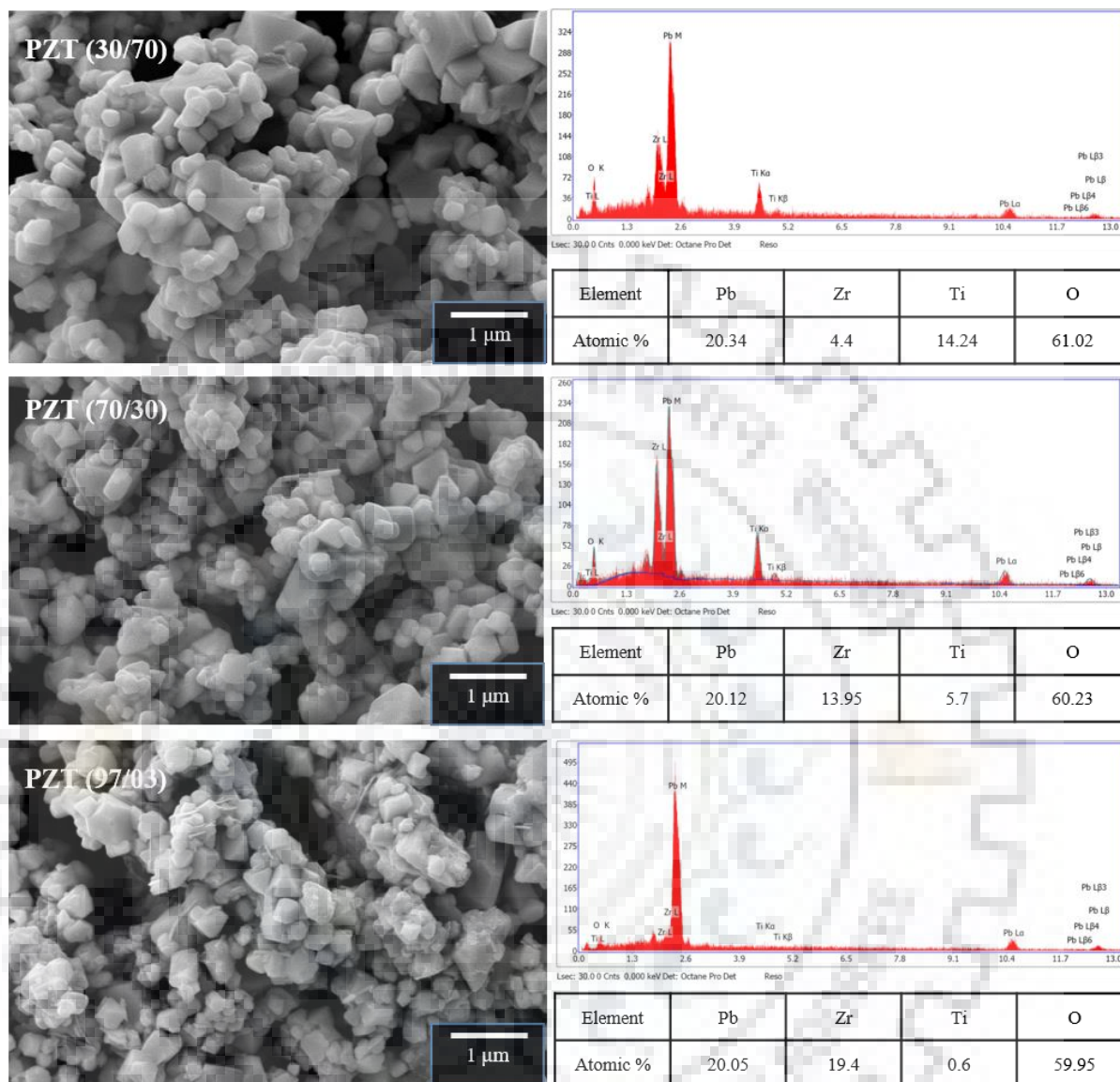


Fig. 4.2 Scanning electron micrographs and EDS spectra of $\text{PbZr}_{0.3}\text{Ti}_{0.7}\text{O}_3$, $\text{PbZr}_{0.7}\text{Ti}_{0.3}\text{O}_3$ and $\text{PbZr}_{0.97}\text{Ti}_{0.03}\text{O}_3$ calcined at 900°C .

4.1.3 Structural characterization of PZT specimens

Fig. 4.3 depicts the XRD patterns of PZT(30/70), PZT(70/30) and PZT(97/03) after background correction. The patterns show formation of pure perovskite structure with no detectable impurity phase(s). An enlarged view of the XRD patterns of 2θ range 36° to 46° is also shown to highlight the characteristic peaks. It can be observed that, for PZT (30/70) sample, the single $\{111\}$ peak along with strong splitting of $\{200\}$ peaks confirms the tetragonal phase structure. The XRD pattern matches with PDF 01-070-4055 having $P4mm$ space group. For a rhombohedral phase

structure, the $\{111\}$ peaks split and the $\{200\}$ peaks do not split, as explained in Chapter 3. Thus, the PZT (70/30) sample conforms to the rhombohedral structure which matches PDF 01-089-1278 with $R3c$ space group. As the (Zr/Ti) ratio increases to (97/03), the $\{200\}$ peaks split again with some broadening of $\{111\}$ peak. The PZT (97/03) composition matches PDF 01-089-8012 with $Pnmm$ space group.

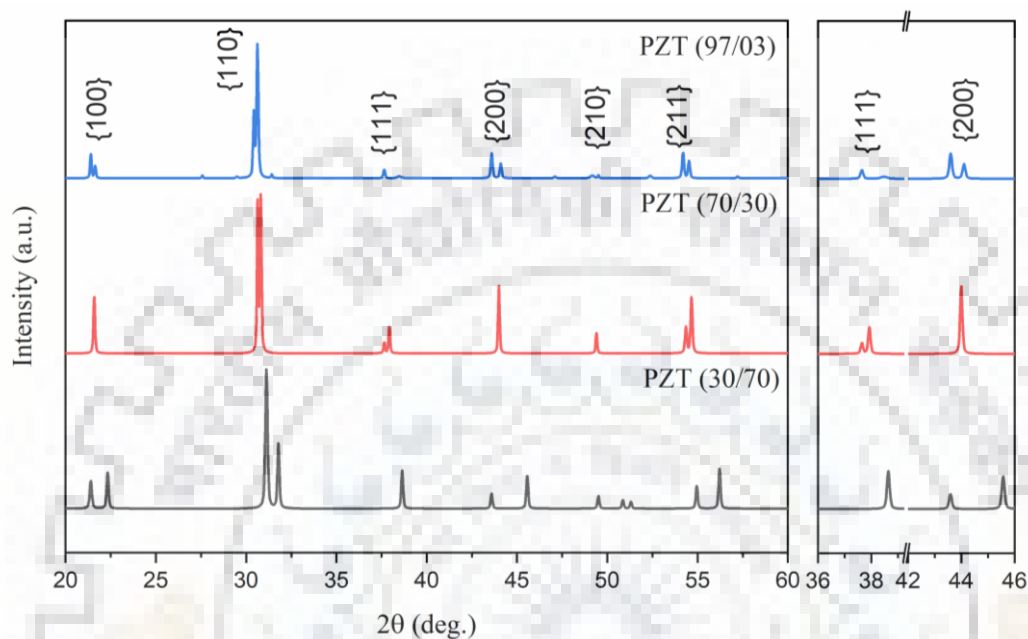


Fig. 4.3 Diffraction profiles of $\text{PbZr}_{0.3}\text{Ti}_{0.7}\text{O}_3$, $\text{PbZr}_{0.7}\text{Ti}_{0.3}\text{O}_3$ and $\text{PbZr}_{0.97}\text{Ti}_{0.03}\text{O}_3$ calcined at 900°C .

4.1.4 Spark plasma sintering of PZT specimens

The samples were consolidated by rapid sintering technique, SPS with a target sintering temperature of 900°C subjected to uniaxial load of 60 MPa. The samples were rapidly heated to the sintering temperature at a heating rate of $100^\circ\text{C}/\text{min}$ with a soaking time of 5 min. The uniaxial pressure was kept constant throughout the sintering cycle. The sintering was done under vacuum to avoid oxidation of graphite spacers and dies utilized in sintering chamber. SPS profile for PZT(30/70) as a representative is shown in Fig. 4.4. It can be observed that the sintering is completed within minutes with axial compression of ~ 2.5 mm. The sintered pellets (dark in appearance) obtained were polished to remove any graphite layers adhered to the surface. Thereafter, the pellets were annealed at 800°C for 4 hours to compensate the effect of reducing atmosphere used in SPS. The annealed samples were found to be white in color. Fig. 4.5 depicts the variation of density and relative density with PZT composition. The sintered samples exhibit relative density ($> 98\%$) which signifies the benefit of using SPS to sinter the ceramics.

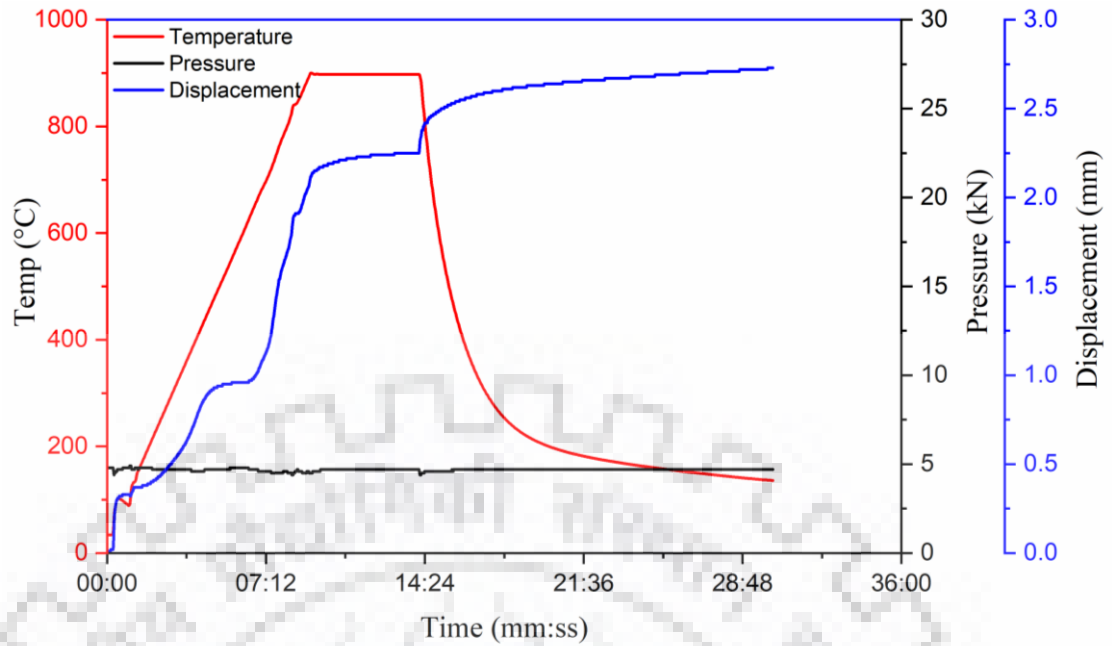


Fig. 4.4 SPS profile adopted for $\text{PbZr}_{0.3}\text{Ti}_{0.7}\text{O}_3$ sample sintered at 900°C subjected to uniaxial load of 60 MPa.

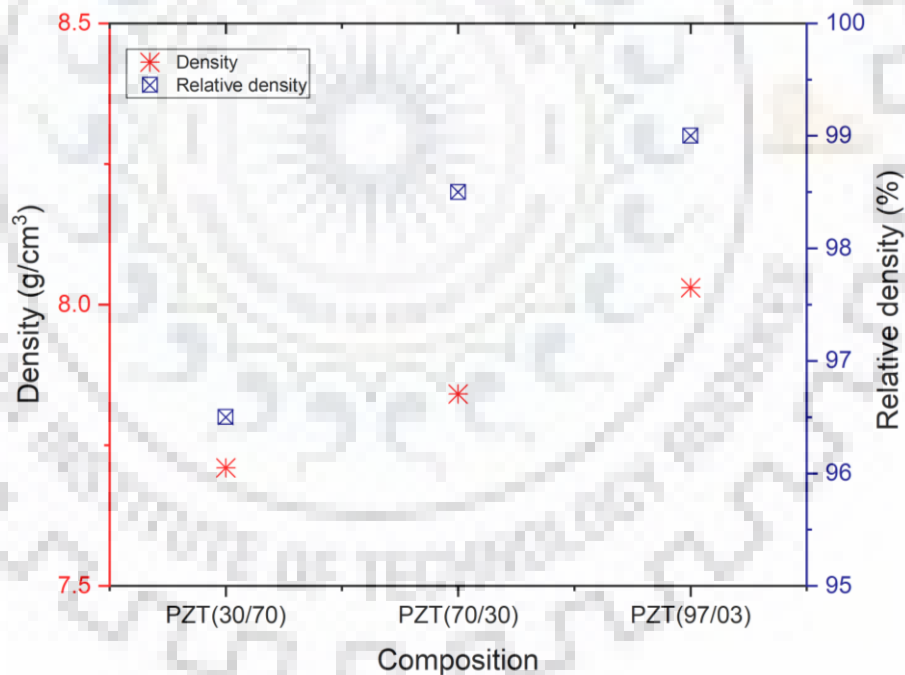


Fig. 4.5 Density and relative density of $\text{PbZr}_{0.3}\text{Ti}_{0.7}\text{O}_3$, $\text{PbZr}_{0.7}\text{Ti}_{0.3}\text{O}_3$ and $\text{PbZr}_{0.97}\text{Ti}_{0.03}\text{O}_3$ sintered at 900°C by SPS method.

4.1.5 Microstructural observation of sintered PZT samples

Fig. 4.6 depicts the microstructure of PZT samples having different compositions. It can be observed that the samples exhibit dense microstructure with very low porosity. The mean grain size of the different samples was calculated by linear intercept method. The physical properties

of all the samples are presented in Table 4.2 along with the average grain size for reference. It can be clearly observed that the spark plasma sintering technique was used successfully to densify the ceramics. The average grain size of the PZT samples lie between 35 and 50 nm and is found to increase on increase of (Zr/Ti) ratio.

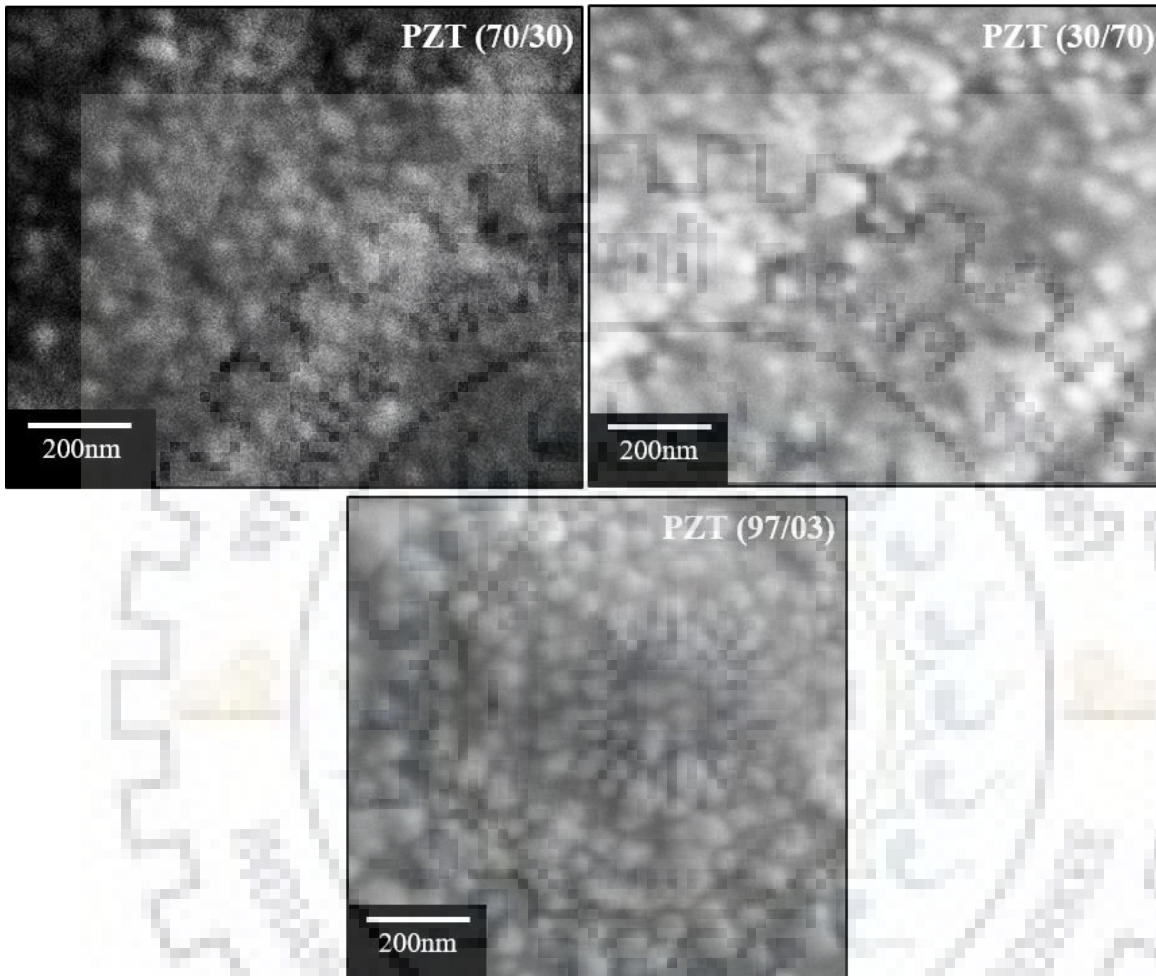


Fig. 4.6 SEM images of sintered pellets of $\text{PbZr}_{0.7}\text{Ti}_{0.3}\text{O}_3$, $\text{PbZr}_{0.3}\text{Ti}_{0.7}\text{O}_3$ and $\text{PbZr}_{0.97}\text{Ti}_{0.03}\text{O}_3$.

Table 4.2 Physical properties of $\text{PbZr}_{0.3}\text{Ti}_{0.7}\text{O}_3$, $\text{PbZr}_{0.7}\text{Ti}_{0.3}\text{O}_3$ and $\text{PbZr}_{0.97}\text{Ti}_{0.03}\text{O}_3$ samples.

PZT composition	Mean grain size (μm)	Mean grain size	Bulk Density (g/cm^3)	Relative density (%)
	(Clarke and Glazer 1976; Mishra and Pandey 1997)	(nm)		
PZT (30/70)	3.64	35.51(12)	7.71(5)	96.5
PZT (70/30)	1.29	39.95(4)	7.84(11)	98.5
PZT (97/03)	1.01	49.33(17)	8.03(3)	99

4.1.6 Compositional fluctuation in PZT specimens

Fig. 4.7 depicts the XRD patterns of tetragonal PZT (30/70) in calcined, sintered and annealed conditions. The reference pattern of the above PZT phase has also been added for comparison. It can be observed that the desired phase structure of PZT irrespective of any impurity phase was achieved in the calcined condition. However, there exists compositional variation after sintering which gives rise to intermediate phases due to the reducing sintering atmosphere adopted in SPS that leads to oxygen deficiencies in the sintered specimens. The formation of intermediate phases and pyrochlore phase has been marked in the XRD pattern.

(Wu et al. 2002) have also reported compositional fluctuation in $\text{PbZr}_{0.3}\text{Ti}_{0.7}\text{O}_3$ sintered by SPS technique. Short sintering periods in SPS leads to formation of non-equilibrium phases of PZT. They reported that the compositional fluctuation was greatly reduced when the PZT sintered pellets were annealed for more than 1 hour. Similarly, the intermediate complexes that are composed of lead, titanium and zirconium oxides were greatly reduced for the current set of PZT samples (PZT(30/70), PZT(70/30), PZT(97/03)) after annealing and the desired phase constitution was achieved.

4.2 Phase composition and dielectric properties of spark plasma sintered $\text{PbZr}_{0.52}\text{Ti}_{0.48}\text{O}_3$

The objective of this section is to study the effect of spark plasma sintering temperature variation on PZT ceramic oxide having MPB composition through (i) qualitative and quantitative analyses of crystallographic phases using Rietveld refinement, (ii) microstructural studies of the samples treated at different sintering temperatures, (iii) temperature dependent dielectric performance. The data reveal that the higher dielectric constant of the sample sintered at 900°C, may be due to the increased number of available polarization domain states pertaining to coexistence of phases, but not due to densification. This observation greatly helps to select the sintering temperature of lead-based ferroelectric ceramic systems.

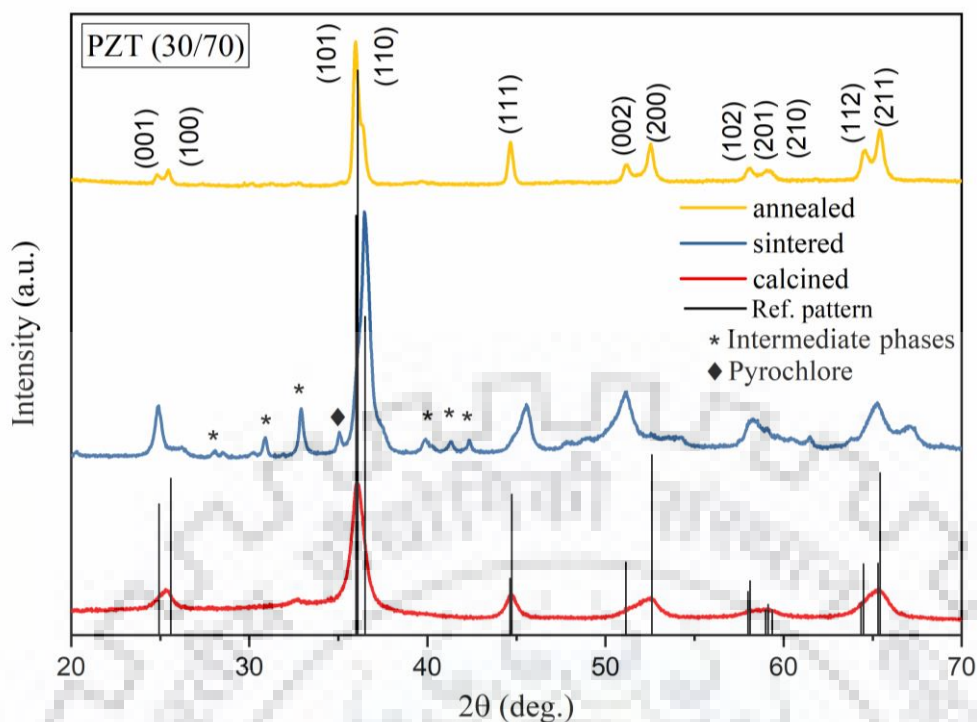


Fig. 4.7 Variation of XRD pattern of calcined, sintered and annealed $\text{PbZr}_{0.3}\text{Ti}_{0.7}\text{O}_3$ along with its reference pattern.

4.2.1 SEM analysis

Fig. 4.8(a) shows the scanning electron micrograph of $\text{PbZr}_{0.52}\text{Ti}_{0.48}\text{O}_3$ powder calcined at 900°C for 4 hours. The particles of the powder have largely faceted shape along with some particles having irregular appearance. The average particle size varies from as low as 100 nm to 350 nm. However, there are some larger particles having size ~ 650 nm also. EDS spectrum of the compound along with its elemental composition is shown in Fig. 4.8(b) confirming that the composition of the compound has desired stoichiometry.

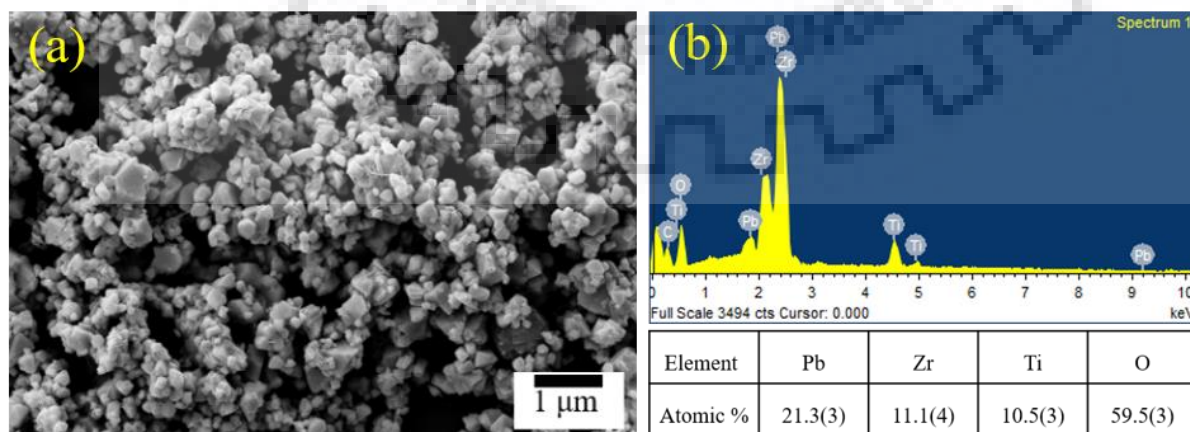


Fig. 4.8 (a) Scanning electron micrograph and (b) EDS spectrum of $\text{PbZr}_{0.52}\text{Ti}_{0.48}\text{O}_3$ powders calcined at 900°C for 4 hours.

4.2.2 XRD analysis

Fig. 4.9 presents the XRD patterns of $\text{PbZr}_{0.52}\text{Ti}_{0.48}\text{O}_3$ powders calcined at 800, 850, 900 and 950°C for 4 hours. The analysis of the patterns indicates that all the samples show the typical perovskite structure and are indexed as tetragonal crystal system having $P4mm$ space group matching largely with PDF file no. 04-011-8847. It can be observed that samples calcined at 800°C and 850°C have pyrochlore as impurity phase (Vittayakorn et al. 2003) and sample calcined at 950°C has unreacted ZrO_2 phase, which remains due to volatilization of PbO at higher temperature. The calcination temperature of 900°C appears to be the optimum temperature to get pure perovskite phase with no detectable traces of the pyrochlore phase. Tetragonal and rhombohedral MPB structures were expected and identified by the split of XRD peaks $\{001\}$, $\{101\}$, $\{002\}$, $\{102\}$ and $\{112\}$ (Joshi and Acharya 2016). As the sample calcined at 900°C shows the relevant phases, the same material was further studied for other investigations.

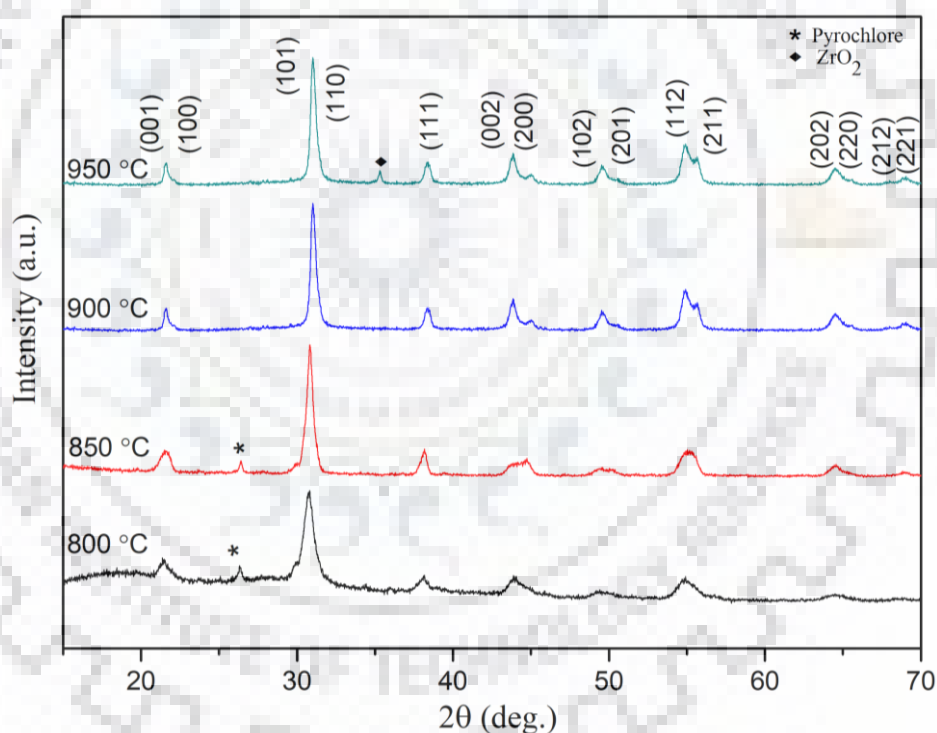


Fig. 4.9 XRD patterns of $\text{PbZr}_{0.52}\text{Ti}_{0.48}\text{O}_3$ powders calcined at 800°C, 850°C, 900°C and 950°C.

4.2.3 Temperature and pressure profiles used in Spark plasma sintering

The samples calcined at 900°C were sintered by SPS method at different temperatures varying between 800 and 950°C. The SPS profile for the representative SPS-950 sample is depicted in Fig. 4.10 and the same profile was used for sintering samples at other temperatures. The temperature profile is divided into three stages: (i) T1 over which a heating rate of 100°C/min

was applied from room temperature to the temperature which is 100°C lower than the sintering temperature; (ii) T2 over which a heating rate of 33°C/min was applied up to sintering temperature; (iii) T3 over which soaking was done. At stage T1, higher heating rate was chosen to reduce grain growth leading to higher bulk density of the samples (Stanciu, Kodash, and Groza 2001). At stage T2, lower heating rate is applied to allow sufficient time for atomic diffusion (mainly through grain boundary and the initiation of lattice diffusion). The pressure profile is also divided into three stages namely P1, P2, and P3. At stage P1, the pressure is just sufficient to maintain powder particles in contact which is maintained until the sintering temperature is attained to allow the liquid phase to flow (PbO liquid phase) to aid the sintering process. At P2, the pressure is increased to 60 MPa at the beginning of the sintering stage. The increased pressure tends to closure of the remaining pores in the samples. At P3, the pressure is released just before the cooling process begins so as to prevent cracking of ceramic samples (Stanciu, Kodash, and Groza 2001).

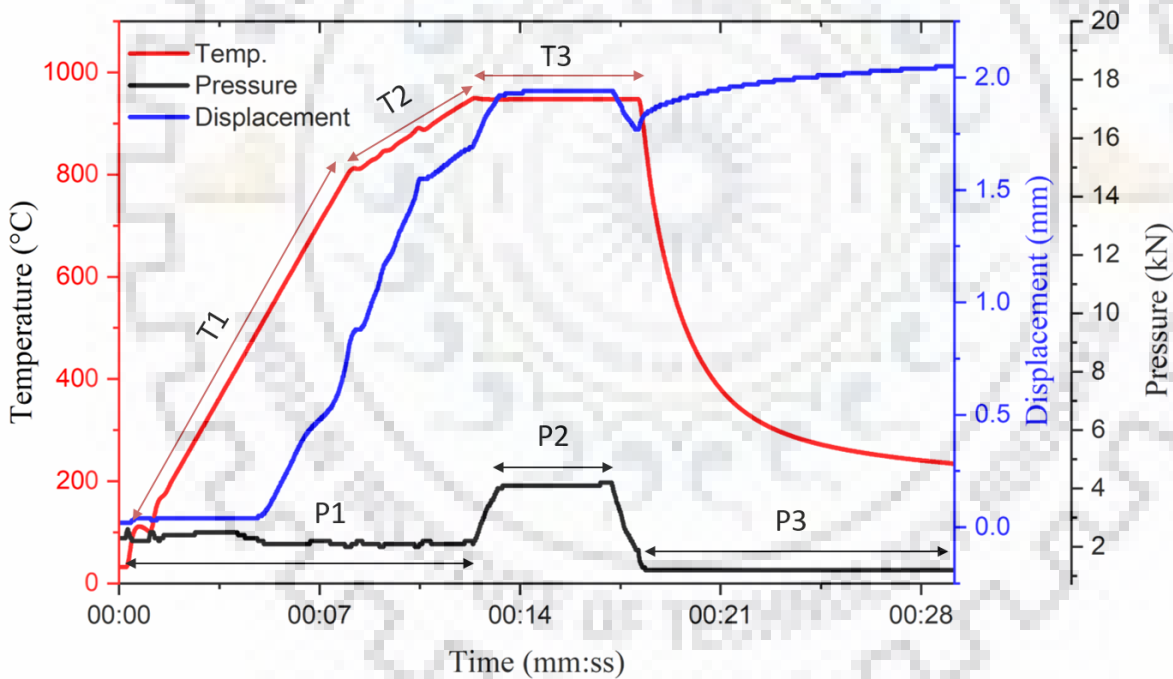


Fig. 4.10 SPS profile adopted for sample sintered at 950°C (SPS-950) showing different temperature and pressure stages during a sintering cycle.

Table 4.3 shows the density data of all SPS sintered samples which were calcined at 900°C. It can be observed that the sample has been densified even at 800°C ($\rho = 7.93 \text{ g/cm}^3$). The difference between density data of the samples sintered at different temperatures (between 800 and 950°C) is less than 0.4%. However, the phase composition of the samples sintered at different temperatures is different and this has been discussed in section 4.2.4. The composition change in

the phase diagram corresponds to changes in the crystal structure which has a direct influence on the dielectric performance of the compound as the polarization vectors of different phases are different.

Table 4.3 Calcination, sintering and annealing temperature along with relative densities of samples sintered at 800°C, 850°C, 900°C and 950°C by SPS method.

Calcination Temp. (°C)	Sintering Temp. (°C)	Annealing Temp. (°C)	Density (g/cm ³)	Relative Density (%)
900	800	800	7.93 (2)	99.17
900	850	800	7.94 (1)	99.30
900	900	800	7.97 (2)	99.58
900	950	800	7.96 (2)	99.44

4.2.4 Structural analysis

The crystal structures of $\text{Pb}(\text{Zr}_x\text{Ti}_{1-x})\text{O}_3$ ceramics at room temperature are found tetragonal for $x \leq 0.52$ and rhombohedral for $x \geq 0.53$. While for $x = 0.52 - 0.53$, both the tetragonal phase (T phase) and the rhombohedral phase (R phase) coexist corresponding to morphotropic phase boundary (Mishra and Pandey 1997; Mishra, Pandey, and Singh 1996). The coexistence of R and T phases was complemented by the doublet nature of (111) and (200)/(002) reflections on the powder XRD patterns. However, (Noheda et al. 1999) postulated that the MPB composition also has a monoclinic phase. Thereafter, (Ragini et al. 2002) stated that earlier established phase composition of tetragonal and rhombohedral is actually tetragonal and monoclinic phases.

In order to get a clear view on phase composition, Rietveld refinement of the XRD patterns was done using PDXL software with PDF4+ ICDD database. The reference CIF files mapped were of tetragonal, rhombohedral and monoclinic symmetry of PZT(52/48). In addition, the CIF file of PbO phase was also incorporated to account for any excess PbO phase present in the sample. The XRD patterns along with difference plots are shown in Fig. 4.11. In addition, the nature of variation of diffraction peaks (110), (111), (200) with sintering temperature is shown in Fig. 4.12. The refinement data clearly reveals that the sample SPS-800 has a tetragonal structure ($P4mm$). Similarly, for SPS-850, the tetragonal symmetry ($P4mm$) with pyrochlore phase shows good fit ($\chi^2 = 3.59$) to the experimental data. The tetragonal nature of both SPS-800

and SPS-850 samples can also be inferred by visualizing the singlet nature of (111) and doublet nature of (200) as depicted in Fig. 4.12. It is interesting to note that, although the calcined powder was of desired stoichiometry, the composition of the sample sintered in SPS differs from that of calcined powder signifying the effect of sintering temperature on PZT composition.

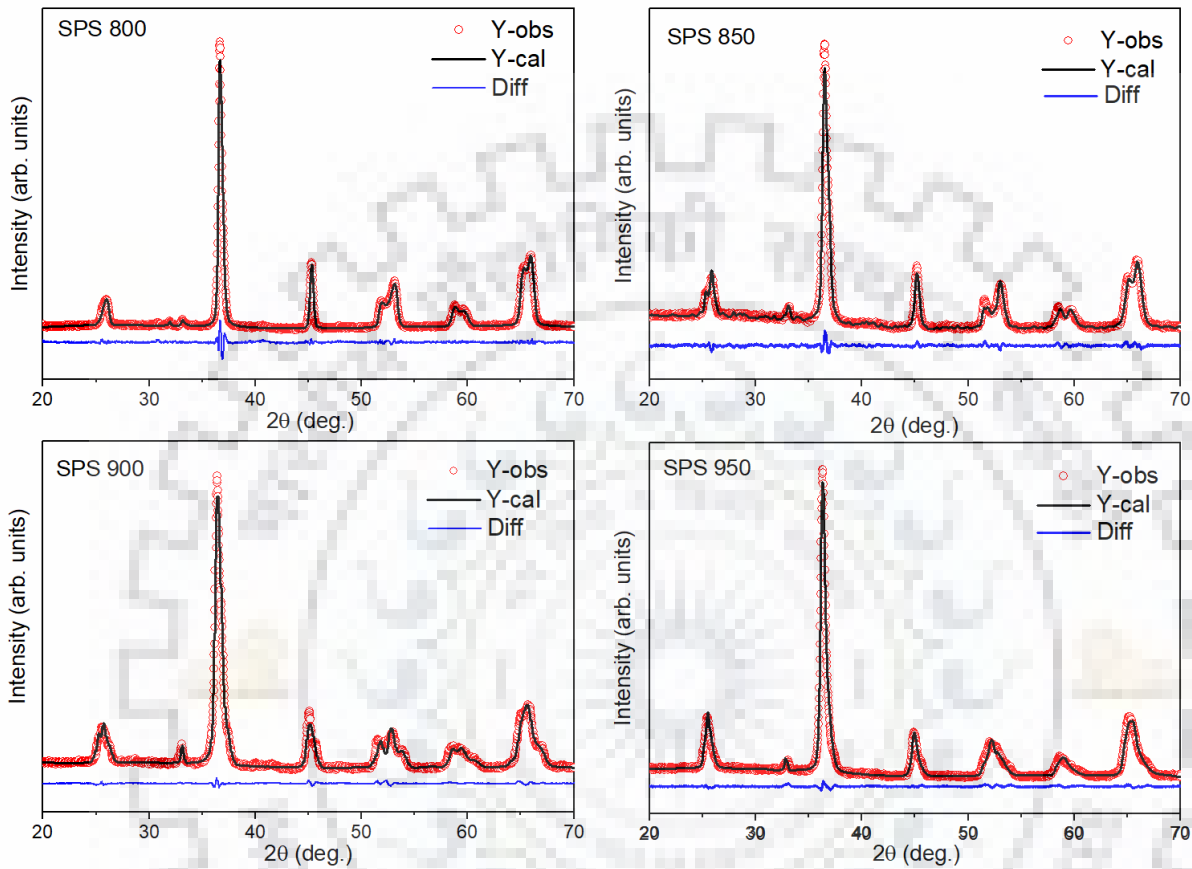


Fig. 4.11 Observed, calculated and difference profiles generated in Rietveld refinement of samples sintered at 800°C, 850°C, 900°C and 950°C by SPS method.

Rietveld refinement of SPS-900 sample was carried out using tetragonal ($P4mm$ space group) symmetry but the profile fitting was not found to be proper on the basis of tetragonal symmetry alone. The coexistence of tetragonal and monoclinic phases can be clearly seen for the sample sintered at 900°C, through peak splitting observed with (111) and (200) peaks. (200) peak clearly splits into three for SPS-900 sample which is a characteristic of pseudo tetragonal monoclinic phase with space group Cm (Ragini et al. 2002). After mapping both tetragonal ($P4mm$) and monoclinic (Cm) symmetry, the fit improves drastically with the corresponding $\chi^2 = 3.19$. This coexistence of the phases has also been reported by (Guo et al. 2000) and (Ragini et al. 2002). (Guo et al. 2000) mentioned that the monoclinic structure of $PbZr_{0.52}Ti_{0.48}O_3$ is derived from the tetragonal structure by shifts of the Pb and Zr/Ti atoms along the tetragonal [110] axis and suggested that the local monoclinic structure forms a bridge between the tetragonal and

rhombohedral phases. Since the monoclinic cell permits rotation of the polar axis along its symmetry plane, a high dielectric response is expected from the material/chemical compound possessing the monoclinic phase and thereby from SPS-900 sample.

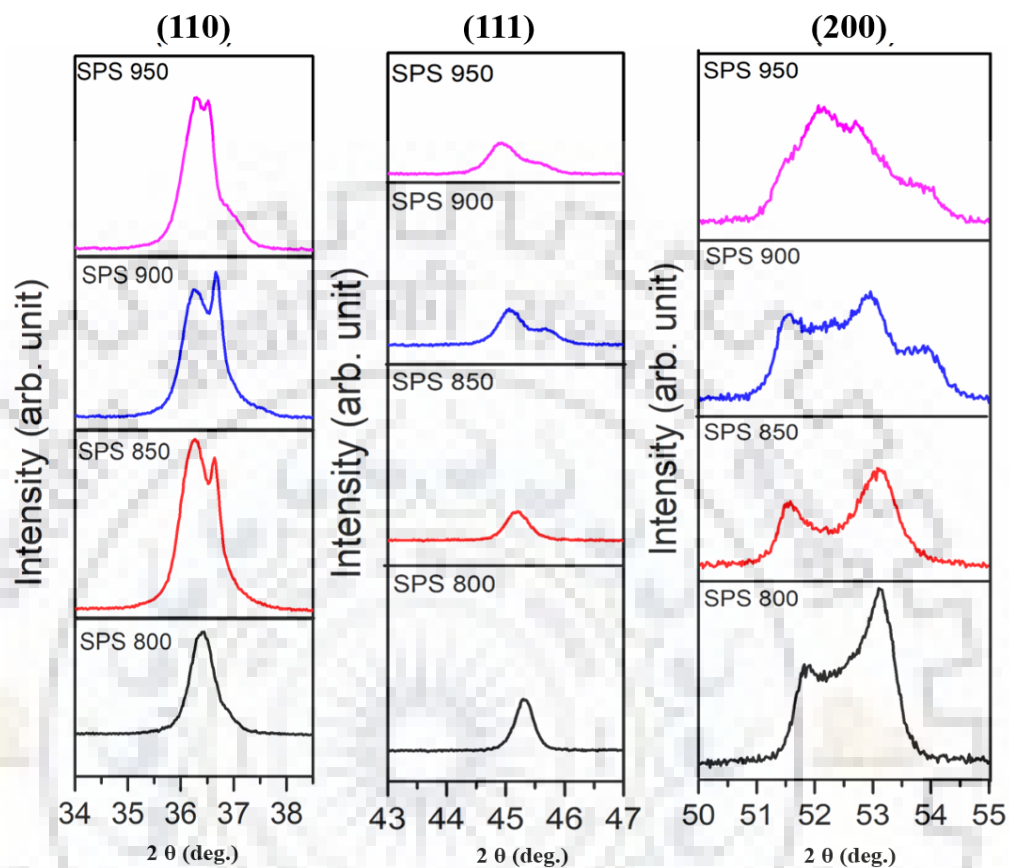


Fig. 4.12 Room temperature XRD (110), (111) and (200) peaks of SPS-800, SPS-850, SPS-900 and SPS-950.

For SPS-950, the split (200) peaks tend to merge and become almost a singlet with a full width at half maximum (FWHM) greater than that of (200) peaks of other samples. Further, the (110) and (111) peaks are still doublets which suggest coexisting pseudorhombohedral tetragonal phase as found by (Ragini et al. 2002). Accordingly, Rietveld refinement was carried out by considering the coexistence of tetragonal ($P4mm$) and rhombohedral ($R3c$) phases. The fit between the observed and calculated profiles is satisfactory with $\chi^2 = 3.39$. Thus, the ‘morphotropic phase’ transitions from tetragonal phase to the mixed phases of tetragonal ($P4mm$) with monoclinic (Cm) at 900°C and tetragonal with rhombohedral ($R3c$) at 950°C with increase in sintering temperature from 800 to 950 °C. The refined parameters of crystal structures for each sample are given in Table 4.4.

Table 4.4 Refined structural parameters for samples sintered at 800°C, 850°C, 900°C and 950°C by SPS method.

Sintering temperature	800°C	850°C	900°C		950°C	
Space group	<i>P4mm</i>	<i>P4mm</i>	Two phase compositions			
			<i>P4mm</i>	<i>Cm</i>	<i>P4mm</i>	<i>R3c</i>
a(Å)	4.000054	4.019(2)	3.9617(14)	5.722(2)	4.0326(10)	5.757(7)
b(Å)	4.000054	4.019(2)	3.9617(14)	5.6935(16)	4.0326(10)	5.757(7)
c(Å)	4.090632	4.104(3)	4.139(2)	4.1061(8)	4.1347(12)	14.12(3)
β (deg.)	90.0	90.0	90.0	90.0(4)	90.0	90.0
Pb(x/y/z)	0/0/0	0.5/0.5/ 0.5224	0/0/0	0.5/0/0.0(2)	0/0/0	0/0/0.28
Zr(x/y/z)	0.5/0.5/0.5 281	0/0/0.00 (18)	0/0/- 0.05(2)	0.52(2)/0/ 0.47(3)	0.5/0.5/0.5 71(6)	0/0/0.031 (15)
Ti(x/y/z)	0.5/0.5/0.5 281	0/0/0.00 (18)	0/0/- 0.05(2)	0.52(2)/0/ 0.47(3)	0.5/0.5/0.5 71(6)	0/0/0.031 (15)
O1(x/y/z)	0.5/0/0.61 3	0.5/0/0.1 (17)	0.5/0/0.0 (2)	0.49(17)/0/- 0.04(8)	0.5/0/0.51 (5)	0.2(2)/0.3 23(17)/ 0.086(8)
O2(x/y/z)	0.5/0.5/0.1 34	0/0/0.66 (11)	0/0/0.35 (4)	0.33(3)/0.22 (2)/0.51(12)	0.5/0.5/0.0 6(3)	
Phase fraction	100	100	69(5)	31(5)	58.8(12)	41.2(11)
R_{wp}	5.1	5.4	5.43		5.92	
χ^2	3.21	3.59	3.19		3.39	

4.2.5 Microstructural analysis of spark plasma sintered samples

SEM micrographs of the spark plasma sintered samples annealed at 800°C for 4 hours for compensation of oxygen deficiency that occurred on sintering, are illustrated in Fig. 4.13. The grain size distribution of each sample is depicted in Fig. 4.14. It can be seen that sintering leads to very small grained (15 - 40 nm) microstructure and the grains are smaller than that of conventionally sintered samples for which the obtained grain size range is 1 - 3 μm (Cao and Randall 1996). The average grain size of the samples increases from 15.47 ± 0.35 nm to $19.41 \pm$

0.41 nm with the increase in sintering temperature for SPS-800, SPS-850 and SPS-900 implying that the grain size increase with increase in sintering temperature is insignificant. However, the average grain size of SPS-950 (37.26 ± 0.42 nm) is almost two times that of the samples sintered at other three different temperatures.

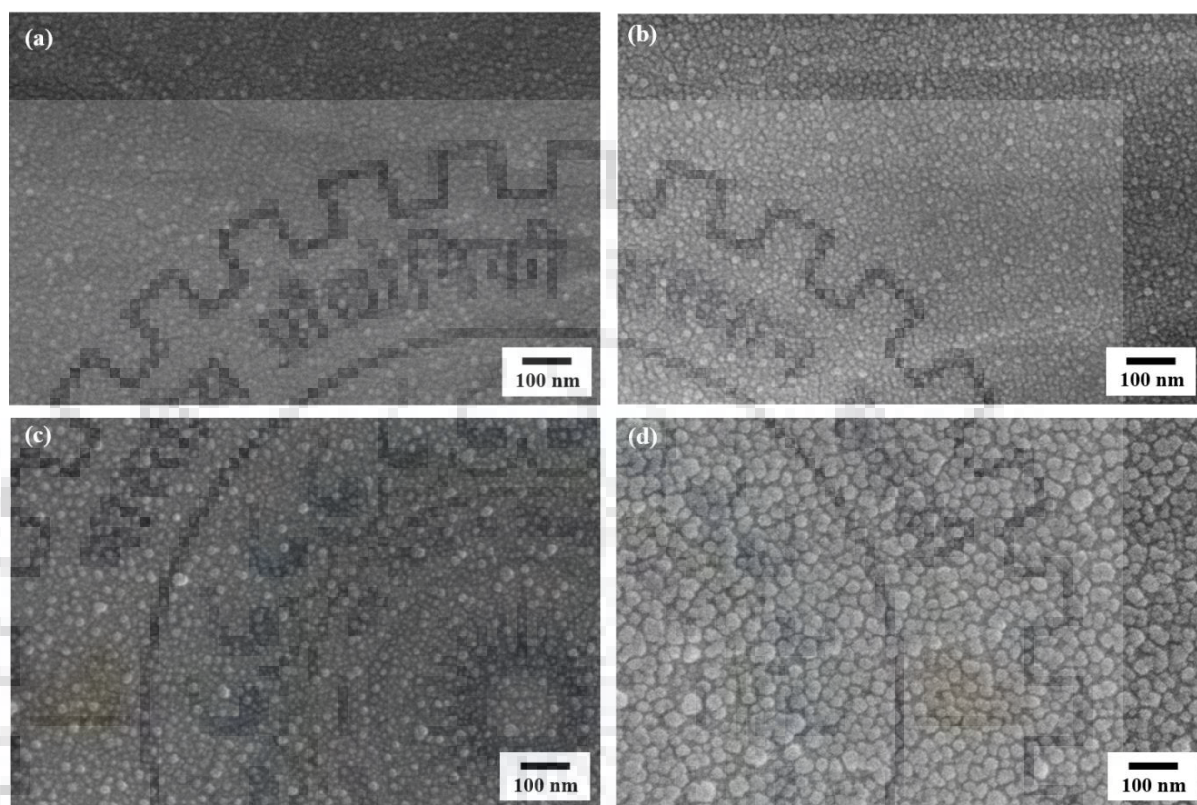


Fig. 4.13 Microstructures of $\text{PbZr}_{0.52}\text{Ti}_{0.48}\text{O}_3$ samples spark plasma sintered at different temperatures (a) 800°C, (b) 850°C, (c) 900°C and (d) 950°C.

The macroscopic driving force operative during sintering of powders is the reduction of excess energy associated with surfaces of the powder particles. This can happen by (a) reduction of total surface area by increase in the average size of particles, leading to coarsening and / or (b) the elimination of solid interfaces and the creation of grain boundary area, followed by grain growth, causing densification. These two mechanisms are usually in competition. It may be considered that atomic processes that lead to densification reaches saturation up to the temperature of 900°C (as observed by the density values in Table 4.3) and grain coarsening is largely effective above 900°C which may explain the surge in grain size for SPS-950 sample (Barsoum 2019).

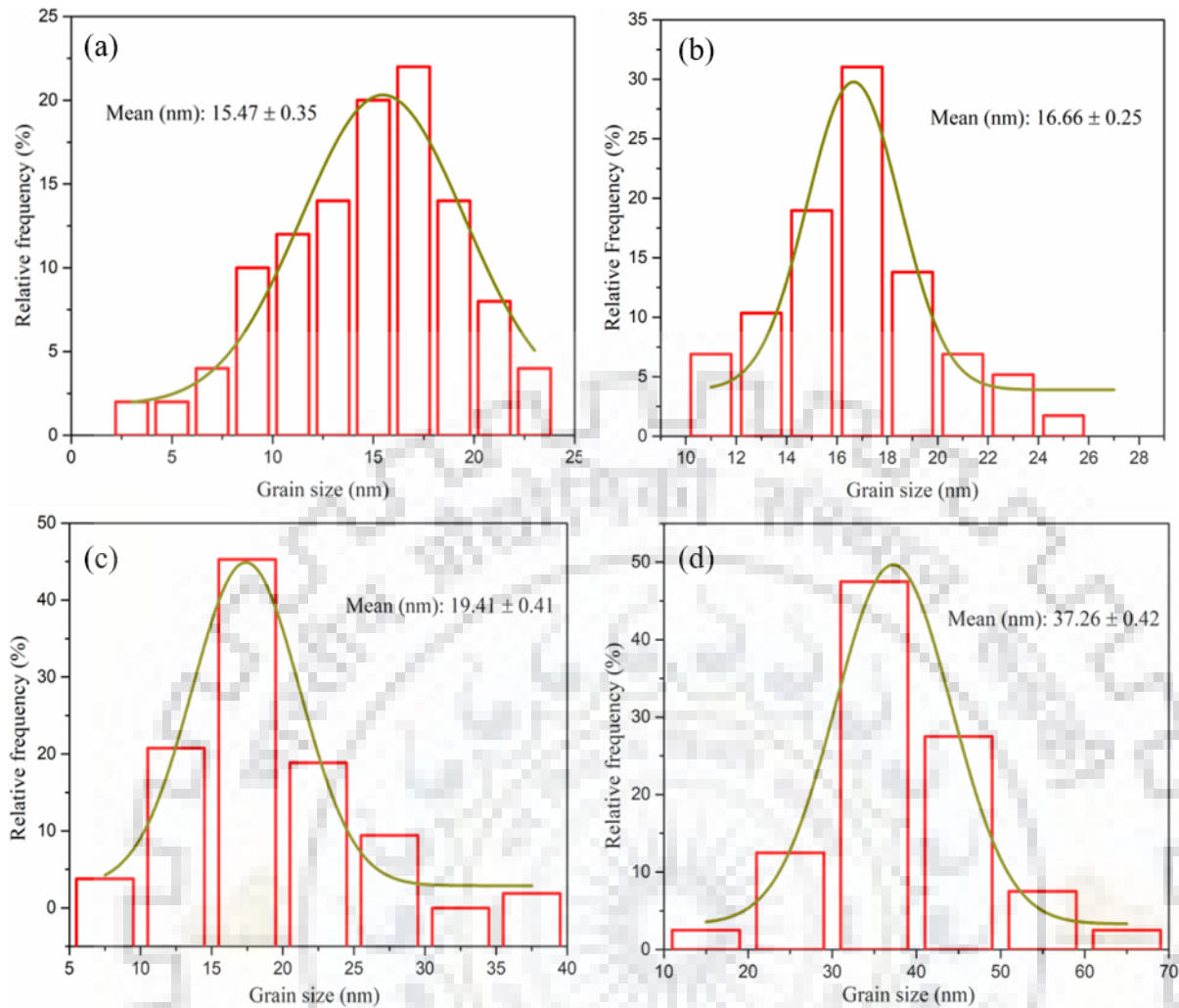


Fig. 4.14 Histogram of grain size distribution in (a) SPS-800, (b) SPS-850, (c) SPS-900 and (d) SPS-950.

Fig. 4.15 illustrates the EDS spectra of different samples obtained by area scan method. The results indicate that the atomic ratios of Pb:Zr:Ti:O for SPS-800 is 97:44:56:290 and for SPS-850 is 95:46:54:280 which is approximately consistent with the composition of PZT that exhibits a tetragonal perovskite structure. The atomic ratio for the sample SPS-900 and SPS-950 are 96:53:47:280 and 95:57:43:269 respectively. Therefore it may be inferred that the elemental composition of SPS-900 and SPS-950 compared to that of SPS-800 and SPS-850 are preferably closer to the desired MPB composition of (100:52:48:300). It is noteworthy to mention that the EDS analysis is in agreement with the findings of Rietveld refinement pertaining to the coexistence of phases as discussed in section 4.2.4. As a result, higher dielectric performance is expected for SPS-900 and SPS-950 due to increased number of available polarization directions. The peaks in the EDS spectrum at about 0.1 keV corresponding to oxygen element is not labelled in the auto-generated EDS spectrum.

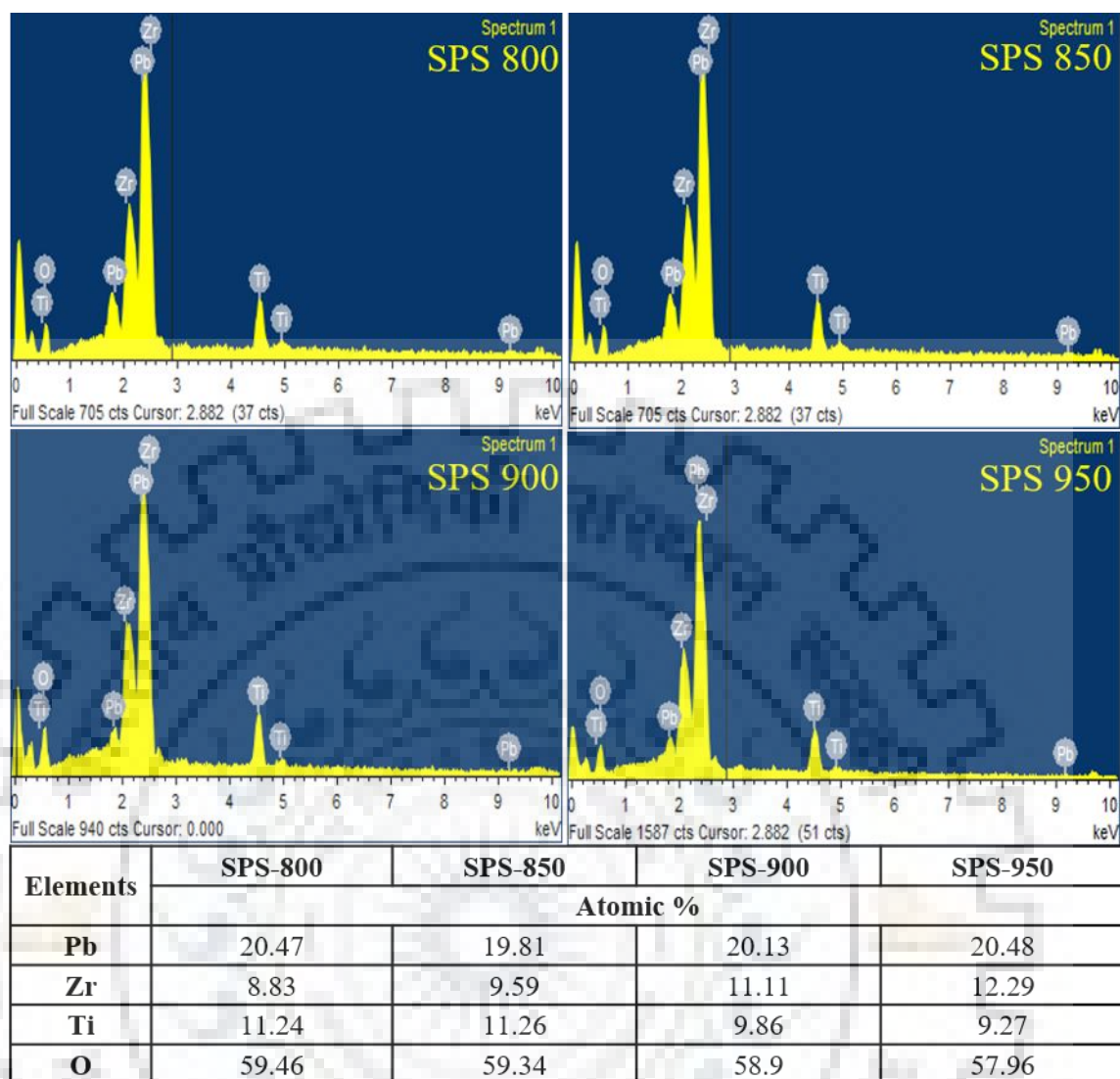


Fig. 4.15 EDS spectra of SPS-800, SPS-850, SPS-900 and SPS-950 samples.

4.2.6 Dielectric measurements

Fig. 4.16(a) and 4.16(b) represent the frequency-dependent behaviour of dielectric constant and dielectric loss tangent ($\tan \delta$) of SPS-800, SPS-850, SPS-900, SPS-950 samples over the frequency range 42 Hz - 5 MHz. Fig. 4.16(a) shows that the plateau in the dielectric spectra extends from 42 Hz to 100 kHz. The plateau region is followed by dielectric dispersion at the frequency range from 100 kHz to 1 MHz. Thereafter, dielectric constant reaches to static values at frequencies above 1 MHz. Such dispersion behaviour can be explained by Maxwell-Wagner type interfacial polarization involving Koop's theory for ferroelectric materials. Koops suggested that the bulk conducting grains and insulating grain boundaries can be represented as an inhomogeneous dielectric structure as reported by Maxwell and Wagner (Koops 1951; Wagner 1913). Different types of polarization namely ionic, electronic, orientation, and space charge may be induced by structural defects such as grain boundary charge defect, oxygen vacancies in ABO_3

type of perovskite structure etc. Dielectric constant decreases drastically at higher frequencies since only ionic and electronic polarization act and the charge carriers cannot follow the applied electric field (Rani, Kolte, and Gopalan 2015). The dielectric constant of SPS-900 sample is the highest among all the different samples studied, which is in agreement with the phase analysis by Rietveld refinement results. In Fig. 4.16(b), dielectric loss is nearly constant up to 10 kHz. The dielectric loss peak is observed at frequencies below 1 MHz for SPS-800 and SPS-850 specimens. It can be clearly observed that the peak shifts towards higher frequency for samples SPS-900 and SPS-950 which may be due to the availability of many possible domain states (Ahmed, Bishay, and Abdelatif 2001; Bokov and Ye 2004; Yu and Ang 2002).

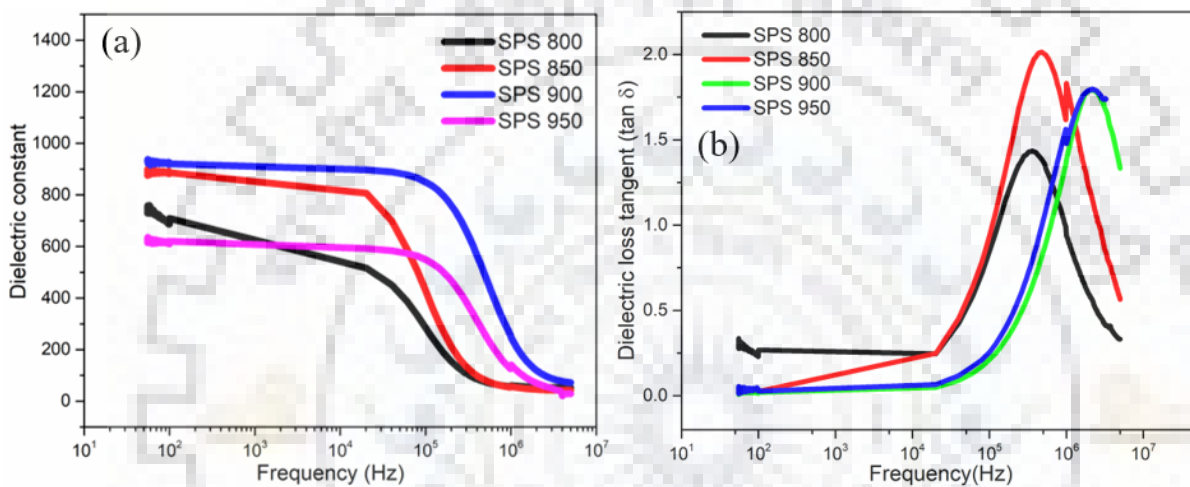


Fig. 4.16 Variation of (a) dielectric constant, (b) dielectric loss tangent with frequency of SPS-800, SPS-850, SPS-900 and SPS-950 samples at room temperature.

The dependence of dielectric constant on temperature for PZT has been examined from room temperature to 500°C. Fig. 4.17 illustrates the variation of dielectric constant with the temperature observed at a frequency of 100 kHz and confirms the ferroelectric nature of PZT samples. The dielectric constant increases with increase in temperature and peaks at a particular temperature known as Curie temperature after which it decreases due to the transition from ferroelectric phase to paraelectric phase. The Curie temperature is found to be 320°C for SPS-950 and ~ 335°C for other samples. For comparison, Geetika et al. obtained a dielectric constant of ~ 6000 at 100 kHz for conventionally sintered $\text{PbZr}_{0.5}\text{Ti}_{0.5}\text{O}_3$ at the transition temperature (Srivastava, Goswami, and Umarji 2013). It is noteworthy to mention that both SPS-900 and SPS-950 show higher dielectric constant at the Curie temperature relative to the other two samples. The calculated FWHM values of dielectric relaxation peak for SPS-800, SPS-850, SPS-900, SPS-950 are 194.4°, 68.93°, 78.1°, 84.95° respectively. However, sharp dielectric relaxation peaks are observed for SPS-900 and SPS-950 which suggests that the peak broadening is reduced

due to the reduction in compositional fluctuation. This is in close agreement with the calculated phase composition confirmed through Rietveld refinement for different SPS samples.

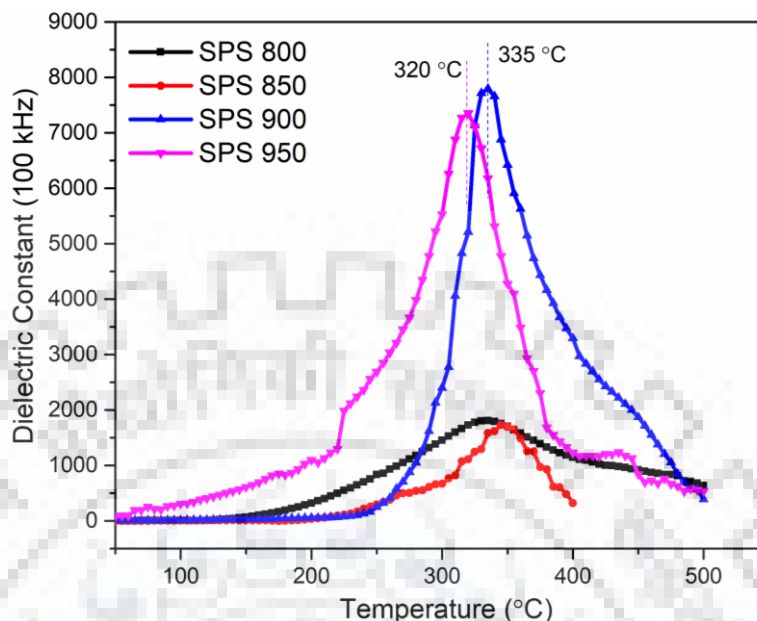


Fig. 4.17 Room temperature dielectric constant of SPS-800, SPS-850, SPS-900 and SPS-950 samples as a function of temperature measured at 100 kHz.

Dielectric performance of SPS-900 and SPS-950 are significantly enhanced relative to other samples. The average grain size of the samples increases from 15.47 ± 0.35 nm to 19.41 ± 0.41 nm with the increase in sintering temperature for SPS-800, SPS-850 and SPS-900 implying that the increase in grain size with sintering temperature is insignificant. However, the average grain size of SPS-950 (37.26 ± 0.42 nm) is almost the twice of that of the other three samples. In addition, all samples have been densified by spark plasma sintering as shown in Table 4.3. Considering the above points, the dielectric properties depend considerably on the presence of phase constituents. Rietveld refinement reveals that in addition to tetragonal phase, the existence of monoclinic phase in SPS-900 and rhombohedral phase in SPS-950 samples lay emphasis on the importance of sintering temperature on the phase composition. Coexistence of phases has been known to induce ultra-high dielectric response due to increase in the availability of polarization domains (Isupov 1968). For a monoclinic phase, the polar axis is not determined by symmetry rather it can be directed anywhere within the monoclinic ac plane (Noheda et al. 2000) whereas polarization vector in tetragonal phase and rhombohedral phase lies along fixed [001] and [111] respectively. Therefore, SPS-900 specimen shows the highest dielectric performance due to the presence of monoclinic phase. As the dielectric performance of SPS-950 is comparable to that of SPS-900, it is to infer that the increased grain size maybe the dominant cause of increase in its dielectric constant (Kamel and de With 2008).

4.2.7 Summary

The bulk nanocrystalline $\text{PbZr}_{0.52}\text{Ti}_{0.48}\text{O}_3$ synthesized by spark plasma sintering method has been investigated thoroughly by FESEM, XRD and EDS analyses. It is suggested that optimum calcination temperature of 900°C is needed for complete single perovskite phase formation above which PbO volatilization leads to the formation of impure phases. The fine-grained ceramics obtained by spark plasma sintering at four different temperatures 800 , 850 , 900 and 950°C have grain sizes in the range of $15 - 37$ nm for which increase in grain size was observed with increase in sintering temperature. It is proposed that the compositional fluctuation occurred due to rapid sintering rate adopted in SPS which has a significant effect on dielectric performance. Since the grain size variation is not very significant for the samples sintered at different temperatures, the factor affecting dielectric performance is perhaps the stoichiometry/composition. Rietveld refinement reveals that SPS-900 having a mixture of both monoclinic and tetragonal phases shows highest dielectric performance due to higher number of available polarization directions. The phase transformation from tetragonal to cubic state occurs at a Curie temperature of 335°C . Rietveld refinement and EDS analysis results are in good agreement suggesting the formation of MPB phase in SPS-900 and SPS-950 in which the former shows the highest dielectric response.

Chapter 5

Effect of sintering temperature on spark plasma sintered PZT with MPB composition: Impedance and energy storage analyses

5.1 Introduction

The dielectric properties of $\text{PbZr}_{0.52}\text{Ti}_{0.48}\text{O}_3$ samples sintered at different temperatures (800 - 950°C) were presented in the last chapter. The effect of phase constitution on dielectric properties was investigated. In this chapter, the impedance and electric modulus studies on the PZT samples at room temperature are presented to investigate the different electrical relaxation mechanisms. In addition, the energy storage properties have been investigated for the different PZT specimens. An effort has been made to correlate the energy storage performance of the PZT specimens to their electrical relaxation processes.

5.2 X-ray diffraction analysis of spark plasma sintered $\text{PbZr}_{0.52}\text{Ti}_{0.48}\text{O}_3$

The XRD patterns of the heat-treated samples were reported and analyzed in the previous chapter. The XRD patterns of the four samples SPS-800, SPS-850, SPS-900, and SPS-950 prior to the heat treatment stage are presented in Fig. 5.1 to analyze the phases. All the samples are perovskite type having tetragonal crystal structure with $P4mm$ space group. The peak $\{200\}$ splitting also confirms the tetragonal structure. A peak at about $2\theta = 33^\circ$ corresponding to impurity pyrochlore phase in the samples (Vittayakorn et al. 2003) has been observed in all the patterns. Though the intensity of the impurity peak is negligibly small compared to those of the parent phase, peak intensity seems to increase with the increase in sintering temperature. The characteristic peaks for identification of phases in PZT typically lie in the range $2\theta = 50^\circ$ to 56° for Co X-ray target ($\lambda = 1.79 \text{ \AA}$). The XRD pattern of PZT (52/48) with tetragonal phase exhibits peaks (002) and

(200) at $2\theta = 51.355^\circ$ and 52.67° respectively as per PDF file 01-070-4264. Whereas, XRD pattern of PZT (52/48) with monoclinic phase exhibits peaks (200), (002) and (220) at $2\theta = 36.519^\circ$, 51.183° and 52.634° respectively as per PDF file 01-070-4059. It is also to be noted that the peaks (002) and (200) corresponding to tetragonal phase may shift further apart if the (Zr/Ti) ratio departs from the 52:48 ratio. Therefore, multiple peaks may be observed if there is a coexistence of phases and overlapping or shifting may be observed due to compositional fluctuation in the material. The XRD pattern shows multiple peaks at $2\theta = 50^\circ - 56^\circ$ for SPS-900 and SPS-950, which is in agreement to the above mentioned facts and suggest the coexistence of phases. Moreover, the peak intensity at $\sim 36.6^\circ$ is found to be higher for SPS-900 relative to other samples due to the merging of peaks corresponding to tetragonal (110)_T and monoclinic (200)_M symmetry.

For correct identification of phases, Rietveld analysis was conducted and reported for heat treated samples in the previous chapter. The results revealed that a mixture of tetragonal and monoclinic phases was observed for SPS-900 specimen whereas, a mixture of tetragonal and rhombohedral phase was observed for SPS-950. The intensity of peak {200} splitting is lower for all sintered PZT specimens when compared to annealed PZT specimens. However, the {200} splitting for SPS-950 specimen is distinctly observed, while the split peaks tend to merge together in the heat-treated condition. It is also to be noted that the impurity (pyrochlore) phase still remained in the heat-treated samples.

The heat treatment of samples is essential to eliminate any carbon residues and to reduce compositional fluctuation due to rapid sintering technique used in SPS. The spark plasma sintered samples were heat-treated in air at 800°C to compensate for the oxygen deficiencies. All specimens showed highly dense microstructure with smaller grain sizes having relative density near $\sim 99.37\%$ with difference $\Delta\rho = \pm 0.2$. SPS samples are typically known to exhibit higher permittivity than that of conventionally sintered PZT samples due to higher density along with submicrometer grain size (Zhou et al. 2004). In the present study, however, the difference in density values between the samples is low. Thus, it is assumed that any significant effect on impedance and ferroelectric properties due to density is not expected in between the samples.

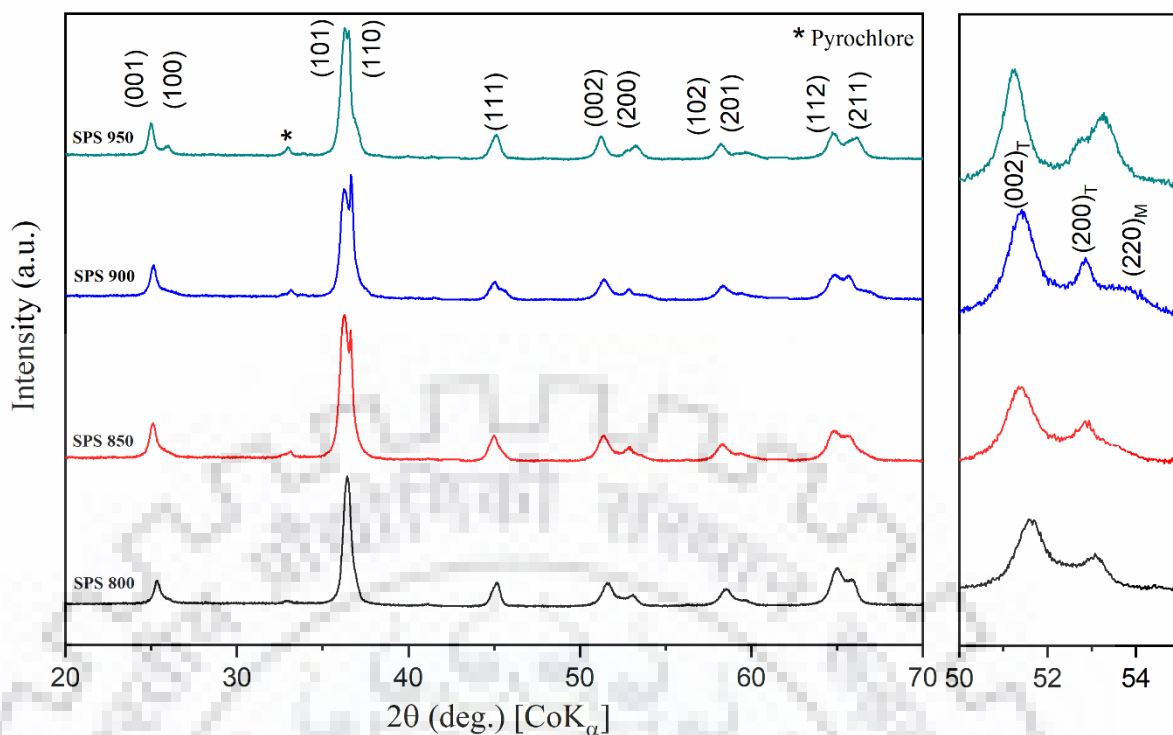


Fig. 5.1 XRD patterns of SPS-800, SPS-850, SPS-900 and SPS-950 samples along with magnified views of {002} splitting.

5.3 Variation of Z' with frequency

Fig. 5.2(a) shows the variation of real part of impedance (Z') with frequency for all the samples over frequency range 0.01 Hz - 1 MHz. It is observed that Z' decreases with frequency for all the samples, indicating an increase in AC conductivity with the frequency which follows from the empirical relationship, $\sigma_{ac} = \omega \epsilon_r \epsilon_0 \tan \delta$.

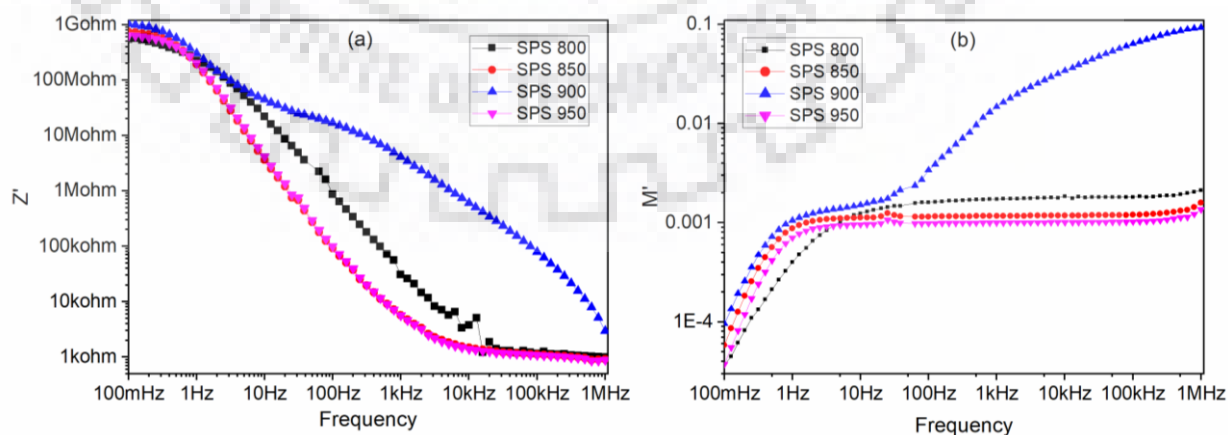


Fig. 5.2 Frequency dependent plots of (a) real part of impedance, Z' (b) real part of electric modulus, M' of SPS-800, SPS-850, SPS-900 and SPS-950 samples at room temperature.

At low frequency region, samples show high impedance meaning grain boundary relaxation phenomenon is dominant. This is due to the fact that the material is nanostructured and therefore, the grain boundary contribution is significant (Hungria et al. 2008a; Q. M. Zhang et al. 1994). At lower frequencies, the charge carriers are blocked at the grain boundaries, thereby enhancing localized relaxation (Kleitz, Dessemond, and Steil 1995). The grain boundary blocking effect is reduced on increasing frequency, and the charge carriers start to diffuse between the grains through the defects. The variation of Z' becomes independent of frequency from about 10 kHz for the samples SPS-850 and SPS-950, however, for the sample SPS-800, this occurs at a higher frequency of about 25 kHz. Such high frequency point could not be observed for the sample SPS-900 within the frequency range studied. The distinct nature of Z' vs. frequency variation for SPS-900 could be attributed to the crystalline phases as this sample has monoclinic phase in addition to tetragonal phase. The coexistence of monoclinic and tetragonal phases perhaps tends to set up a relaxation behaviour at higher frequency (beyond the upper limit of frequency of the measurement range used) for SPS-900. Again the value of the real part of impedance (Z') for SPS-900 sample is significantly greater almost over the entire frequency range which implies that material synthesis has increased the area of the potential barrier between the grains and offered more resistance for charge carriers.

5.4 Variation of M' with frequency

Fig. 5.2 (b) shows the variation of real part of electric modulus (M') with frequency for all the samples. The complex modulus, $M^* = M' + jM''$, corresponds to the dielectric relaxation process in the materials and is the inverse of complex permittivity (ϵ^*) of the material, $M^* = 1/\epsilon^*$ (Anand, Kuchhal, and Sarah 2015; Bonanos, Steele, and Butler 2005; Cao et al. 2015; Chandra Sati, Kumar, and Chhoker 2015; Coondoo et al. 2012; Jacob, Nair, and Isac 2015; Kumar, Murari, and Katiyar 2009; Lvovich 2012; Prasad, Sekhar, and Kumar 2008). It is observed from the modulus plots, that M' approaches to its negligibly small value at the low frequency limit implying negligible or absence of electrode polarization. Such behaviour may also be interpreted as due to long range conduction of charge carriers or their cooperative hopping which leads to dc conduction. At frequencies beyond 1 Hz, a plateau region is observed in the M' vs frequency plots for all samples except SPS-800 for which plateau starts at about 100Hz. However for SPS-900, after a small plateau region M' further increases from about 100 Hz which corresponds towards attaining another relaxation process corresponding to the second peak in M'' vs

frequency plot in Fig. 5.4. These observations are significant to show evidence of the role of phase constituents in the material to dielectric performance.

5.5 Variation of Z'' with frequency

Fig. 5.3 shows variation of imaginary part of impedance (Z'') as a function of frequency over 0.01 Hz - 1 MHz. For all the samples, broadening of the Z'' peaks at about 1 Hz suggests that there is a spread of relaxation time, i.e. the existence of material synthesis process parameter dependent electrical relaxation phenomenon in the material (Sambasiva Rao et al. 2008). It is reiterated that the distinction of different samples is by sintering (SPS) at four different temperatures. The relaxation phenomenon in the material may be due to the presence of immobile species/electron at low temperature and defects/vacancies at higher temperature. It can be observed that the peaks for all the samples appear nearly at the same frequency. At frequencies above 100 Hz, the Z'' profile of all samples merge with each other and remain frequency independent up to the maximum frequency limit of 1 MHz. This is apparently due to the presence of the space charge polarization effect at lower frequencies, which ceases to exist at higher frequencies (beyond 100 Hz in this case). The asymmetric broadening of the Z'' peaks observed for the samples confirms that the relaxation processes in the materials are of non-Debye type (Hungria et al. 2008b).

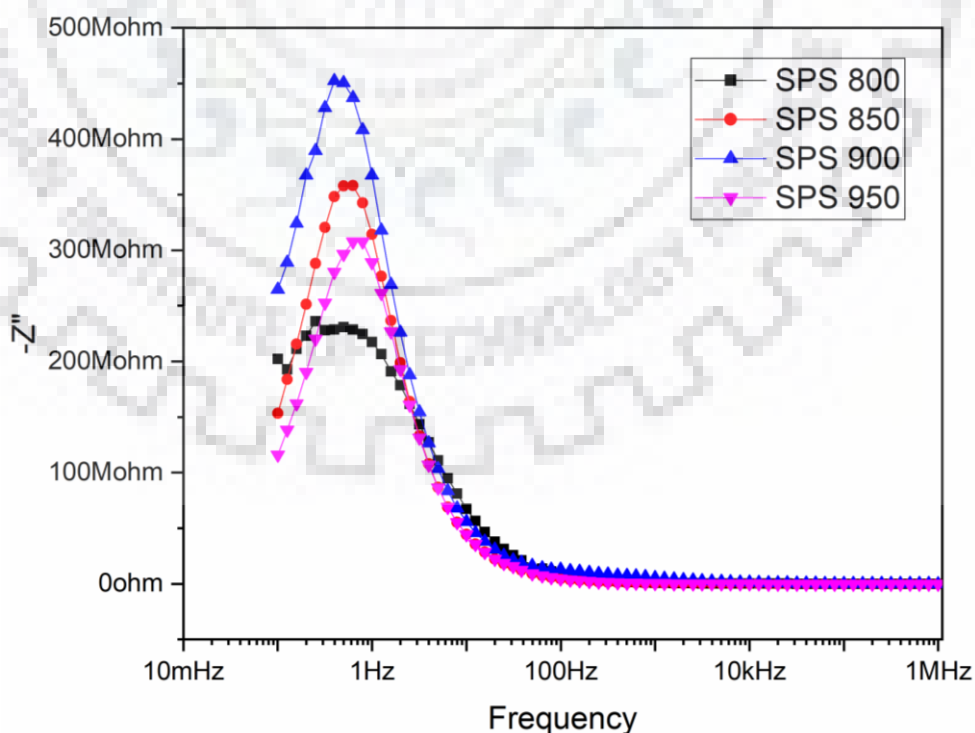


Fig. 5.3 Frequency dependent Z'' plots of SPS-800, SPS-850, SPS-900 and SPS-950 samples at room temperature.

5.6 Variation of M'' with frequency

The modulus plots, shown in the Fig. 5.4 for all the samples, are found to increase in higher frequency region (above 100 kHz). This nature confirms the presence of complex defects associated with lead (Pb) and oxygen (O) vacancies. The presence of broad asymmetric peaks in the modulus loss spectrum reveals that there are multiple relaxation times with different time constants and therefore correspond to non-Debye type relaxation. The low frequency peak generally suggests long range mobility of ions, whereas the high frequency peak suggests the confinement of charge carriers in their potential well (K. Chen et al. 2016; Prasad et al. 1998; Prasad, Srinivas, and James 2003; Sekhar and Prasad 2006). It can be observed that all samples exhibit M'' peak in the low frequency region of the plots. Moreover, M'' peak at high frequency is observed only for SPS-900 whereas, for other samples, a monotonic increase in M'' at high frequency region can be observed. The high frequency M'' peak for SPS-900 appearing within the frequency range signifies that the associated relaxation process has a higher time constant as compared to other samples. This may be attributed to the highest overall dielectric permittivity (and capacitance) observed for SPS-900 among all the samples studied as reported in the previous chapter. Therefore the electric modulus spectra suggest that the hopping mechanism is responsible for conduction process in all the materials studied (Khatri, Behera, and Choudhary 2009), however, for which evidence is clearly demonstrated by the material SPS-900.

SPS-800 and SPS-850 have nearly same M''_{max} values but at different relaxation frequencies which suggest that the samples have same capacitances but with different resistance components. In addition, SPS-850 and SPS-950 have same f_{max} but different M''_{max} suggesting that both resistance (R) and capacitance (C) are different for the samples (Sinclair and West 1994). Suppose the resistance increases due to increased resistivity of the material, the associated M''_{max} would remain unchanged. In the present case, volume fraction of a particular phase has increased since the f_{max} remains unchanged. It can also be noted that the sample SPS-900 has highest M''_{max} in the low frequency region, which means that the capacitance of the grain boundary region at lower frequencies is lowest among all the samples.

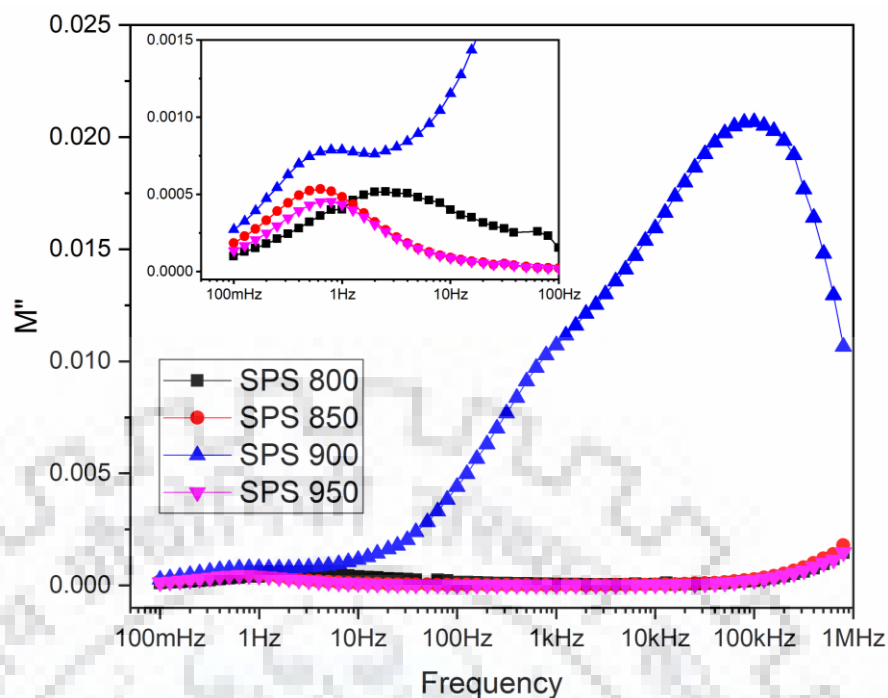


Fig. 5.4 Frequency dependent M'' plots of SPS-800, SPS-850, SPS-900 and SPS-950 samples at room temperature along with inset showing the same from 0.01 Hz to 100 Hz.

5.7 Analysis of combined impedance (Z'') and electric modulus (M'') spectroscopic plots against frequency

Fig. 5.5(a-d) depict the variation of Z'' and M'' with frequency for all four samples. The purpose of showing the combined impedance and modulus spectroscopy plots is that Z'' can highlight phenomena with the largest resistance while M'' features lowest capacitance. This also helps to distinguish the relaxation mechanisms that occur due to long range or short range movement of charge carriers. It is observed that Z'' has single peak for all samples, whereas, for M'' , the plots of three samples SPS-800, SPS-850 and SPS-950 depict a peak at low frequency region. However, for the sample SPS-900, both the low and high frequency peak appears within the measurement range. The low frequency peaks of Z'' and M'' vs. frequency plots fall at the same frequency for SPS-850, SPS-900, and SPS-950 suggesting delocalized relaxation mechanism or long range motion of charge carriers. Whereas, for SPS-800, low frequency peaks of Z'' and M'' appear at different frequencies implying localized relaxation mechanism or short range interaction of charge carriers (Prasad, Sekhar, and Kumar 2008).

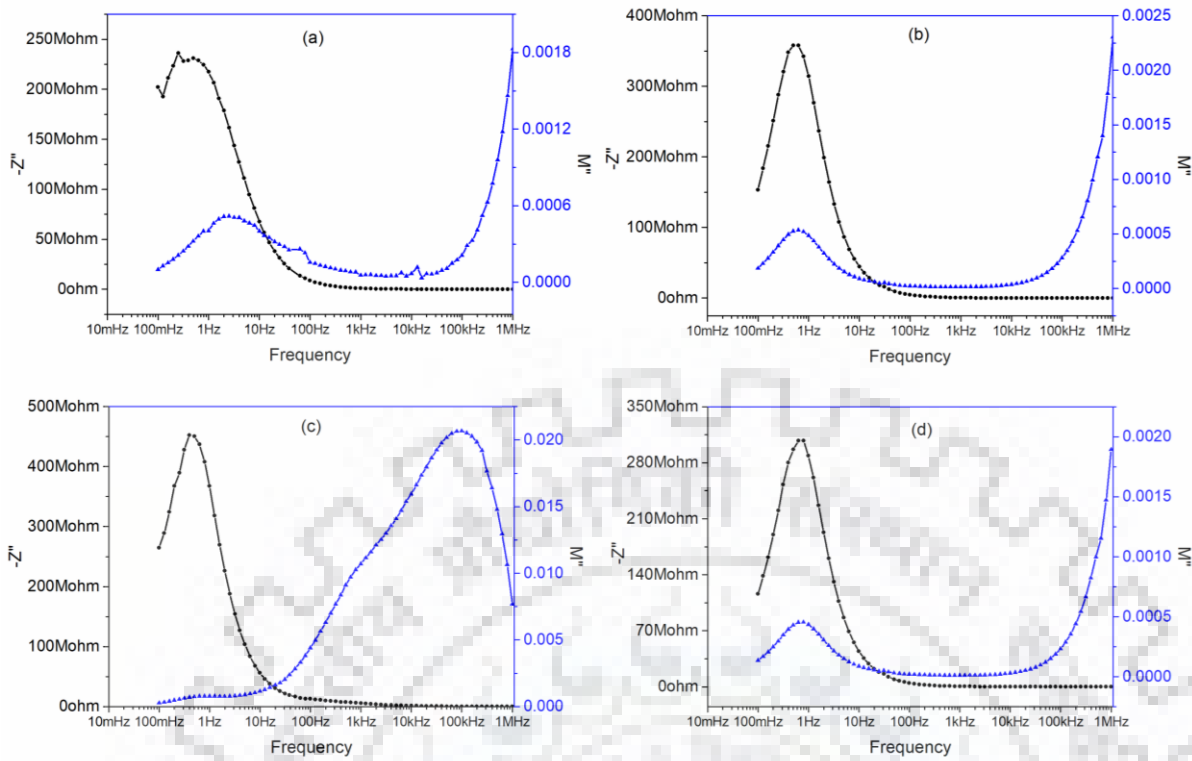


Fig. 5.5 Frequency dependent Z'' and M'' plots of (a) SPS-800, (b) SPS-850, (c) SPS-900 and (d) SPS-950 at room temperature.

Relaxation time (τ) can be calculated from the formula $\omega_{max} \tau = (2\pi f_{max}) \tau = 1$ for the peaks in M'' vs frequency plots as discussed in section 3.5.6. The τ , resistances (R_g , R_{gb}) and capacitances (C_g , C_{gb}) of grain (g) and grain boundary (gb) are calculated for sample SPS-900. The grain and grain boundary capacitances have been calculated at the relaxation points ($\omega_{max} \tau = 1$) in M'' vs frequency plots by the relation $M'' = C_o/2C$. Thereafter, resistance values can be calculated from eq. 3.19. The calculated τ , R_g , R_{gb} and C_g , C_{gb} values of grain (g) and grain boundary (gb) are presented in Table 5.1. In the absence of high frequency peaks for the samples SPS-800, SPS-850 and SPS-950, the parameters related to these sample grains could not be estimated.

Table 5.1 Calculated relaxation time, capacitance, resistance parameters for grain and grain boundary relaxation process.

Sample	τ_g (s)	τ_{gb} (s)	R_g (Ω)	R_{gb} (Ω)	C_g (F)	C_{gb} (F)
SPS-800		6.34×10^{-2}		2.27×10^8		2.79×10^{-10}
SPS-850		2.53×10^{-1}		6.78×10^8		3.73×10^{-10}
SPS-900	1.60×10^{-6}	2.49×10^{-1}	1.06×10^5	5.80×10^8	1.60×10^{-11}	2.57×10^{-10}
SPS-950		2.22×10^{-1}		5.90×10^8		3.76×10^{-10}

5.8 Analysis of Nyquist plots and complex modulus spectra

Fig. 5.6(a) shows Nyquist plots ($-Z''$ vs. Z') and Fig. 5.6(b) shows complex modulus spectrum (M'' vs M') for all the samples. Perfect semi-circular plots are most plausible only when the ferroelectric grains grow at the expense of space charge carriers accumulated at the grain-electrode interfaces (T. C. Chen, Thio, and Desu 1997). In Nyquist plots, these semi-circular arcs represent different relaxation processes. Usually, semi-circular arc at lower frequency region represents grain boundary relaxation process, and the one at higher frequencies gives the information on grain relaxation.

In Fig. 5.6(a), the spectra show depressed semi-circular arcs with their centers lying below the real axis for all samples. The depressed nature of the arcs suggests that there is a distribution of relaxation time and the arc cannot be fitted using an ideal capacitor C . Therefore, in order to account for non-Debye behaviours, a well-established approach of replacing the specific capacitance “ C ” by a phenomenological constant phase element (CPE) was used. The impedance of CPE is given by: -

$$Z_{CPE} = \frac{1}{Q(j\omega)^\beta} \quad (5.5)$$

where Q is a constant independent of frequency and β is a measure of deviation of relaxation process from Debye type behaviour which ranges from 0 to 1. For an ideal Debye process, the β should be unity.

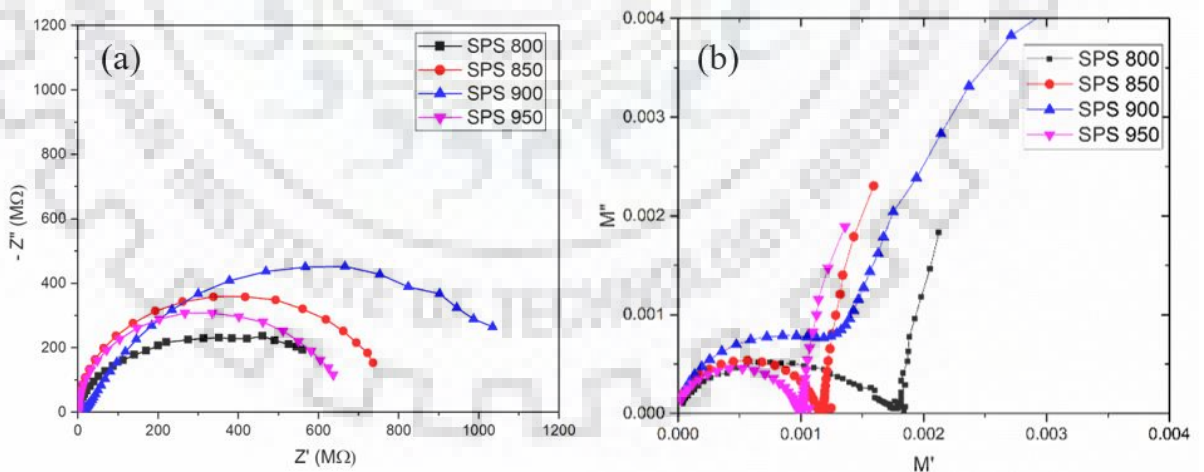


Fig. 5.6 (a) Complex impedance and **(b)** complex modulus plots of SPS-800, SPS-850, SPS-900 and SPS-950 samples at room temperature.

It is observed that the impedance of SPS-900 is the highest among the samples as can be inferred by its largest semi-circular arc. The asymmetric semi-circular arc is composed of both

grain and grain boundary relaxation phenomena. However, deconvolution of the arcs is needed to separate different contributions of grain and grain boundary.

As a result for clear understanding, the complex modulus spectrum is also plotted in Fig. 5.6(b) which clearly separates the two semi-circular arcs. It is evident from the complex electric modulus plots that both grain and grain boundary relaxation processes contribute to the physical properties of all samples. The appearance of inclined like behaviour (less than 60°) observed at high frequency region for all the samples is certainly due to hopping-conduction phenomena (Kakegawa et al. 2005). The higher grain/grain boundary impedance values generally give information about defects such as oxygen and lead vacancies accumulated at interfaces. The intercepts of low frequency semi-circular arc in the electric modulus spectrum is found to be highest for SPS-900 at $M'' = 0.002$ (approx.) and corresponds to grain boundary relaxation.

5.9 Conductivity studies

The ac conductivity response with frequency was also studied for the samples to confirm the Maxwell-Wagner polarization at lower frequencies (<1 kHz). Frequency dependent ac conductivities (σ_{ac}) were determined in the range $0.1 \text{ Hz} \leq f \leq 1 \text{ MHz}$ for all the samples and the results are shown in Fig. 5.7. Frequency independent behaviour of ac conductivity at very low frequencies (up to 1 Hz) indicates the dominance of dc conductivity to conduction mechanism and the absence of hopping charge carrier polarization in this very low frequency range. The dc conductivities are found to decrease for the samples with an increase in sintering temperature with the exception of SPS-950. For frequencies > 1 Hz, conductivity shows dispersion up to 100 kHz. The decrease in slope of the conductivity profile of SPS-900 is due to active conduction via grain relaxation phenomena. Beyond 10 kHz, a plateau is observed in the conductivity profile for all samples. However, for SPS-900, conductivity is found to increase up to 1 MHz. At 1 MHz frequency, the conductivity profiles of all samples tend to merge together, suggesting localized mobility of charge carriers.

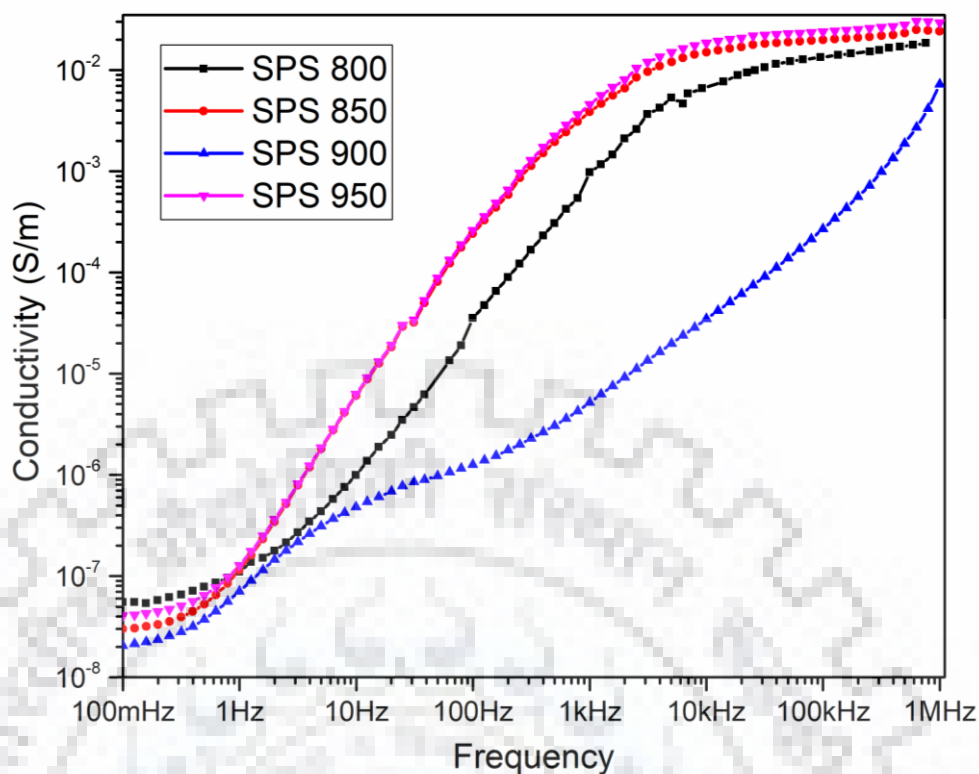


Fig. 5.7 Frequency dependent conductivity plots of SPS-800, SPS-850, SPS-900 and SPS-950 samples at room temperature.

5.10 Energy storage studies

Fig. 5.8 shows ferroelectric hysteresis (P-E) loops of all the samples that depict a typical ferroelectric behaviour with an applied electric field maximum up to 50 kV/cm. The nature of the loops indicates that at room temperature, the samples are ferroelectric. It can be observed that for the samples SPS-800, SPS-850 and SPS-900 the P-E loops are thinner than that of sample SPS-950. The mean grain size of SPS-800, SPS-850 and SPS-900 lies in the range of 15 ~ 20 nm, whereas the mean grain size of SPS-950 sample is 37.26 ± 0.42 nm as reported in the previous chapter. The decrease in ferroelectric behaviour for such materials is explained by the decrease in tetragonality as the grain size reduces to submicrometer scale. Moreover, the grain size also influences the domain size and density (Arlt and Pertsev 1991). The polarization may alter by depolarizing field due to space charge accumulation on grain boundaries which excludes polarization charge on grain surface (Joshi and Acharya 2016). The decrease in macroscopic polarization and hysteresis loop area together with a gradual tilting of the P-E loops appear to be a general trend when the grain size is decreased, as reported in many previous studies (Buscaglia et al. 2006; Curecheriu et al. 2012; Helbig 2007).

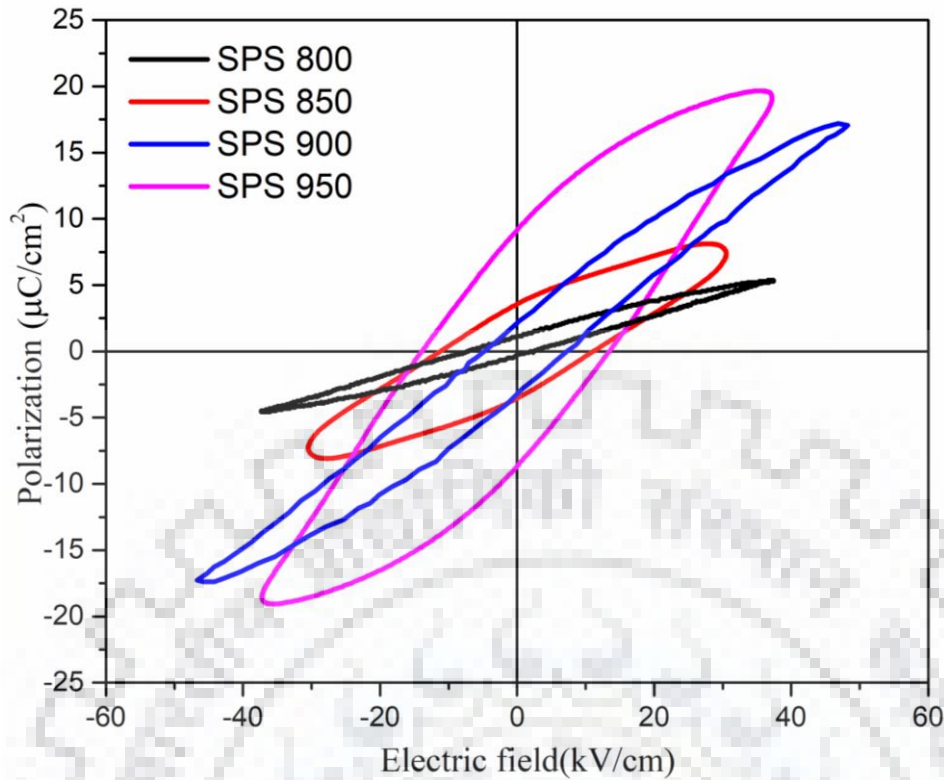


Fig. 5.8 Ferroelectric hysteresis loops of SPS-800, SPS-850, SPS-900 and SPS-950 samples at room temperature with an applied electric field maximum up to 50 kV/cm.

The energy storage density can be estimated by integrating the area between the P-E curve and polarization axis given by the equation:

$$W_{st} = \int_0^{P_{max}} EdP \quad (5.6)$$

The energy stored during the charging process cannot be entirely released on discharging process. The hysteresis area of the P-E curve represents the energy lost (W_{loss}) while discharging. Thus, the recoverable energy density (W_{re}) can be estimated by calculating the difference between W_{st} and W_{loss} or by the equation:

$$W_{re} = \int_{P_r}^{P_{max}} EdP \quad (5.7)$$

The energy efficiency of the ferroelectric material is given by the ratio of recoverable energy density and stored energy density by equation:

$$\eta = \frac{W_{re}}{W_{st}} \quad (5.8)$$

The SPS-900 and SPS-950 ceramics exhibit significantly higher saturation polarization values than the other two samples, which co-relates to the presence of multiple phases. The increase in number of available polarization states due to the phase coexistence has been known

to induce high permittivity (Isupov 1968). The ceramics with large grains tend to exhibit larger P_r (Sun et al. 2015) which is in agreement with the ferroelectric properties of SPS-950 for which the grain size is double the grain size of SPS-900. SPS-950 shows higher hysteresis with P_r (8.93 $\mu\text{C}/\text{cm}^2$) and E_c (20.39 kV/cm) compared to P_r (2.67 $\mu\text{C}/\text{cm}^2$) and E_c (5.92 kV/cm) of SPS-900 sample. The recoverable energy density (0.75 J/cm^3) and energy efficiency ($\eta = 66.38\%$) of SPS-900 is highest among all samples. The energy storage properties for all the samples are presented in Table 5.2.

Table 5.2 Energy storage parameters for SPS-800, SPS-850, SPS-900 and SPS-950 samples at room temperature.

Sample	P_s/P_r ($\mu\text{C}/\text{cm}^2$)	E_c/E_{max} (kV/cm)	E.S.D. (J/cm^3)	Recoverable Energy density (J/cm^3)	Energy Efficiency (%)
SPS-800	4.97/0.70	4.10/41.65	0.27	0.19	70.37
SPS-850	8.11/3.55	11.15/30.50	0.42	0.11	26.19
SPS-900	17.32/2.67	5.92/46.67	1.13	0.75	66.38
SPS-950	19.36/8.93	20.39/37.41	1.37	0.47	34.31

5.11 Summary

The phase analysis, different relaxation mechanisms, dominant conduction mechanism and energy storage performance of spark plasma sintered $\text{PbZr}_{0.52}\text{Ti}_{0.48}\text{O}_3$ (PZT) material at different temperatures (800, 850, 900, and 950°C) have been presented. The following conclusions can be stated:

- 1) Preliminary XRD analysis confirmed the presence of tetragonal perovskite structure having $P4mm$ space group along with the pyrochlore phase (impurity phase) for all samples. However, peak splitting's are observed in the characteristic {200} for SPS-900 and SPS-950 specimens, suggesting the presence of multiple phases. Similar findings were reported by Wang et al. (Geetika and Umarji 2010; X. Wang et al. 2016). Li et al. have also reported multiple phases for perovskite barium titanate under heat treatment conditions of 900°C/20h and 950°C/8h.
- 2) The nature of dispersion of real part (Z') of complex impedance Z^* for SPS-900 is distinctly different from remaining three samples SPS-800, SPS-850 and SPS-950 for which Z' decreases almost six orders of magnitude over the frequency variation from

100 mHz to 10 kHz, whereas, about five orders of Z' decrease over frequency variation from 100 mHz to 1 MHz is found for SPS-900. The decrease in Z' with frequency is typically due to increase in ac conductivity (Nasri et al. 2016).

- 3) Real part of the electric modulus (M') variation with frequency reveals supporting evidence of Z' variation. Interestingly small plateau seen in the Z' profile of SPS-900 over the frequency around 10 Hz is complimented in the M' variation. The increasing trend of M' from about 50 Hz with frequency implies different polarization mechanisms in the material compared to other samples for which polarization becomes independent of frequency from about 10 Hz. Therefore the simultaneous study of Z' and M' variations throws light on relaxation mechanism of the sample materials.
- 4) The Nyquist plots of samples showing depressed semi-circular arc confirm non Debye type behaviour. The impedance of SPS-900 is the highest among the samples as can be inferred from its largest semi-circular arc. However, the separation between grain and grain boundary relaxation phenomena is not observed. Therefore, complex modulus spectra were used to identify the different relaxation processes, as reported in many perovskites (Coşkun et al. 2018).
- 5) Complex electric modulus spectra were studied to deconvolute the grain and grain boundary relaxation mechanisms for which complex impedance spectra has a limitation. The low frequency peak of Z'' and M'' vs frequency plots fall at the same frequency for SPS-850, SPS-900, and SPS-950, suggesting delocalized relaxation mechanism or long range motion of charge carriers. Prasad et al. (Prasad, Sekhar, and Kumar 2008) have also reported delocalized relaxation in PZT ceramics as the peak maxima of Z'' and M'' lie near the same frequency region. Grain boundaries are more resistive and capacitive as compared to grains as found in sample SPS-900. The capacitance and resistance values of grain and grain boundary contributions of SPS-900 are determined as $C_g = 1.60 \times 10^{-11}$ F, $R_g = 1.06 \times 10^5 \Omega$ and $C_{gb} = 2.57 \times 10^{-10}$ F, $R_{gb} = 5.80 \times 10^8 \Omega$.
- 6) The ac conductivity with frequency confirms the Maxwell-Wagner polarization at lower frequencies (<1 kHz) for all samples. For frequencies > 1 Hz, conductivity shows dispersion up to nearly 10 kHz. However for SPS-900, conductivity shows a continuous increasing trend up to upper limit (1 MHz) of measurement.
- 7) Peng et al. (2015) and Joshi et al. (2016) reported recoverable energy density of 0.1067 J/cm³ ($\eta = 24.12\%$) and 0.127 J/cm³ ($\eta = 14.2\%$) in undoped PZT (52/48) ceramics respectively. In the present work, SPS-900 specimen exhibits maximum energy storage

efficiency of 66.38 %, recoverable energy density of 0.75 J/cm^3 and saturated polarisation (P_s) of $17.32 \text{ } \mu\text{C/cm}^2$ at E_{max} of 46.67 kV/cm . The enhanced energy storage performance is attributed to optimum sintering temperature used and its respective phase constitution (tetragonal and monoclinic phases).

- 8) Hence it may be inferred from the range of studies conducted in the present work that the compositional fluctuation in spark plasma sintered PZT ceramics leads to change in the respective phase constitution at MPB composition. The impedance and modulus spectra revealed a significant difference in relaxation species between the samples suggesting a difference in phase constitution. The ferroelectric material $\text{PbZr}_{0.52}\text{Ti}_{0.48}\text{O}_3$ spark plasma sintered at 900°C shows the highest recoverable energy density and energy storage efficiency along with superior electrical characteristics.



Chapter 6

Comparative evaluation of spark plasma and conventional sintering of PZT ceramic with MPB composition

6.1 Introduction

There have been extensive reports that focusses on the size effect of perovskites in PT (Fernández et al. 1998; Jiang and Bursill 1999) and PZT (Cao and Randall 1996; Fernández et al. 1998; Randall et al. 2005) ceramics. The fine microstructure with nano-sized grains in these ceramics significantly influences the phase transition, ferroelectric properties and energy storage properties. Generally, the low permittivity grain boundary layers were reported as the key factor in influencing the dielectric properties in nano ceramics. However, less attention has been paid to the influence of these nano-sized grains on the energy storage properties of the material. This chapter discusses how $\text{PbZr}_{0.52}\text{Ti}_{0.48}\text{O}_3$ compound was synthesized via solid state reaction and sintered by both SPS as well as conventional sintering (CS). The microstructure, X-ray diffraction analysis and sintering parameters have been discussed for both the PZT specimens. The difference in physical properties and phase constitution has been noted. Thereafter, dielectric, conductivity and energy storage studies have been investigated. The probable causes for enhanced dielectric and energy storage performance of spark plasma sintered specimens have been discussed.

6.2 SEM analysis of calcined powder used for SPS and CS samples

The preparation of calcined powders for SPS and CS samples has already been discussed in Chapter 3. The powders were mixed thoroughly for 6 hours under toluene solvent. The zirconia ball to charge ratio was taken as 10:1 to ensure sufficient compressive pressure for uniform mixing. The mixture was then dried and calcined at 900°C for 4 hours in a muffle furnace. Fig.

6.1 depicts the scanning electron micrograph of calcined powders along with elemental composition that confirms the desired target composition. The atomic ratios 21:11:10:59.5 is fairly consistent with the desired stoichiometry of $\text{PbZr}_{0.52}\text{Ti}_{0.48}\text{O}_3$. The morphology of the calcined powders has been already discussed in section 4.2.1.

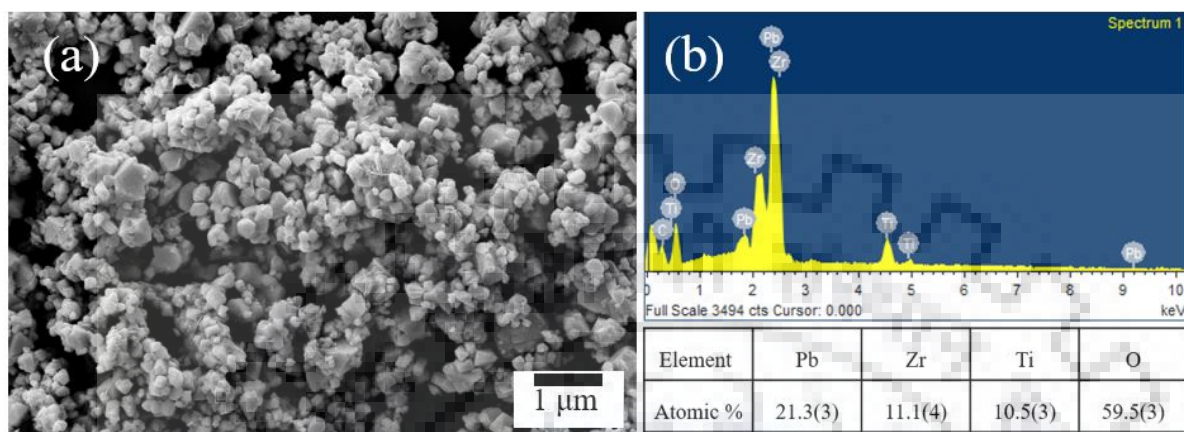


Fig. 6.1 (a) Scanning electron micrograph and (b) EDS analyses of $\text{PbZr}_{0.52}\text{Ti}_{0.48}\text{O}_3$ powders calcined at 900°C .

6.3 Sintering profiles used for SPS and CS samples

The sintering profile adopted for SPS samples as depicted in Fig. 6.2 have already been described in section 4.2.3. The sintering of CS samples was conducted at sintering temperature of 1200°C with a soaking time of 2 hours. The maximum heating rate of $5^\circ\text{C}/\text{min}$ was applied which took ~ 4 hours to reach the target temperature. After soaking, the CS samples were furnace cooled to room temperature. Table 6.1 presents the sintering parameters used for SPS and CS samples. It is to be noted that the conventional sintering technique is a pressure-less technique whereas axial compressive pressure is applied onto SPS samples during sintering. This in turn ensures breaking down of agglomerates even prior to sintering which facilitates uniform heating of powders in SPS samples. The typical sintering time for CS samples is in hours relative to minutes for SPS samples. The sintered samples were then polished to flat pellets for further characterization of dielectric and energy storage properties measurements.

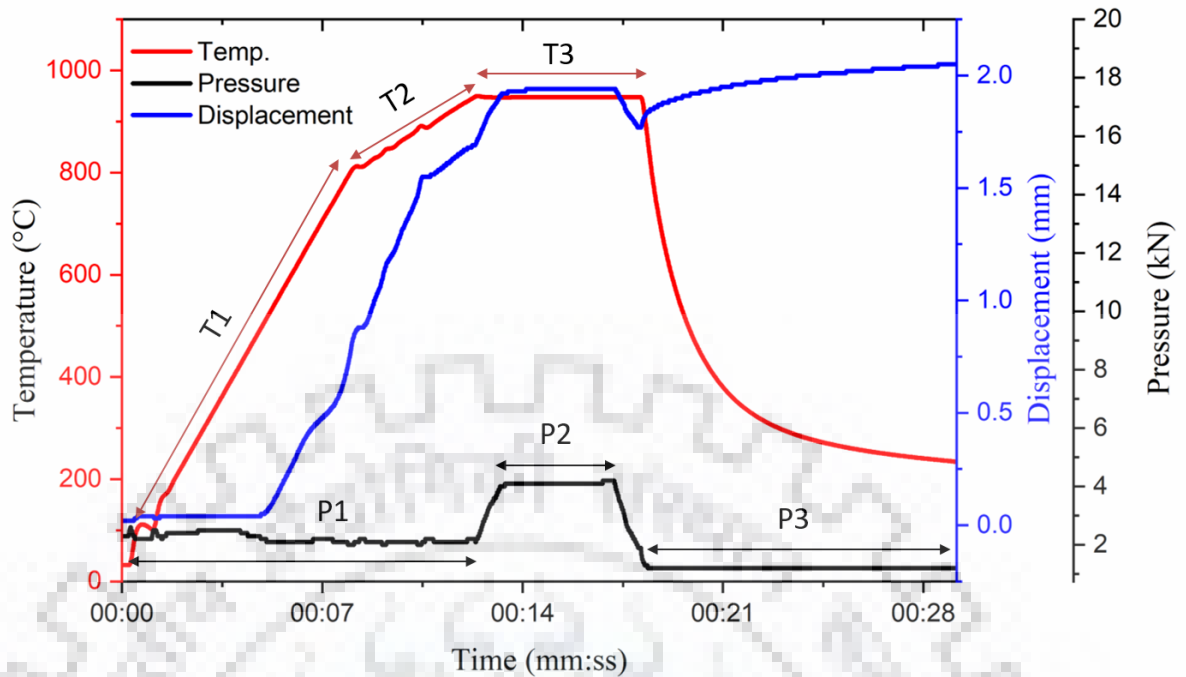


Fig. 6.2 SPS profile adopted for $\text{PbZr}_{0.52}\text{Ti}_{0.48}\text{O}_3$ showing different temperature and pressure stages during a sintering cycle.

Table 6.1 Sintering parameters for $\text{PbZr}_{0.52}\text{Ti}_{0.48}\text{O}_3$ ceramics sintered by SPS and CS method.

	Sintering Temp	Holding time	Heating rate	Pressure	Cooling time to 200°C
SPS	900°C	5 min	100°C/min up to 800°C; 33°C/min up to 900°C	60 MPa	5 min
CS	1200°C	2 hrs	5°C/min	NA	8 hrs

6.4 Microstructure analysis

The scanning electron micrographs of the cross sectional area of SPS and CS samples are presented in Fig. 6.3. SPS samples exhibit uniform and fine grained microstructure with negligible porosity, whereas the microstructure of CS samples exhibit irregular grain size and shape with clearly visible pores. The SPS samples depict dense microstructure with relative density ~ 99.6%. On the other hand, the CS specimen shows relative density of ~ 93.7%. The average grain size of SPS and CS specimens calculated using the linear intercept method are ~

40 nm and $\sim 1.5 \mu\text{m}$ showing narrow and broad grain size distributions respectively. The grain size of CS sample varies from as low as $\sim 0.4 \mu\text{m}$ to $\sim 1.98 \mu\text{m}$.

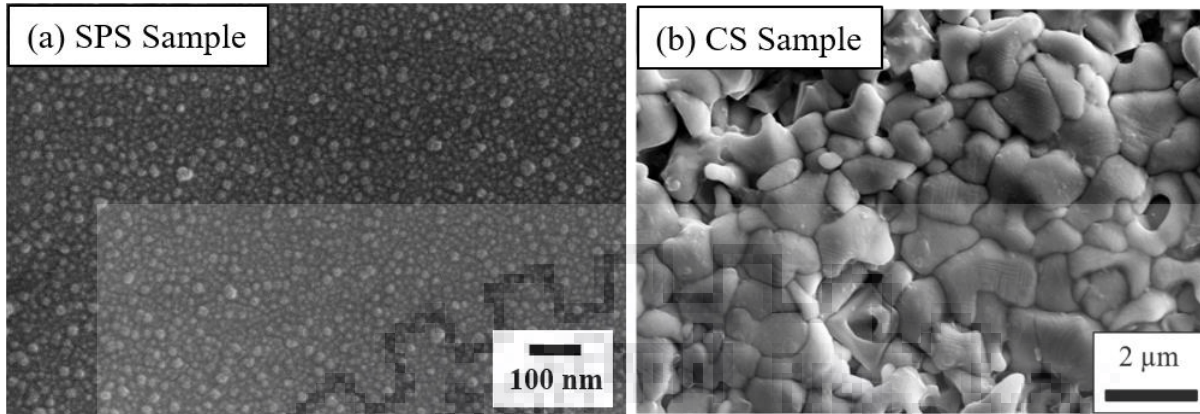


Fig. 6.3 Scanning electron micrographs of $\text{PbZr}_{0.52}\text{Ti}_{0.48}\text{O}_3$ sintered by (a) SPS at 900°C and (b) conventional sintering at 1200°C .

6.5 XRD analysis

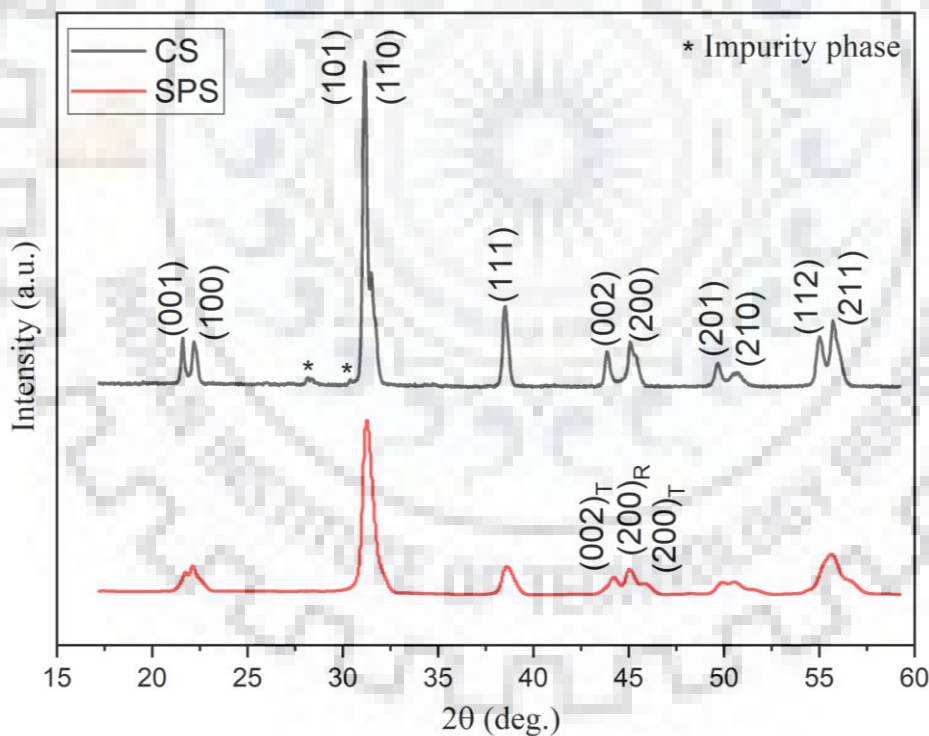


Fig. 6.4 X-ray diffractograms of $\text{PbZr}_{0.52}\text{Ti}_{0.48}\text{O}_3$ sintered by CS and SPS method.

Fig. 6.4 depicts the XRD patterns of SPS and CS samples for the data collected over 2θ range of 15° to 60° . The SPS samples show pure perovskite structure with no detectable impurity phases whereas for CS samples, intermediate phases prior to perovskite phase formation can be detected. This is due to the high sintering temperature used in CS samples which leads to PbO evaporation

resulting in change in the desired stoichiometric composition. The split of diffraction peaks at higher angles ($2\theta = 43 - 46^\circ$) corresponds to tetragonal perovskite crystal structure with space group $P4mm$ for CS samples. The calculated FWHM values for the {110} peak are 0.638° and 1.2693° for CS and SPS sample respectively. The peaks are typically broadened for SPS samples than in CS samples which is due to the nano-sized grains. At 2θ range of $43^\circ - 46^\circ$, the SPS samples show presence of characteristic peaks of both tetragonal (200), (002) and rhombohedral phase (200) which suggest MPB composition. Table 6.2 shows that the tetragonality of SPS sample is lower than the CS sample. This may be due to the decrease in lattice distortion along c axis for nano-sized grains in SPS sample (Zhao et al. 2004).

Table 6.2 Lattice parameters and tetragonality of $\text{PbZr}_{0.52}\text{Ti}_{0.48}\text{O}_3$ ceramics sintered by SPS and CS method.

Sintering method	Lattice parameter, c	Lattice parameter, a	Tetragonality c/a
SPS	4.145	4.03	1.0285
CS	4.15	4.004	1.0365

6.6 Dielectric studies

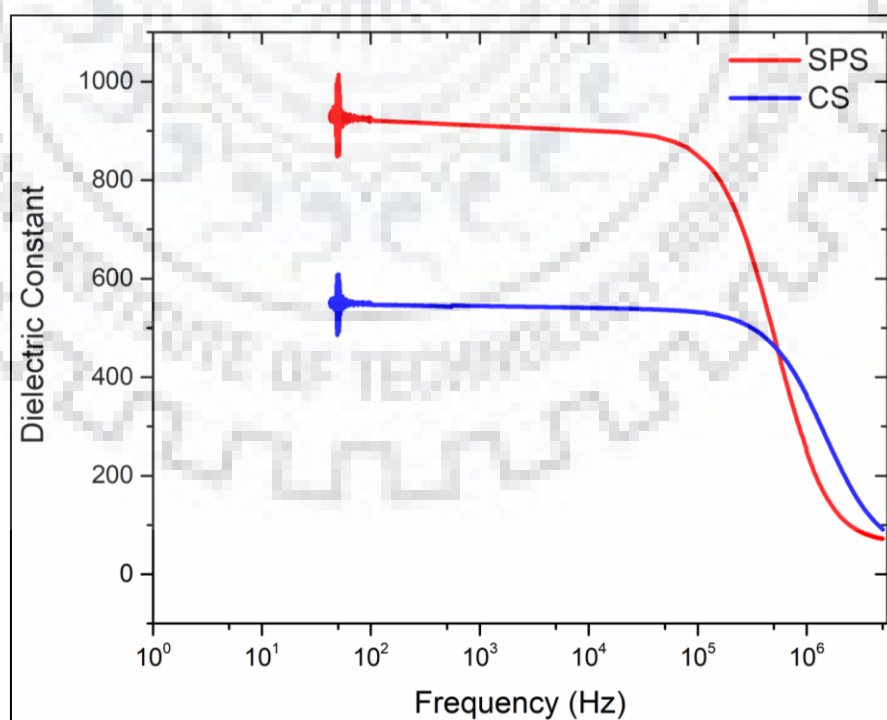


Fig. 6.5 Variation of dielectric constant with frequency of $\text{PbZr}_{0.52}\text{Ti}_{0.48}\text{O}_3$ at room temperature sintered by SPS and CS method.

Fig. 6.5 shows the frequency dependence of dielectric constant for the SPS and CS PZT samples. It can be observed that the room temperature dielectric constant for SPS ceramic ($\epsilon_r \sim 910$ at 1 kHz) is considerably higher than the CS counterpart ($\epsilon_r \sim 545$ at 1 kHz) and remains so up to ~ 500 kHz. At frequencies near and above 500 kHz, the dielectric constant of both the SPS and CS samples decreases considerably which is presumably due to the absence of low frequency polarization mechanisms (orientational and interfacial polarization). The dielectric constant is a function of polarization, which directly depends on the material composition and microstructure. Typically, large amount of the low permittivity layers (grain boundaries) reduce the overall dielectric constant of the material (Algueró et al. 2009; Buscaglia et al. 2006). However, the distinct behaviour of SPS sample in this case, may be due to its high density. Since, the desired phase composition is same for both samples, the dense microstructure may be the deciding factor for enhanced dielectric constant.

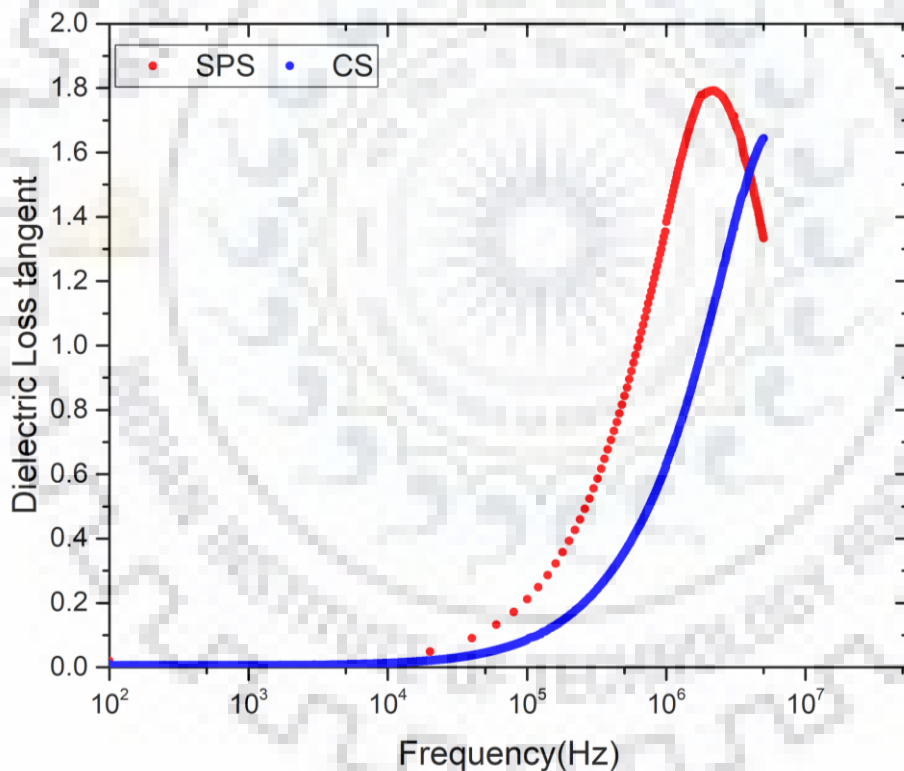


Fig. 6.6 Variation of dielectric loss tangent with frequency of $\text{PbZr}_{0.52}\text{Ti}_{0.48}\text{O}_3$ at room temperature sintered by SPS and CS method.

Fig 6.6 depicts the dependence of dielectric loss tangent on frequency. It can be observed that for both specimens, the dielectric loss tangent is independent of frequency up to ~ 20 kHz. On further increase of frequency, the dielectric loss tangent curve peaks at ~ 20 MHz for SPS specimen. Though the dielectric loss peak of CS specimen is not clearly visible in the plot, it can

be inferred that the loss peak for SPS specimen occurs at frequencies lower than that of CS specimen. The underlying reason for such dissipation of electrical energy for SPS samples may be due to the higher relaxation contribution from large volume of grain boundaries i.e. low permittivity layers.

6.7 Conductivity studies

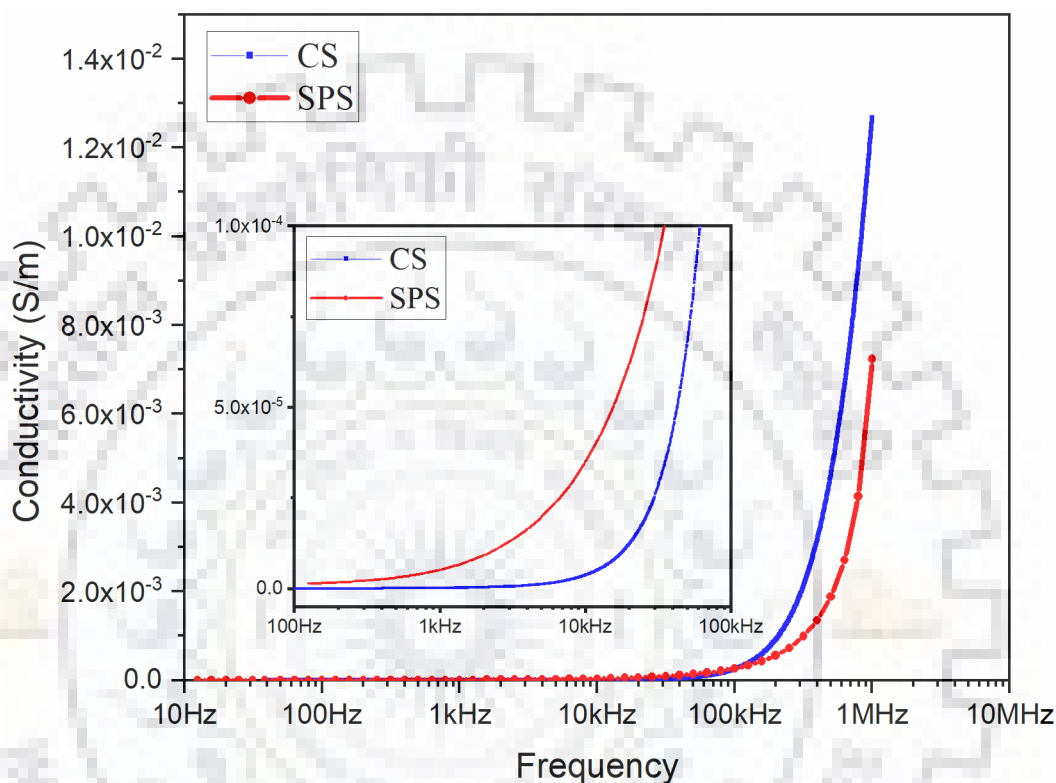


Fig. 6.7 Frequency dependent AC conductivity plots of $\text{PbZr}_{0.52}\text{Ti}_{0.48}\text{O}_3$ sintered by SPS and CS method.

The variation of conductivity with frequency for SPS and CS samples is given in Fig. 6.7. The conductivity of both the samples is independent of frequency until ~ 100 kHz. On further increase of frequency, the conductivity of both the samples increases significantly. The rise in conductivity begins at relatively lower frequency for CS specimen than that for SPS sample. The large volume of grain boundaries acting as amorphous phase in SPS specimen perhaps limit the transition of mobile charge carriers and result in decrease of conductivity relative to that of CS specimen.

6.8 Temperature dependent dielectric studies

Fig. 6.8 illustrates the variation of dielectric constant with temperature over the range $30 - 500^\circ\text{C}$ at different frequencies for SPS and CS specimens. Typically, the dielectric constant increases

with increase in temperature up to the Curie point (T_C) signifying ferroelectric to paraelectric transition in PZT ceramics. The dielectric constant peaks are observed at $\sim 320^\circ\text{C}$ and $\sim 450^\circ\text{C}$ which correspond to the phase transitions in the material. The presence of two phase transition peaks in the permittivity curves indicates coexistence of phases in the samples. The specimen's exhibit rhombohedral to tetragonal phase transition near $\sim 320^\circ\text{C}$ and tetragonal to cubic phase transition at $T_C \sim 450^\circ\text{C}$. In conventionally sintered ceramics, the dielectric peak near $\sim 320^\circ\text{C}$ is very broad, whereas it is relatively narrow and clearly visible for SPS sample. The Curie temperature peak is relatively narrow and distinctly observed for both the specimens with a maximum dielectric constant of ~ 7550 and ~ 25000 for CS and SPS samples respectively at 1 kHz. The ferroelectric to paraelectric phase transition peak is suppressed at higher frequencies as polarization severely reduces at high frequencies (>1 kHz).

It is to be noted that few authors have reported broad dielectric relaxation peaks for spark plasma sintered ceramics (Mesquita et al. 2012; Park, Chung, and Kim 2006; Zuo et al. 2007), whereas in the current work, low peak broadening is observed which may suggest that the peak broadening, in addition to grain size, also depends on the degree of compositional fluctuation. It appears from above that the phase constitution and composition of the SPS sample are very close to the desired/target value. As a result, narrow dielectric peaks are observed for spark plasma sintered PZT ceramics.

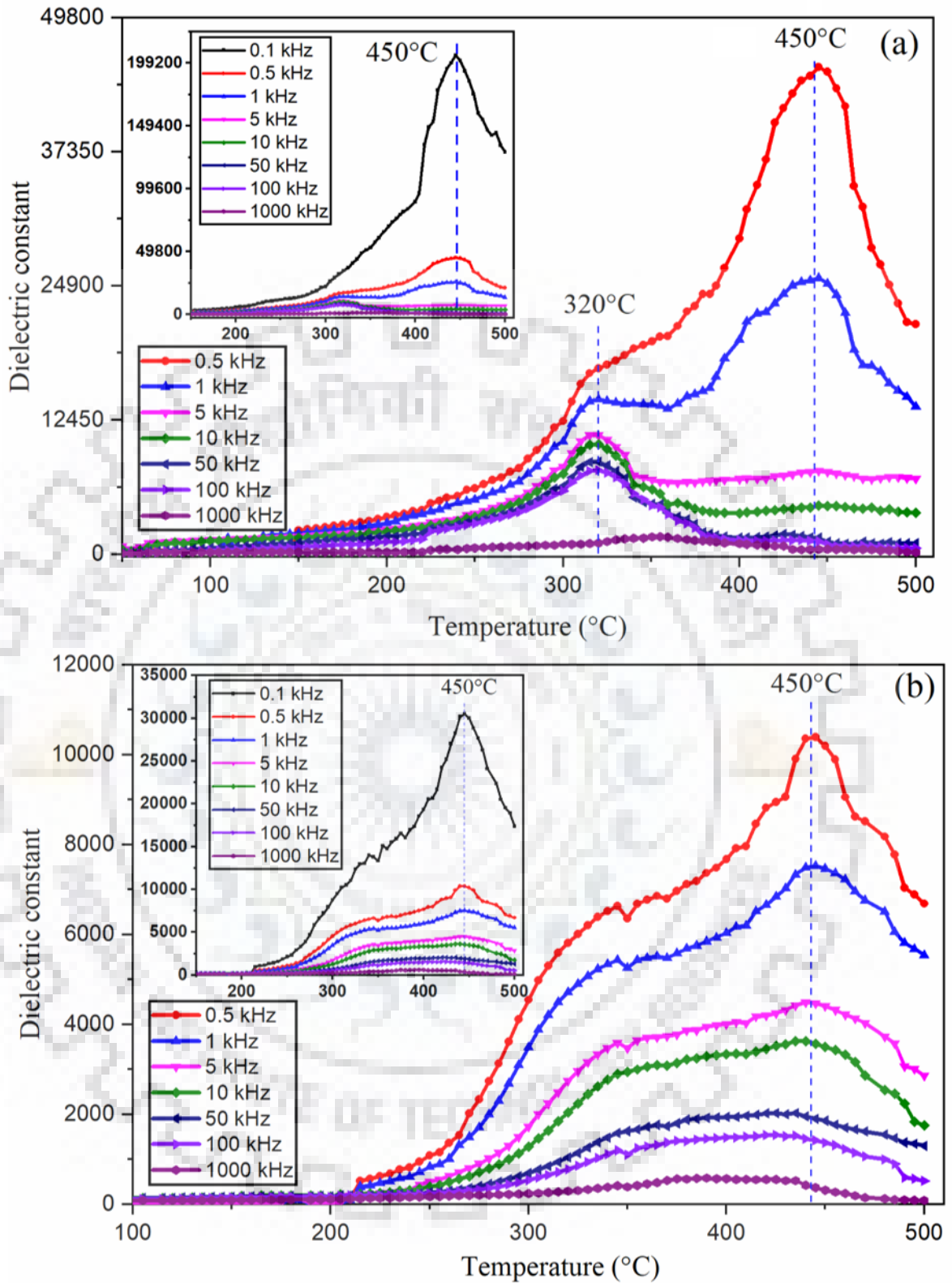


Fig. 6.8 Variation of dielectric constant with temperature of (a) spark plasma and (b) conventionally sintered $\text{PbZr}_{0.52}\text{Ti}_{0.48}\text{O}_3$ sample at 0.5, 1, 5, 10, 50, 100 and 1000 kHz frequencies.

6.9 Energy storage studies

The energy storage performance is evaluated via electrical parameters (P_s , P_r , E_c , E_{max} , E_{st} , E_{re} , η) as explained in Chapter 3. The P - E loops are illustrated in Fig. 6.9 for SPS and CS samples at room temperature and at a frequency of 50 Hz under maximum applied electric field of ~ 50 kV/cm. The nature of the P - E loops conforms to the ferroelectric behaviour of both the samples. The SPS sample exhibits thin P - E loop when compared to that for CS sample. It can be observed that the CS sample exhibits higher polarization values than the SPS specimen. The thin P - E loops and decrease in electrical polarization and hysteresis area for fine-grained PZT ceramics have been reported elsewhere (Buscaglia et al. 2006; Curecheriu et al. 2012; Helbig 2007). However, the hysteresis area of the P - E loops i.e. the energy dissipation for the PZT ceramics is higher in CS samples. Table 6.3 shows the energy storage parameters for SPS and CS samples. It can be observed that the SPS sample exhibits higher energy efficiency almost two times relative to energy efficiency of CS sample which can be attributed to low remnant polarization and the thin nature of P - E loops. (Zheng et al. 2017b) reported similar behaviour for fine grained SPS ceramics and proposed that the suppression of hysteresis behaviour may be due to lower values of remnant polarization caused by clamping of domain wall motion.

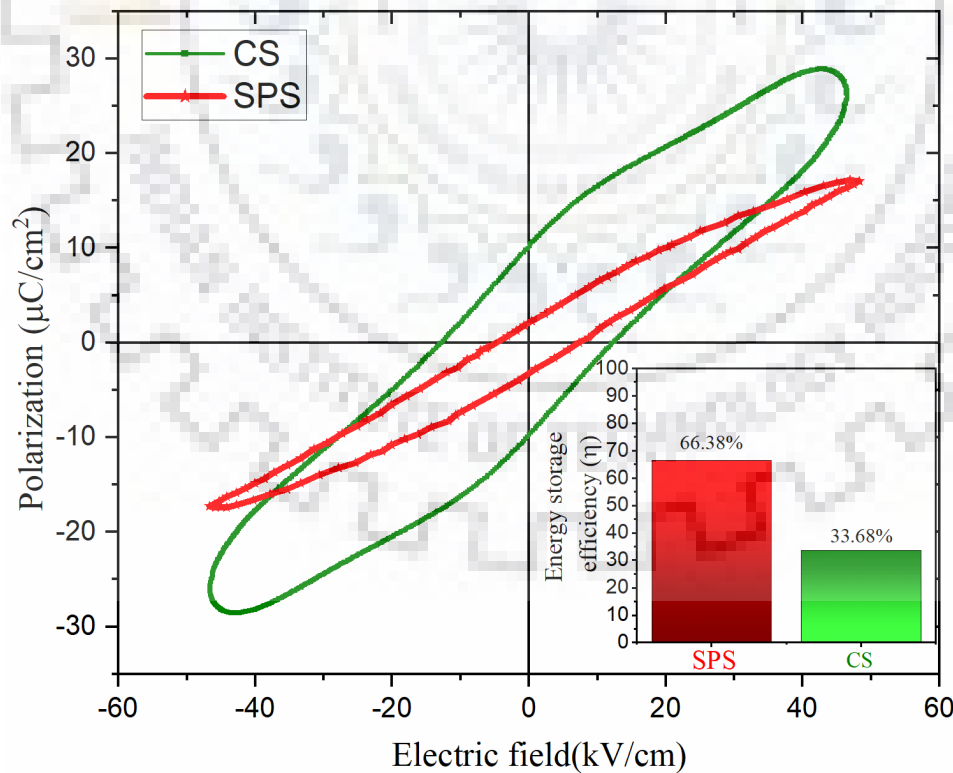


Fig. 6.9 Ferroelectric hysteresis loop of $\text{PbZr}_{0.52}\text{Ti}_{0.48}\text{O}_3$ sintered by SPS and CS method under maximum applied electric field of ~ 50 kV/cm.

Table 6.3 Energy storage parameters for $\text{PbZr}_{0.52}\text{Ti}_{0.48}\text{O}_3$ sintered by SPS and CS method.

	P_s / P_r ($\mu\text{C}/\text{cm}^2$)	E_c / E_{max} (kV/cm)	E.S.D. (J/cm^3)	Recoverable Energy density (J/cm^3)	Efficiency (%)
SPS	17.32/2.68	5.92/46.67	1.13	0.75	66.38
CS	28.745/9.728	12.54/44.57	2.11	0.71	33.68

6.10 Summary

The microstructure, sintering profiles, phase structure, dielectric and energy storage studies were performed for conventional and spark plasma sintered $\text{PbZr}_{0.52}\text{Ti}_{0.48}\text{O}_3$ samples and the results were compared and discussed. The SPS and CS samples were sintered at 900°C and 1200°C respectively. The sintering time was greatly reduced in SPS samples with time period of the order of minutes relative to time requirement of hours for CS samples. The SPS specimen exhibited dense microstructure with grains in nano-scale region whereas for CS specimen, the microstructure shows broad grain size distribution with micro-scale grains. The degree of porosity was greatly reduced for SPS sample as compared to CS sample. The phase composition of SPS specimen was very close to the desired MPB composition as observed by the Rietveld refinement data reported in Chapter 4 which suggests low compositional variation. The high sintering temperature applied in CS sample increases the evaporation of PbO leading to compositional variation. The dielectric constant of SPS sample is higher than that of CS sample which may be attributed to its dense microstructure. The large volume of grain boundaries in SPS sample act as disordered amorphous phase which limits mobility of charge carriers and results in low conductivity compared to CS sample. The temperature dependent permittivity curves reveal two phase transition peaks, one at $\sim 320^\circ\text{C}$ and the other at $T_C \sim 450^\circ\text{C}$. However the broad dielectric peaks observed for CS sample may indicate the compositional fluctuation. The Rietveld refinement data revealed that the SPS specimen has the desired phase composition and constitution which is in agreement with the distinct narrow peaks observed at each phase transition in the temperature dependent permittivity curve. The analysis of P vs E data reveals that the constituting P-E loops are slimmer having lower remnant polarization for SPS samples. In addition, the energy storage efficiency of SPS sample is two times that of CS sample. The underlying reason for such behaviour is due to the suppression of hysteresis behaviour in fine-grained SPS samples due to increased clamping of domain wall motion which leads to lower remnant polarization.

Chapter 7

Dielectric and energy storage studies of 2 mol % La doped $\text{PbZr}_{0.52}\text{Ti}_{0.48}\text{O}_3$ spark plasma sintered ceramics

7.1 Introduction

In this chapter, the phase composition, microstructure, dielectric permittivity and energy storage performance of 2 mol% La doped PZT (52/48) ceramics have been presented. Since La^{3+} is a soft dopant, it is expected to increase the dielectric permittivity of PZT ceramics. The enhanced dielectric permittivity will directly influence the energy storage performance due to the increase in polarization. In addition, the above mentioned properties of PLZT ceramics are compared to that of undoped PZT ceramics.

7.2 Experimental descriptions

The stoichiometric composition of 2 mol % La_2O_3 was added to the raw oxide precursors used to prepare $\text{Pb}(\text{Zr}_{0.52}\text{Ti}_{0.48})\text{O}_3$ ceramic. The resulting mixture was wet milled with ball-to-charge ratio of 10:1 for 8 hours at 450 rpm using toluene as the solvent. The milled powders were filtered out by 600 μm stainless steel mesh as shown in Fig. 7.1. The detailed experimental procedure is already explained in Chapter 3. The stoichiometric equation is given below by assuming that the La^{3+} ions substitute the Pb^{2+} ions on A site (Garg and Goel 1999; Shannigrahi, Choudhary, and Acharya 1999; Sharma et al. 1994):



The milled powders were calcined at 900°C for 4 hours with a heating rate of 5°/min in a muffle furnace to achieve the desired phase composition. The calcination temperature was selected based on the optimization studies conducted for PZT ceramics in Chapter 4. The calcined powders were further grounded and placed inside a graphite die (diameter: 10 mm) for

consolidation by spark plasma sintering technique. The theoretical density of 2 mol % La^{3+} doped PZT ceramics was reported as $\sim 8.06 \text{ g/cm}^3$ (Pdungsap et al. 2005). The SPS profile adopted will be discussed in the upcoming section. Finally, the sintered pellets were annealed at 800°C for 4 hours to eliminate any oxygen deficiencies developed due to the reducing atmosphere adopted in SPS. The flat surfaces of the samples were polished and silver paste was applied for electroding of electrical and ferroelectric measurements.



Fig. 7.1 The ball milled PLZT powders separated from zirconia balls by a $600 \mu\text{m}$ stainless steel mesh.

7.3 SEM analysis of calcined PLZT ceramic

The scanning electron micrograph of the calcined powder of PLZT ceramic is presented in Fig. 7.2. The histogram data was collected by averaging the particle size of over 100 particles. The particles have spherical morphology with particle size ranging between $\sim 142.8 \text{ nm}$ and $\sim 380.95 \text{ nm}$. In comparison, the PZT (52/48) calcined powders exhibited faceted morphology and nearly same range of particle size. Similar reports by (Li 2005) had stated that for calcination temperature $\leq 900^\circ\text{C}$, the average particle size of La doped PZT ceramic was found to be under $\sim 200 \text{ nm}$.

Fig. 7.3 depicts the EDS mapping of calcined PLZT powders for elements Pb, Zr, Ti and La. It can be observed that the oxides are uniformly distributed and mixed homogeneously. This suggests that the milling parameters used for mixing the powders were appropriate.

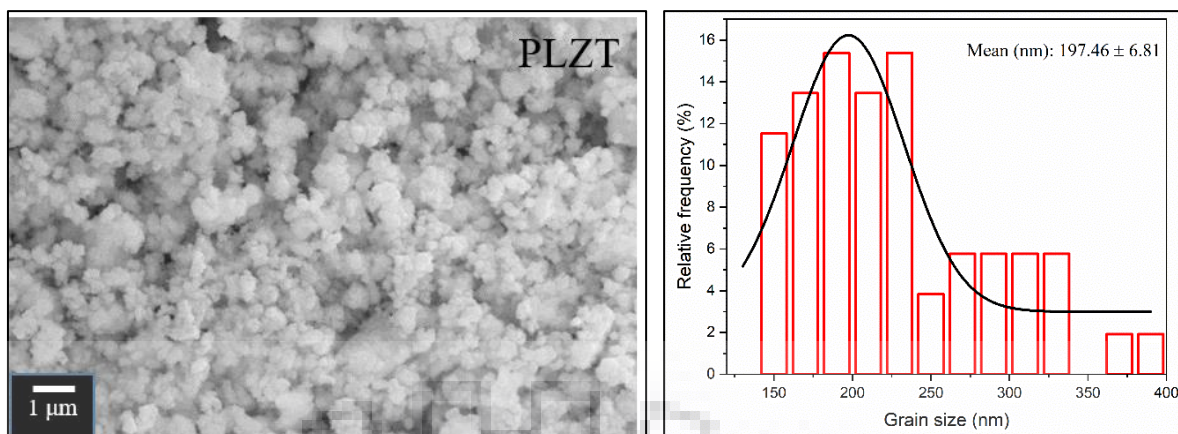


Fig. 7.2 SEM image along with histogram of particle size distribution of PLZT powders calcined at 900°C.

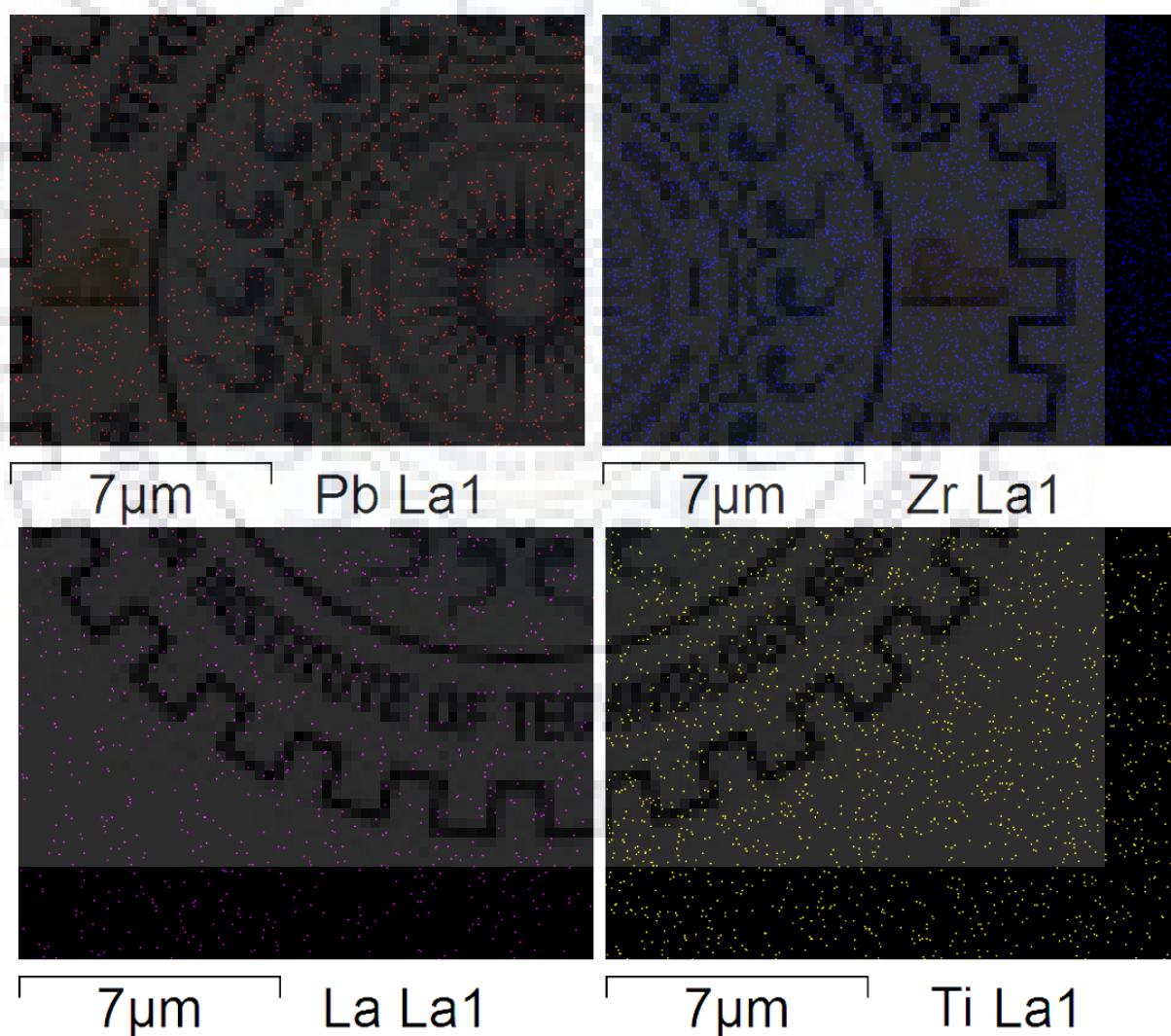


Fig. 7.3 EDS mapping of Pb, Zr, La and Ti elements in the studied PLZT sample.

7.4 X-ray diffraction studies of PLZT ceramic

The XRD patterns of calcined PLZT ceramics in the range $2\theta = 20 - 70^\circ$ are presented in Fig. 7.4. The calcined powders show typical perovskite structure with appropriate peak splitting's observed in the $\{100\}$, $\{110\}$, $\{200\}$, $\{210\}$, $\{211\}$ and $\{220\}$. The XRD patterns reveal tetragonal phase structure with $P4mm$ space group which matches to reference PDF file no. 00-053-0698. The spurious peak near $2\theta \sim 30^\circ$ signifies the presence of pyrochlore impurity phase. An enlarged view of 2θ range $37 - 45^\circ$ is also depicted in Fig. 7.4. The presence of single (111) peak and $\{200\}$ peak splitting also suggests tetragonal phase symmetry of PLZT ceramics. Separate peaks corresponding to lanthanum were not detected in the XRD patterns which suggest substitution of La^{3+} ($\sim 1.15 \text{ \AA}$) to Pb^{2+} (1.32 \AA) positions. The PZT perovskite structure was not affected by the doping of La^{3+} ions, however small peak shifting was observed relative to XRD pattern of undoped PZT (52/48) which suggests occupancy of La^{3+} ions. Therefore, change in lattice parameters and tetragonality of PLZT sample is also expected. On comparison with undoped PZT, the intensity of $\{200\}$ peaks was enhanced for PLZT sample. Similar behaviour was reported elsewhere (Dai, Xu, and Viehland 1996).

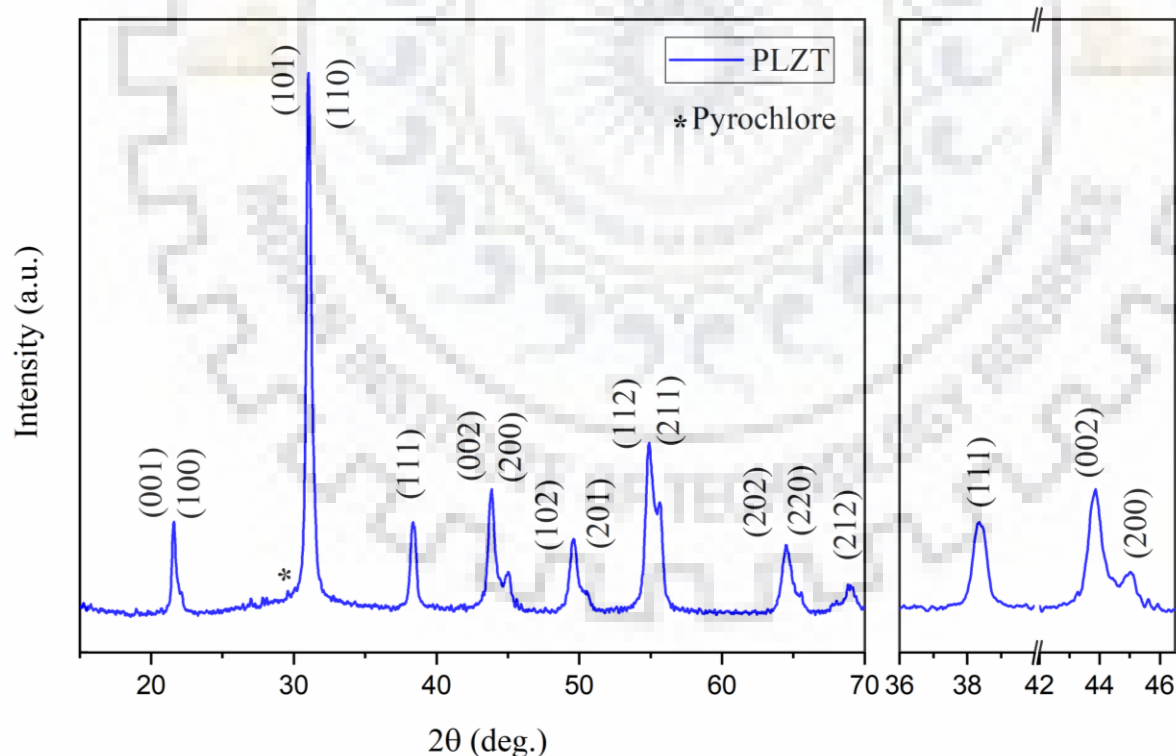


Fig. 7.4 XRD pattern of PLZT powders calcined at 900°C along with magnified views of $\{111\}$ and $\{002\}$ splitting.

7.5 SPS profile adopted for PLZT ceramic

Fig. 7.5 depicts the spark plasma sintering profile adopted for high speed consolidation of PLZT ceramic powders. The target sintering temperature was kept at 900°C for a soaking time of 5 minutes under an axial load of 60 MPa. The detailed explanation of the sintering profile is already explained in Chapter 3. It can be observed that shrinkage takes place over the temperature range 300 - 450°C and remains stable up to 600°C which may be due to evaporation of volatile and gaseous entrapments. Thereafter, the rate of shrinkage remains constant until the target temperature of 900°C is reached. Such consolidation behaviour suggests that the grain boundary and lattice diffusion mechanisms may start to operate above 600°C. During the soaking stage, the displacement curve starts to saturate after ~ 2 min of holding time. Therefore it can be inferred that the sintering temperature of 900°C and a soaking time of 5 min is sufficient for complete consolidation of powders. During the cooling stage, the shrinkage increases further which is due to the closing of isolated pores. The total shrinkage achieved for the PLZT powder was ~ 3.9 mm. It is to be noted that the rate of shrinkage remains independent of the heating rate applied to the sample, whereas the same was not true for SPS profile of PZT (52/48) sample.

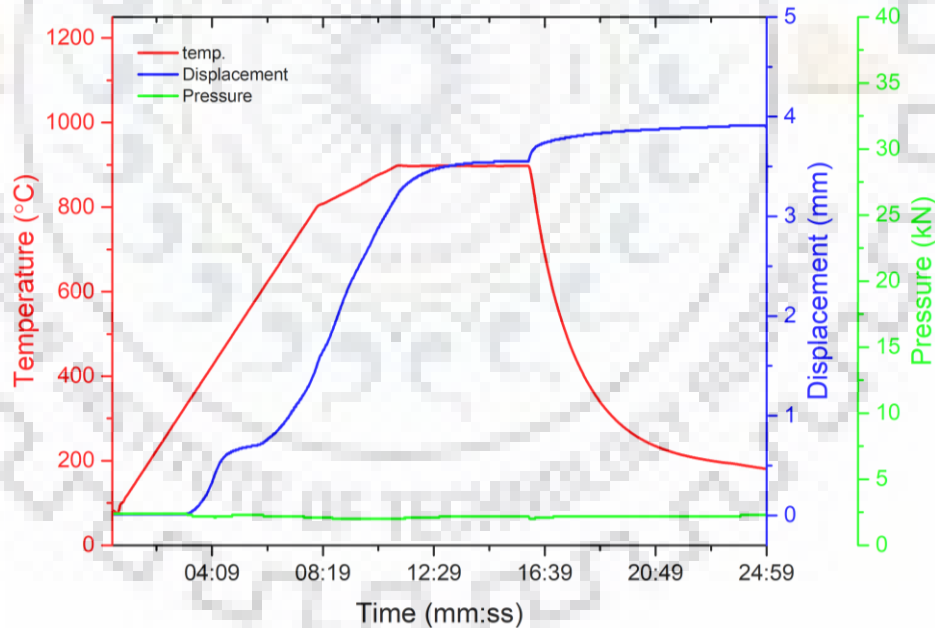


Fig. 7.5 SPS profile adopted for PLZT ceramic sintered at 900°C subjected to a uniaxial load of 60 MPa.

The bulk density of PLZT ceramic was estimated as ~ 7.99 g/cm³ which amounts to ~ 99.13% relative density. Such high density of PLZT ceramics signify the importance of using SPS technique. The spark discharge created between powder particles during sintering cleans the surface of particles and aids in rapid diffusion of material. (Li 2005) also reported more than 99%

theoretical density for PLZT ceramic spark plasma sintered at 900°C with average grain size of ~ 372 nm. In comparison, the conventionally sintered PLZT ceramics exhibited relative density of ~ 95.28% with grain size of ~ 1.3 μm as reported by (Pdungsap et al. 2005).

7.6 SEM analysis of sintered PLZT ceramic

Fig. 7.6 depicts the scanning electron micrograph of cross-sectional area of sintered PLZT specimen. The PLZT ceramic shows largely uniform and homogenous microstructure with grain size in the nanoscale region. The histogram data reveals that the size of fine grains ranges from ~ 5 nm to ~ 30 nm with an average grain size of ~ 12.34 nm. In comparison, the microstructure of PZT (52/48) ceramic also revealed uniform and homogenous distribution of finer grains with an average grain size of ~ 19.41 nm. The reduction in grain size of La doped PZT ceramics has been reported elsewhere for conventionally sintered samples (Pdungsap et al. 2005). The ionic radii of La^{3+} ion is smaller than the Pb^{2+} ion to be replaced, this in turn, decreases the lattice parameters of the doped PZT ceramic. Therefore, the crystallite size is reduced causing reduction in the grain size. The other factor which might be responsible for grain size reduction is the presence of La^{3+} ions at the grain boundary which slows down diffusion through grain boundaries and restricts grain growth (Langman, Runk, and Butler 1973).

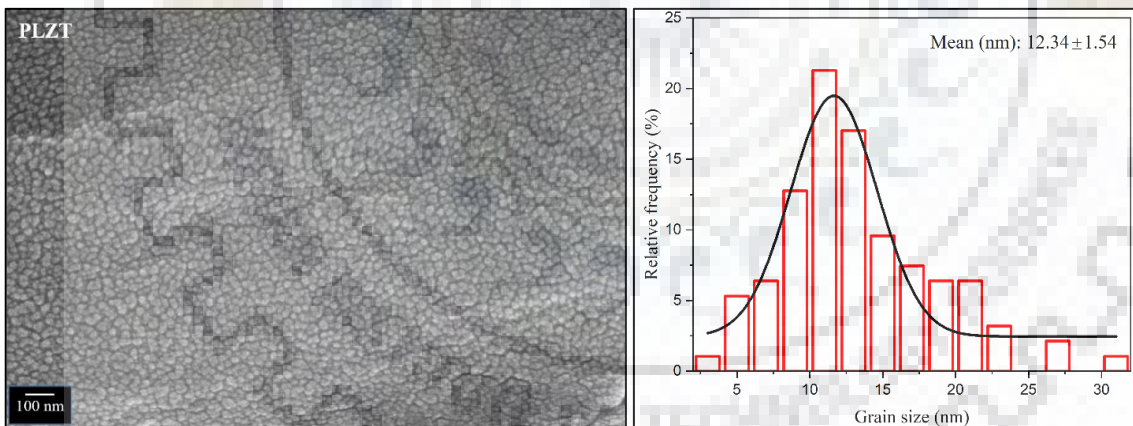


Fig. 7.6 SEM image along with histogram of grain size distribution of PLZT ceramic sintered at 900°C.

7.7 Dielectric studies of PLZT ceramic

The variation of dielectric permittivity and dielectric loss tangent with frequency is shown in Fig. 7.7. The dielectric studies were conducted at frequencies ranging in 42 Hz to 5 MHz at room temperature. It can be observed that the low frequency ϵ_r is high ~ 15,000 for PLZT ceramic as compared to ϵ_r ~ 900 of PZT (52/48) ceramics. This is related to the decrease in tetragonality of

La doped PZT, as the La^{3+} ions decreases spontaneous strain and increases domain wall mobility resulting in high permittivity (Kour et al. 2016). The spark plasma sintered PLZT ceramic shows $\epsilon_r \sim 2312$ at 1 kHz, whereas $\epsilon_r \sim 1424$ at 1 kHz was reported for conventionally sintered PLZT ceramics (Pdungsap et al. 2005). The enhanced permittivity of PLZT ceramics is due to its highly dense fine-grained microstructure. (Mah et al. 2000) also reported similar findings for enhanced dielectric constant. The dielectric loss tangent ($\tan \delta$) remains constant up to 10 kHz and increases when the frequency is increased further. This suggests that there is no dissipation of electrical energy up to 10 kHz as there is no delay in the material response to the applied electric field. Above 10 kHz, $\tan \delta$ increases due to physical processes such as electrical conduction, dielectric relaxation, loss due to delay in material response etc.

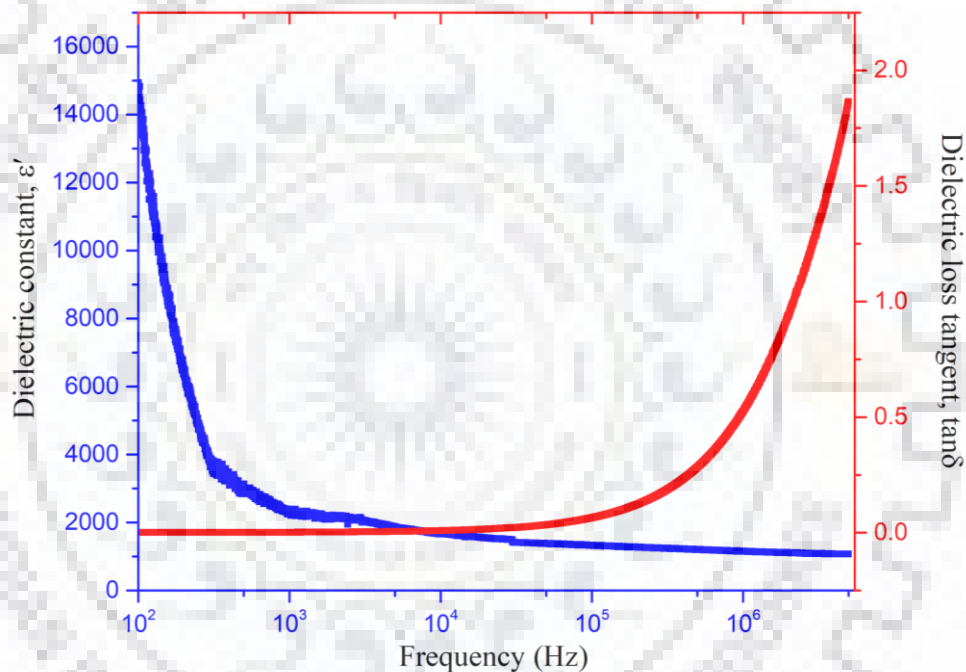


Fig. 7.7 Variation of dielectric constant (ϵ') and dielectric loss tangent ($\tan \delta$) with frequency of PLZT ceramic at room temperature.

The dielectric response to temperature was studied to analyze the ferroelectric-paraelectric transition for the PLZT ceramic. Fig. 7.8(a) depicts the variation of dielectric constant of the material with temperature ranging from 30 to 500°C at different frequencies (100 Hz, 1 kHz, 10 kHz, 100 kHz, 1 MHz and 5 MHz). The dielectric constant of the material increases as the temperature increases and reaches maxima at the Curie temp, $T_C \sim 294^\circ\text{C}$. As discussed in Chapter 4, the T_C of PZT ceramics were reported $\geq 320^\circ\text{C}$, thus, it can be stated that the Curie temp. of PZT ceramics decreases on La^{3+} doping. (Kour et al. 2016; Mah et al. 2000) reported similar findings and stated that the decrease in Curie temperature is due to the degradation in

ferroelectric ordering by La^{3+} on Pb^{2+} sites. Moreover, the maximum value of dielectric constant decreases as the frequency is increased. This is primarily due to polarization mechanisms such as interfacial polarization and space charge polarization being active at low frequencies and contribute to high ϵ_r , however such mechanisms have large relaxation time and cannot follow high frequency electric fields.

The temperature dependence of dielectric loss tangent ($\tan \delta$) for PLZT specimen at different frequencies is depicted in Fig. 7.8(b). The loss tangent curves remain stable for frequencies 100 kHz to 5 MHz, whereas it increases rapidly for other frequencies as temperature increases. The relaxation peak occurs at temperature near $\sim 300^\circ\text{C}$, where dielectric loss tangent values of all samples lie below 0.7. In addition, the loss tangent values are higher for low frequency curves relative to high frequency curves.

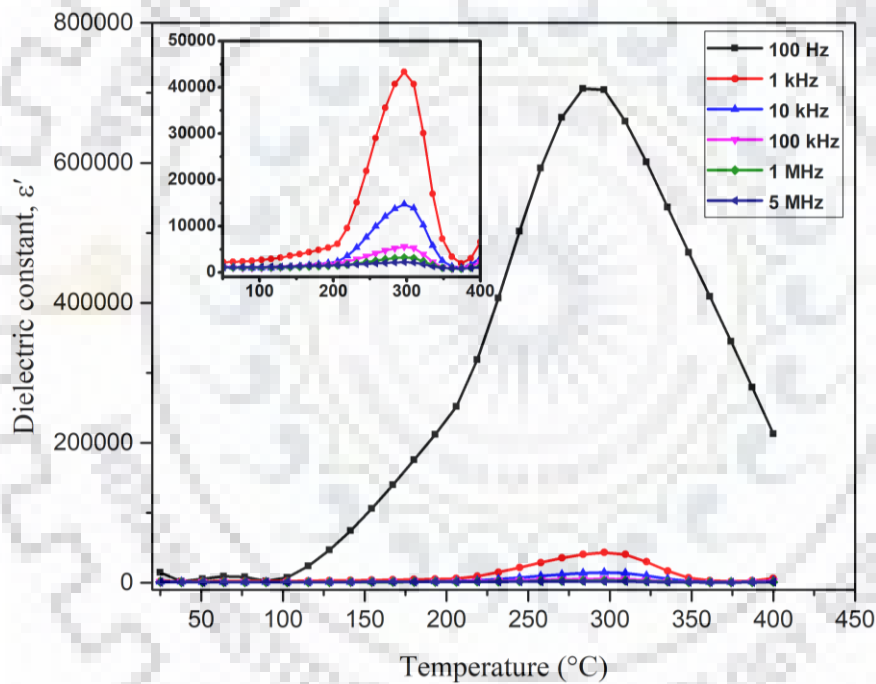


Fig. 7.8 (a) Temperature dependent plots of dielectric constant (ϵ') at selected frequencies of PLZT ceramic. The inset shows the same for frequencies other than 100 Hz.

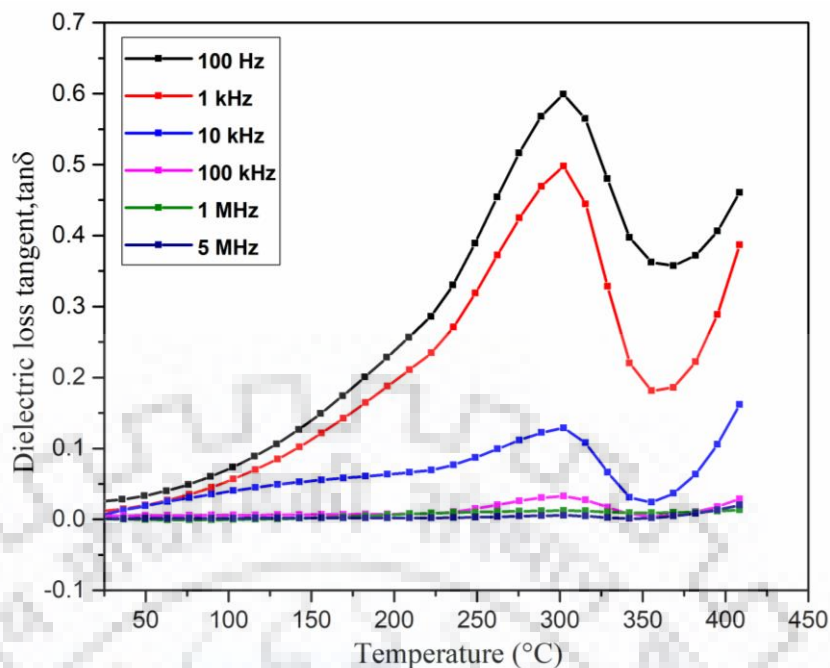


Fig. 7.8 (b) Temperature dependent plots of dielectric loss tangent ($\tan \delta$) at selective frequencies of PLZT ceramic.

7.8 Impedance and modulus spectroscopy studies

Fig. 7.9 illustrates the variation of impedance parameters (Z' and Z'') over the frequency range 50 Hz - 5 MHz at room temperature. It can be observed that Z' remains constant i.e. independent of frequency up to 100 kHz and then readily decreases on further increase of frequency. The high values of Z' at low frequencies are caused due to the polarization mechanisms operative at low frequency namely space charge and interfacial polarization. The fine grained microstructure of PLZT ceramics have large amount of grain boundaries that act as interface between the grains and thereby enhance interfacial polarization leading to higher Z' values. The Z' values of PLZT ceramic are stable up to 1 MHz, whereas the Z' values of undoped PZT (52/48) ceramic decreases by 6 orders up to 1 MHz. The sigmoidal curve in Z' vs $\log f$ plot observed at higher frequencies (> 100 kHz) conforms to the high frequency relaxation peak observed in the Z'' vs $\log f$ plot at ~ 2 MHz.

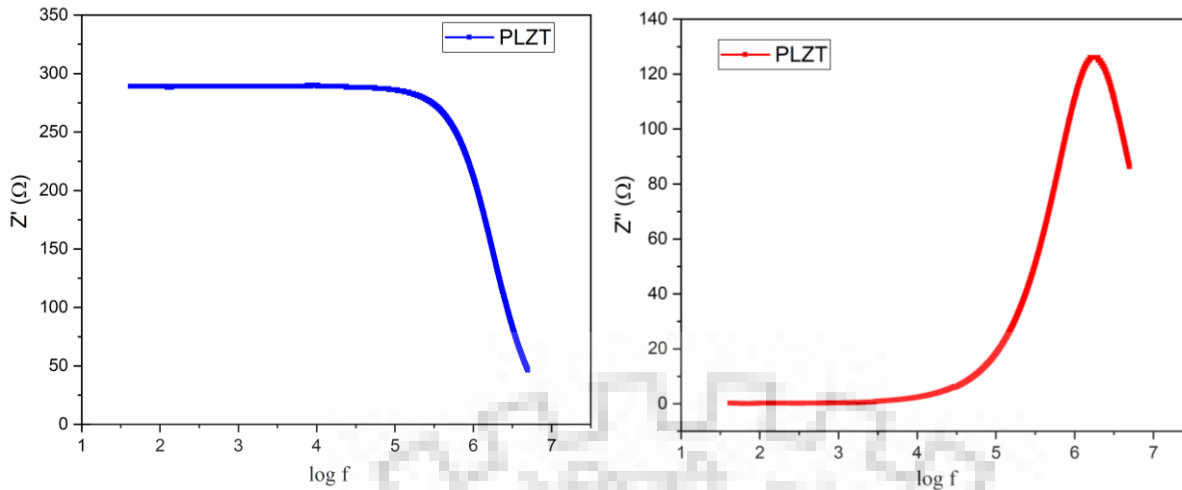


Fig. 7.9 Frequency dependent plots of (a) real part of impedance, Z' (b) imaginary part of impedance, Z'' of PLZT ceramic at room temperature.

Fig. 7.10 depicts the variation of electric modulus parameters (M' and M'') over frequency range 50 Hz – 5 MHz at room temperature. The analysis of modulus plots provides complementary information to data collected by analysis of impedance plots. It can be observed that M' shows very low magnitudes at lower frequency region (< 100 Hz) and then gradually increases up to ~ 2 MHz and then appears to be constant on further increase of frequency. Such sigmoidal curve nature represents relaxation behaviour. The imaginary part of electric modulus (M'') remains stable up to 50 kHz and then rapidly increases and depicts a loss peak at relaxation frequency near ~ 2 MHz. It is to be noted that both the Z'' and M'' plots show relaxation peak at the same frequency near ~ 2 MHz that suggests delocalized relaxation i.e. long range conductivity. In comparison, the high frequency relaxation peak for undoped PZT ceramic is near ~ 100 kHz. The increase in relaxation frequency for La doped PZT ceramic is due to the substitution of La^{3+} ions at A-site that increases domain wall mobility.

The analysis of complex plane spectra gives information about type of relaxation mechanisms in the material. Fig. 7.11 depicts the Nyquist plot and electric modulus spectrum of PLZT ceramic. From the Nyquist plot, it can be observed that there exists a single semicircle, however it does not appear to be a perfect semi-circle as the centre lies below the Z' axis that suggests spread of relaxation times. Moreover, it is difficult to detect the contribution of grains at high frequency. The relaxation time from the Nyquist plot is estimated to be $\tau = 9.15 \times 10^{-8}$ s ($f_{max} = 1.74 \times 10^6$ Hz).

On the other hand, the electric modulus spectrum highlights the contribution from the least capacitance electro-active region. It can be observed that the deconvolution of the arc is

necessary since the contributions of grain and grain boundary are not distinctly observed. Both electric modulus spectrum and Nyquist plots depict single semi-circle that combines electrical relaxation processes of bulk and grain boundary. The variation of these plots with temperature helps to analyze and deconvolute the different contributions. The relaxation time from electric modulus plot is also estimated to be, $\tau = 6.69 \times 10^{-8}$ s ($f_{max} = 2.38 \times 10^6$ Hz).

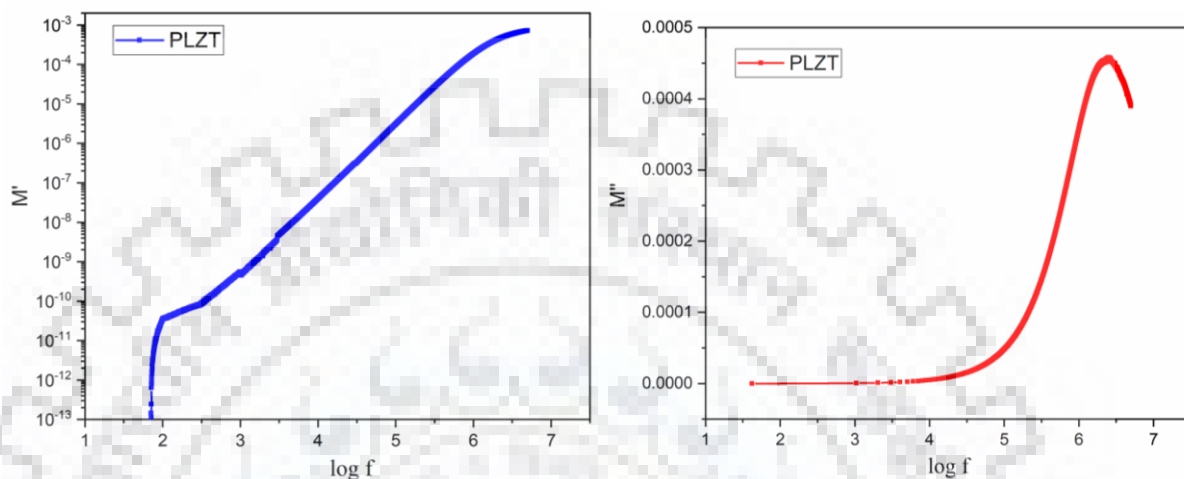


Fig. 7.10 Frequency dependent plots of (a) real part of complex electric modulus, M' (b) imaginary part of complex electric modulus, M'' of PLZT ceramic at room temperature.

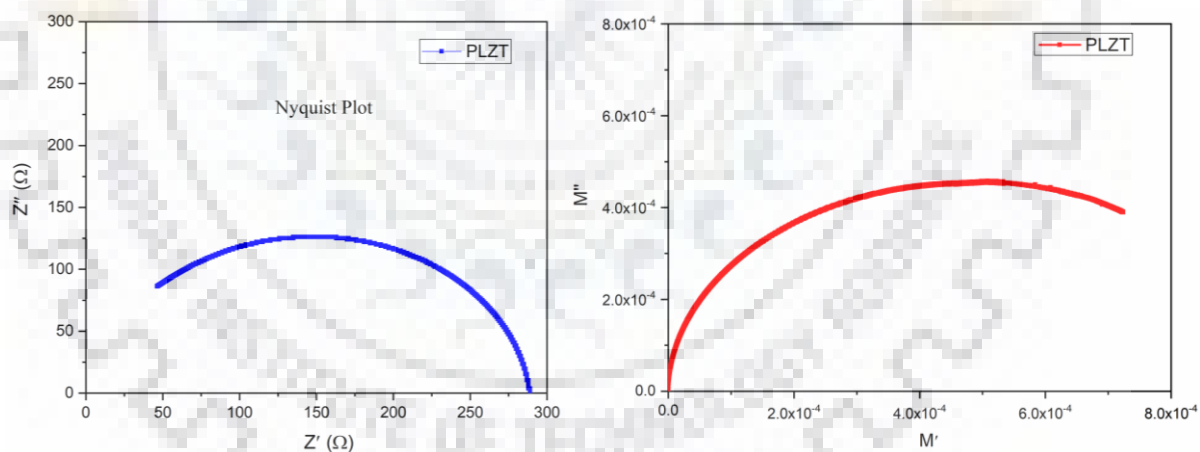


Fig. 7.11 Complex impedance and complex modulus spectra of PLZT ceramic at room temperature.

The analysis of impedance and modulus functions with temperature provides information about the electrical relaxation mechanisms that are temperature dependent. In addition, it also helps to separate electrical contributions from bulk and grain boundary regions. Fig. 7.12 shows the variation of Z' and Z'' with frequency at different temperatures (100°C, 200°C, 300°C, 350°C and 400°C). The frequency independent behaviour of Z' at lower frequency region has already been explained in the sections above. In Fig. 7.12, the Z' values show temperature dependent

behaviour, in which Z' decreases as the temperature is increased from 100 - 350°C. However, the magnitude of Z' is considerably higher at temperature of 400°C. This may be attributed to the ferroelectric-paraelectric transition of the material. The Z' curves appear to merge at high frequencies (~ 5 MHz) for all temperatures. The analysis of Z'' vs frequency curves at different temperatures reveals that there is a wider distribution of relaxation times as shown by the broadening of peaks. At lower temperatures, Z'' falls rapidly beyond the relaxation frequency which suggests that the motion of charge carriers is restricted. Moreover, it can be observed that the relaxation frequency shifts to the higher value as the temperature is increased. Such behaviour suggests distinct or well-defined relaxation mechanism that operates over large range of frequencies. However, the trend of relaxation peak changes for 400°C. The relaxation time can be calculated at that frequency where Z'' maxima occurs for different temperatures. The values of relaxation time estimated from impedance plot ($\ln(\tau_z)$) are plotted against $1/T$ and shown in Fig. 7.12(c).

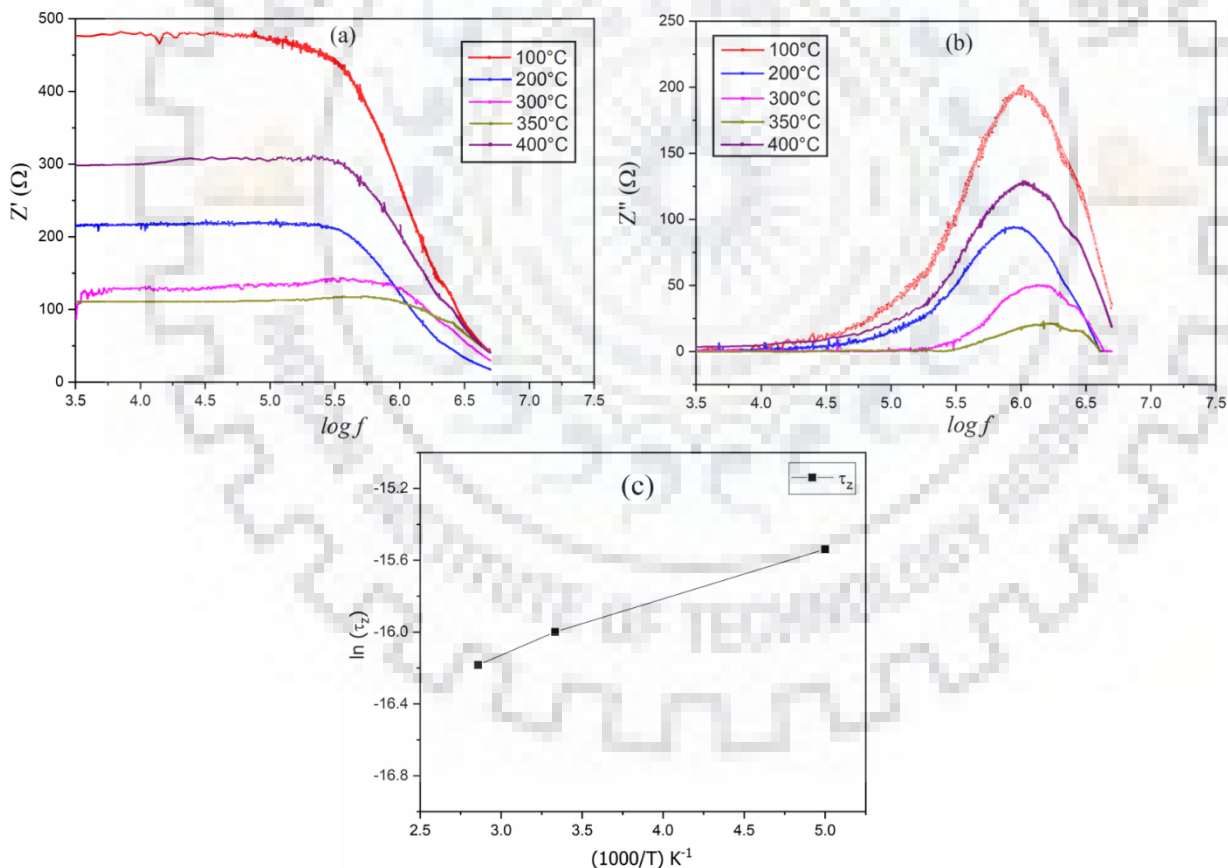


Fig. 7.12 (a) Frequency dependent plots of real part of impedance, Z' (b) frequency dependent plots of imaginary part of impedance, Z'' at 100°C, 200°C, 300°C, 350°C and 400°C temperatures; (c) variation of relaxation time estimated from impedance plot, $\ln(\tau_z)$ as a function of inverse of absolute temperature of $(\text{Pb}_{0.98}\text{La}_{0.02})(\text{Zr}_{0.52}\text{Ti}_{0.48})\text{O}_3$.

Fig. 7.13 depicts the variation of electrical modulus parameters (M' and M'') with frequency at different temperatures. It can be observed that M' increases as the temperature increases in the higher frequency region (> 100 kHz) for PLZT ceramic. Moreover, the dispersion in M' curves with frequency suggests short range mobility of charge carriers (Khatri, Behera, and Choudhary 2009). The M'' vs $\log f$ curves show relaxation peak near ~ 1 MHz for all temperatures. As the temperature increases, the relaxation peak in the modulus plot shifts to higher frequencies, whereas the trend reverses at 400°C . The relaxation frequencies at different temperatures are noted and the corresponding τ values are calculated. The $\log \tau_m$ vs $1/T$ plot as shown in Fig. 7.13(c) follows the Arrhenius equation, $\tau = \tau_0 e^{-E_a/k_B T}$ (Hodge, Ingram, and West 1976). (Prasad, Sekhar, and Kumar 2008) also observed that M'' peaks are widely distributed in the frequency region. Such behaviour represents relaxor like nature which is typical for ABO_3 type structure of materials. It is to be noted that the relaxation frequency in both Z'' and M'' vs freq. curves lie in the same frequency region that suggests delocalized relaxation i.e. long range conductivity.

The Nyquist plots and the complex electrical modulus spectra for different temperatures are presented in Fig. 7.14. The Nyquist plot clearly indicates two depressed semi-circles for all the temperatures shown. The low frequency arc (grain boundary contribution) is completely visible compared to the high frequency arc (bulk contribution) in the Nyquist plot. The presence of electrode-specimen contribution could not be detected which signifies absence of any electrode polarization. The depressed nature of the arcs suggest distribution of relaxation times and the semi-circular arc cannot be fitted with an ideal capacitor. Instead, a constant phase element (CPE) is used to identify the non-Debye behavior. As the temperature increases, the diameter of the semi-circular arc decreases which signifies negative temperature coefficient of resistance (NTCR). Such temperature dependent behaviour is typical of semi-conductor materials. It can be noticed from the figure that the resistance of grain boundaries are much higher compared to grains. This is expected as the fine grained microstructure of PLZT ceramics have a large volume of low permittivity grain boundaries. The capacitance (C_{gb}) and resistance (R_{gb}) values corresponding to grain boundary contribution are calculated from the Nyquist plots and are presented in Table 7.1. It can be observed that the grain boundaries are more resistive than the grains. As the temperature increases, the resistance of grain boundary decreases suggesting an activated conduction mechanism. On the other hand, the complex electric modulus spectra show a single semi-circular arc and the separation of grain and grain boundary contributions is not visible. The complex electrical modulus spectrum shows spur or inclined like behaviour ($<$

60°) at low frequencies which signifies hopping of mobile charge carriers i.e. localized relaxation (Prasad, Sekhar, and Kumar 2008).

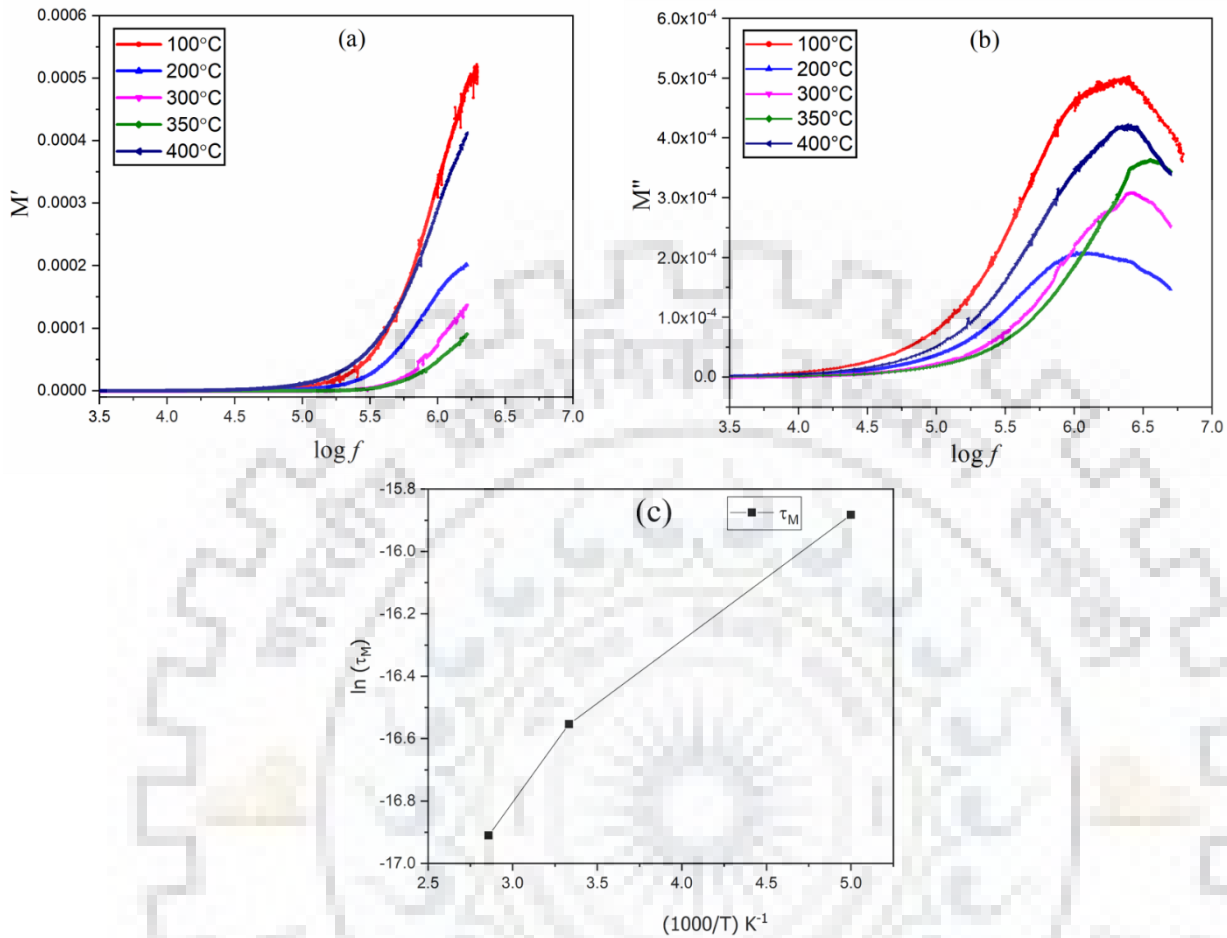


Fig. 7.13 (a) Frequency dependent plots of real part of electric modulus, M' (b) frequency dependent plots of imaginary part of electrical modulus, M'' at 100°C, 200°C, 300°C, 350°C and 400°C temperatures; (c) variation of relaxation time estimated from modulus plot, $\ln(\tau_m)$ as a function of inverse of absolute temperature of $(\text{Pb}_{0.98}\text{La}_{0.02})(\text{Zr}_{0.52}\text{Ti}_{0.48})\text{O}_3$.

Table 7.1 Calculated values of τ_{gb} , R_g , R_{gb} and C_{gb} at selective temperatures of PLZT specimen.

Temp. (°C)	τ_{gb} (s)	R_g (Ω)	R_{gb} (Ω)	C_{gb} (F)
100	1.54×10^{-7}	39.12	440.66	3.49×10^{-10}
200	1.73×10^{-7}	25.66	199.07	8.69×10^{-10}
300	1.13×10^{-7}	37.19	106.05	10.66×10^{-10}
350	0.85×10^{-7}	52.51	65.7	12.94×10^{-10}
400	1.49×10^{-7}	39.35	270.8	5.5×10^{-10}

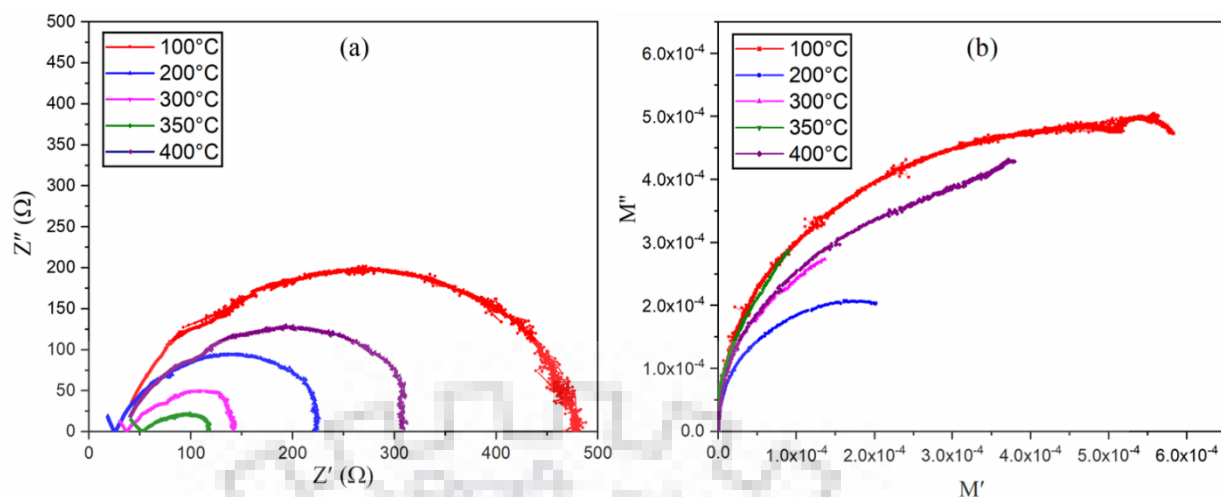


Fig. 7.14 (a) Complex impedance and (b) complex modulus plane plots of $(\text{Pb}_{0.98}\text{La}_{0.02})(\text{Zr}_{0.52}\text{Ti}_{0.48})\text{O}_3$ ceramic measured at 100°C, 200°C, 300°C, 350°C and 400°C temperatures.

7.9 Conductivity studies

The variation of AC conductivity (σ_{ac}) over the frequency range of 42 Hz - 5 MHz at different temperatures (100°C, 200°C, 300°C, 350°C and 400°C) is depicted in Fig. 7.15. The conductivity curves show frequency independent behaviour up to ~ 1 MHz. This signifies that the dc conductivity dominates over the respective frequency range. The trend in conductivity curves is in agreement with the impedance and modulus curves that show relaxation frequency nearly at 1 MHz. The characteristic feature of switching from frequency independent behaviour to frequency dependent behaviour is typical for systems that have more disordered regions or phase transitions or systems with inherent defects (Prasad, Sekhar, and Kumar 2008). On increasing the frequency further, the conductivity sharply increases. Generally the dispersion of conductivity with frequency follows the universal power law (Dutta and Choudhary 2008) at high frequencies. As the temperature increases, the conductivity increases as the mobile charge carriers get sufficient energy to cross their potential barriers. The difference in conductivity values at the lower frequency region at different temperatures suggests that the mobile charge carriers can perform hopping at neighbouring sites. Moreover, the merging of the conductivity curves for all temperatures at high frequencies signifies that such behaviour supports long range conductivity in the high frequency region. In addition, the slope of the conductivity curves are different for different temperatures at high frequency region which certainly confirms the classical hopping mechanism. Therefore, it can be stated that the conduction is a thermally activated process.

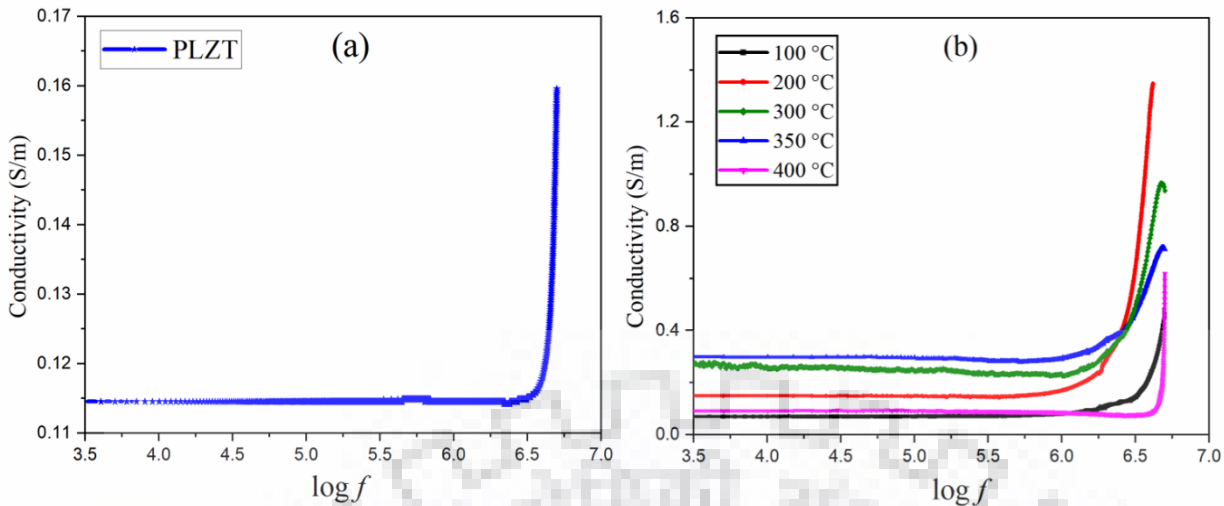


Fig. 7.15 Frequency dependent conductivity plots of PLZT ceramics at (a) room temperature and (b) 100, 200, 300, 350, 400 °C temperatures.

7.10 Energy storage studies of PLZT ceramic

The analysis of ferroelectric properties of PLZT ceramic was evaluated by studying the P - E loop under an applied maximum electric field of ~ 45 kV/cm. The well-defined loops of PLZT ceramics confirms the ferroelectric nature of the sample. The substitution of La^{3+} ions to the Pb^{2+} ions at A-site creates multi domain polarization systems. As a result, higher polarization values are expected for La doped PZT ceramics. The PZT (52/48) ceramics exhibited P_s ($17.32 \mu\text{C}/\text{cm}^2$) and P_r ($2.67 \mu\text{C}/\text{cm}^2$) as reported in Chapter 5. In comparison, both the saturation and remnant polarization are largely enhanced for PLZT ceramics. The remnant polarization of PLZT ceramics is higher than two times the remnant polarization of PZT (52/48) ceramics which suggests the diffusivity of La^{3+} ions (Kour et al. 2016). Therefore, it can be stated that the ferroelectric material gets softer on doping with La^{3+} ions. It is to be noted that though the grain size is reduced on doping with La^{3+} ions, this does not seem to affect the ferroelectric properties of the material. The energy storage density is a measure of the capability of storing energy in the material. The polarization (P_r , P_s) and electric field (E_c , E_{max}) parameters of doped and undoped PZT are depicted in Table 7.2. In addition, the energy storage parameters (E_{st} , E_{re} , η) are also tabulated. On comparison to undoped PZT, the PLZT ceramic exhibits lower energy efficiency due to higher hysteresis. The remnant polarization and coercive field also show higher values for PLZT ceramics over undoped PZT ceramics which might be due to the decrease in grain size (Mah et al. 2000).

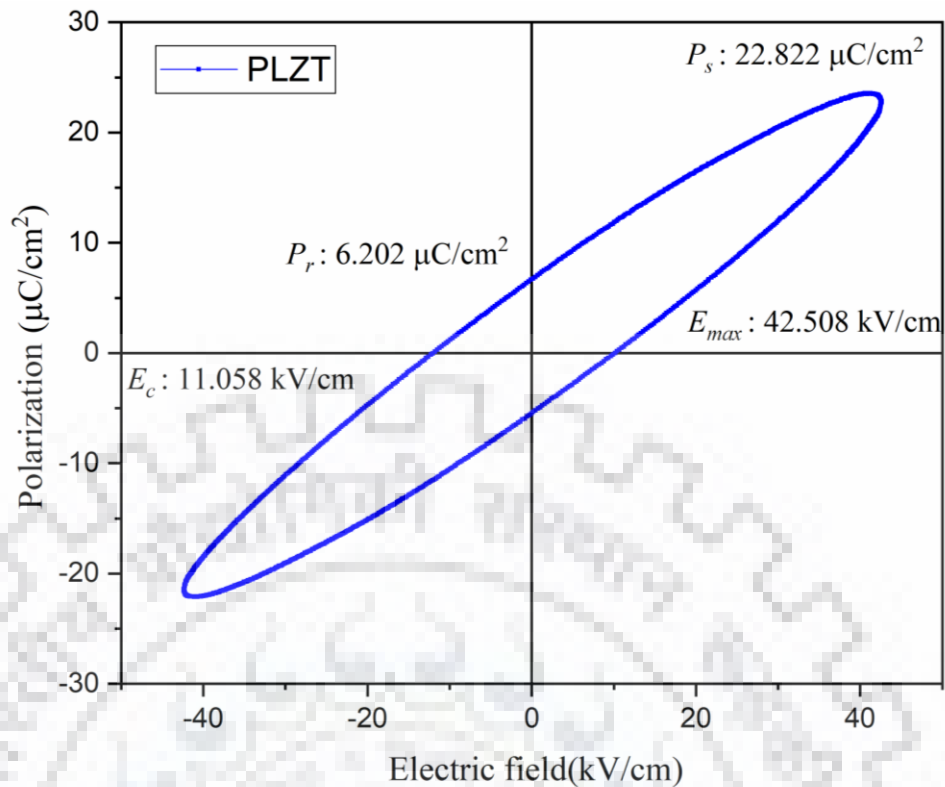


Fig. 7.16 Ferroelectric hysteresis loops of PLZT sample under an applied maximum electric field of ~45 kV/cm at room temperature.

Table 7.2 Energy storage parameters of PLZT sample compared to undoped PZT.

Sample	P_s/P_r ($\mu\text{C}/\text{cm}^2$)	E_c/E_{max} (kV/cm)	E.S.D. (J/cm^3)	Recoverable Energy density (J/cm^3)	Energy efficiency (%)
PLZT	22.82/6.20	11.06/42.51	0.66	0.30	45.45
PZT (52/48)	17.32/2.67	5.92/46.67	1.13	0.75	66.38

7.11 Summary

The effect of doping with La^{3+} ions in spark plasma sintered PZT ceramics on phase constitution, microstructure, dielectric and energy storage properties was investigated. In addition, the different relaxation mechanisms in the material were analyzed by means of complex impedance and electrical modulus spectroscopy. The particle size of calcined PLZT powders was about ~ 200 nm similar to undoped PZT powders. The analysis of XRD patterns of PLZT ceramics revealed peak shift suggesting diffusion of La^{3+} ions and change in lattice parameters. The phase has tetragonal perovskite structure with $P4mm$ space group. The spark plasma sintering profile adopted was similar to undoped PZT ceramics and the sintered specimen developed > 99%

relative density. The analysis of microstructure revealed decrease in grain size of PLZT ceramics over PZT ceramics due to smaller ionic radii of La^{3+} ions. The room temperature dielectric constant of SPS ceramics was significantly higher than the conventional counterparts reported. Moreover, the PLZT ceramics exhibited higher dielectric permittivity than the PZT ceramics investigated in Chapter 4 due to enhanced domain wall motion. The ϵ_r vs. T curves are more broadened compared to undoped ceramics which suggests increased diffusivity of La^{3+} ions. The impedance and modulus studies confirm the presence of grain and grain boundary relaxation mechanisms in the PLZT ceramics where the bulk resistance of grain boundaries are higher. Impedance analysis reveals increase in relaxation frequency of PLZT ceramics which is due to substitution of La^{3+} ions at A site of PZT. The relaxation frequency shifts to higher frequencies on increase in temperature suggesting well defined relaxation mechanism that operate over large frequencies. The imaginary component of complex impedance and modulus lie in the same frequency region suggesting delocalized relaxation. The deconvolution of different relaxation mechanisms are visible in the Nyquist plots and are used to calculate the resistance and relaxation time for bulk and grain boundary contributions. The depressed nature of semi-circular arcs suggest spread of relaxation times and the diameter decreases on increase in temperature suggesting NTCR effect. The conductivity profiles show relaxation at similar frequencies as reported for impedance and modulus curves. Low frequency conductivity behaviour suggests hopping of charge carriers whereas long range conductivity is revealed at high frequency region. The energy storage studies of PLZT ceramics has revealed higher remnant polarization and coercive field. The saturation polarization has increased for PLZT ceramics, however, the energy efficiency is decreased by 20% due to high hysteresis in PLZT ceramics.

Chapter 8

Dielectric characterization and energy storage performance of Cr (0.2, 0.4, 0.6, 0.8 wt.%) doped $\text{PbZr}_{0.52}\text{Ti}_{0.48}\text{O}_3$ ceramics

8.1 Introduction

In this chapter, the microstructure, phase analysis, impedance and modulus spectroscopy, dielectric and energy storage characteristics of Cr doped (0.2, 0.4, 0.6, 0.8 wt.%) PZT (52/48) ceramics have been presented. The effect of dopants (acceptor dopants) such as Al^{3+} , Bi^{3+} , Fe^{3+} , Na^+ etc. that have lower valency than that of the B-site ion in PZT ceramics on dielectric property has been reported in the past (Atkin, Holman, and Fulrath 1971; Rukmini, Choudhary, and Rao 1998). However, the behaviour of Cr dopant is unique, as it is believed that it acts as a donor as well as an acceptor ion primarily due to its multi valent nature. (Nejezchleb 1980b) reported that the trivalent Cr ions oxidise into hexavalent Cr ions during PZT material synthesis. In addition, the author stated that the dielectric properties of Cr doped PZT ceramics depend on the oxygen partial pressure during sintering process. Therefore, the present chapter emphasizes on the effect of spark plasma sintering technique on the functional properties of Cr doped PZT ceramics.

8.2 Experimental descriptions

The $\text{PbZr}_{0.52}\text{Ti}_{0.48}\text{O}_3 + x \text{ wt.} \% \text{Cr}_2\text{O}_3$ ($x = 0, 0.2, 0.4, 0.6$ and $0.8 \text{ wt.} \%$) ceramics were synthesized by solid state route by mixing the different oxides of raw materials. The oxide mixture was wet milled (toluene as solvent) at a ball to charge ratio of 10:1 for 8 hours at 450 RPM. The milled powder slurry was dried in an oven at 100°C and re-grounded prior to calcination. The grounded powders were calcined at 900°C for 4 hours in a muffle furnace with heating rate of $5^\circ/\text{min}$ to achieve the desired perovskite phase. The calcined powders were sintered by SPS process which will be discussed in the upcoming section in detail. The sintered powders were annealed at 800°C to eliminate any carbon residue developed by the graphite foil enclosure over the samples used

in SPS. The annealed pellets were fine polished so as to reduce the thickness of the sample to ~ 1 mm and silver electroded for dielectric and energy storage studies.

8.3 SEM analysis of calcined Cr doped PZT ceramics

Fig. 8.1 depicts the scanning electron micrographs of Cr doped PZT ceramics that are calcined at 900°C. It can be observed that the particles are of largely faceted type similar to undoped PZT particles shown in Chapter 4. However, as the Cr content is increased to 0.8 wt.%, the particles tend to acquire spherical morphology. The particle size lies in the range 200-500 nm for 0.2, 0.4, 0.6 wt.% Cr doped PZT ceramics, whereas for 0.8 wt.% Cr doped PZT ceramics, the particle size range becomes higher i.e. 400 - 800 nm. In comparison, the particle size of undoped PZT (< 350 nm) and La doped PZT (< 200 nm) ceramics are smaller. Moreover, the particle size distribution of Cr doped PZT ceramics is uniform and significant agglomeration for all the samples can be noticed.

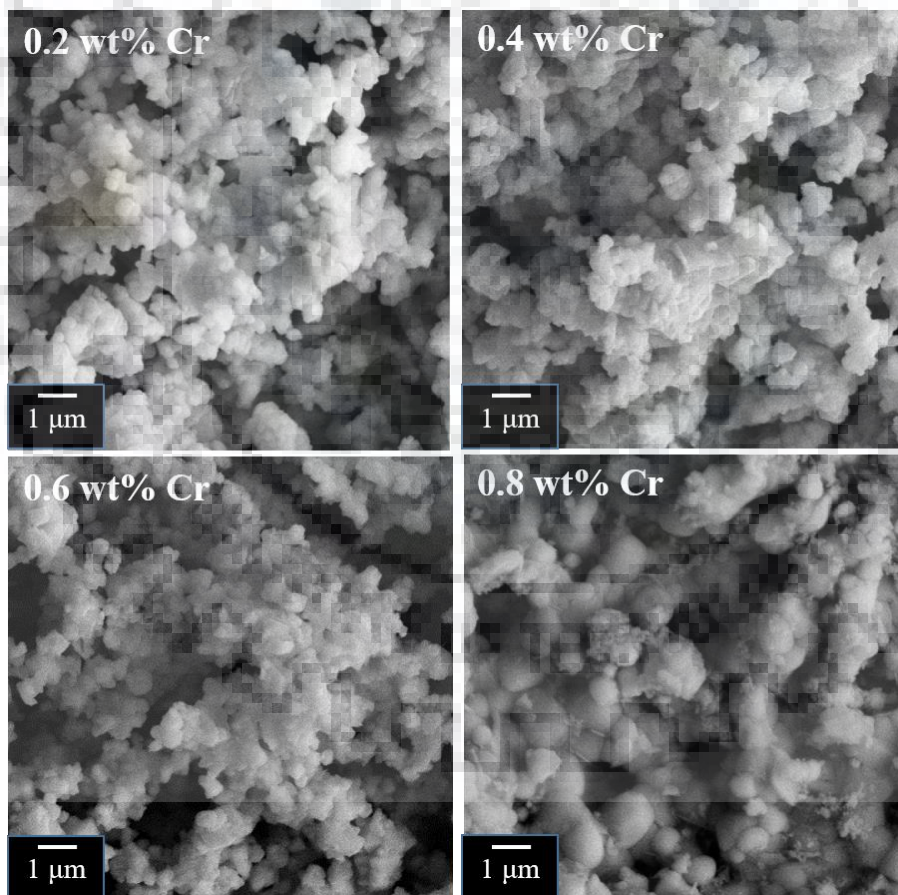


Fig. 8.1 Scanning electron micrographs of $\text{PbZr}_{0.52}\text{Ti}_{0.48}\text{O}_3 - x\text{Cr}$ powders calcined at 900°C.

The Energy-dispersive X-ray spectroscopy (EDS) spectra along with its elemental composition for Cr doped PZT ceramics are shown in Fig. 8.2. The different elements (Pb, Zr, Ti, and O) that constitute the sample composition are detected and their respective atomic percent

values are also shown. The (Zr/Ti) atomic ratio are calculated to be near the desired morphotropic phase boundary composition of PZT. Moreover, the presence of Cr can also be detected and its atomic percent values are found to increase with the increase in dopant concentration as expected.

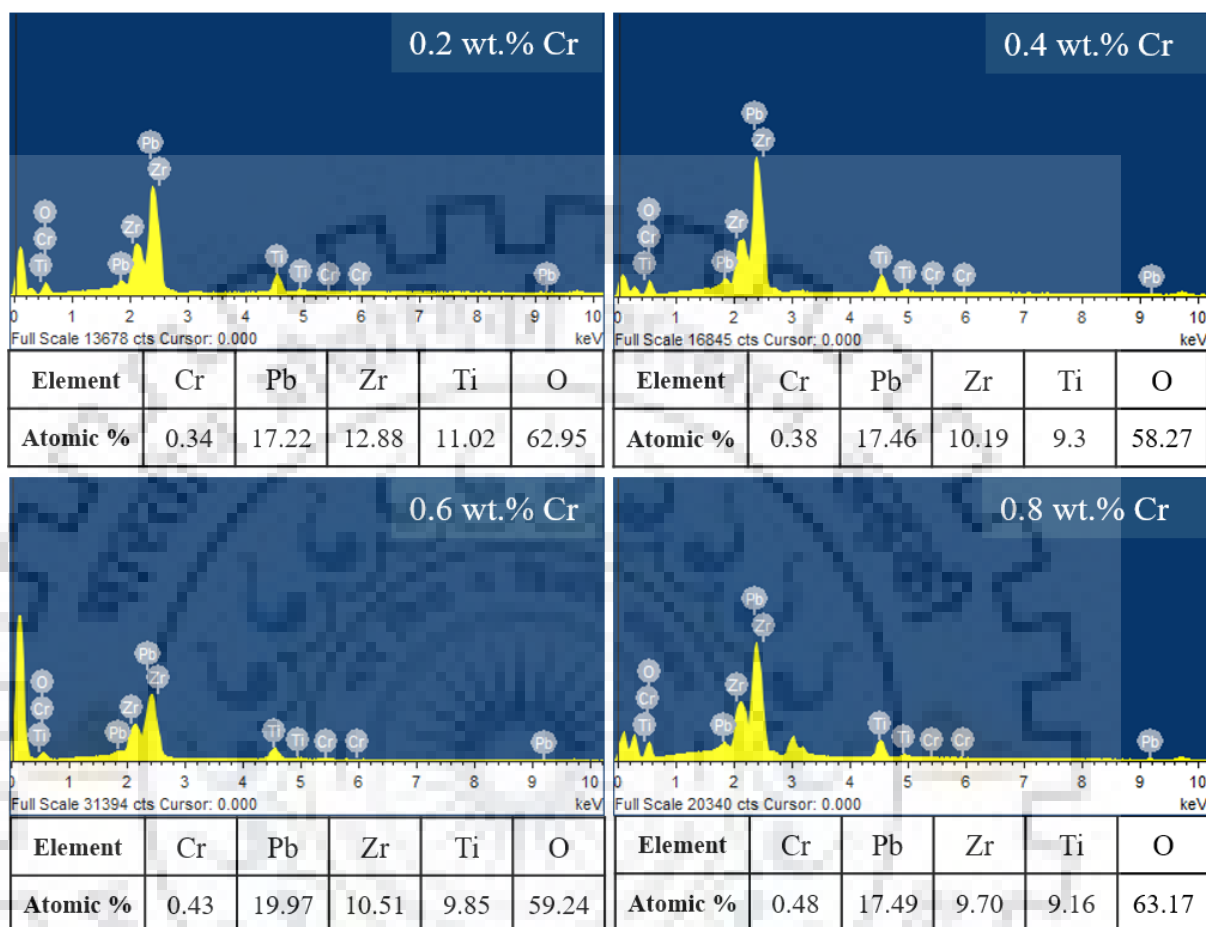


Fig. 8.2 EDS graphs of $\text{PbZr}_{0.52}\text{Ti}_{0.48}\text{O}_3 - x\text{Cr}$ powders calcined at 900°C .

8.4 XRD analysis of calcined Cr doped PZT ceramics

Fig. 8.3 depicts the XRD patterns of Cr doped PZT ceramics calcined at 900°C . The peak splitting's corresponding to the $\{100\}$, $\{110\}$, $\{200\}$, $\{210\}$, $\{211\}$ and $\{220\}$ planes indicate the presence of perovskite structure with tetragonal crystal system having $P4mm$ space group. The XRD patterns match the reference PDF file no. 04-011-8847. It can be observed that the doping of Cr ions has not distorted the perovskite structure and presence of any separate peaks corresponding to chromium cannot be identified. As a result, it can be inferred qualitatively that the dopant forms solid solution in PZT and the lattice parameters remain unchanged. However, the increase in tetragonality can be readily noticed as the amount of Cr dopant increases in PZT ceramics as shown in the enlarged view of 2θ range $42 - 47^\circ$. The presence of pyrochlore phase can be identified by its characteristic peak near $2\theta = 26.5^\circ$. In addition, the presence of spurious peak near $2\theta = 30^\circ$ is attributed to baddeleyite-type ZrO_2 phase (marked by '*' symbol in Fig.

8.3). The presence of these phases have also been reported by (Uchida and Ikeda 1967) in Cr doped MPB PZT compositions.

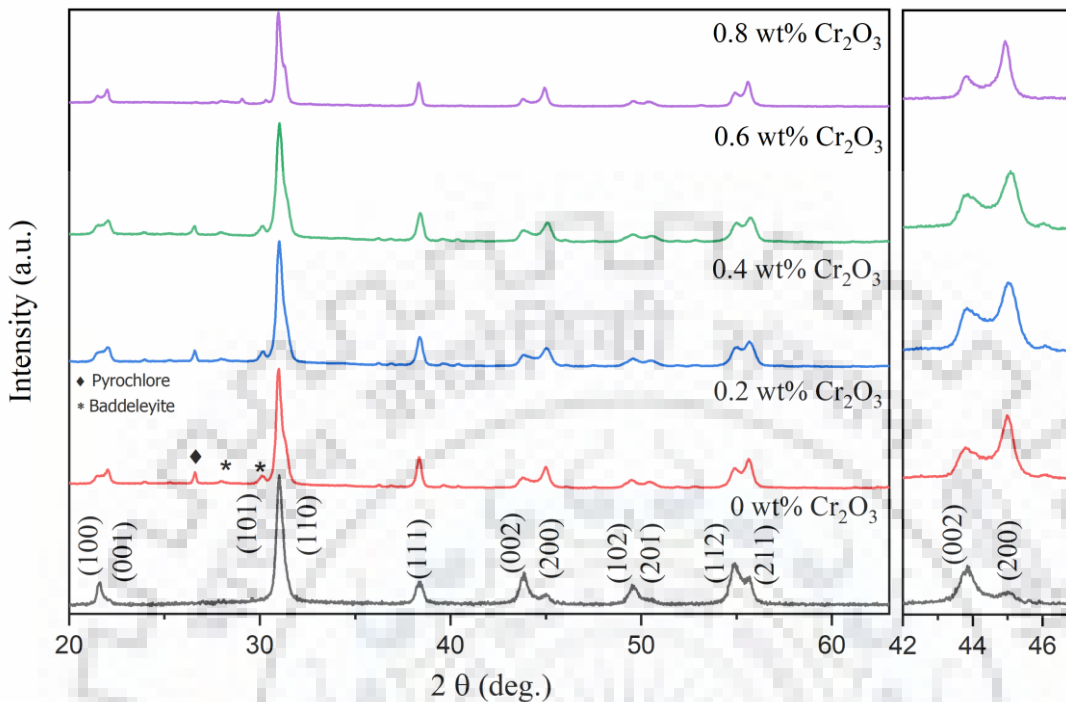


Fig. 8.3 XRD patterns of $\text{PbZr}_{0.52}\text{Ti}_{0.48}\text{O}_3 - x\text{Cr}$ powders for $x = 0, 0.2, 0.4, 0.6$ and 0.8 calcined at 900°C .

8.5 SPS profile employed for Cr doped PZT ceramics

Fig. 8.4 depicts the spark plasma sintering profiles adopted for Cr doped samples. The samples were sintered at 900°C with a soaking time of 5 min. The samples were heated at $100^\circ\text{C}/\text{min}$ up to 800°C . Thereafter, the heating rate was reduced to $33^\circ\text{C}/\text{min}$ up to the sintering temperature to allow sufficient time for atomic diffusion. The calcined powders were subjected to a minimum axial load until the target sintering temperature of 900°C was achieved. The axial load was increased to 60 MPa at the start of soaking stage and kept constant until the sample was cooled down to room temperature. The different steps in the temperature and pressure profiles of SPS and their effects on sintering have been explained in detail in Chapter 3. The displacement profile reflects the net compression (mm) of the sample during sintering. It can be observed that the densifying diffusion mechanisms (grain boundary and lattice) activate above $\sim 550^\circ\text{C}$ for all Cr_2O_3 doped PZT specimens. Moreover, it can be noticed that the displacement profile flattens near the completion of soaking stage, which suggests that the sintering parameters used are adequate for good consolidation of powders.

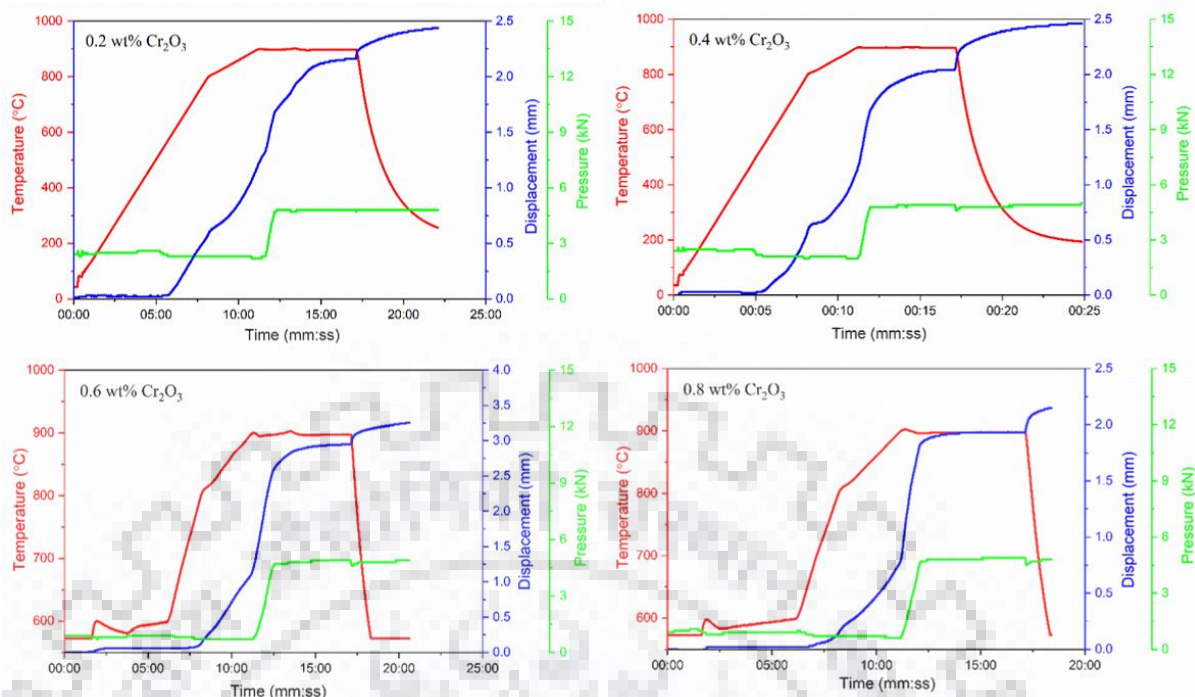


Fig. 8.4 SPS profiles adopted for $\text{PbZr}_{0.52}\text{Ti}_{0.48}\text{O}_3 - x\text{Cr}$ ceramics sintered at 900°C .

8.6 SEM analysis of sintered Cr doped PZT ceramics

The Cr doped PZT ceramics sintered by SPS technique were polished to remove any graphite layers adhered to the surface of pellets due to the graphite enclosure used in sintering. Thereafter, the pellets were annealed at 800°C for 4 hours to eliminate any carbon contamination and also to compensate for oxygen deficiencies developed during sintering. Fig. 8.5 depicts the microstructural features of the fracture surface of Cr doped PZT ceramics with different Cr_2O_3 contents. It can be observed that the microstructure of the prepared ceramic is highly dense with negligible porosity. The ceramics show uniform and homogenous microstructure with grain size in the nanometric region. It can be inferred that the Cr doping does not influence the microstructure significantly. Fig. 8.6 depicts the histogram data of grain size distribution for all the sintered specimens. It can be observed that the average grain size decreases for Cr doped PZT ceramics ($\sim \leq 18 \text{ nm}$) over undoped PZT ceramics ($\sim 19 \text{ nm}$). In comparison, (Selvamani et al. 2018a) reported an average grain size of $\sim 1.3 \mu\text{m}$ for conventionally sintered Cr doped PZT ceramics. As the Cr content is increased from 0.2 wt.% to 0.8 wt.%, the average grain size of the ceramics is further reduced as shown by the histogram data. (Yang et al. 2007a) similarly reported the decrease of grain size of Cr doped PZT ceramics as the Cr content increased beyond 0.2 wt.%. They stated that the addition of Cr dopant hinders grain growth in doped PZT ceramics as the Cr ions get accumulated at the grain boundaries resulting in reduction of grain size. The theoretical density of Cr doped PZT ceramics for Cr_2O_3 content ranging from 0.2 - 0.8 wt.% is

near $\sim 8.06 \text{ g/cm}^3$ (Yang et al. 2007a). (Bajpai et al. 2019) reported that the relative density decreased on Cr addition in PZT ceramics leading to large porosity for the conventionally sintered specimens. However, in the current study, no reduction in relative density for SPS sintered Cr doped PZT ceramics was observed. All sintered specimens show $\geq 99.3 \%$ relative density up to addition of 0.8 wt.% Cr_2O_3 . Therefore, to achieve highly dense Cr doped PZT ceramics, SPS sintering technique is significantly useful. To the best of the author's knowledge, dielectric and energy storage studies have not been reported yet for spark plasma sintered Cr doped PZT ceramics.

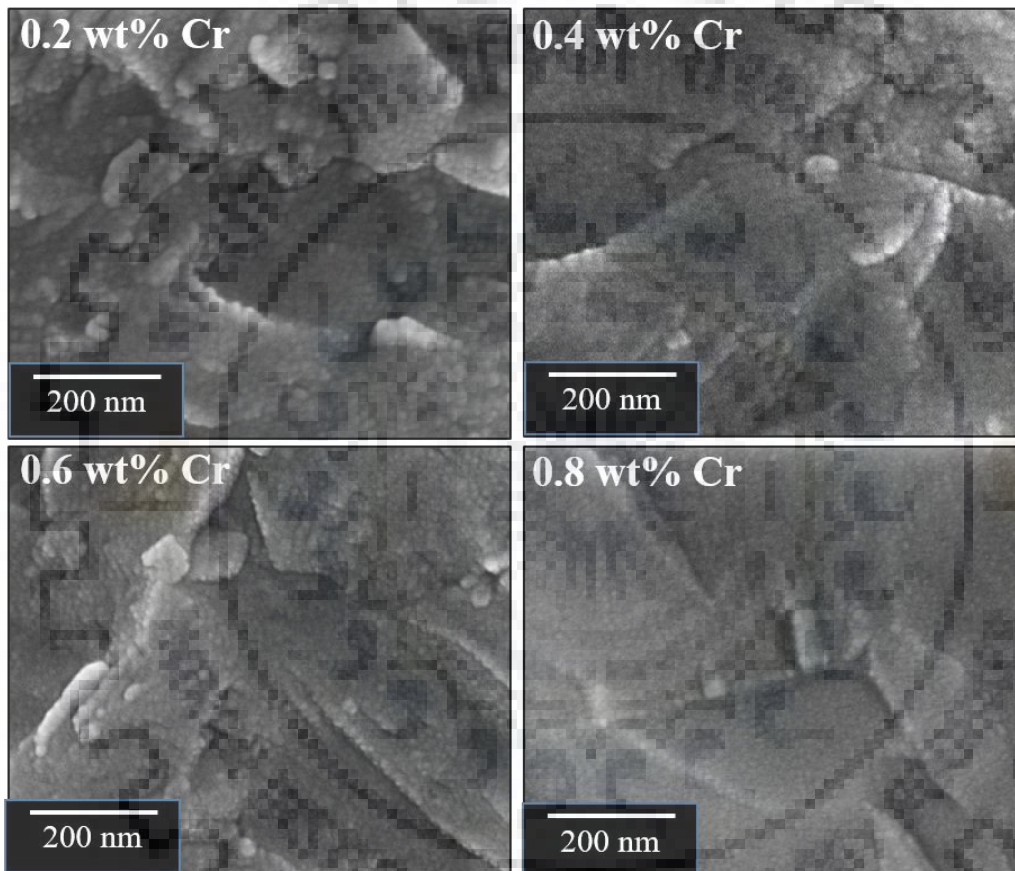


Fig. 8.5 Microstructure of $\text{PbZr}_{0.52}\text{Ti}_{0.48}\text{O}_3 - x\text{Cr}$ ceramics sintered by SPS method at 900°C .

8.7 XRD analysis of sintered Cr doped PZT ceramics

The X-ray diffraction patterns of PZT ceramics doped with different Cr_2O_3 contents were obtained at room temperature using the X-ray diffractometer employing $\text{CoK}\alpha$ radiation ($\lambda = 1.79 \text{ \AA}$). The diffractograms of each Cr doped PZT specimen with an enlarged view of 2θ range $48 - 56^\circ$ are depicted in Fig. 8.7. The sharp and well defined intensity peaks of the specimens indicate the formation of polycrystalline Cr doped PZT ceramics. It can be observed that on Cr doping in PZT, the diffraction peaks shift towards lower angle of diffraction. The analysis of all XRD patterns of Cr doped PZT ceramics show typical perovskite structure having $P4mm$ space group.

The reference PDF file no. 00-053-0698 matches the XRD patterns with tetragonal phase structure. In addition, the impurity phases of Baddeleyite ZrO_2 and pyrochlore phase are also detected which are marked by respective symbol shown in Fig. 8.7. It is to be noted that the pyrochlore phase reduces as the Cr content increases to 0.6 wt.% and becomes absent in 0.8 wt.% Cr doped PZT ceramic. (Uchida and Ikeda 1967) also reported similar spurious peaks near 2θ range $30 - 34^\circ$ for Cr doped MPB PZT composition specimens. Any separate peaks corresponding to Cr were not detected showing its solubility in the PZT ceramic. The enlarged view of the characteristic $\{200\}$ peak reveals that the coexistence of phases (tetragonal/ monoclinic/ rhombohedral) is not clearly visible for Cr doped PZT specimens relative to undoped PZT ceramic sintered at 900°C . This suggests that the addition of Cr ions have either shifted the MPB region or has narrowed the coexistence region. It is to be noted that the coexistence region can still be achieved by changing the Zr/Ti ratio in Cr doped PZT ceramics, however this has not been discussed here.

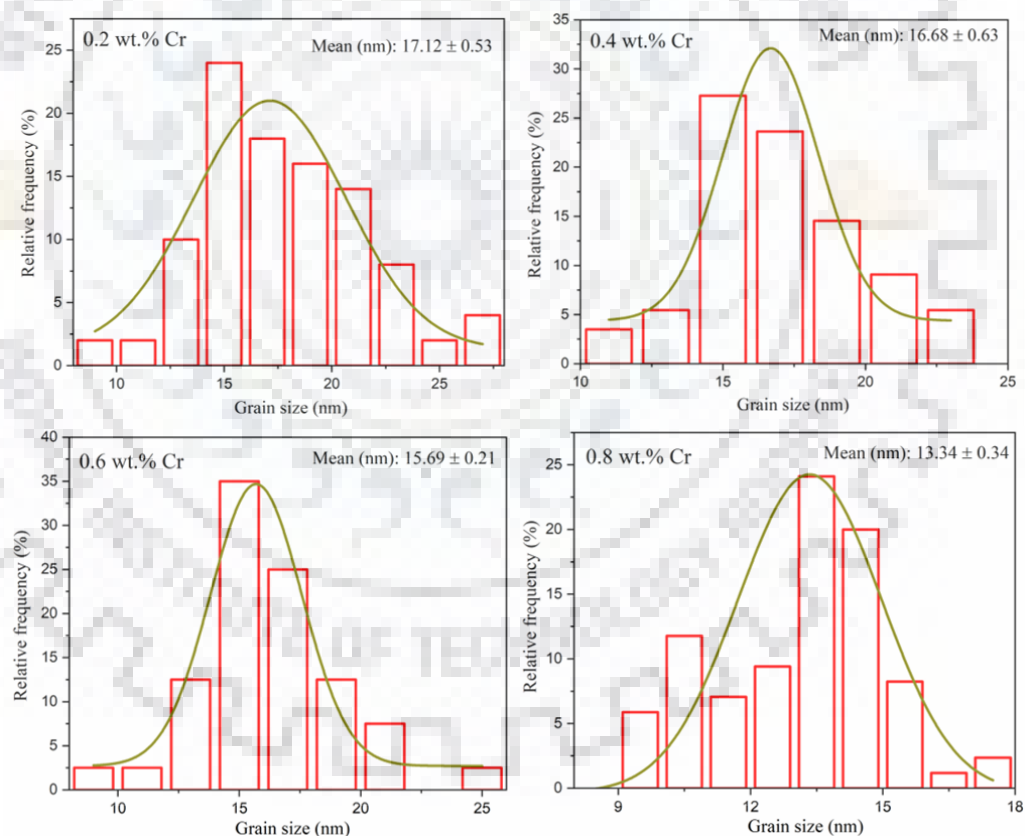


Fig. 8.6 Histogram of grain size distribution of $PbZr_{0.52}Ti_{0.48}O_3 - xCr$ ceramics sintered by SPS method at 900°C .

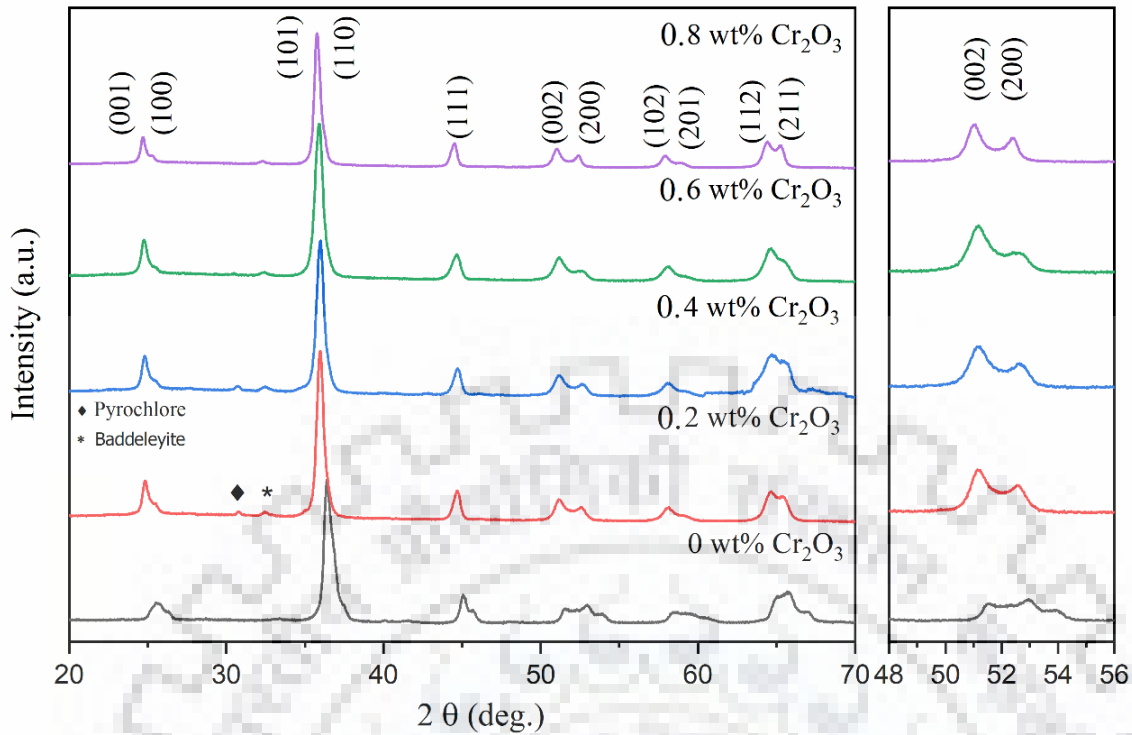


Fig. 8.7 XRD patterns of $\text{PbZr}_{0.52}\text{Ti}_{0.48}\text{O}_3 - x\text{Cr}$ ceramics for $x = 0, 0.2, 0.4, 0.6$ and 0.8 sintered at 900°C .

8.8 XPS analyses of Cr doped PZT ceramics

The Cr ions exist in multiple valence states when doped in PZT as reported in many previous studies (He et al. 2001; Katiyar, Srivastava, and Singh 1994; Nejezchleb 1980a; Selvamani et al. 2018b; Xia et al. 2016; Yang et al. 2007b). The ionic radius of Cr^{3+} , Cr^{5+} and Cr^{6+} are 0.755, 0.630 and 0.580 Å respectively, whereas the ionic radii of Pb^{2+} , Zr^{4+} and Ti^{4+} are 1.32, 0.720 and 0.605 Å respectively. Thus, the preferred site for substitution of chromium ions are at the B-site of PZT (Pauling 1929). When the chromium ion mainly exists in the +3 oxidation state on substitution of Zr^{4+} or Ti^{4+} , it acts as an acceptor ion which leads to creation of oxygen vacancies to maintain electrical neutrality. The oxygen vacancies restrict the motion of ferroelectric domain walls leading to reduction of saturation polarization and dielectric permittivity. Moreover, the defect complexes of acceptor ions and oxygen vacancies restrict easy reversal of domains and suppress domain switching thereby increasing the coercivity (He et al. 2001; Xia et al. 2016). On the other hand, Cr^{5+} or Cr^{6+} ions act as donor ions and lead to creation of A-site defects which enhances the dielectric permittivity and piezoelectric performance (Selvamani et al. 2018b). The substitution of Cr^{5+} or Cr^{6+} having smaller ionic radii than Cr^{3+} leads to lattice shrinkage and aids in domain reversal (Xia et al. 2016). The XPS spectra of Cr $2p_{3/2}$ for each Cr doped PZT specimen were recorded with an X-ray photoelectron spectrometer, VersaProbe III PHI 5000 using $\text{Al-K}\alpha$

X-ray source. The XPS spectra were investigated to identify the correct valence state of Cr ion and are shown in Fig. 8.8. The C 1s spectrum was taken as reference standard for peak shift correction of other elements by taking 284.5 eV as reference for C-C bond. The binding energy of Cr^{3+} , Cr^{5+} and Cr^{6+} are 576.6, 578.6 and 580.1 eV respectively. The experimental peaks were fitted with Gaussian-Lorentz curves and Shirley background function. The best fitting results were obtained by fitting individual peaks with peak center located at 576.6 and 578.6 eV corresponding to Cr^{3+} and Cr^{5+} as shown in Fig. 8.8. The atomic concentration of each ion for different Cr doped PZT specimens are tabulated below. It can be observed that the Cr^{3+} concentration has increased from 0.2 wt.% to 0.6 wt.% Cr doped PZT, whereas it decreased for 0.8 wt.% Cr doped PZT specimen. The solubility limit of Cr_2O_3 in PZT structure close to the MPB composition is ~ 0.5 wt%. As the Cr_2O_3 content is increased beyond the solubility limit, a second phase (PbCrO_5 or Pb_2CrO_5) is formed preferably at the grain boundaries. Cr^{6+} or Cr^{5+} gets released with reducing oxygen partial pressure and higher sintering temperatures (similar conditions are achieved during SPS), and can replace Zr or Ti arousing donor like behavior in the system via formation of Pb vacancies. Such anomalous behaviour has been reported in several studies. (He et al. 2001) reported both hard and soft behaviour in Cr doped PZTMN on variation in Cr content. The piezoelectric properties were found to increase below 0.08 wt.% Cr which was attributed to the +5 oxidation state of Cr. (Xia et al. 2016) performed XPS analysis on BCZT ceramics and identified Cr^{3+} and Cr^{5+} at lower and higher concentrations respectively. (He and Li 2000) performed Electron Spin Resonance (ESR) studies on MnO doped PZT ceramics which revealed coexistence of Mn^{2+} and Mn^{3+} ions. They reported acceptor and donor ion behaviour of Mn ion above and below 0.5 mol % Mn which leads to variation in piezoelectric properties. The above results show that the oxidation state of chromium may influence the dielectric and energy storage properties of Cr doped PZT ceramics and the same has been discussed in the upcoming sections.

Table 8.1 Atomic concentration of individual peak profile in Cr 2p_{3/2} XPS spectra of $\text{PbZr}_{0.52}\text{Ti}_{0.48}\text{O}_3 - x\text{Cr}$ ceramics.

Cr₂O₃ content (wt.%)	Atomic concentration (%)	
	Cr³⁺	Cr⁵⁺
0.2	26.54	73.46
0.4	34.58	65.42
0.6	41.78	58.22
0.8	23.54	76.46

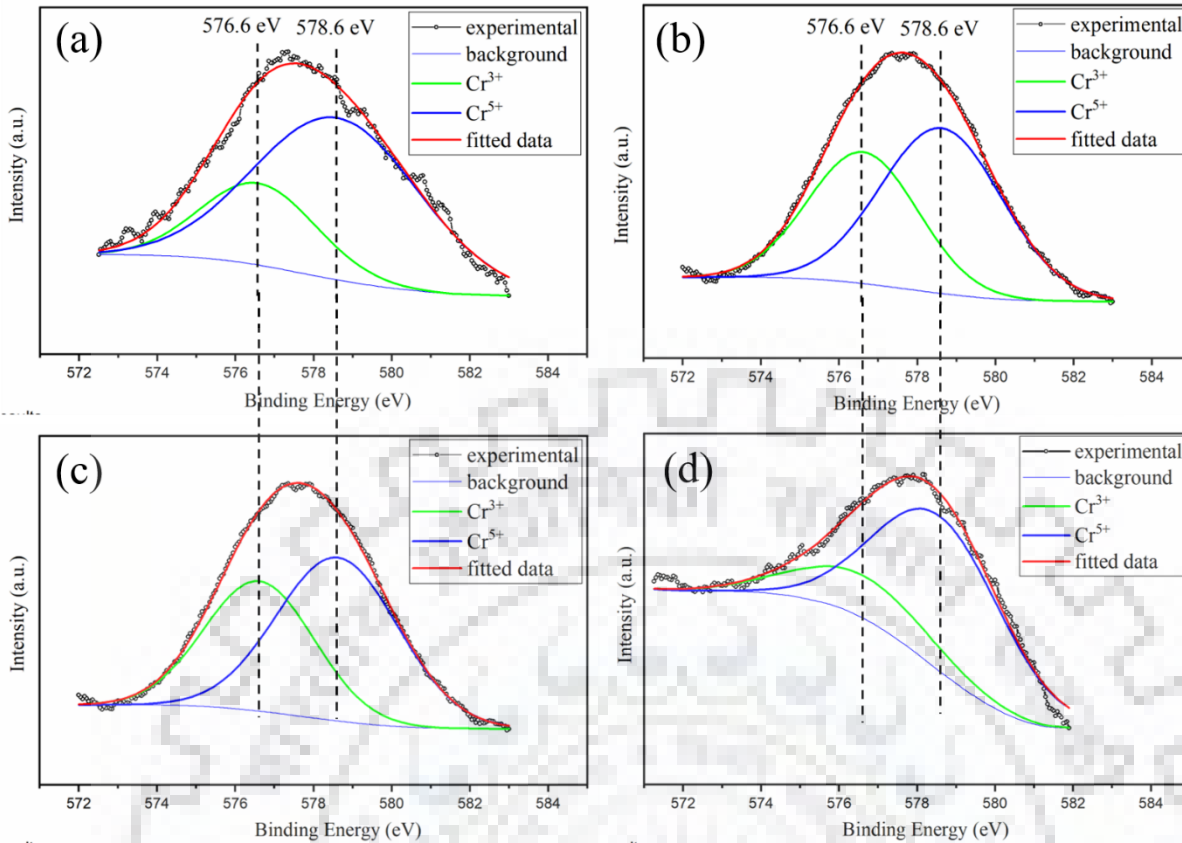


Fig. 8.8 XPS spectra of Cr $2p_{3/2}$ of $\text{PbZr}_{0.52}\text{Ti}_{0.48}\text{O}_3 - x\text{Cr}$ for (a) $x = 0.2$, (b) $x = 0.4$, (c) $x = 0.6$ and (d) $x = 0.8$ ceramics.

8.9 Dielectric studies of Cr doped PZT ceramics

The dielectric studies of Cr doped PZT ceramics were conducted over the temperature range of 35 - 450°C for selective frequencies of 1 kHz, 10 kHz, 100 kHz and 1 MHz. It can be observed that the dielectric constant increases as the temperature is increased up to the Curie temperature (T_C) as shown in Fig. 8.9. Such behaviour indicates the typical ferroelectric nature of all Cr doped PZT samples. The variation in T_C as Cr content increases from 0.2 wt.% to 0.8 wt.% is not significant ($\Delta T_C \leq 8^\circ\text{C}$). When a trivalent ion replaces the A site of PZT perovskite structure, the charge compensation takes place by introduction of A site vacancies. Such vacancies distort the ferroelectrically active oxygen octahedra and leads to creation of short range polarized regions. This in turn changes the T_C and leads to relaxor like behaviour in PLZT ceramics (Selvamani et al. 2018a). However, in the present case, the change in T_C is insignificant and so the Cr ions do not modify the short range polarized regions and in turn substitutes in the B site (Selvamani et al. 2018a). The maximum dielectric constant (ϵ_m) decreases with Cr content increasing above 0.2 wt.%, however ϵ_m increases for 0.8 wt.% Cr doped specimen. The XPS spectra analysis revealed that the atomic concentration of Cr^{3+} ions increases from 0.2 wt.% to 0.6 wt.% Cr doped PZT

specimen. The increase in acceptor ion behaviour leads to creation of oxygen vacancies thereby decreasing the permittivity. On the other hand, when the Cr content is increased to 0.8 wt.%, the increase in dielectric maxima indicates that the Cr acts as donor ion. Such behaviour is in agreement to the XPS spectra analysis as shown in Fig. 8.8. It is to be noted that the multi-valent nature of Cr ions lead to non-linear variation in dielectric constant with addition of Cr content. The ϵ_m decreases for each specimen with increase of frequency which indicates the relaxation phenomena, as the low frequency polarization mechanisms i.e. space charge and interfacial polarization are absent and the dipole response cannot follow the applied electric field at high frequencies. The Curie temperature decreases on addition of Cr_2O_3 above 0.4 wt.%. Similar findings were reported by Uchida et al. (Uchida and Ikeda 1967). The T_C and ϵ_m of each Cr doped PZT specimen is presented in Table 8.2. The full width at half maximum (FWHM) values from temperature dependent dielectric curves have been calculated at the Curie temperature. The FWHM values for 0.2 wt.%, 0.4 wt.%, 0.6 wt.%, 0.8 wt.% Cr are 118.27, 152.75, 166.3, 86.6 respectively. Therefore, it can be inferred that PZT ceramics with 0.2 and 0.8 wt.% Cr content behave as a normal ferroelectric material, whereas PZT ceramics with 0.4 and 0.6 wt.% Cr content behave more like a diffused ferroelectric material.

Table 8.2 The observed values of Curie temperature ($^{\circ}\text{C}$) and maximum dielectric constant (ϵ_m) at 1, 10, 100 and 1000 kHz of $\text{PbZr}_{0.52}\text{Ti}_{0.48}\text{O}_3 - x\text{Cr}$ ceramics.

Cr_2O_3 content (wt.%)	Frequency (kHz)	Curie Temperature ($^{\circ}\text{C}$)	Maximum Dielectric constant (ϵ_m)
0.2	1	318	6289
	10	318	5565
	100	318	5057
	1000	318	4638
0.4	1	326	4238
	10	326	3464
	100	326	3425
	1000	326	3107
0.6	1	324	4911
	10	324	3908
	100	324	3200
	1000	324	2998

0.8	1	314	10110
	10	314	7925
	100	314	7400
	1000	314	6266

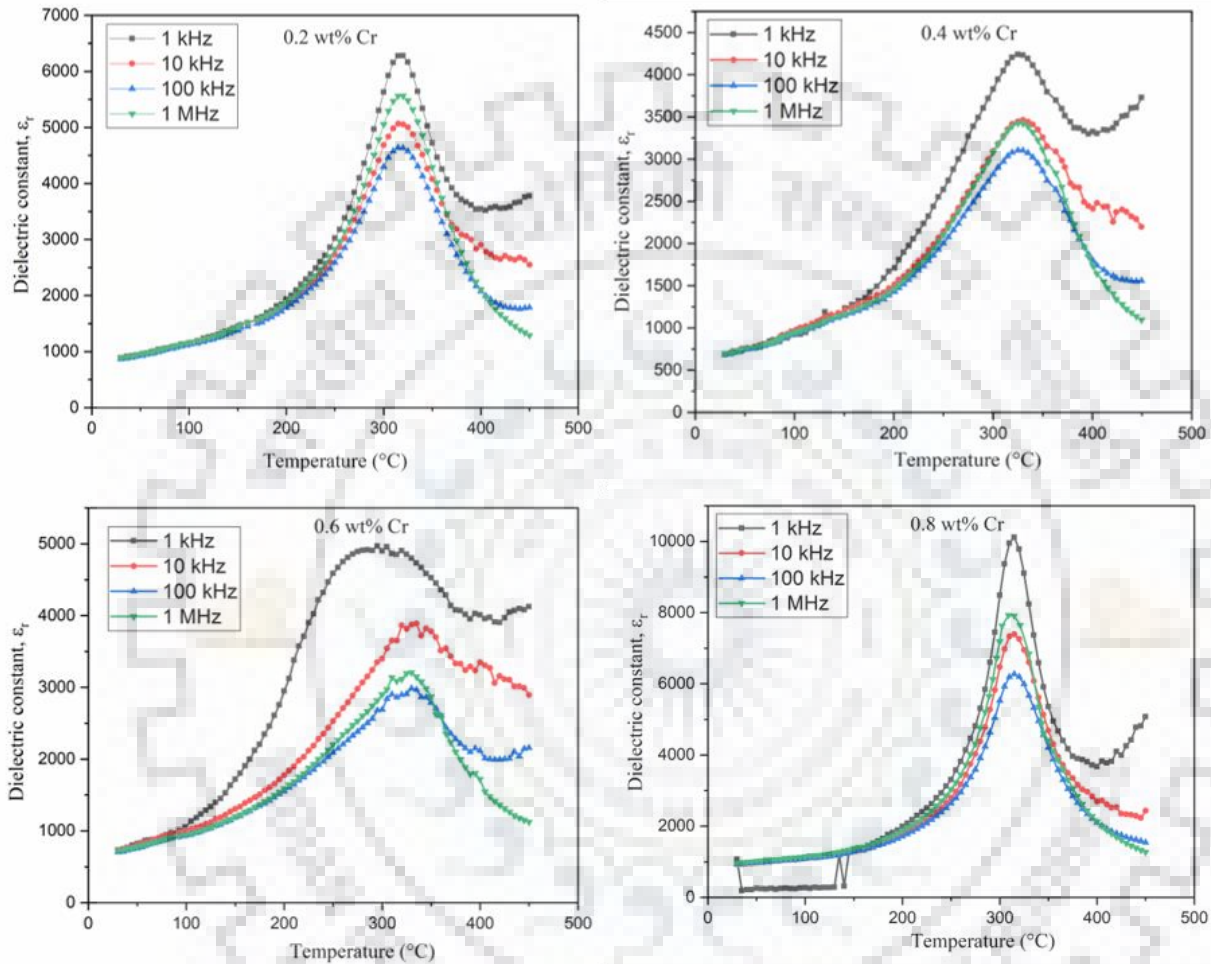


Fig. 8.9 Temperature dependent plots of dielectric constant (ϵ_r) of $\text{PbZr}_{0.52}\text{Ti}_{0.48}\text{O}_3 - x\text{Cr}$ ceramics at 1, 10, 100, 1000 kHz frequencies.

Fig. 8.10 shows the variation of dielectric loss tangent ($\tan \delta$) with temperature for each of the Cr doped PZT specimens at selected frequencies of 1 kHz, 10 kHz, 100 kHz and 1 MHz. The specimens typically show higher value of loss tangent for lower frequencies (1 kHz and 10 kHz), whereas the loss tangent values are significantly lower for higher frequency region (> 10 kHz). It can be clearly observed that the loss tangent curves remain constant when the temperature is below the T_C . As the temperature approaches T_C , the loss tangents increase significantly for all Cr doped specimens.

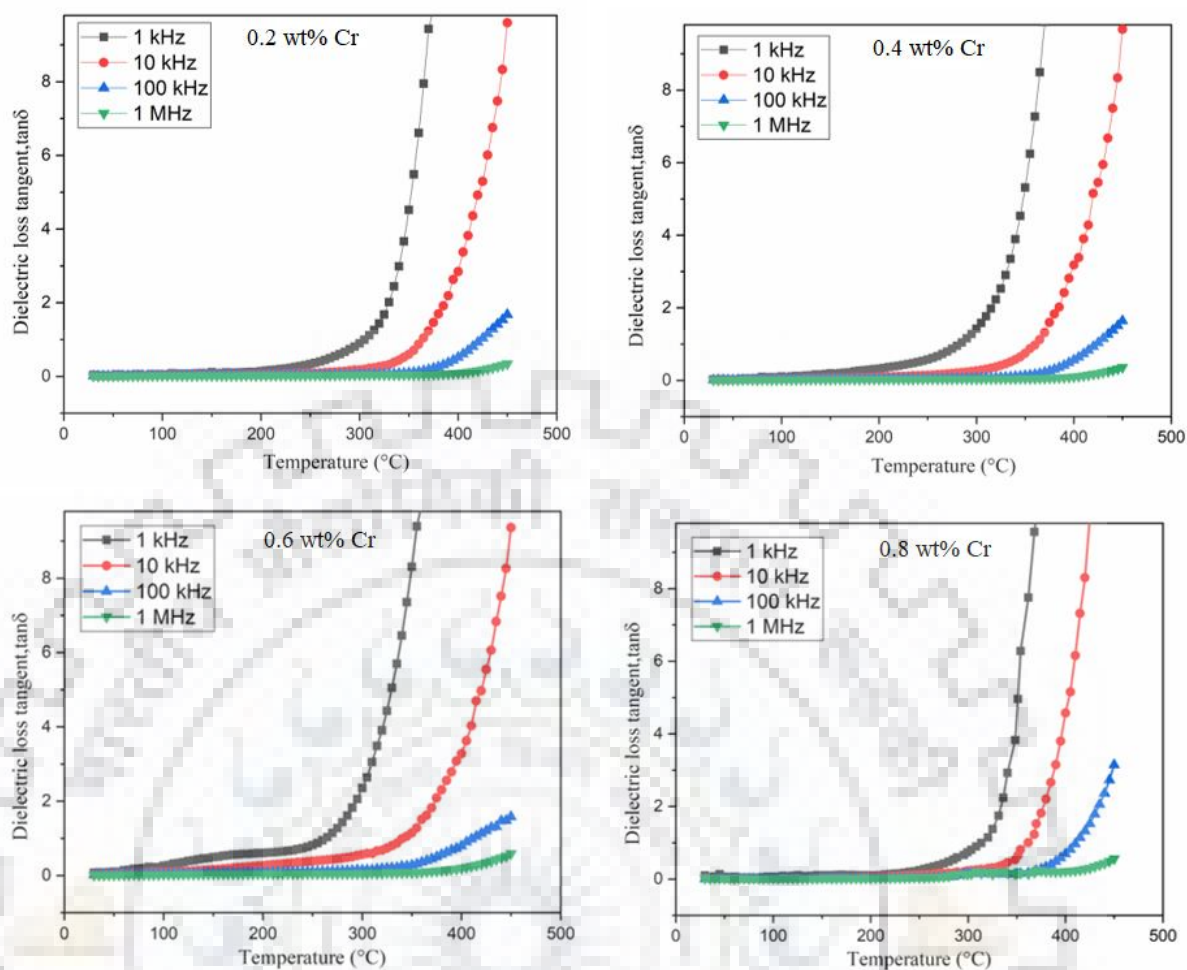


Fig. 8.10 Temperature dependent plots of dielectric loss tangent ($\tan \delta$) of $\text{PbZr}_{0.52}\text{Ti}_{0.48}\text{O}_3 - x\text{Cr}$ ceramics at 1, 10, 100, 1000 kHz frequencies.

8.10 Impedance and modulus spectroscopy studies of Cr doped PZT ceramics

Fig. 8.11 depicts the variation of real part of impedance (Z') with frequency at selective temperatures ranging from 150 - 400°C for PZT ceramics doped with different Cr_2O_3 contents. It can be observed that the Z' values are higher at lower frequency region (< 1 kHz) which is due to the low frequency polarization mechanisms being active. At frequencies greater than 1 kHz, the Z' remains stable for the entire frequency range. Such behaviour is reciprocated for each of the Cr doped PZT specimens. On the other hand, the Z' value decreases as the temperature increases at the lower frequency region (< 1 kHz), whereas the Z' curves for all temperatures merge together as the frequency is increased beyond 1 kHz. Such behaviour is exhibited by each Cr doped PZT specimen.

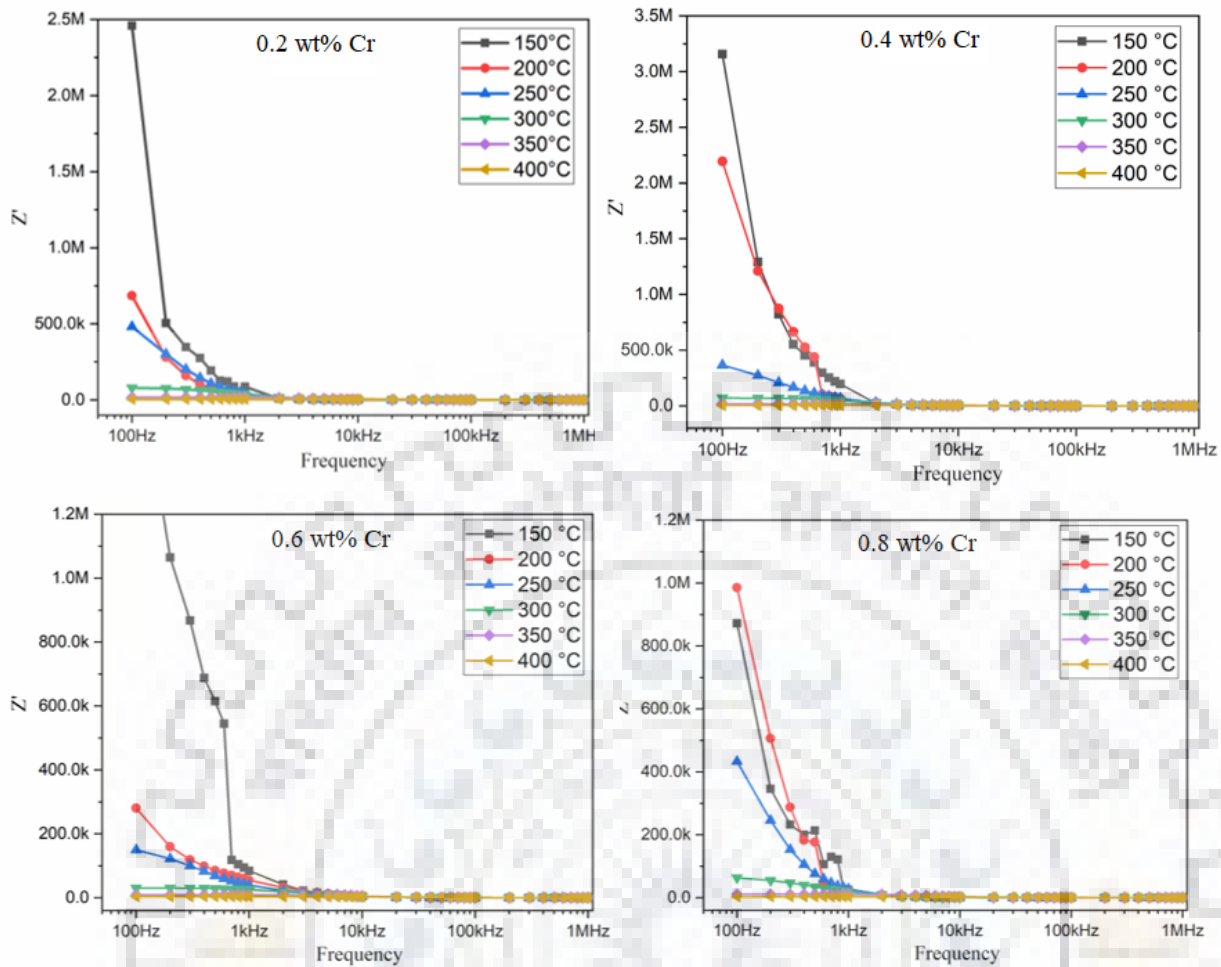


Fig. 8.11 Frequency dependent plots of real part of impedance (Z') of $\text{PbZr}_{0.52}\text{Ti}_{0.48}\text{O}_3 - x\text{Cr}$ ceramics at 150°C, 200°C, 250°C, 300°C, 350°C and 400°C temperatures.

Fig. 8.12 depicts the variation of imaginary part of impedance (Z'') with frequency at selective temperatures ranging from 150 to 400°C for PZT ceramics doped with different Cr_2O_3 contents. For better representation, the Z'' curves for operating temperatures 150, 200 and 250°C are shown in the respective inset of each graph. At temperatures $< 250^\circ\text{C}$, the Z'' values fall rapidly as the frequency is increased and any relaxation peak is not observed. However, for temperatures $\geq 250^\circ\text{C}$, the Z'' curves exhibit relaxation peaks. The relaxation peak can be clearly observed for all Cr doped PZT specimens at 300, 350 and 400°C operating temperature. The appearance of relaxation peak indicates presence of relaxation process in the material. Moreover, the relaxation occurs at higher frequencies as temperature is increased for all the doped specimens. On the other hand, the Z'' value at the relaxation frequency also decreases as the temperature is increased for all Cr doped PZT specimens. The difference in the degree of broadening in Z'' curves with increase in temperature is indicative of non-Debye type relaxation i.e. spread of relaxation time constants. The broadening of Z'' peaks on increase of temperature indicates temperature

dependent relaxation phenomena in the Cr doped PZT specimens. Such behaviour is due to the increase in mobility of mobile charge carriers with increase in temperature. Moreover, the Z'' curves for all specimens merge together at high frequencies which is due to the accumulation of space charges in the material. The relaxation time (τ) for each composition at respective temperatures can be calculated at the relaxation frequency (ω_{max}) by the relation $\omega_{max} \tau = 1$. Fig. 8.13 depicts the variation of $\log(\tau)$ calculated from relaxation peaks in Z'' curves as a function of $1000/T$ along with the respective activation energy values. The nature of the τ vs T curves follow the Arrhenius equation, $\tau = \tau_0 e^{-E_a/k_B T}$, where k_B is the Boltzmann constant (Hodge, Ingram, and West 1976).

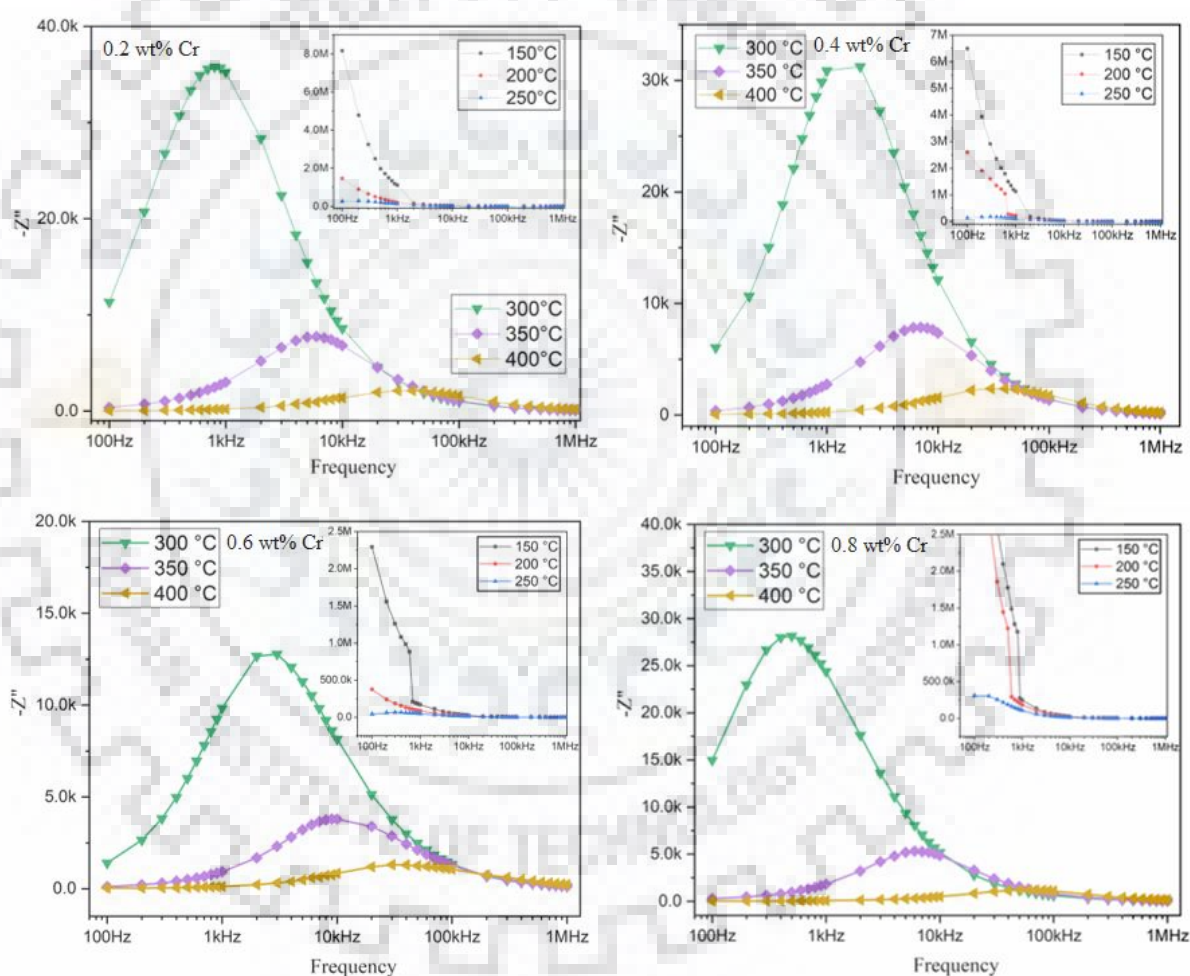


Fig. 8.12 Frequency dependent plots of imaginary part of impedance (Z'') of $\text{PbZr}_{0.52}\text{Ti}_{0.48}\text{O}_3 - x\text{Cr}$ ceramics at 300°C, 350°C and 400°C temperatures. The inset shows the same for 150°C, 200°C and 250°C temperatures.

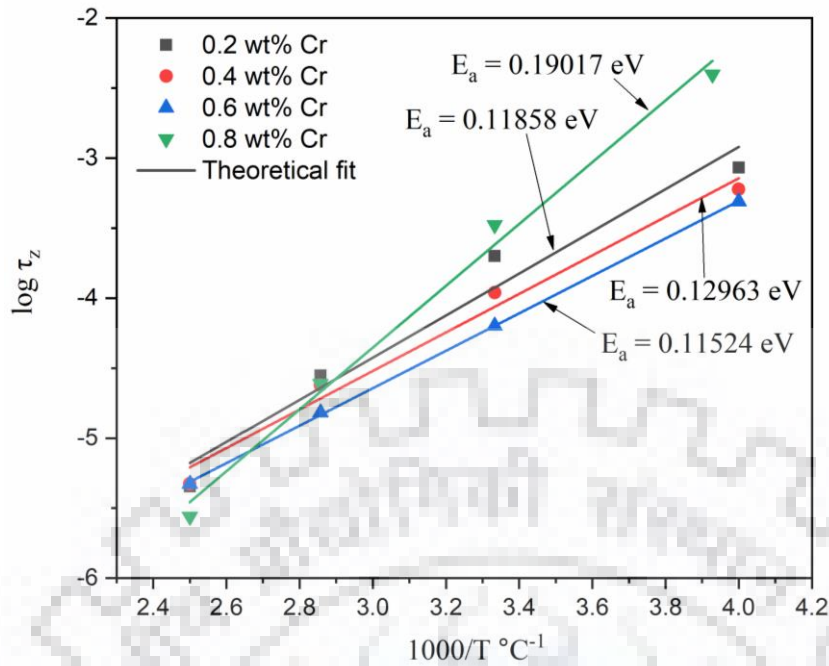


Fig. 8.13 Variation of relaxation time estimated from impedance plot, $\log(\tau_z)$ as a function of inverse of absolute temperature of $\text{PbZr}_{0.52}\text{Ti}_{0.48}\text{O}_3 - x\text{Cr}$ ceramics. The calculated activation energy (E_a) values are marked onto the fitted data.

The Nyquist plot provides separate contributions of grain and grain boundary relaxations in a material. Fig. 8.14 depicts the complex impedance plots or Nyquist plots at different temperatures 150, 200, 250, 300, 350 and 400°C for PZT ceramics doped with different Cr_2O_3 contents. The inset shows the Nyquist plots at temperatures 150, 200 and 250°C for better representation for each specimen. Generally the semi-circular arc at lower frequency region represents the contribution from grain boundary relaxation, whereas the semi-circular arc at high frequency region represents the contribution from grain or bulk relaxation. However, only single semi-circular arcs are observed for all the Cr doped PZT specimens which also suggests relaxation phenomena in the material. It can be noticed that the bulk resistance (R_g) decreases as the temperature increases for all Cr doped compositions. 0.2 wt.% Cr doped composition exhibits $R_g = 0.6 \text{ M}\Omega$ and $5 \text{ k}\Omega$ at an operating temperature of 250°C and 400°C respectively. Such decrease of bulk or grain resistance with increase of temperature indicates NTCR (negative temperature coefficient of resistance) effect similar to effect in semi-conductor materials. Moreover, it can be observed that the bulk resistance of the material decreases as Cr content increases up to 0.6 wt.%, whereas it increases again for 0.8 wt.% Cr content as depicted by the decrease in diameter of the semi-circular arcs. The relaxation time is given by $\tau = R_g C_g$, where R_g can be directly obtained by the intercept of semi-circular arc on the x-axis of Nyquist plot. The relaxation time (τ) can be calculated at the relaxation frequency in Nyquist plots by relation $\omega_{max} \tau = 1$. The bulk parameters

τ_g , R_g and C_g are calculated from the Nyquist plots by fitting the semi-circular arc to an equivalent circuit consisting of parallel RC component and the results are tabulated in Table 8.3. It can be inferred from the tabulated results, that for the most part, the capacitance (C_g) values increases on increase in Cr content from 0.2 wt.% to 0.6 wt.%, and then again reduces on further increase to 0.8 wt.% Cr.

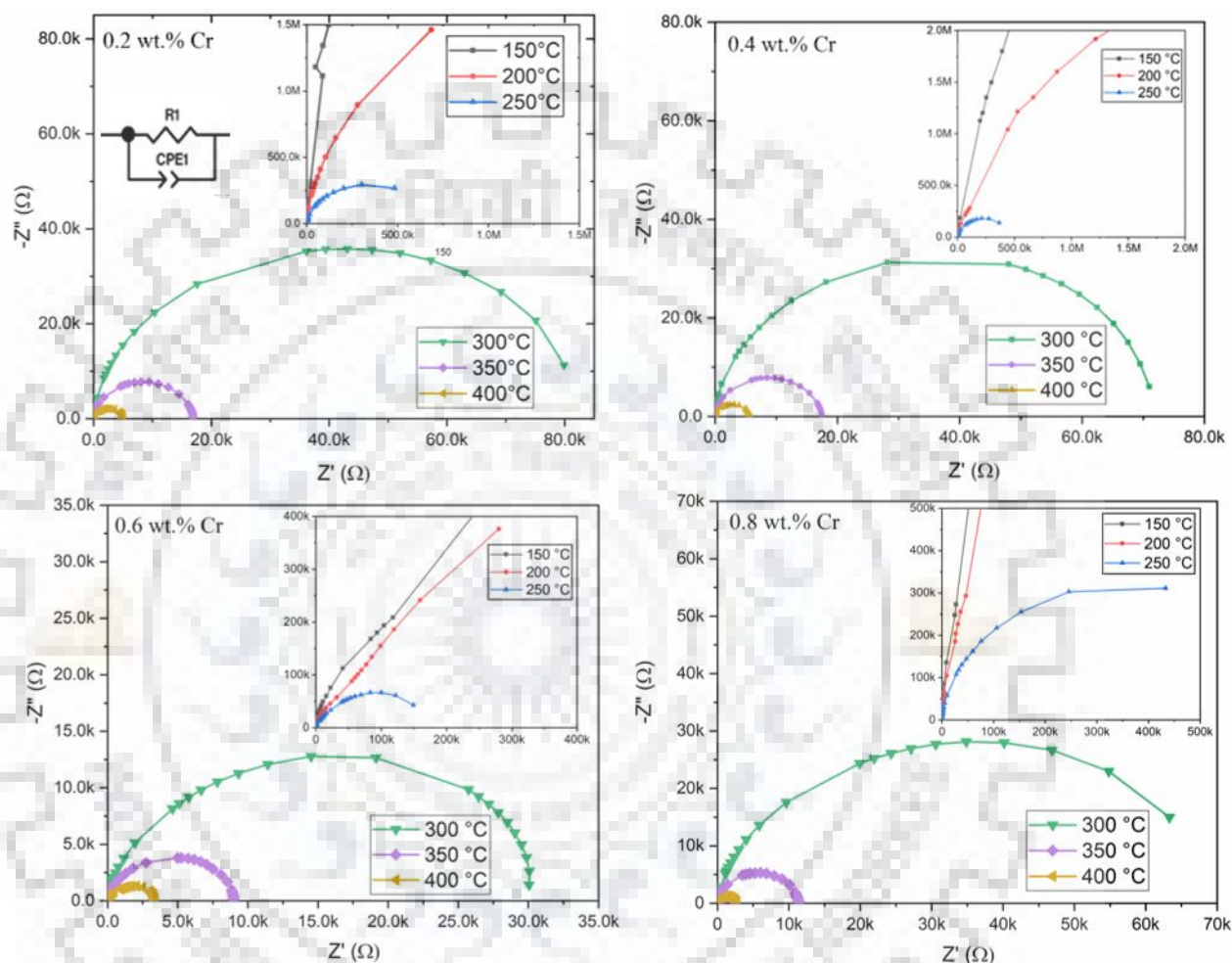


Fig. 8.14 Nyquist plot of $\text{PbZr}_{0.52}\text{Ti}_{0.48}\text{O}_3 - x\text{Cr}$ ceramics at 300°C, 350°C and 400°C temperatures. The inset shows the same for 150°C, 200°C and 250°C temperatures.

Table 8.3 Calculated values of τ_g , R_g and C_g at selective temperatures of $\text{PbZr}_{0.52}\text{Ti}_{0.48}\text{O}_3 - x\text{Cr}$ ceramics.

Cr content (wt.%)	Temperature (°C)	τ_g (s)	R_g (Ω)	C_g (nF)
0.2	250	8.6×10^{-4}	625994	1.37
	300	2.02×10^{-4}	82228	2.46
	350	2.9×10^{-5}	16908	1.71

	400	4.53×10^{-6}	5043	0.86
0.4	250	6.01×10^{-4}	441974	1.36
	300	1.12×10^{-4}	71956	1.56
	350	2.4×10^{-5}	17419	1.38
	400	4.72×10^{-6}	5759	0.82
0.6	250	4.9×10^{-4}	176350	2.78
	300	6.34×10^{-5}	30196	2.1
	350	1.51×10^{-5}	9010	1.68
	400	4.72×10^{-6}	3407	1.39
0.8	250	3.95×10^{-3}	673643	0.56
	300	3.33×10^{-4}	71000	4.7
	350	2.45×10^{-5}	11507	2.13
	400	2.75×10^{-6}	2710	1.01

Fig. 8.15 depicts the variation of real part of electric modulus (M') with frequency at different temperatures (150, 200, 250, 300, 350 and 400°C) for PZT ceramics doped with different Cr_2O_3 contents. The M' values are calculated from the impedance parameters by the relation $M' = (2 \pi A \varepsilon_0 f Z'')/t$, where A is the surface area, t is the thickness and f is frequency. The M' values for all Cr doped specimens are very low (near zero) at lower frequency region (~100 Hz) which confirms the absence of electrode effects and such effects can be ignored while performing modulus formalisms. Typically, the M' values increase on increase of frequency for low temperature curves (150 - 300°C), whereas it remains stable up to 1 kHz and increases rapidly thereafter for high temperature curves (350, 400°C) for all Cr doped specimens. This continuous dispersion behaviour of M' curves with change in frequency indicates short range mobility of charge carriers (Khatri, Behera, and Choudhary 2009).

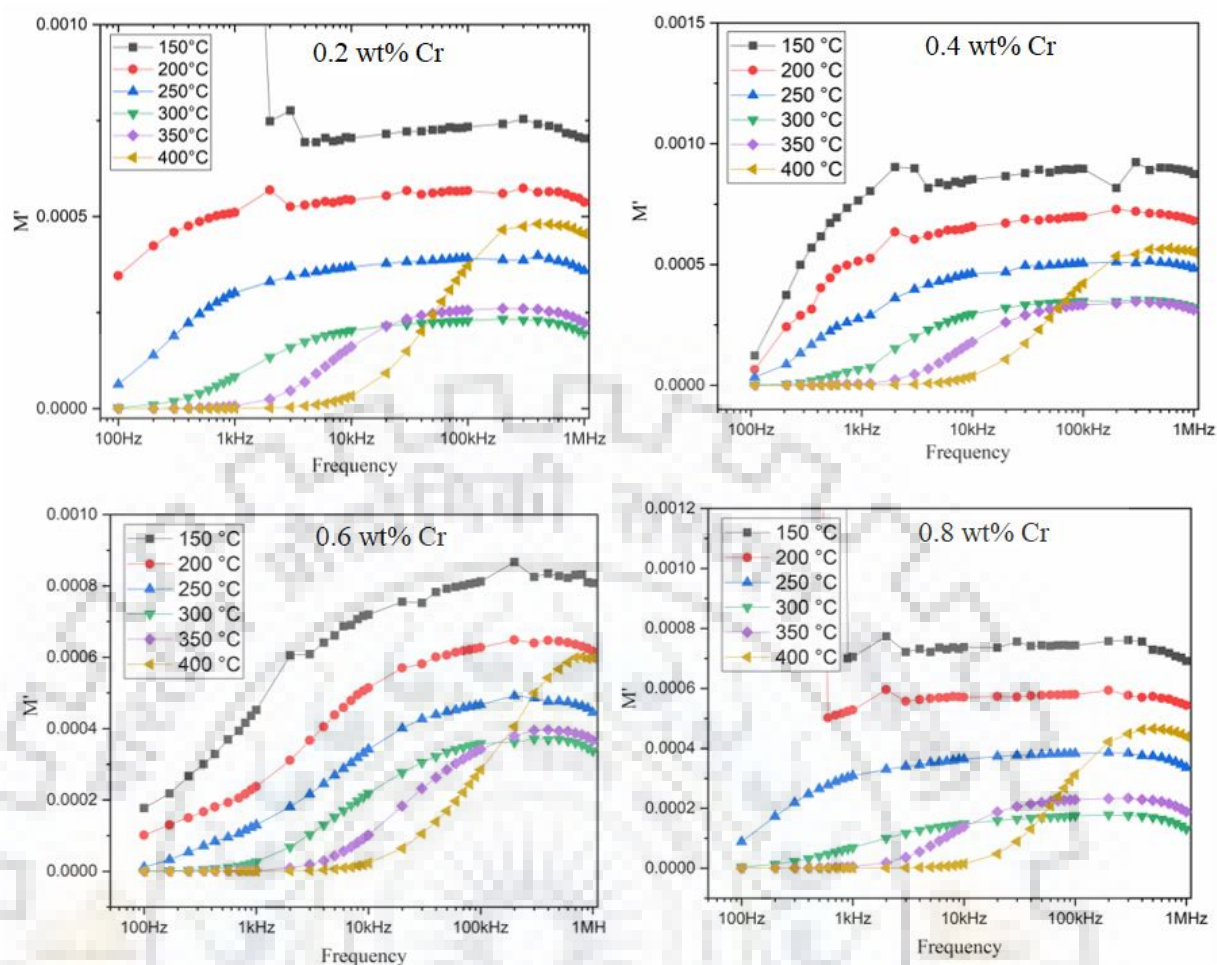


Fig. 8.15 Frequency dependent plots of real part of electric modulus (M') of $\text{PbZr}_{0.52}\text{Ti}_{0.48}\text{O}_3 - x\text{Cr}$ ceramics at 150°C, 200°C, 250°C, 300°C, 350°C and 400°C temperatures.

Fig. 8.16 depicts the variation of imaginary part of electric modulus (M'') with frequency at different temperatures (150, 200, 250, 300, 350 and 400°C) for PZT ceramics doped with different Cr_2O_3 contents. The modulus peaks are clearly observed at temperatures higher than 250°C for all Cr doped PZT specimens which again indicates presence of relaxation phenomena in the material. The modulus peaks exhibit broad and asymmetric nature at different temperatures for all samples. As the temperature increases, the asymmetric peaks shift to higher frequency that signify interaction between motions of mobile charge carriers (Khatri, Behera, and Choudhary 2009). The non-Debye type relaxation is confirmed by the broad nature of modulus peaks i.e. spread of relaxation times. Moreover, it can be observed that the modulus peaks that exist at low frequency region (≤ 1 kHz) indicate that the mobile charge carriers can move over long distances, whereas peaks at high frequency region indicate confinement of the charge carriers at their potential well. Such electric modulus spectrum behaviour indicates charge carrier hopping mechanism in the material (Prasad et al. 1998; Prasad, Srinivas, and James 2003). The results

obtained from electric modulus analysis conforms to the Complex impedance spectroscopy (CIS) results based on the temperature dependent relaxation mechanisms observed in both complex modulus spectra. The relaxation time (τ) can be calculated from the M'' peaks from the M'' vs f curves and the variation of $\log(\tau)$ with $1000/T$ is shown in Fig. 8.17. It can be observed that the activation energy (E_a) values calculated from both the Z'' and M'' curves are in agreement with each other.

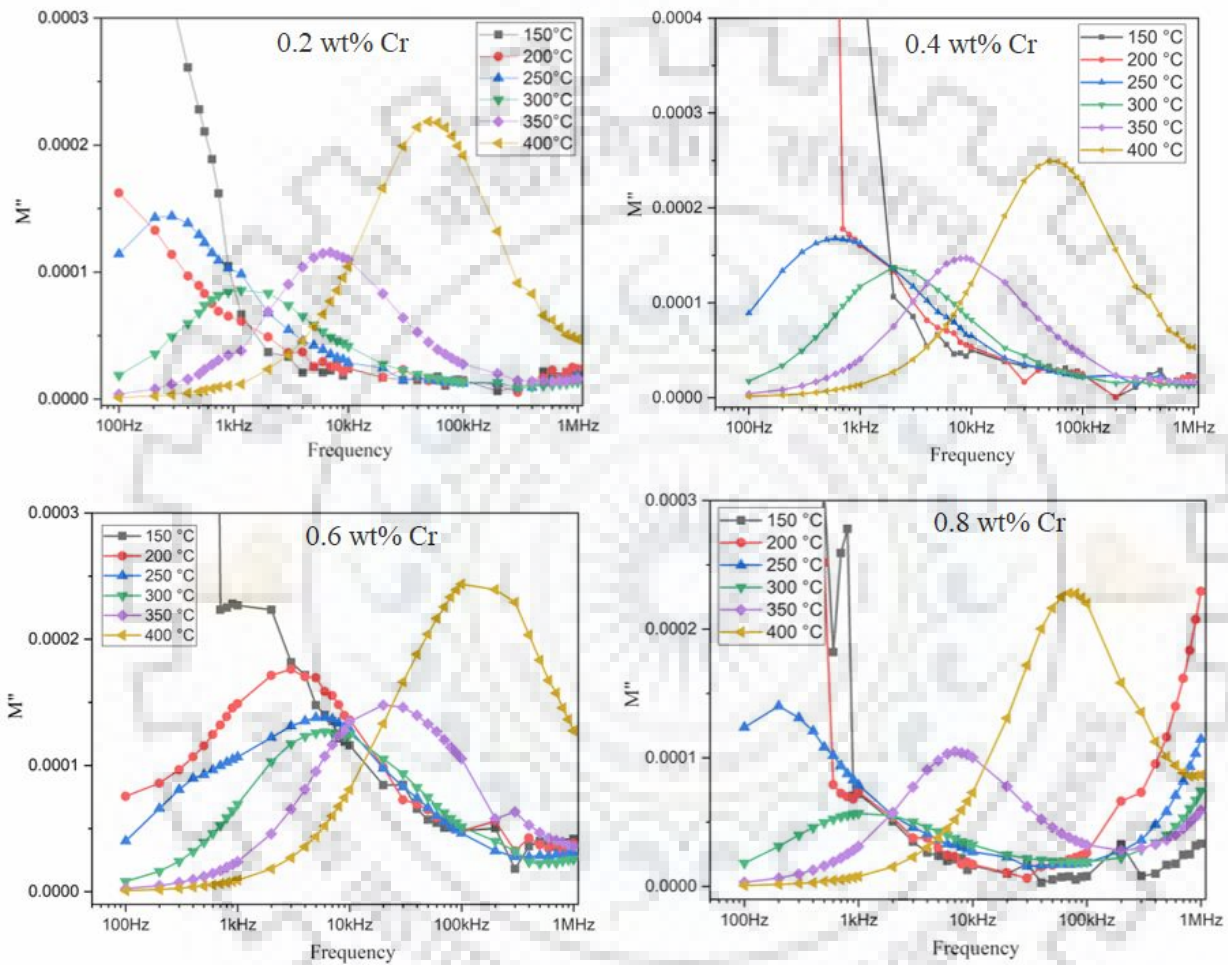


Fig. 8.16 Frequency dependent plots of imaginary part of electric modulus (M'') of $\text{PbZr}_{0.52}\text{Ti}_{0.48}\text{O}_{3-x}\text{Cr}$ ceramics at 150 °C, 200 °C, 250 °C, 300 °C, 350 °C and 400 °C temperatures.

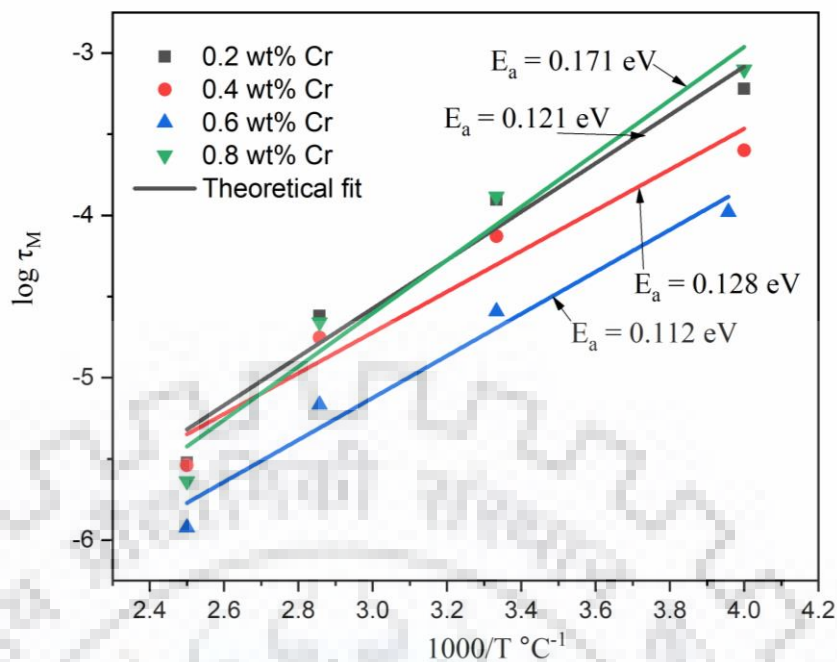


Fig. 8.17 Variation of relaxation time estimated from modulus plot, $\log(\tau_m)$ as a function of inverse of absolute temperature of $\text{PbZr}_{0.52}\text{Ti}_{0.48}\text{O}_3 - x\text{Cr}$ ceramics. The calculated activation energy (E_a) values are marked onto the fitted data.

8.11 Conductivity studies of Cr doped PZT ceramics

The ac conductivity profile of the different Cr doped PZT specimens was calculated by the relation $\sigma_{ac} = \omega \epsilon_0 \epsilon_r \tan \delta$ (discussed in Chapter 3), where ϵ_0 is the permittivity of free space, $\tan \delta$ is the dielectric loss tangent, $\omega = 2\pi f$ is the angular frequency and ϵ_r is the relative permittivity. Fig. 8.18 depicts the variation of AC conductivity with frequency at selective temperatures (150, 200, 250, 300, 350 and 400°C) for PZT ceramics doped with different Cr_2O_3 contents. It can be observed that the ac conductivity increases as the frequency increases, since the mobile charge carriers that have large relaxation times are less in number and are only operative at low frequencies. At higher frequencies, the mobile charge carriers cross the low barrier potential easily and contribute to conductivity at high frequencies. For each Cr doped composition, the conductivity is higher at high temperatures relative to low temperatures since the thermal energy provides sufficient energy to the mobile charge carriers to cross the energy barrier. It can be observed that ac conductivity curves show dispersion (non-linear) with frequency at lower temperatures ($< 350^\circ\text{C}$), whereas conductivity shows linear behaviour with frequency at higher temperatures (350°C, 400°C). Such dispersion behaviour at low temperatures indicate hopping conduction mechanism in the material which are in agreement to the results obtained by electric modulus studies (M'' vs f).

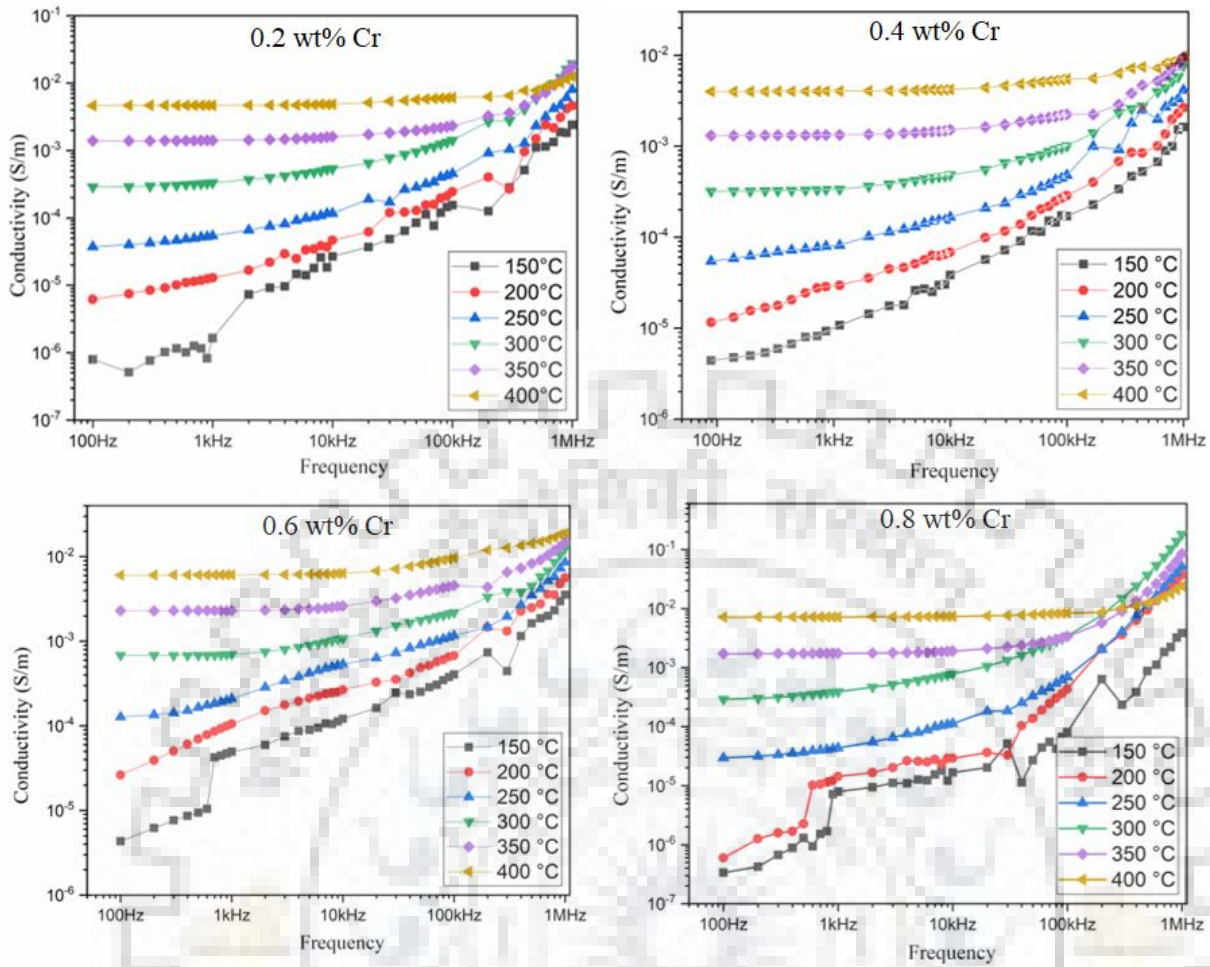


Fig. 8.18 Frequency dependent plots of AC conductivity of $\text{PbZr}_{0.52}\text{Ti}_{0.48}\text{O}_3 - x\text{Cr}$ ceramics at 150°C, 200°C, 250°C, 300°C, 350°C and 400°C temperatures.

The DC conductivity values of different Cr doped PZT specimens were obtained by extrapolating the ac conductivity curves to the lowest frequency independent region. The dependence of temperature on dc conductivity was studied by plotting the σ_{dc} vs $1000/T$ curves and the activation energy values were calculated by fitting the plot data to the Arrhenius equation, $\sigma = \sigma_0 e^{-E_a/k_B T}$. Fig. 8.19 depicts the temperature dependant dc conductivity curves for all Cr doped compositions. The activation energy values are in agreement to the CIS and electric modulus results.

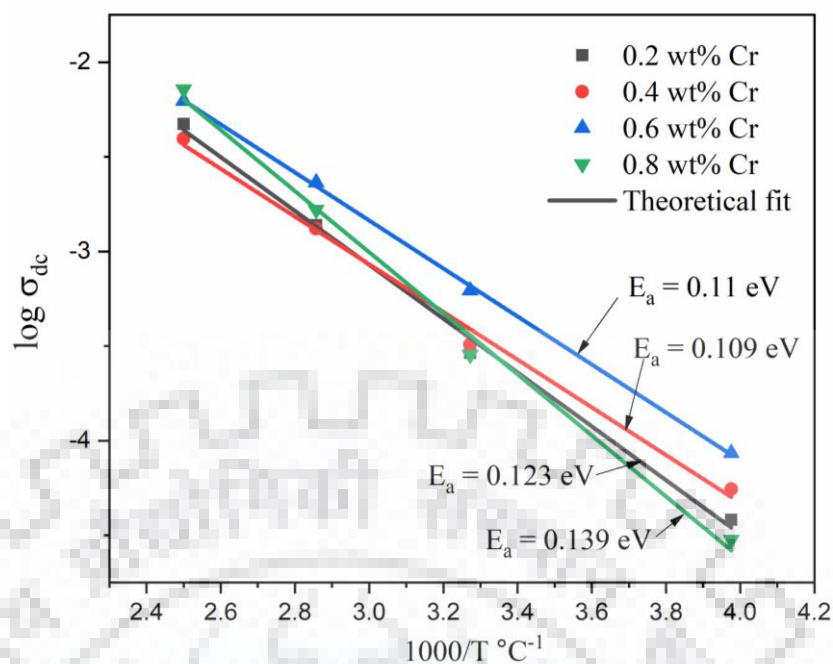


Fig. 8.19 Variation of dc conductivity as a function of inverse of absolute temperature of $\text{PbZr}_{0.52}\text{Ti}_{0.48}\text{O}_3 - x\text{Cr}$ ceramics. The calculated activation energy (E_a) values are marked onto the fitted data.

8.12 Energy storage studies of Cr doped PZT ceramics

The energy storage studies of PZT ceramics doped with different Cr_2O_3 contents were carried out by observing the P - E loops (Polarization vs Electric field) under an applied electric field maximum up to ~ 25 kV/cm as shown in Fig. 8.20. It can be observed that all the Cr doped compositions exhibit well defined hysteresis behaviour indicating their ferroelectric nature. Due to the fine grained microstructure of Cr doped PZT ceramics, decrease in macroscopic polarization and slim loops are observed. Such peculiar behaviour on decrease of grain size appears to be a general trend as reported in many studies (Buscaglia et al. 2006; Curecheriu et al. 2012; Helbig 2007). The remnant polarization, saturation polarization, coercive field, maximum electric field, energy storage density and energy efficiency calculated from the P - E loops are presented in Table 8.4. It can be noticed that the remnant polarization increases for the specimens as Cr content increases from 0.2 wt.% to 0.6 wt.%. This result is in agreement with the results obtained from ϵ_r vs T curves as dielectric constant is a function of polarization. In addition, the result further strengthens the dominant presence of +3 oxidation state of Cr (acceptor ion) above 0.2 wt.% Cr doped PZT, as observed by the decrease in dielectric permittivity (Fig. 8.9) and saturation polarization (P_s) values (Fig. 8.20). However, the increase in saturation polarization and dielectric constant for 0.8 wt.% Cr doped PZT suggests that the Cr ions are no longer in the

+ 3 state, rather they prefer to exist in +5 or +6 oxidation state acting as donor ions (Xia et al. 2016). It is noteworthy to mention that the Cr^{+3} ions should also increase the coercivity of the material, since the creation of oxygen vacancies pin the domains and increase the stability of domain walls. Similar behaviour is observed for 0.4 wt.% and 0.6 wt.% Cr, as can be observed by the high coercivity values in Fig. 8.20 (e). The above results and estimations are in agreement to the XPS results as shown in Fig. 8.8. The highest energy storage density is achieved for 0.2 and 0.8 wt.% Cr doped PZT specimens with energy efficiency greater than 63 % which is attributed to the dominant presence of donor Cr^{5+} ion.

Table 8.4 Energy storage parameters calculated from the P - E hysteresis loops of $\text{PbZr}_{0.52}\text{Ti}_{0.48}\text{O}_3 - x\text{Cr}$ ceramics.

Cr₂O₃ content (wt.%)	P_s/P_r (μC/cm²)	E_c/E_{max} (kV/cm)	E.S.D. (J/cm³)	Recoverable Energy density (J/cm³)	Energy Efficiency (%)
0.2	6.55/1.17	4.07/24.7	0.1	0.064	64.01
0.4	4.859/1.23	5.794/25.29	0.079	0.04	50.63
0.6	5.67/1.57	6.2/24.4	0.091	0.043	47.25
0.8	6.583/0.886	3.29/24.38	0.098	0.062	63.27

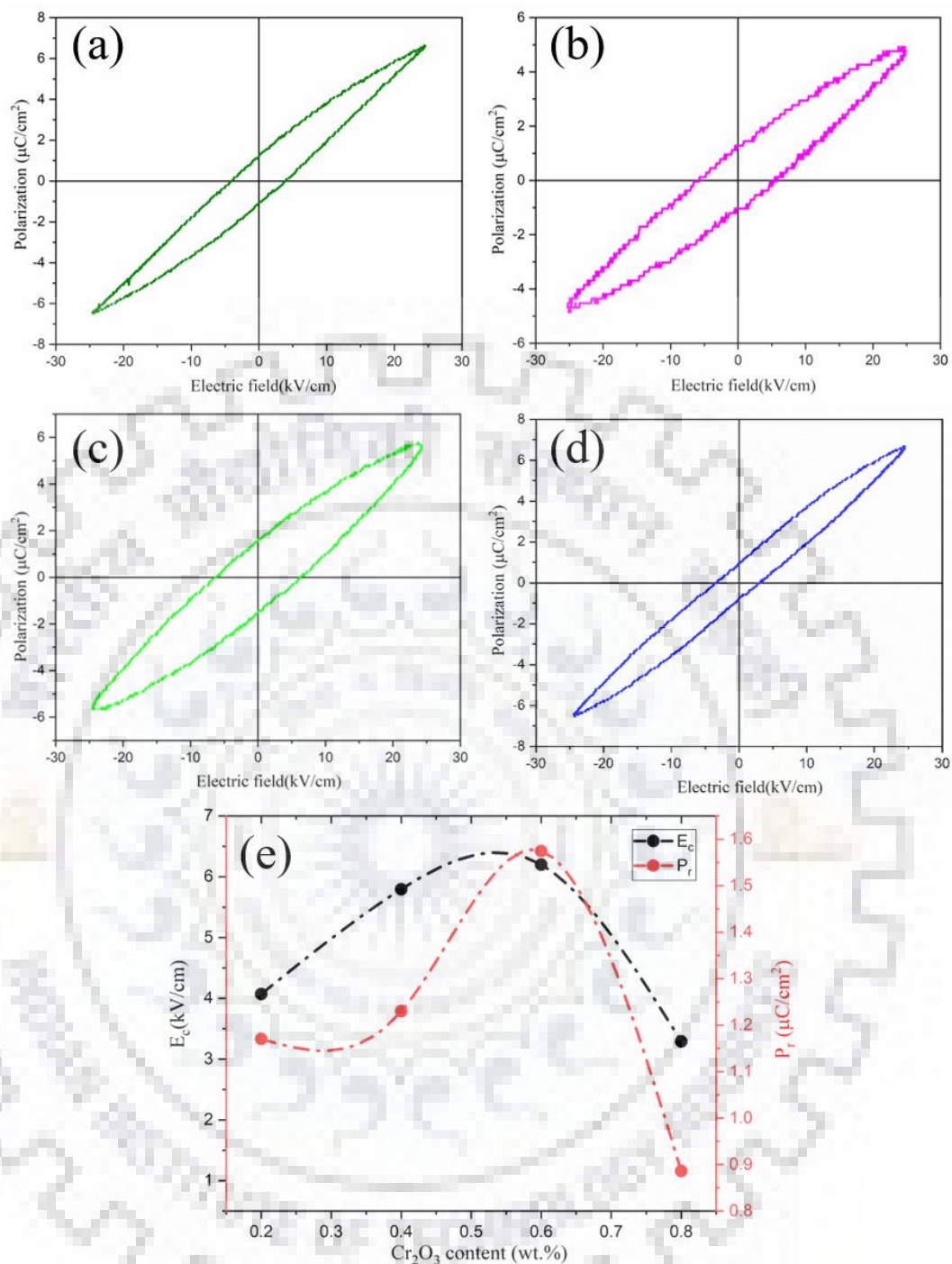


Fig. 8.20 Ferroelectric hysteresis loops of $\text{PbZr}_{0.52}\text{Ti}_{0.48}\text{O}_3 - x\text{Cr}$ ceramics for (a) $x = 0.2$, (b) $x = 0.4$, (c) $x = 0.6$ and (d) $x = 0.8$; (e) variation of coercive field and remnant polarization with Cr_2O_3 content.

8.13 Summary

The microstructure, phase analysis, dielectric studies, impedance and modulus spectroscopy and energy storage behaviour have been investigated for spark plasma sintered Cr doped PZT ceramics having 0.2, 0.4, 0.6, 0.8 wt.% Cr_2O_3 content. The range of particle size lies between

200 and 500 nm and the particles mostly exhibit faceted morphology. The XRD patterns reveal tetragonal phase structure with $P4mm$ space group for each of the doped specimens. The perovskite structure is not distorted by introduction of Cr ions and no separate peaks related to Cr has been detected which indicates solubility of Cr ions in the PZT ceramics. The displacement profiles for all the specimens reach a constant value prior to the completion of soaking stage which indicates that the SPS parameters are adequate. The Cr doped specimen's exhibit ≥ 99.3 % relative density and highly dense microstructure. The average grain size of Cr doped specimens is lower than the average grain size of undoped PZT specimens. The average grain size is further reduced on increase of Cr content as the Cr ions accumulate at the grain boundaries and hinders grain growth. The analysis of XRD patterns of sintered Cr doped specimens reveal change in lattice parameters and the presence of pyrochlore impurity phase reduce on increase of Cr content to 0.8 wt.%. The dielectric constant of the doped specimens decreases on addition of Cr ions up to 0.6 wt.% Cr and then further increases for 0.8 wt.% Cr. Such dielectric behavior has been explained on the basis of multivalent nature of Cr ions that may exist in +3, +5 or +6 states. The decrease in dielectric permittivity obtained from 0.2 to 0.6 wt.% Cr addition are attributed to the Cr^{3+} ions acting as acceptor ions as observed in XPS spectra analysis. However, it is suggested that the Cr^{3+} ions oxidize to +5 or +6 oxidation states as shown by the enhanced dielectric properties of 0.8 wt.% Cr doped specimen. The impedance and modulus spectroscopic studies reveal the contributions from grain relaxation in the material and confirm the non-Debye type of relaxation in the material. The loss peaks signify relaxation process in the material, and it was used to calculate the respective relaxation time (τ) from the impedance and modulus plots. The plots of $\log(\tau)$ vs $10^3 T^{-1}$ for each of the doped specimens follow the Arrhenius behaviour and the curves were fitted to the Arrhenius equation to calculate the activation energy values. The modulus studies reveal the presence of hopping mechanism in the material. The DC conductivity curves show a typical Arrhenius type behaviour of electrical conductivity. The activation energy for 0.6 wt.% Cr doped PZT specimen was calculated to be 0.11 eV. The energy storage studies reveal well defined hysteresis loops typical of ferroelectric materials. The remnant polarization of the doped specimens increased on addition of Cr up to 0.6 wt.% which are in agreement to the analysis of XPS spectra and dielectric properties. The highest energy storage density ($\sim 0.1 \text{ J/cm}^3$) and efficiency ($\sim 64\%$) was observed for both 0.2 wt.% and 0.8 wt.% Cr doped PZT specimen which is attributed to the dominant presence of donor Cr^{5+} ion.

Chapter 9

Conclusion and Future scope

In this chapter, the overall conclusion and future scope of the thesis are presented.

9.1 Conclusions

The spark plasma sintered PZT ceramics having different phase compositions are synthesized successfully and characterized. All sintered PZT specimens exhibited density greater than 98% of theoretical density. Moreover, the PZT ceramics with MPB composition are also synthesized and the effect of spark plasma sintering temperature on dielectric and energy storage performance has been investigated. The average grain size lies in the range of 15 - 37 nm for which the increase in grain size is observed with an increase in sintering temperature. It is observed that all specimens having MPB composition show highly dense nanostructured morphology. However, the specimens sintered at 900°C and 950°C show superior dielectric and energy storage performance as compared to other samples. The analysis of XRD data by Rietveld refinement reveals the coexistence of phases in these samples which contribute to the enhanced dielectric performance. The presence of monoclinic phase in the specimen sintered at 900°C permits increased number of polarization domains resulting in higher dielectric performance. The variation in phase composition with sintering temperature suggests that the spark plasma sintering conditions also need to be optimized.

The complex impedance and modulus spectroscopy studies reveal grain and grain boundary relaxation phenomena in the PZT specimens. The low frequency peaks in the respective plots of Z'' and M'' vs frequency fall at the same frequency for SPS-850, SPS-900, and SPS-950, suggesting delocalized relaxation mechanism or long range motion of charge carriers. The Nyquist plots of all PZT samples show depressed semi-circular arcs that confirm non Debye type behaviour. Grain boundaries are found to be more resistive and capacitive as compared to grains. Complex electric modulus spectra are studied to deconvolute the grain and grain boundary contributions to the relaxation mechanism for which the complex impedance spectra has a limitation. The capacitance and resistance of grain and grain boundary contributions of SPS-900

are determined and the values are $C_g = 1.60 \times 10^{-11}$ F, $R_g = 1.06 \times 10^5$ Ω and $C_{gb} = 2.57 \times 10^{-10}$ F, $R_{gb} = 5.80 \times 10^8$ Ω . Hence it may be inferred from the range of studies conducted that ferroelectric material $\text{PbZr}_{0.52}\text{Ti}_{0.48}\text{O}_3$ spark plasma sintered at 900°C shows highest energy storage efficiency of 66.38 % and saturation polarization (P_s) of $17.32 \mu\text{C}/\text{cm}^2$ at E_{max} of 46.67 kV/cm along with highest ϵ_{max} of ~ 8000 ($T_C \sim 335^\circ\text{C}$) at 100 kHz.

The dielectric and energy storage performance of spark plasma sintered $\text{PbZr}_{0.52}\text{Ti}_{0.48}\text{O}_3$ is compared with that of conventionally sintered (CS) counterpart. The sintering time is greatly reduced to the order of minutes for the SPS samples as compared to time requirements of hours for CS samples. The high sintering temperature applied in the CS sample increases the evaporation of PbO resulting in compositional variation. The large volume of grain boundaries in SPS sample act as amorphous phase, which limits the mobility of charge carriers resulting in low conductivity compared to that of CS sample. The temperature dependent permittivity curves reveal two dielectric peaks, one at $T_C \sim 320^\circ\text{C}$ and the other at $T_C \sim 450^\circ\text{C}$. However, the broad dielectric peaks observed for CS sample may indicate the compositional fluctuation. The analysis of P vs E data reveals that the constituting P - E loops are slimmer having lower remnant polarization for SPS samples. In addition, the energy storage efficiency of SPS sample is two times that of CS sample. The underlying reason for such behaviour is due to the suppression of hysteresis behaviour in fine-grained SPS samples and low compositional fluctuation.

The effect of 2 mol % La^{3+} doped PZT(52/48) ceramics on phase composition, microstructure, dielectric permittivity and energy storage performance has been studied. The spark plasma sintered La doped PZT ceramics shows increased dielectric permittivity than its conventionally sintered counterparts as also reported in the literature. The analysis of microstructure reveals decrease in grain size of PLZT ceramics over PZT ceramics due to smaller ionic radius of La^{3+} ions. The relaxation frequency occurs at higher frequencies on temperature increase of the samples, which suggests well defined relaxation mechanism that operates over large frequencies. The imaginary component of complex impedance and modulus lie in the same frequency suggesting Debye type relaxation. Low frequency conductivity behaviour indicates hopping of charge carriers, whereas long range conductivity is revealed at high frequency region. The energy storage studies of PLZT ceramics show higher remnant polarization and coercive field over undoped PZT ceramics. The polarization attainable at the maximum electric field applied is found to be higher for PLZT ceramics, however, the energy efficiency is decreased by 20% due to large hysteresis relative to undoped PZT ceramics.

The microstructure, phase analysis, impedance and modulus spectroscopy, dielectric and energy storage characteristics have been investigated on Cr doped (0.2, 0.4, 0.6 and 0.8 wt.%) PZT (52/48) ceramics. The range of particle size lies between 200 and 500 nm and the particles mostly exhibit faceted morphology. The Cr doped specimens exhibit ≥ 99.3 % relative density and highly dense microstructure. The average grain size is further reduced on increase of Cr content as the Cr ions accumulate at the grain boundaries and hinder grain growth. The dielectric constant of the doped specimens increases on addition of Cr ions up to 0.6 wt.% Cr and then further reduces for 0.8 wt.% Cr. Such dielectric behavior has been explained on the basis of multivalent nature of Cr ions that may exist in +3, +5, +6 states. The impedance and modulus spectroscopic studies reveal the contributions from grain relaxation in the material and confirm the non-debye type of relaxation in the material. The modulus studies reveal the presence of hopping mechanism in the material. The DC conductivity curves show a typical Arrhenius type behaviour of electrical conductivity. The remnant polarization and coercive field of the doped specimens increase on addition of Cr up to 0.6 wt.% which are in agreement to the dielectric properties results. The highest energy storage density ($\sim 0.1 \text{ J/cm}^3$) and efficiency ($\sim 64.01\%$) is observed for both 0.2 wt.% and 0.4 wt.% Cr doped PZT specimens.

9.2 Comparative features

In this section, the comparative features on aspects of crystallite size, lattice parameters, lattice strain, dielectric performance and ferroelectric properties are discussed.

9.2.1 Variation in lattice parameters, crystallite size and lattice strain with sintering temperature

Table 9.1 presents the crystallite size, lattice parameters and lattice strain values of PZT samples sintered at different temperatures. The tetragonality (c/a) of PZT ceramic increases slightly with increase in sintering temperature with the exception of PZT ceramic sintered at 900°C. The SPS-900 sample shows an increase in tetragonality by 2.3%, which may be attributed to the coexistence of monoclinic and tetragonal phases in the material. On the increase of sintering temperature from 800°C, 850°C, 900°C to 950°C, the crystallite size increases from 127 Å to 353 Å. This is due to the effect of grain growth with temperature increase. The lattice strain is estimated to be higher for SPS-900 and SPS-950 samples due to coexistence of phases in the materials.

Table 9.1 Lattice parameters, crystallite size and lattice strain values of PZT samples sintered at different temperatures.

Parameters	SPS-800	SPS-850	SPS-900	SPS-950
a	4.000054	4.019(2)	3.9617(14)	4.0326(10)
c	4.090632	4.104(3)	4.1390(2)	4.1347(12)
c/a	1.023	1.021(1)	1.045(7)	1.025(3)
Crystallite size (Å)	127(32)	151(11)	181(33)	353(24)
Lattice strain (%)	0.2(4)	0.2(3)	0.4(7)	1.1(6)

9.2.2 Variation in crystallite size and lattice strain with composition of PZT

Table 9.2 presents the crystallite size and lattice strain values of undoped and doped PZT samples prepared by SPS as well as conventional sintering technique. The crystallite size of spark plasma sintered PZT (181 Å) is very small when compared to the conventionally sintered sample (1963 Å) due to the difference in sintering mechanism and lower sintering temperature used. The sintering temperature used in SPS and CS sample are 900°C and 1200°C respectively. The crystallite size of PZT doped with 2 mol% La becomes lower compared to the undoped PZT sample as the substituent La^{2+} (1.22 Å) ion is smaller than the substituting Pb^{2+} (1.32 Å) ion. Whereas for Cr doped PZT samples, the crystallite size is found to increase with increase in Cr content as Cr^{3+} (0.755 Å) ion is bigger than $\text{Zr}^{4+}/\text{Ti}^{4+}$ (~0.68 Å) ions. The lattice strain is estimated to be higher for doped PZT samples as the dopants induce lattice distortion and may impact the ferroelectric and dielectric properties of PZT.

Table 9.2 Variation of crystallite size and lattice strain with compositions of PZT.

	PbZr_{0.52}Ti_{0.48}O₃	PbZr_{0.52}Ti_{0.48}O₃ (CS)	Pb_{0.98}La_{0.02}Zr_{0.52}Ti_{0.48}O₃	PbZr_{0.52}Ti_{0.48}O₃ – 0.2Cr	PbZr_{0.52}Ti_{0.48}O₃ – 0.4Cr	PbZr_{0.52}Ti_{0.48}O₃ – 0.6Cr	PbZr_{0.52}Ti_{0.48}O₃ – 0.8Cr
Crystallite size (Å)	181(33)	1963(96)	120(53)	155(51)	168(28)	210(20)	238(24)
Lattice strain (%)	0.1(7)	0.4(2)	0.3(2)	0.2(4)	0.4(2)	0.5(6)	0.4(3)

9.2.3 Variation of dielectric properties with different composition of the PZT samples

Table 9.3 presents dielectric constant, complex impedance, complex modulus and conductivity values of different samples obtained at room temperature and at 1 kHz frequency. The dielectric constant at T_c of spark plasma sintered PZT sample (~26000) is significantly higher than that of conventionally sintered sample (~7500) which is mainly due to the high density achieved in SPS ceramics. For doped PZT samples, the dielectric constant is estimated to be highest for La doped (soft dopant) and lowest for Cr doped (hard dopant) PZT sample. The underlying reason is associated with the softening and hardening mechanisms in the material as discussed in section 2.5.1. The ac conductivity value at 1 kHz for SPS sample is found to be higher when compared to conventional sintering (CS) sample. For doped PZT samples, the conductivity decreases for Cr doped PZT samples, whereas it is higher for La doped PZT samples. The Z' and Z'' values are lower for Cr – doped PZT and La – doped PZT samples compared to undoped PZT samples. Similar observations could also be made for complex modulus parameters.

Table 9.3 Room temperature dielectric constant (ϵ_{RT}), real part (Z') and imaginary part (Z'') of complex impedance, real part (M') and imaginary part (M'') of complex modulus and conductivity (σ) values at 1 kHz. (Dielectric maxima (ϵ_m) is measured at T_c).

	ϵ_m at T_c	ϵ_{RT}	σ (S/m)	Z' (Ω)	Z'' (Ω)	M'	M''
PbZr_{0.52}Ti_{0.48}O₃	25966	910	51.94 $\times 10^{-7}$	40.7 $\times 10^5$	56.12 $\times 10^5$	147.7 $\times 10^{-4}$	107.1 $\times 10^{-4}$
PbZr_{0.52}Ti_{0.48}O₃ (CS)	7550	545	1.65 $\times 10^{-7}$				
(Pb_{0.98}La_{0.02}) (Zr_{0.52}Ti_{0.48})O₃	43482	2312	0.114	289	0.287	4.46 $\times 10^{-10}$	0.032 $\times 10^{-4}$
PbZr_{0.52}Ti_{0.48}O₃ – 0.2Cr	6289	863.5	5.72 $\times 10^{-7}$	8.71 $\times 10^5$	11.13 $\times 10^5$	26.4 $\times 10^{-4}$	0.83 $\times 10^{-4}$
PbZr_{0.52}Ti_{0.48}O₃ – 0.4Cr	4238	684.1	10.12 $\times 10^{-7}$	1.97 $\times 10^5$	11.27 $\times 10^5$	8.04 $\times 10^{-4}$	4.8 $\times 10^{-4}$
PbZr_{0.52}Ti_{0.48}O₃ – 0.6Cr	4911	704.9	7.13 $\times 10^{-7}$	8.41 $\times 10^5$	1.68 $\times 10^5$	4.52 $\times 10^{-4}$	2.27 $\times 10^{-4}$
PbZr_{0.52}Ti_{0.48}O₃ – 0.8Cr	10110	922.4	2.39 $\times 10^{-7}$	2.52 $\times 10^5$	2.47 $\times 10^5$	7.05 $\times 10^{-4}$	0.72 $\times 10^{-4}$

9.2.4 Variation of ferroelectric properties with different composition of the PZT samples

Table 9.4 presents the energy storage parameters calculated from the P-E loops measured for different samples. The saturation polarization (P_s) and remnant polarization (P_r) values of undoped PZT ceramics increases on doping PZT with La ions, whereas P_s and P_r decrease on doping PZT with Cr ions. Such behaviour is presumably due to the soft and hard dopant behaviour of La and Cr ions. On the other hand, the P_s and P_r of CS samples are higher than that of SPS samples due to large grain size and less number of grain boundaries. The grain boundary region acts as low permittivity layers that decrease polarization by creating internal bias fields. The highest energy storage density is observed for CS samples, whereas it is lowest for Cr doped PZT ceramics. However, the energy efficiency for CS samples (< 34%) is the lowest due to high remnant polarization. The energy storage efficiency of undoped PZT and Cr doped PZT are observed at or near ~65%. It is to be noted that SPS samples have higher energy efficiency compared to CS sample which can be attributed to low remnant polarization and low coercivity.

Table 9.4 Energy storage parameters calculated from the P - E loops of undoped and doped compositions of PZT.

	P_s ($\mu\text{C}/\text{cm}^2$)	P_r ($\mu\text{C}/\text{cm}^2$)	E_c (kV/cm)	E_{max} (kV/cm)	E_{st} (J/cm^3)	E_{re} (J/cm^3)	η (%)
PbZr_{0.52}Ti_{0.48}O₃	17.32	2.67	5.92	46.67	1.13	0.75	66.38
PbZr_{0.52}Ti_{0.48}O₃ (CS)	28.745	9.73	12.54	46.57	2.11	0.71	33.68
(Pb_{0.98}La_{0.02}) (Zr_{0.52}Ti_{0.48})O₃	22.82	6.2	11.06	42.51	0.66	0.3	45.45
PbZr_{0.52}Ti_{0.48}O₃ – 0.2Cr	6.55	1.17	4.07	24.7	0.1	0.064	64.01
PbZr_{0.52}Ti_{0.48}O₃ – 0.4Cr	4.859	1.23	5.794	25.29	0.079	0.04	50.63
PbZr_{0.52}Ti_{0.48}O₃ – 0.6Cr	5.67	1.57	6.2	24.4	0.091	0.043	47.25
PbZr_{0.52}Ti_{0.48}O₃ – 0.8Cr	6.583	0.886	3.29	24.38	0.098	0.062	63.27

9.3 Future scope

The present study reports the synthesis of doped and undoped PZT ceramics by using SPS technique to understand and evaluate the effects of sintering parameters on dielectric and energy storage performance. It is suggested that further investigations on the following points can be conducted for future work: -

- The analysis of ferroelectric domains by transmission electron microscopy (TEM) for doped and undoped PZT specimens to develop a processing-domain structure-property relation,
- The piezoelectric and pyroelectric studies on spark plasma sintered PZT specimens,
- The simulation studies to further expand and evaluate the findings of the present work,
- The effect of variation in soaking time of the spark plasma sintering of the specimens to find its influence on the degree of compositional fluctuation.
- The studies related to initiation and identification of defects during spark plasma sintering and their effect on dielectric and energy storage performance of the sintered materials.
- The temperature dependent energy storage behaviour on spark plasma sintered specimens followed by electrical fatigue behaviour studies.

Bibliography

- Ahmed, M.A., Samiha T. Bishay, and G. Abdelatif. 2001. "Effect of Ytterbium on the Electrical Properties of Li–Co Ferrite." *Journal of Physics and Chemistry of Solids* 62(6): 1039–46.
- Algueró, M. et al. 2009. "Macroscopic Ferroelectricity and Piezoelectricity in Nanostructured BiScO₃-PbTiO₃ Ceramics." *Applied Physics Letters* 94(1).
- Anand, Gagan, Piyush Kuchhal, and P. Sarah. 2015. "AC and DC Conductivity Studies on Lead-Free Ceramics: Sr_{1-x}Ca_xBi₄Ti₄O₁₅ (x = 0, 0.2, 0.4, 0.6, 0.8)." *Particulate Science and Technology* 33(1): 41–46.
- Anselmi-Tamburini, U. et al. 2012. "Field Assisted Sintering Mechanisms." In Springer, Berlin, Heidelberg, Sintering. *Engineering Materials* (35)159–93.
- Arlt, G. 1987. "The Role of Domain Walls on the Dielectric, Elastic and Piezoelectric Properties of Ferroelectric Ceramics." *Ferroelectrics* 76(1): 451–58.
- . 1989. "Microstructure and Domain Effects in Ferroelectric Ceramics." *Ferroelectrics* 91(1): 3–7.
- . 1990. "The Influence Of Microstructure On The Properties Of Ferroelectric Ceramics." *Ferroelectrics* 104(1): 217–27.
- Arlt, G., and N. A. Pertsev. 1991. "Force Constant and Effective Mass of 90° domain Walls in Ferroelectric Ceramics." *Journal of Applied Physics* 70(4): 2283–89.
- Atkin, R. B., R. L. Holman, and Richard M. Fulrath. 1971. "Substitution of Bi and Nb Ions in Lead Zirconate-Titanate." *Journal of the American Ceramic Society* 54(2): 113–15.
- Bain, Ashim Kumar, and Prem Chand. 2017. *Ferroelectrics*. Weinheim, Germany: Wiley-VCH Verlag GmbH & Co. KGaA.
- Bajpai, K. K., K. Sreenivas, Ajai K. Gupta, and A. K. Shukla. 2019. "Cr-Doped Lead Lanthanum Zirconate Titanate (PLZT) Ceramics for Pyroelectric and Energy Harvesting Device Applications." *Ceramics International* 45(11): 14111–20.
- Barnett, Harold M. 1962. "Evidence for a New Phase Boundary in the Ferroelectric Lead Zirconate-Lead Titanate System." *Journal of Applied Physics* 33(4): 1606.
- Barsoum, Michel. 2019. "Fundamentals of Ceramics." *CRC Press*.

- Becker, A. et al. 2012. "The Effect of Peltier Heat during Current Activated Densification." *Applied Physics Letters* 101(1): 013113.
- Bellaiche, L., Alberto García, and David Vanderbilt. 2000. "Finite-Temperature Properties of $\text{Pb}(\text{Zr}_{1-x}\text{Ti}_x)\text{O}_3$ Alloys from First Principles." *Physical Review Letters* 84(23): 5427–30.
- . 2001. "Electric-Field Induced Polarization Paths in $\text{Pb}(\text{Zr}_{1-x}\text{Ti}_x)\text{O}_3$ Alloys." *Physical Review B* 64(6): 060103.
- Berlincourt, D., H. H.A. Krueger, and B. Jaffe. 1964. "Stability of Phases in Modified Lead Zirconate with Variation in Pressure, Electric Field, Temperature and Composition." *Journal of Physics and Chemistry of Solids* 25(7): 659–74.
- Berlincourt, Don. 1992. "Piezoelectric Ceramic Compositional Development." *Journal of the Acoustical Society of America* 91(5): 3034–40.
- Bhalla, A. S., R. Guo, and R. Roy. 2000. "The Perovskite Structure - a Review of Its Role in Ceramic Science and Technology." *Materials Research Innovations* 4(1): 3–26.
- Bokov, A. A., and Z.-G. Ye. 2004. "Domain Structure in the Monoclinic Pm Phase of $\text{Pb}(\text{Mg}_{1/3}\text{Nb}_{2/3})\text{O}_3\text{-PbTiO}_3$ Single Crystals ." *Journal of Applied Physics* 95(11): 6347–59.
- Bonanos, N., B. C. H. Steele, and E. P. Butler. 2005. "Applications of Impedance Spectroscopy." In *Impedance Spectroscopy*, Wiley, 205–537.
- Buscaglia, Maria Teresa et al. 2006. "High Dielectric Constant and Frozen Macroscopic Polarization in Dense Nanocrystalline BaTiO_3 Ceramics." *Physical Review B - Condensed Matter and Materials Physics* 73(6).
- Caglioti, G., A. Paoletti, and F. P. Ricci. 1958. "Choice of Collimators for a Crystal Spectrometer for Neutron Diffraction." *Nuclear Instruments* 3(4): 223–28.
- Cao, Wenwu. 2008. "Constructing Landau-Ginzburg-Devonshire Type Models for Ferroelectric Systems Based on Symmetry." *Ferroelectrics* 375(1): 28–39.
- Cao, Wenwu, and L. Eric Cross. 1993a. "Distribution Functions of Coexisting Phases in a Complete Solid Solution System." *Journal of Applied Physics* 73(7): 3250–55.
- . 1993b. "Theoretical Model for the Morphotropic Phase Boundary in Lead Zirconate-Lead Titanate Solid Solution." *Physical Review B* 47(9): 4825–30.
- Cao, Wenwu, and Clive A. Randall. 1996. "Grain Size and Domain Size Relations in Bulk Ceramic Ferroelectric Materials." *Journal of Physics and Chemistry of Solids* 57(10): 1499–1505.
- Cao, Zhenzhu et al. 2015. "Extrinsic and Intrinsic Contributions for Dielectric Behavior of $\text{La}_2\text{NiMnO}_6$ Ceramic." *Physica B: Condensed Matter* 477: 8–13.

- Chandra Sati, Prakash, Manoj Kumar, and Sandeep Chhoker. 2015. "Low Temperature Ferromagnetic Ordering and Dielectric Properties of $\text{Bi}_{1-x}\text{Dy}_x\text{FeO}_3$ Ceramics." *Ceramics International* 41(2): 3227–36.
- Chen, Haisheng et al. 2009. "Progress in Electrical Energy Storage System: A Critical Review." *Progress in Natural Science* 19(3): 291–312.
- Chen, Kongfa et al. 2016. "Boron Deposition and Poisoning of $\text{La}_{0.8}\text{Sr}_{0.2}\text{MnO}_3$ Oxygen Electrodes of Solid Oxide Electrolysis Cells under Accelerated Operation Conditions." *International Journal of Hydrogen Energy* 41(3): 1419–31.
- Chen, Qin et al. 2008. "High Field Tunneling as a Limiting Factor of Maximum Energy Density in Dielectric Energy Storage Capacitors." *Applied Physics Letters* 92(14): 142909.
- Chen, Qin, Yang Shen, Shihai Zhang, and Q M Zhang. 2015. "Polymer-Based Dielectrics with High Energy Storage Density." *Annual Review of Materials Research* 45(1): 433–58.
- Chen, Shengchen, Xiucui Wang, Tongqing Yang, and Jinfei Wang. 2014. "Composition-Dependent Dielectric Properties and Energy Storage Performance of $(\text{Pb},\text{La})(\text{Zr},\text{Sn},\text{Ti})\text{O}_3$ Antiferroelectric Ceramics." *Journal of Electroceramics* 32(4): 307–10.
- Chen, Tze Chiun, Chai Liang Thio, and Seshu B. Desu. 1997. "Impedance Spectroscopy of $\text{SrBi}_2\text{Ta}_2\text{O}_9$ and $\text{SrBi}_2\text{Nb}_2\text{O}_9$ Ceramics Correlation with Fatigue Behavior." *Journal of Materials Research* 12(10): 2628–37.
- Choi, Doo Hyun et al. 2015. "Energy and Power Densities of Capacitors and Dielectrics." In *IEEE International Workshop on Integrated Power Packaging, IWIPP 2015*, Institute of Electrical and Electronics Engineers Inc., 52–55.
- Christen, Thomas, and Martin W. Carlen. 2000. "Theory of Ragone Plots." *Journal of Power Sources* 91(2): 210–16.
- Clarke, R., and A. M. Glazer. 1976. "Critical Phenomena in Ferroelectric Crystals of Lead Zirconate Titanate." *Ferroelectrics* 14(1): 695–97.
- Coondoo, Indrani et al. 2012. "Impedance Spectroscopy and Conductivity Studies in $\text{SrBi}_2(\text{Ta}_{1-x}\text{W}_x)_2\text{O}_9$ Ferroelectric Ceramics." *Physica B: Condensed Matter* 407(24): 4712–20.
- Cordero, F., F. Craciun, and C. Galassi. 2007. "Low-Temperature Phase Transformations of $\text{PbZr}_{1-x}\text{Ti}_x\text{O}_3$ in the Morphotropic Phase-Boundary Region." *Physical Review Letters* 98(25): 255701.
- Cordero, F, F Trequattrini, F Craciun, and C Galassi. 2011. "Octahedral Tilting, Monoclinic Phase and the Phase Diagram of PZT." *Journal of Physics: Condensed Matter* 23(41): 415901.
- Coşkun, M. et al. 2018. "The Electrical Modulus and Other Dielectric Properties by the Impedance Spectroscopy of LaCrO_3 and $\text{LaCr}_{0.90}\text{Ir}_{0.10}\text{O}_3$ Perovskites." *RSC Advances* 8(9): 4634–48.

- Curecheriu, Lavinia et al. 2012. "Grain Size-Dependent Properties of Dense Nanocrystalline Barium Titanate Ceramics." *Journal of the American Ceramic Society* 95(12): 3912–21.
- Dai, Xunhu, Z. Xu, and Dwight Viehland. 1996. "Long-Time Relaxation from Relaxor to Normal Ferroelectric States in $\text{Pb}_{0.91}\text{La}_{0.06}(\text{Zr}_{0.65}\text{Ti}_{0.35})\text{O}_3$." *Journal of the American Ceramic Society* 79(7): 1957–60.
- Damjanovic, Dragan. 1998. "Ferroelectric, Dielectric and Piezoelectric Properties of Ferroelectric Thin Films and Ceramics." *Reports on Progress in Physics* 61(9): 1267.
- Devonshire, A.F. 1949. "XCVI. Theory of Barium Titanate." *The London, Edinburgh, and Dublin Philosophical Magazine and Journal of Science* 40(309): 1040–63.
- . 1951. "CIX. Theory of Barium Titanate—Part II." *The London, Edinburgh, and Dublin Philosophical Magazine and Journal of Science* 42(333): 1065–79.
- Dincer, Ibrahim. 2000. "Renewable Energy and Sustainable Development: A Crucial Review." *Renewable & sustainable energy reviews* 4(2): 157–75.
- Dissado, L A, and J C Fothergill. 1992. *Electrical Degradation and Breakdown in Polymers*. Peter Peregrinus, London.
- Dutta, S., and R. N.P. Choudhary. 2008. "Effect of Trivalent Iron Substitution on Structure and Properties of PLZT Ceramics." *Applied Physics A: Materials Science and Processing* 90(2): 323–28.
- Eitel, Richard E. et al. 2001. "New High Temperature Morphotropic Phase Boundary Piezoelectrics Based on $\text{Bi}(\text{Me})\text{O}_3\text{-PbTiO}_3$ Ceramics." *Japanese Journal of Applied Physics, Part 1: Regular Papers and Short Notes and Review Papers* 40(10): 5999–6002.
- Eric Cross, Leslie. 1995. "Ferroelectric Materials for Electromechanical Transducer Applications." *Japanese Journal of Applied Physics* 34(5S): 2525–32.
- Essaleh, L. et al. 2016. "Analysis of Complex Impedance of $\text{P-CuIn}_3\text{Se}_5$ by Impedance Spectroscopy." *Journal of Alloys and Compounds* 688: 210–15.
- Fernández, Jose F et al. 1998. "Compositional Fluctuations and Properties of Fine-Grained Acceptor-Doped PZT Ceramics." *Article in Journal of the European Ceramic Society* 18(12): 1695–1705.
- Fousek, Jan, and Václav Janovec. 1969. "The Orientation of Domain Walls in Twinned Ferroelectric Crystals." *Journal of Applied Physics* 40(1): 135–42.
- Fu, Huaxiang, and Ronald E. Cohen. 2000. "Polarization Rotation Mechanism for Ultrahigh Electromechanical Response in Single-Crystal Piezoelectrics." *Nature* 403(6767): 281–83.
- Gao, Jinghui et al. 2011. "Microstructure Basis for Strong Piezoelectricity in Pb-Free $\text{Ba}(\text{Zr}_{0.2}\text{Ti}_{0.8})\text{O}_3\text{-(Ba}_{0.7}\text{Ca}_{0.3})\text{TiO}_3$ Ceramics." *Applied Physics Letters* 99(9): 092901.

- Garg, Ajai, and T. C. Goel. 1999. "Mechanical and Electrical Properties of PZT Ceramics (Zr:Ti = 0.40:0.60) Related to Nd^{3+} Addition." *Materials Science and Engineering B: Solid-State Materials for Advanced Technology* 60(2): 128–32.
- Geetika, and A. M. Umarji. 2010. "The Influence of Zr/Ti Content on the Morphotropic Phase Boundary in the PZT-PZN System." *Materials Science and Engineering B: Solid-State Materials for Advanced Technology* 167(3): 171–76.
- Gerson, R., and Hans Jaffe. 1963. "Electrical Conductivity in Lead Titanate Zirconate Ceramics." *Journal of Physics and Chemistry of Solids* 24(8): 979–84.
- Gerson, Robert. 1960. "Variation in Ferroelectric Characteristics of Lead Zirconate Titanate Ceramics Due to Minor Chemical Modifications." *Journal of Applied Physics* 31(1): 188–94.
- Gharb, N. Bassiri, and S. Trolier-Mckinstry. 2005. "Dielectric Nonlinearity of $\text{Pb}(\text{Yb}_{1/2}\text{Nb}_{1/2})\text{O}_3$ - PbTiO_3 Thin Films with $\{100\}$ and $\{111\}$ Crystallographic Orientation." *Journal of Applied Physics* 97(6): 064106.
- Ginzburg, V. L., and L. D. Landau. 2008. "On the Theory of Superconductivity." In *On Superconductivity and Superfluidity*, Springer Berlin Heidelberg, 113–37.
- Glazer, A. M. et al. 2004. "Influence of Short-Range and Long-Range Order on the Evolution of the Morphotropic Phase Boundary in $\text{Pb}(\text{Zr}_{1-x}\text{Ti}_x)\text{O}_3$." *Physical Review B - Condensed Matter and Materials Physics* 70(18): 1–9.
- "Global Piezoelectric Devices Market, Forecast to 2027." 2019. <https://www.prnewswire.com/news-releases/global-piezoelectric-devices-market-forecast-to-2027-a-42-41-billion-opportunity-301034314.html> (April 4, 2020).
- Goldschmidt, H. J., and J. R. Rait. 1943. "Silicates of the Perovskite Type of Structure." *Nature* 152(3856): 356.
- Gonnard, P., and M. Troccaz. 1978. "Dopant Distribution between A and B Sites in the PZT Ceramics of Type ABO_3 ." *Journal of Solid State Chemistry* 23(3–4): 321–26.
- Gross, Robert, Matthew Leach, and Ausilio Bauen. 2003. "Progress in Renewable Energy." *Environment International* 29(1): 105–22.
- Groza, Joanna R., and Antonios Zavaliangos. 2000. "Sintering Activation by External Electrical Field." *Materials Science and Engineering A* 287(2): 171–77.
- Guney, Mukrimin Sevket, and Yalcin Tepe. 2017. "Classification and Assessment of Energy Storage Systems." *Renewable and Sustainable Energy Reviews* 75: 1187–97.
- Guo, R. et al. 2000. "Origin of the High Piezoelectric Response in $\text{PbZr}_{1-x}\text{Ti}_x\text{O}_3$." *Physical Review Letters* 84(23): 5423–26.
- Haertling, Gene H. 1999. "Ferroelectric Ceramics: History and Technology." *Journal of the American Ceramic Society* 82(4): 797–818.

- Hall, Peter J., and Euan J. Bain. 2008. "Energy-Storage Technologies and Electricity Generation." *Energy Policy* 36(12): 4352–55.
- Han, Bing et al. 2017. "Temperature-Insensitive Piezoelectric Performance in $\text{Pb}(\text{Zr}_{0.52}\text{Ti}_{0.42}\text{Sn}_{0.02}\text{Nb}_{0.04})\text{O}_3$ Ceramics Prepared by Spark Plasma Sintering." *ACS Applied Materials and Interfaces* 9(39): 34078–84.
- Hao, Xihong. 2013. "A Review on the Dielectric Materials for High Energy-Storage Application." *Journal of Advanced Dielectrics* 03(01): 1330001.
- Hao, Xihong, Jiwei Zhai, and Xi Yao. 2009. "Improved Energy Storage Performance and Fatigue Endurance of Sr-Doped PbZrO_3 Antiferroelectric Thin Films." *Journal of the American Ceramic Society* 92(5): 1133–35.
- He, Lian Xing et al. 2001. "Effects of Cr_2O_3 Addition on the Piezoelectric Properties and Microstructure of $\text{PbZr}_x\text{Ti}_y(\text{Mg}_{1/3}\text{Nb}_{2/3})_{1-x-y}\text{O}_3$ Ceramics." *Journal of the European Ceramic Society* 21(6): 703–9.
- He, Lian Xing, and Cheng En Li. 2000. "Effects of Addition of MnO on Piezoelectric Properties of Lead Zirconate Titanate." *Journal of Materials Science* 35(10): 2477–80.
- Helbig, Uta. 2007. "Size Effect in Low Grain Size Neodymium Doped PZT Ceramics." *Journal of the European Ceramic Society* 27(7): 2567–76.
- Helke, G., and K. Lubitz. 2008. "Piezoelectric PZT Ceramics." In *Springer Series in Materials Science*, Springer Verlag, 89–130.
- Herbiet, R., U. Robels, H. Dederichs, and G. Arlt. 1989. "Domain Wall And Volume Contributions To Material Properties Of Pzt Ceramics." *Ferroelectrics* 98(1): 107–21.
- Hinterstein, M. et al. 2015. "Cyclic Electric Field Response of Morphotropic $\text{Bi}_{1/2}\text{Na}_{1/2}\text{TiO}_3$ - BaTiO_3 Piezoceramics." *Applied Physics Letters* 106(22): 222904.
- Hodge, I. M., M. D. Ingram, and A. R. West. 1976. "Impedance and Modulus Spectroscopy of Polycrystalline Solid Electrolytes." *Journal of Electroanalytical Chemistry* 74(2): 125–43.
- Holland, Troy B. et al. 2012. "Effects of Local Joule Heating during the Field Assisted Sintering of Ionic Ceramics." *Journal of the European Ceramic Society* 32(14): 3667–74.
- Hungría, T. et al. 2008. "Nanostructured Ceramics of $0.92\text{PbZn}_{1/3}\text{Nb}_{2/3}\text{O}_3$ - 0.08PbTiO_3 Processed by SPS of Nanocrystalline Powders Obtained by Mechanochemistry." *Nanotechnology* 19(15).
- Ibrahim, H., A. Ilinca, and J. Perron. 2008. "Energy Storage Systems-Characteristics and Comparisons." *Renewable and Sustainable Energy Reviews* 12(5): 1221–50.
- Inoue, Kiyoshi. 1965. U.S Patent 3,198,675, Aug 3 *Electric Discharge Heat Treatment of Metals in Electrolytes*.
- International Energy Agency. 2020. "Global Energy Review 2019 – Analysis - IEA." <https://www.iea.org/reports/global-energy-review-2019> (October 6, 2020).

- Isupov, V. A. 1975. "Comments on the Paper 'X-Ray Study of the PZT Solid Solutions near the Morphotropic Phase Transition.'" *Solid State Communications* 17(11): 1331–33.
- Isupov, V. A. 1968. "Properties of Pb (Ti, Zr) O₃ Piezoelectric Ceramics and Nature of Their Orientational Dielectric Polarization." *Soviet Physics Solid State, Ussr* 10(4): 989–91.
- Jacob, Reenu, Harikrishnan Nair, and Jayakumari Isac. 2015. "Impedance Spectroscopy and Dielectric Studies of Nanocrystalline Iron Doped Barium Strontium Titanate Ceramics." *Processing and Application of Ceramics* 9(2): 73–79.
- Jaffe, B., R.S. Roth, and S. Marzullo. 1955. "Properties of Piezoelectric Ceramics in the Solid-Solution Series Lead Titanate-Lead Zirconate-Lead Oxide: Tin Oxide and Lead Titanate-Lead Hafnate." *Journal of Research of the National Bureau of Standards* 55(5): 239.
- Jaffe, B, W R Cook, and H Jaffe. 1971. "Piezoelectric Ceramics (Academic Press, London, 1971)."
- Jain, Pushkar, and Eugene J. Rymaszewski. 2002. "Embedded Thin Film Capacitors - Theoretical Limits." In *IEEE Transactions on Advanced Packaging*, 454–58.
- Jia, Q. X., X. D. Wu, S. R. Foltyn, and P. Tiwari. 1995. "Structural and Electrical Properties of Ba_{0.5}Sr_{0.5}TiO₃ Thin Films with Conductive SrRuO₃ Bottom Electrodes." *Applied Physics Letters* 66(17): 2197.
- Jiang, B., and L. A. Bursill. 1999. "Phenomenological Theory of Size Effects in Ultrafine Ferroelectric Particles of Lead Titanate." *Physical Review B - Condensed Matter and Materials Physics* 60(14): 9978–82.
- Jin, B M, J. Kim, and S C Kim. 1997. "Effects of Grain Size on the Electrical Properties of PbZr_{0.52}Ti_{0.48}O₃ Ceramics." *Applied Physics A: Materials Science and Processing* 65(1): 53–56.
- Jin, Li, Fei Li, and Shujun Zhang. 2014. "Decoding the Fingerprint of Ferroelectric Loops: Comprehension of the Material Properties and Structures" ed. D. J. Green. *Journal of the American Ceramic Society* 97(1): 1–27.
- Jo, Hwan Ryul, and Christopher S. Lynch. 2016. "A High Energy Density Relaxor Antiferroelectric Pulsed Capacitor Dielectric." *Journal of Applied Physics* 119(2): 0–7.
- Johnsson, Mats, and Peter Lemmens. 2005. "Crystallography and Chemistry of Perovskites." *Handbook of Magnetism and Advanced Magnetic Materials*.
- Joshi, Shraddha, and Smita Acharya. 2016. "Influences of Liquid-Phase Sintering on Structure, Grain Growth, and Dielectric Behavior of PbZr_{0.52}Ti_{0.48}O₃ Ceramics." *International Journal of Applied Ceramic Technology* 13(4): 753–62.
- Takegawa, K. et al. 1977. "A Compositional Fluctuation and Properties of Pb(Zr, Ti)O₃." *Solid State Communications* 24(11): 769–72.

- Kakegawa, K., M. Wada, Y. J. Wu, and N. Uekawa. 2005. "Change in Compositional Fluctuation in $\text{Pb}(\text{Zr}_x\text{Ti}_{1-x})\text{O}_3$ Solid Solution during Spark Plasma Sintering." *Advances in Applied Ceramics* 104(2): 55–58.
- Kakegawa, Kazuyuki, Naofumi Uekawa, Yong Jun Wu, and Yoshinori Sasaki. 2003a. "Change in the Compositional Distribution in Perovskite Solid Solutions during the Sintering by SPS." *Materials Science and Engineering B* 99(1–3): 11–14.
- Kamel, Talal M., and G. de With. 2008. "Grain Size Effect on the Poling of Soft $\text{Pb}(\text{Zr,Ti})\text{O}_3$ Ferroelectric Ceramics." *Journal of the European Ceramic Society* 28(4): 851–61.
- Katiyar, V. K., S. L. Srivastava, and Janardan Singh. 1994. "Dielectric and Piezoelectric Properties of Lead Zirconate Titanate Doped with Chromium Oxide." *Journal of Applied Physics* 76(1): 455–65.
- Khatri, Praveen, Banarji Behera, and R. N.P. Choudhary. 2009. "Structural and Impedance Properties of $\text{Ca}_3\text{Nb}_2\text{O}_8$ Ceramics." *Journal of Physics and Chemistry of Solids* 70(2): 385–89.
- Kim, Tae Song, Chong Hee Kim, and Myung Hwan Oh. 1994. "Structural and Electrical Properties of Rf Magnetron-Sputtered $\text{Ba}_{1-x}\text{Sr}_x\text{TiO}_3$ Thin Films on Indium-Tin-Oxide-Coated Glass Substrate." *Journal of Applied Physics* 75(12): 7998–8003.
- Kleitz, M, L Dessemond, and M C Steil. 1995. "Model for Ion-Blocking at Internal Interfaces in Zirconias." *Solid State Ionics* 75: 107–15.
- Koo, Sang Mo, Seung Hwan Shim, Jong Won Yoon, and Kwang Bo Shim. 2006. "Microstructural Characterization of Fine-Grained $\text{Pb}(\text{Zr}_{0.52}\text{Ti}_{0.48})\text{O}_3$ Ceramics Fabricated by a Spark Plasma Sintering." *Key Engineering Materials* 317–318: 155–58.
- Koops, C. G. 1951. "On the Dispersion of Resistivity and Dielectric Constant of Some Semiconductors at Audiofrequencies." *Physical Review* 83(1): 121–24.
- Kour, P. et al. 2016. "Enhanced Ferroelectric and Piezoelectric Properties in La-Modified PZT Ceramics." *Applied Physics A* 122(6): 591.
- Kousksou, T. et al. 2014. "Energy Storage: Applications and Challenges." *Solar Energy Materials and Solar Cells* 120(PART A): 59–80.
- Kulcsar, Frank. 1959. "Electromechanical Properties of Lead Titanate Zirconate Ceramics Modified with Certain Three-or Five-Valent Additions." *Journal of the American Ceramic Society* 42(7): 343–49.
- . 1965. "Electromechanical Properties of Lead Titanate Zirconate Ceramics Modified with Tungsten and Thorium." *Journal of the American Ceramic Society* 48(1): 54–54.
- Kulkarni, A. K., and G. A. Rohrer. 1989. "Development of Ferroelectric Materials for Memory Applications." In Publ by IEEE, 150–55.

- Kumar, Ashok, N. M. Murari, and R. S. Katiyar. 2009. "Investigation of Dielectric and Electrical Behavior in $\text{Pb}(\text{Fe}_{0.66}\text{W}_{0.33})_{0.50}\text{Ti}_{0.50}\text{O}_3$ Thin Films by Impedance Spectroscopy." *Journal of Alloys and Compounds* 469(1–2): 433–40.
- Kusko, Alexander, and John Dedad. 2007. "Stored Energy - Short-Term and Long-Term Energy Storage Methods." *IEEE Industry Applications Magazine* 13(4): 66–72.
- Langman, RICHARD A., ROBERT B. Runk, and SIDNEY R. Butler. 1973. "Isothermal Grain Growth of Pressure-Sintered PLZT Ceramics." *Journal of the American Ceramic Society* 56(9): 486–88.
- Li, Juan. 2005. "Effects of Preparation Conditions on the Structural and Optical Properties of Spark Plasma-Sintered PLZT (8/65/35) Ceramics." 3331: 3327–31.
- Li, Qi et al. 2014. "High Energy and Power Density Capacitors from Solution-Processed Ternary Ferroelectric Polymer Nanocomposites." *Advanced Materials* 26(36): 6244–49.
- . 2015. "Flexible Higher-temperature Dielectric Materials from Polymer Nanocomposites." *Nature* 523(7562): 576–79.
- Liu, Chang, Feng Li, Ma Lai-Peng, and Hui Ming Cheng. 2010. "Advanced Materials for Energy Storage." *Advanced Materials* 22(8): E28–62.
- Liu, Hong et al. 2015. "Effect of MnO_2 Doping on Piezoelectric, Dielectric and Ferroelectric Properties of PNN–PZT Ceramics." *Ceramics International* 41(9).
- Liu, Wenfeng, and Xiaobing Ren. 2009. "Large Piezoelectric Effect in Pb-Free Ceramics." *Physical Review Letters* 103(25): 257602.
- Liu, Zhen et al. 2015. "Temperature-Dependent Stability of Energy Storage Properties of $\text{Pb}_{0.97}\text{La}_{0.02}(\text{Zr}_{0.58}\text{Sn}_{0.335}\text{Ti}_{0.085})\text{O}_3$ Antiferroelectric Ceramics for Pulse Power Capacitors." *Applied Physics Letters* 106(26): 1–5.
- Lvovich, Vadim F. 2012. *Impedance Spectroscopy: Applications to Electrochemical and Dielectric Phenomena*. Hoboken, NJ, USA: John Wiley and Sons.
- MacDonald, James Ross. 1987. "Impedance Spectroscopy--Emphasizing Solid Materials and Systems." *Wiley-Interscience, John Wiley and Sons*: 1–346.
- Mah, S. B. et al. 2000. "Structural and Electrical Characteristics of $(\text{Pb}_{1-x}\text{La}_x)(\text{Zr}_{0.5}\text{Ti}_{0.5})\text{O}_3$ Thin Film Capacitors." *Materials Research Bulletin* 35(7): 1113–22.
- Mazumder, R., and A. Sen. 2008. "'Ultra'-Low-Temperature Sintering of PZT: A Synergy of Nano-Powder Synthesis and Addition of a Sintering Aid." *Journal of the European Ceramic Society* 28(14): 2731–37.
- McPherson, J. et al. 2002. "Proposed Universal Relationship between Dielectric Breakdown and Dielectric Constant." In *Technical Digest - International Electron Devices Meeting*, 633–36.

- McPherson, J. W. 2016. "On Why Dielectric Breakdown Strength Reduces with Dielectric Thickness." In *IEEE International Reliability Physics Symposium Proceedings*, Institute of Electrical and Electronics Engineers Inc., (3A)31–38.
- McPherson, Joe W. et al. 2003. "Trends in the Ultimate Breakdown Strength of High Dielectric-Constant Materials." *IEEE Transactions on Electron Devices* 50(8): 1771–78.
- McWilliams, Brandon, and Antonios Zavaliangos. 2008. "Multi-Phenomena Simulation of Electric Field Assisted Sintering." *Journal of Materials Science* 43(14): 5031–35.
- Mesquita, Alexandre, Claude Godart, Alain Michalowicz, and Valmor R. Mastelaro. 2012. "Pb_{0.90}Ba_{0.10}Zr_{0.40}Ti_{0.60}O₃ nanostructured Ferroelectric Ceramics Prepared by Spark Plasma Sintering." *Ferroelectrics* 429(1): 69–74.
- Mischenko, A. S. et al. 2006. "Giant Electrocaloric Effect in Thin-Film PbZr_{0.95}Ti_{0.05}O₃." *Science* 311(5765): 1270–71.
- Mishra, S. K., and Dhananjai Pandey. 1997. "Thermodynamic Nature of Phase Transitions in Pb(Zr_xTi_{1-x})O₃ Ceramics near the Morphotropic Phase Boundary. II. Dielectric and Piezoelectric Studies." *Philosophical Magazine B: Physics of Condensed Matter; Statistical Mechanics, Electronic, Optical and Magnetic Properties* 76(2): 227–40.
- Mishra, S. K., Dhananjai Pandey, and Anirudh P. Singh. 1996. "Effect of Phase Coexistence at Morphotropic Phase Boundary on the Properties of Pb(Zr_xTi_{1-x})O₃ Ceramics." *Applied Physics Letters* 69(12): 1707–9.
- Mishra, S. K., A. P. Singh, and Dhananjai Pandey. 1997. "Thermodynamic Nature of Phase Transitions in Pb(Zr_xTi_{1-x})O₃ Ceramics near the Morphotropic Phase Boundary. I. Structural Studies." *Philosophical Magazine B* 76(2): 213–26.
- Morozov, Maxim I., and Dragan Damjanovic. 2008. "Hardening-Softening Transition in Fe-Doped Pb(Zr,Ti)O₃ Ceramics and Evolution of the Third Harmonic of the Polarization Response." *Journal of Applied Physics* 104(3): 034107.
- Munir, Z. A., U. Anselmi-Tamburini, and M. Ohyanagi. 2006. "The Effect of Electric Field and Pressure on the Synthesis and Consolidation of Materials: A Review of the Spark Plasma Sintering Method." *Journal of Materials Science* 41(3): 763–77.
- Munir, Zuhair A., Dat V. Quach, and Manshi Ohyanagi. 2012. "Electric Field and Current Effects on Sintering." In Springer, Berlin, Heidelberg, 137–58.
- Nasri, S., A. L. Ben Hafsia, M. Tabellout, and M. Megdiche. 2016. "Complex Impedance, Dielectric Properties and Electrical Conduction Mechanism of La_{0.5}Ba_{0.5}FeO_{3-δ} Perovskite Oxides." *RSC Advances* 6(80): 76659–65.
- Nejzchleb, K. 1980. "Composition and Temperature Dependence of Resonant Frequency of PbTiO₃-PbZrO₃ Ceramics with Addition of Cr₂O₃." *Ferroelectrics* 26(1): 779–82.

- Neumeister, Peter et al. 2014. "Effect of Mechanical Constraints in Thin Ceramic LTCC/PZT Multilayers on the Polarization Behavior of the Embedded PZT." *International Journal of Applied Ceramic Technology* 11(3): 422–30.
- Neusel, Claudia, and Gerold A. Schneider. 2014. "Size-Dependence of the Dielectric Breakdown Strength from Nano- to Millimeter Scale." *Journal of the Mechanics and Physics of Solids* 63(1): 201–13.
- Noheda, B. et al. 1999. "A Monoclinic Ferroelectric Phase in the $\text{Pb}(\text{Zr}_{1-x}\text{Ti}_x)\text{O}_3$ Solid Solution." *Applied Physics Letters* 74(14): 2059–61.
- . 2000. "Tetragonal-to-Monoclinic Phase Transition in a Ferroelectric Perovskite: The Structure." *Physical Review B - Condensed Matter and Materials Physics* 61(13): 8687–95.
- . 2001. "Stability of the Monoclinic Phase in the Ferroelectric Perovskite $\text{PbZr}_{1-x}\text{Ti}_x\text{O}_3$." *Physical Review B - Condensed Matter and Materials Physics* 63(1): 014103.
- Panwar, N. L., S. C. Kaushik, and Surendra Kothari. 2011. "Role of Renewable Energy Sources in Environmental Protection: A Review." *Renewable and Sustainable Energy Reviews* 15(3): 1513–24.
- Park, Jong-Keuk, Ui-Jin Chung, Nong M. Hwang, and Doh-Yeon Kim. 2001. "Preparation of Dense Lead Magnesium Niobate-Lead Titanate ($\text{Pb}(\text{Mg}_{1/3}\text{Nb}_{2/3})\text{O}_3\text{-PbTiO}_3$) Ceramics by Spark Plasma Sintering ." *Journal of the American Ceramic Society* 84(12): 3057–59.
- Park, Jong Keuk, Ui Jin Chung, and Doh Yeon Kim. 2006. "Application of Spark Plasma Sintering for Growing Dense $\text{Pb}(\text{Mg}_{1/3}\text{Nb}_{2/3})\text{O}_3\text{-35 mol\% PbTiO}_3$ Single Crystal by Solid-State Crystal Growth." *Journal of Electroceramics* 17(2–4): 509–13.
- Pauling, Linus. 1929. "The Principles Determining the Structure of Complex Ionic Crystals." *Journal of the American Chemical Society* 51(4): 1010–26.
- Pdungsap, Laddawan, Nitinai Udomkan, Supakorn Boonyuen, and Pongtip Winotai. 2005. "Optimized Conditions for Fabrication of La-Dopant in PZT Ceramics." *Sensors and Actuators, A: Physical* 122(2).
- Peláiz-Barranco, A., Y. González-Abreu, Jinfei Wang, and Tongqing Yang. 2014. "Energy Storage Power of Antiferroelectric and Relaxor Ferroelectric Ceramics." *Revista Cubana de Física* 31(2): 98–100.
- Peng, Pei et al. 2015. "Magnetoelectric Effect of $\text{CoFe}_2\text{O}_4/\text{Pb}(\text{Zr},\text{Ti})\text{O}_3$ Composite Ceramics Sintered via Spark Plasma Sintering Technology." *Ceramics International* 41(5): 6676–82.
- Prabakar, K., and S. P. Mallikarjun Rao. 2007. "Complex Impedance Spectroscopy Studies on Fatigued Soft and Hard PZT Ceramics." *Journal of Alloys and Compounds* 437(1–2): 302–10.
- Prabu, M., I. B. Shameem Banu, S. Gobalakrishnan, and Murthy Chavali. 2013. "Electrical and Ferroelectric Properties of Undoped and La-Doped PZT (52/48) Electroceramics Synthesized by Sol-Gel Method." *Journal of Alloys and Compounds* 551: 200–207.

- Prasad, N. V. et al. 1998. "Synthesis and Electrical Properties of $\text{SmBi}_5\text{Fe}_2\text{Ti}_3\text{O}_{18}$." *Modern Physics Letters B* 12(10): 371–81.
- Prasad, N. V., M. Chandra Sekhar, and G. S. Kumar. 2008. "Impedance Spectroscopic Studies on Lead Based Perovskite Materials." *Ferroelectrics* 366(1): 55–66.
- Prasad, N. V., K. Srinivas, and A. R. James. 2003. "Impedance Spectroscopic Studies on $\text{SmBi}_3\text{Ti}_3\text{O}_{12}$ Ceramics." *Ferroelectrics* 282: 217–28.
- Ragini, Rajeev Ranjan, S. K. Mishra, and Dhananjai Pandey. 2002. "Room Temperature Structure of $\text{Pb}(\text{Zr}_x\text{Ti}_{1-x}\text{O}_3)$ around the Morphotropic Phase Boundary Region: A Rietveld Study." *Journal of Applied Physics* 92(6): 3266–74.
- Rahaman, M. N. 2017. Ceramic Processing and Sintering, Second Edition *Ceramic Processing and Sintering, Second Edition*. CRC Press.
- Randall, C. A., D. J. Barber, and R. W. Whatmore. 1987. "Ferroelectric Domain Configurations in a Modified-PZT Ceramic." *Journal of Materials Science* 22(3): 925–31.
- Randall, Clive A. et al. 2005. "Intrinsic and Extrinsic Size Effects in Fine-Grained Morphotropic-Phase-Boundary Lead Zirconate Titanate Ceramics." *Journal of the American Ceramic Society* 81(3): 677–88.
- Rani, Alka, Jayant Kolte, and Prakash Gopalan. 2015. "Phase Formation, Microstructure, Electrical and Magnetic Properties of Mn Substituted Barium Titanate." *Ceramics International* 41(10): 14057–63.
- Rietveld, H. M. 1969. "A Profile Refinement Method for Nuclear and Magnetic Structures." *Journal of Applied Crystallography* 2(2): 65–71.
- Rukmini, H. R., R. N.P. Choudhary, and V. V. Rao. 1998. "Effect of Doping Pairs (La, Na) on Structural and Electrical Properties of PZT Ceramics." *Materials Chemistry and Physics* 55(2): 108–14.
- Ryu, Jungho, Jong-Jin Choi, and Hyoun-Ee Kim. 2001. "Effect of Heating Rate on the Sintering Behavior and the Piezoelectric Properties of Lead Zirconate Titanate Ceramics." *Journal of the American Ceramic Society* 84(4): 902–4.
- Sambasiva Rao, K., D. Madhava Prasad, P. Murali Krishna, and Joon Hyung Lee. 2008. "Synthesis, Electrical and Electromechanical Properties of a Tungsten-Bronze Ceramic Oxide: $\text{Pb}_{0.68}\text{K}_{0.64}\text{Nb}_2\text{O}_6$." *Physica B: Condensed Matter* 403(12): 2079–87.
- Sapriel, J. 1975. "Domain-Wall Orientations in Ferroelastics." *Physical Review B* 12(11): 5128–40.
- Schmitt, Ljubomira A et al. 2007. "Composition Dependence of the Domain Configuration and Size in $\text{Pb}(\text{Zr}_{1-x}\text{Ti}_x)\text{O}_3$ Ceramics." *Journal of Applied Physics* 101: 074107.

- Schwesig, D et al. 2011. "From Nanoparticles to Nanocrystalline Bulk: Percolation Effects in Field Assisted Sintering of Silicon Nanoparticles." *Nanotechnology* 22(13): 135601.
- Scott, J. F. 2007. "Applications of Modern Ferroelectrics." *Science* 315(5814): 954–59.
- Sekhar, M. Chandra, and N. Venkata Prasad. 2006. "Dielectric, Impedance, Magnetic and Magnetoelectric Measurements on YMnO_3 ." *Ferroelectrics* 345(1): 45–57.
- Selvamani, Rachna, Gurvinderjit Singh, V. S. Tiwari, and A. K. Karnal. 2018. "Dielectric and Piezoelectric Properties of Cr_2O_3 -Doped PLZT (7/65/35) Hot Pressed Ceramics." *Materials Today Communications* 15(March): 100–104.
- Shannigrahi, S. R., R. N.P. Choudhary, and H. N. Acharya. 1999. "Structural and Dielectric Properties of Nd Modified $\text{Pb}(\text{Zr}_{0.60}\text{Ti}_{0.40})\text{O}_3$ Ceramics." *Materials Science and Engineering B: Solid-State Materials for Advanced Technology* 60(1): 31–39.
- Sharma, H. D. et al. 1994. "Dielectric and Pyroelectric Characteristics of PZT Doped with Gadolinium." *Materials Science and Engineering B* 25(1): 29–33.
- Shen, Yang et al. 2017. "Polymer Nanocomposite Dielectrics for Electrical Energy Storage." *National Science Review* 4(1): 23–25.
- Shen, Zhijian, Mats Johnsson, Zhe Zhao, and Mats Nygren. 2002. "Spark Plasma Sintering of Alumina." *Journal of the American Ceramic Society* 85(8): 1921–27.
- Sherrill, Stefanie A., Parag Banerjee, Gary W. Rubloff, and Sang Bok Lee. 2011. "High to Ultra-High Power Electrical Energy Storage." *Physical Chemistry Chemical Physics* 13(46): 20714–23.
- Shimojo, Y. et al. 2008. "Dielectric Characters of $0.7\text{Pb}(\text{Mg}_{1/3}\text{Nb}_{2/3})\text{O}_3$ - 0.3PbTiO_3 ceramics Fabricated at Ultra-Low Temperature by the Spark-Plasma-Sintering Method." *Ceramics International* 34(6): 1449–52.
- Shirane, G., F. Jona, and R. Pepinsky. 1955. "Some Aspects of Ferroelectricity." *Proceedings of the IRE* 43(12): 1738–93.
- Shirane, G., E. Sawaguchi, and Y. Takagi. 1951. "Dielectric Properties of Lead Zirconate." *Physical Review* 84(3): 476–81.
- Shirane, Gen, and Kazuo Suzuki. 1952. "Crystal Structure of $\text{Pb}(\text{Zr-Ti})\text{O}_3$." *Journal of the Physical Society of Japan* 7(3): 333.
- Shirane, Gen, Kazuo Suzuki, and Akitsu Takeda. 1952. "Phase Transitions in Solid Solutions of PbZrO_3 and PbTiO_3 (II) X-Ray Study." *Journal of the Physical Society of Japan* 7(1): 12–18.
- Shirane, Gen, and Akitsu Takeda Tokyo. 1952. "Phase Transitions in Solid Solutions of PbZrO_3 and PbTiO_3 Small Concentrations of PbTiO_3 ." *Journal of the Physical Society of Japan* 7(1): 5–11.

Simons, Hugh et al. 2011. "Electric-Field-Induced Strain Mechanisms in Lead-Free 94% ($\text{Bi}_{1/2}\text{Na}_{1/2}$) TiO_3 -6% BaTiO_3 ." *Applied Physics Letters* 98(8): 082901.

Sinclair, D. C., and A. R. West. 1989. "Impedance and Modulus Spectroscopy of Semiconducting BaTiO_3 Showing Positive Temperature Coefficient of Resistance." *Journal of Applied Physics* 66(8): 3850–56.

———. 1994. "Effect of Atmosphere on the PTCR Properties of BaTiO_3 Ceramics." *Journal of Materials Science* 29(23): 6061–68.

Skandan, G. et al. 1994. "The Effect of Applied Stress on Densification of Nanostructured Zirconia during Sinter-Forging." *Materials Letters* 20(5–6): 305–9.

Soares, M.R., A.M.R. Senos, and P.Q. Mantas. 2000. "Phase Coexistence Region and Dielectric Properties of PZT Ceramics." *Journal of the European Ceramic Society* 20(3): 321–34.

Solanki, Ravindra Singh et al. 2013. "Evidence for a Tricritical Point Coinciding with the Triple Point in $(\text{Pb}_{0.94}\text{Sr}_{0.06})(\text{Zr}_x\text{Ti}_{1-x})\text{O}_3$: A Combined Synchrotron x-Ray Diffraction, Dielectric, and Landau Theory Study." *Physical Review B* 88(18): 184109.

Srivastava, Geetika, Ankur Goswami, and A. M. Umarji. 2013a. "Temperature Dependent Structural and Dielectric Investigations of $\text{PbZr}_{0.5}\text{Ti}_{0.5}\text{O}_3$ Solid Solution at the Morphotropic Phase Boundary." *Ceramics International* 39(2): 1977–83.

Stanciu, L. A., V. Y. Kodash, and J. R. Groza. 2001. "Effects of Heating Rate on Densification and Grain Growth during Field-Assisted Sintering of $\alpha\text{-Al}_2\text{O}_3$ and MoSi_2 Powders." *Metallurgical and Materials Transactions A: Physical Metallurgy and Materials Science* 32(10): 2633–38.

Su, Shi et al. 2011. "Poling Dependence and Stability of Piezoelectric Properties of $\text{Ba}(\text{Zr}_{0.2}\text{Ti}_{0.8})\text{O}_3$ - $(\text{Ba}_{0.7}\text{Ca}_{0.3})\text{TiO}_3$ Ceramics with Huge Piezoelectric Coefficients." In *Current Applied Physics*, North-Holland, S120–23.

Suarez, M. et al. 2013. "Challenges and Opportunities for Spark Plasma Sintering: A Key Technology for a New Generation of Materials." In *Sintering Applications*, InTechOpen.

Sun, Huajun et al. 2015. "Effects of CuO Additive on Structure and Electrical Properties of Low-Temperature Sintered $\text{Ba}_{0.98}\text{Ca}_{0.02}\text{Zr}_{0.02}\text{Ti}_{0.98}\text{O}_3$ Lead-Free Ceramics." *Ceramics International* 41(1): 555–65.

Takahashi, Sadayuki. 1982. "Effects of Impurity Doping In Lead Zirconate-Titanate Ceramics." *Ferroelectrics* 41(1): 143–56.

Takahiro, Yamakawa, Kataoka Masako, and Sashida Norikazu. 2000. "Influence of Poling Conditions on the Piezoelectric Properties of PZT Ceramics." *Journal of Materials Science: Materials in Electronics* 1(11): 425–28.

Takeuchi, Tomonari, Yasuo Takeda, et al. 2000. "Rapid Preparation of Dense $(\text{La}_{0.9}\text{Sr}_{0.1}\text{CrO}_3)$ Ceramics by Spark-Plasma Sintering." *Journal of The Electrochemical Society* 147(11): 3979.

- Takeuchi, Tomonari, Mitsuharu Tabuchi, et al. 2000. "Synthesis of Dense Lead Titanate Ceramics with Submicrometer Grains by Spark Plasma Sintering." *Journal of the American Ceramic Society* 83(3): 541–44.
- Takeuchi, Tomonari et al. 2004. "Synthesis of Dense Lead Titanate Ceramics with Submicrometer Grains by Spark Plasma Sintering." *Journal of the American Ceramic Society* 83(3): 541–44.
- Tandon, R P. 1998. "Impedance Spectroscopy of Lanthanum Modified $\text{Pb}(\text{Zr},\text{Ti})\text{O}_3$ Ceramics." 32: 327–29.
- Tejuca, L.G. 1992. Properties and Applications of Perovskite-Type Oxides *Properties and Applications of Perovskite-Type Oxides*. CRC Press.
- Tiwari, Vineet, and Geetika Srivastava. 2015. "The Effect of Li_2CO_3 Addition on the Structural, Dielectric and Piezoelectric Properties of PZT Ceramics." *Ceramics International* 41(2): 2774–78.
- Tokita, Masao. 2013. "Spark Plasma Sintering (SPS) Method, Systems, and Applications." In *Handbook of Advanced Ceramics: Materials, Applications, Processing, and Properties: Second Edition*, Elsevier Inc., 1149–77.
- Tuan, Dang Anh, Nguyen Trong Tinh, Vo Thanh Tung, and Truong Van Chuong. 2015. "Ferroelectric and Piezoelectric Properties of Lead-Free BCT-xBZT Solid Solutions." *Materials Transactions* 56(9): 1370–73.
- Uchida, Naoya, and Takuro Ikeda. 1967. "Studies on $\text{Pb}(\text{Zr-Ti})\text{O}_3$ Ceramics with Addition of Cr_2O_3 ." *Japanese Journal of Applied Physics* 6(11): 1292–99.
- Udayakumar, K. R. et al. 1995. "Thickness-Dependent Electrical Characteristics of Lead Zirconate Titanate Thin Films." *Journal of Applied Physics* 77(8): 3981–86.
- Ueda, Ichiro. 1972. "Effects of Additives on Piezoelectric and Related Properties of PbTiO_3 Ceramics." *Japanese Journal of Applied Physics* 11(4): 450–62.
- Ulrich, Richard, Len Schaper, David Nelms, and Matt Leftwich. 2000. "Comparison of Paraelectric and Ferroelectric Materials For Applications as Dielectrics in Thin Film Integrated Capacitors." *The International Journal of Microcircuits and Electronic Packaging* 23: 172–81.
- Upadhyay, Ashutosh, and Akhilesh Kumar Singh. 2016. "Electric Field Induced Structural Transformations across the Morphotropic Phase Boundary of $(1-x)\text{Bi}(\text{Mg}_{1/2}\text{Ti}_{1/2})\text{O}_3$ -x PbTiO_3 Piezoceramics." *Scripta Materialia* 115: 71–74.
- Valasek, J. 1921. "Piezo-Electric and Allied Phenomena in Rochelle Salt." *Phys. Rev.* 17(4): 475–81.
- Vanderbilt, David, and Morrel H. Cohen. 2001. "Monoclinic and Triclinic Phases in Higher-Order Devonshire Theory." *Physical Review B - Condensed Matter and Materials Physics* 63(9): 094108.

- Vittayakorn, Naratip et al. 2003. "Perovskite Phase Formation and Ferroelectric Properties of the Lead Nickel Niobate-Lead Zinc Niobate-Lead Zirconate Titanate Ternary System." *Journal of Materials Research* 18(12): 2882–89.
- Wada, Takahiro, Kenji Tsuji, Takehisa Saito, and Yoshihiro Matsuo. 2003. "Ferroelectric NaNbO₃ Ceramics Fabricated by Spark Plasma Sintering." *Japanese Journal of Applied Physics, Part 1: Regular Papers and Short Notes and Review Papers* 42(9B): 6110–14.
- Wagner, Karl Willy. 1913. "Zur Theorie Der Unvollkommenen Dielektrika." *Annalen der Physik* 345(5): 817–55.
- Walker, Julian et al. 2016. "Dual Strain Mechanisms in a Lead-Free Morphotropic Phase Boundary Ferroelectric." *Scientific Reports* 6(1): 1–8.
- Wang, Xiucui et al. 2016. "Phase Transition and Dielectric Properties of (Pb,La)(Zr,Sn,Ti)O₃ ceramics at Morphotropic Phase Boundary." *Journal of Alloys and Compounds* 673: 67–72.
- Warren, W. L. et al. 1995. "Alignment of Defect Dipoles in Polycrystalline Ferroelectrics." *Applied Physics Letters* 67(12): 1689.
- . 1996. "Defect-Dipole Alignment and Tetragonal Strain in Ferroelectrics." *Journal of Applied Physics* 79(12): 9250–57.
- Warren, William L. et al. 1996. "Oxygen Vacancy Motion in Perovskite Oxides." *Journal of the American Ceramic Society* 79(2): 536–38.
- Whittingham, M. Stanley. 2008. "Materials Challenges Facing Electrical Energy Storage." *MRS Bulletin* 33(4): 411–19.
- Wongdamnern, N. et al. 2008. "Comparative Studies of Dynamic Hysteresis Responses in Hard and Soft PZT Ceramics." *Ceramics International* 34(4).
- Wu, Yong Jun, Ryo Kimura, et al. 2002. "Spark Plasma Sintering of Transparent PbZrO₃-PbTiO₃-Pb(Zn_{1/3}Nb_{2/3})O₃ Ceramics." *Japanese Journal of Applied Physics, Part 2: Letters* 41(2 B): 5–8.
- Wu, Yong Jun et al. 2005. "Effects of Preparation Conditions on the Structural and Optical Properties of Spark Plasma-Sintered PLZT (8/65/35) Ceramics." *Journal of the American Ceramic Society* 88(12): 3327–31.
- Wu, Yong Jun, Naofumi Uekawa, and Kazuyuki Kakegawa. 2003. "Sandwiched BaNd₂Ti₄O₁₂/Bi₄Ti₃O₁₂/BaNd₂Ti₄O₁₂ Ceramics Prepared by Spark Plasma Sintering." *Materials Letters* 57(24–25): 4088–92.
- Wu, Yong Jun, Naofumi Uekawa, Kazuyuki Kakegawa, and Yoshinori Sasaki. 2002. "Compositional Fluctuation and Dielectric Properties of Pb(Zr_{0.3}Ti_{0.7})O₃ Ceramics Prepared by Spark Plasma Sintering." *Materials Letters* 57(3): 771–75.

- Wu, Yong Jun, Naofumi Uekawa, Yoshinori Sasaki, and Kazuyuki Kakegawa. 2002. "Microstructures and Pyroelectric Properties of Multicomposition $0.9\text{PbZrO}_3 \cdot x\text{PbTiO}_3 \cdot (0.1-x)\text{Pb}(\text{Zn}_{1/3}\text{Nb}_{2/3})\text{O}_3$ Ceramics." *Journal of the American Ceramic Society* 85(8): 1988–92.
- Xia, Xiang et al. 2016. "Effects of Cr_2O_3 Doping on the Microstructure and Electrical Properties of $(\text{Ba,Ca})(\text{Zr,Ti})\text{O}_3$ Lead-Free Ceramics." *Frontiers of Materials Science* 10(2): 203–10.
- Xu, Yuhuan. 1991. "Other Ferroelectric Crystal Materials." In *Ferroelectric Materials and Their Applications*, Elsevier, 301–27.
- Yanagisawa, Osamu, Tomei Hatayama, and Kazuhiro Matsugi. 1994. "Recent Research on Spark Sintering Process." *Materia Japan* 33(12): 1489–96.
- Yang, Letao et al. 2019. "Perovskite Lead-Free Dielectrics for Energy Storage Applications." *Progress in Materials Science* 102(May 2018): 72–108.
- Yang, Zupei, Rui Zhang, Lili Yang, and Yunfei Chang. 2007. "Effects of Cr_2O_3 Doping on the Electrical Properties and the Temperature Stabilities of PNW-PMN-PZT Ceramics." *Materials Research Bulletin* 42(12): 2156–62.
- Yao, Kui et al. 2011. "Nonlinear Dielectric Thin Films for High-Power Electric Storage With Energy Density Comparable With Electrochemical Supercapacitors." *IEEE Transactions on Ultrasonics, Ferroelectrics, and Frequency Control* 58(9): 1968–74.
- Yao, Zhonghua et al. 2017. "Homogeneous/Inhomogeneous-Structured Dielectrics and Their Energy-Storage Performances." *Advanced Materials* 29(20).
- Yu, Zhi, and Chen Ang. 2002. "Maxwell–Wagner Polarization in Ceramic Composites BaTiO_3 – $(\text{Ni}_{0.3}\text{Zn}_{0.7})\text{Fe}_{2.1}\text{O}_4$." *Journal of Applied Physics* 91(2): 794–97.
- Zhang, L. X., and X. Ren. 2005. "In Situ Observation of Reversible Domain Switching in Aged Mn-Doped BaTiO_3 Single Crystals." *Physical Review B - Condensed Matter and Materials Physics* 71(17): 174108.
- Zhang, Ling, Shenglin Jiang, Baoyan Fan, and Guangzu Zhang. 2015. "Enhanced Energy Storage Performance in $(\text{Pb}_{0.858}\text{Ba}_{0.1}\text{La}_{0.02}\text{Y}_{0.008})(\text{Zr}_{0.65}\text{Sn}_{0.3}\text{Ti}_{0.05})\text{O}_3$ - $(\text{Pb}_{0.97}\text{La}_{0.02})(\text{Zr}_{0.9}\text{Sn}_{0.05}\text{Ti}_{0.05})\text{O}_3$ Anti-Ferroelectric Composite Ceramics by Spark Plasma Sintering." *Journal of Alloys and Compounds* 622: 162–65.
- Zhang, Q. M., H. Wang, N. Kim, and L. E. Cross. 1994. "Direct Evaluation of Domain-Wall and Intrinsic Contributions to the Dielectric and Piezoelectric Response and Their Temperature Dependence on Lead Zirconate-Titanate Ceramics." *Journal of Applied Physics* 75(1): 454–59.
- Zhang, Wenli, and Richard E. Eitel. 2013. "Sintering Behavior, Properties, and Applications of Co-Fired Piezoelectric/Low Temperature Co-Fired Ceramic (PZT-SKN/LTCC) Multilayer Ceramics." *International Journal of Applied Ceramic Technology* 10(2): 354–64.

Zhang, X. L., Z. X. Chen, L. E. Cross, and W. A. Schulze. 1983. "Dielectric and Piezoelectric Properties of Modified Lead Titanate Zirconate Ceramics from 4.2 to 300 K." *Journal of Materials Science* 18(4): 968–72.

Zhao, Zhe et al. 2004. "Grain-Size Effects on the Ferroelectric Behavior of Dense Nanocrystalline BaTiO₃ Ceramics." *Physical Review B - Condensed Matter and Materials Physics* 70(2): 1–8.

Zheng, M. P. et al. 2013. "Effect of Valence State and Incorporation Site of Cobalt Dopants on the Microstructure and Electrical Properties of 0.2PZN-0.8PZT Ceramics." *Acta Materialia* 61(5): 1489–98.

Zheng, Mupeng, Yudong Hou, Zhirong Ai, and Mankang Zhu. 2017. "Nanocrystalline Buildup, Relaxor Behavior, and Polarization Characteristic in PZT–PNZN Quaternary Ferroelectrics." *Journal of the American Ceramic Society* 100(7): 3033–41.

Zhou, L J et al. 2004. "Preparation and Properties of Lead Zirconate Stannate Titanate Sintered by Spark Plasma Sintering." *Journal of the American Ceramic Society* 87(4): 606–11.

Zhou, Longjie et al. 2006. "Electric Fatigue in Ferroelectric Lead Zirconate Stannate Titanate Ceramics Prepared by Spark Plasma Sintering." *Journal of the American Ceramic Society* 89(12): 3868–70.

Zhou, Xin et al. 2009. "Electrical Breakdown and Ultrahigh Electrical Energy Density in Poly(Vinylidene Fluoride-Hexafluoropropylene) Copolymer." *Applied Physics Letters* 94(16): 162901.

Zuo, Ruzhong, Torsten Granzow, Doru C. Lupascu, and Jürgen Rödel. 2007. "PMN-PT Ceramics Prepared by Spark Plasma Sintering." *Journal of the American Ceramic Society* 90(4): 1101–6.